UNIVERSITY *of* TASMANIA

University of Tasmania
School of Physical Sciences

NUMERICAL SIMULATIONS OF EVOLVING ATMOSPHERIC VORTICES USING 'TANGENT PLANE' APPROXIMATIONS

Jason Michael Cosgrove
BSc (Hons)

October 2017

A thesis submitted in fulfilment
of the requirements for the degree of
Doctor of Philosophy

Supervisors: Professor L. K. Forbes and Dr. Michael Brideson

Declaration

Except where stated this thesis is, to the best of my knowledge, my own work and my supervisor has approved its submission.

Signed by student:

Date: 5 October 2017

Signed by supervisor:

Date: 5 October 2017

Statement of Published Work

Statement of Co-Authorship

The following people and institutions contributed to the publication of work undertaken as part of this thesis: Jason Cosgrove, School of Physical Sciences = **Candidate**

Larry Forbes, University of Tasmania = **Author 1**

Paper 1

Cosgrove, J. M. and Forbes, L. K., The formation of large-amplitude fingers in atmospheric vortices, *ANZIAM Journal*, **56**, 2016, 395 – 416.

Located primarily in Chapter 4

Candidate was the primary author and Author 1 contributed to the idea, its formalisation and development. Candidate - 70%, Author 1 - 30%

Paper 2

Cosgrove, J. M. and Forbes, L. K., Nonlinear behaviour of interacting mid-latitude atmospheric vortices, *Journal of Engineering Mathematics*, **104**, 2017, 41 – 62.

Located primarily in Chapter 5

Candidate was the primary author and Author 1 contributed to the idea, its formalisation and development. Candidate - 80%, Author 1 - 20%

Paper 3

Cosgrove, J. M. and Forbes, L. K., A δ-plane simulation of anticyclones perturbing circumpolar flows to form a transient north polar hexagon, *Monthly Notices of the Royal Astronomical Society*, **469**, 2017, 4133 – 4147.

Located primarily in Chapter 6

Candidate was the primary author and Author 1 contributed to the idea, its formalisation and development. Candidate - 90%, Author 1 - 10%

We the undersigned agree with the above stated "proportion of work undertaken" for each of the above published peer-reviewed manuscripts contributing to this thesis:

Signed:

	Professor Larry Forbes	Professor John Dickey
	Supervisor	Head of School
	School of Physical Sciences	School of Physical Sciences
	University of Tasmania	University of Tasmania
Date:	5 October 2017	5 October 2017

Acknowledgements

This journey started long before I was admitted into the Ph.D. program. The one constant in my life has been a passion for mathematics, which was encouraged by my high school mathematics teacher Mr. Chris Clark. My love for mathematics was further enhanced by Dr. David Paget who for some reason gave a mischievous boy with no significant role model a chance to participate in one of his maths camps.

I would like to thank my supervisor Professor Larry Forbes. Without his endless enthusiasm and guidance I would not have been able to undertake such a task. His generosity with his time will be forever appreciated. Larry's support has also enabled me to present the material in this thesis at internationally recognised conferences and publish in peer-reviewed journals.

I would also like to thank Dr. Michael Brideson who I often interrupted with conversations about almost everything apart from mathematics. I should mention he often helped with the mathematics as well and was never too busy to help.

To the most powerful person in the School of Mathematics and Physics, Karen Bradford, thank you for constantly looking out for me and ensuring I had every resource I required to complete this thesis. Also for being the first person to give me the opportunity to teach mathematics and to uncover the diamonds in the rough amongst my students. I will be forever indebted to you.

The work in this thesis was originally supported by the Tasmania Graduate Research Scholarship and later by an Australian Government Research Training Program Scholarship. I am grateful to the Australian Bureau of Meteorology for firstly being able to use their satellite images, and in particular to Mike Willmott for retrieving the data, secondly, giving permission to use their mean

sea-level pressure maps. I would also like to thank NASA for the use of their satellite images and Elsevier for the use of a previously published image.

I would also like to thank the reviewers of the three published papers. The quality of the articles and this thesis has greatly benefited from their thoughtful and constructive comments.

Last but not least I would like to thank my family - Anita and my three lovely sons Toby, Samuel and Joshua, you are the most important people in my life. I don't know how you put up with my idiosyncrasies. Without your belief in me this would have been a far greater task.

Abstract

Numerical simulations of evolving atmospheric phenomena are considered. The height of the vortices is small with respect to their width and depending on the atmospheric phenomenon being considered can have a diameter of hundreds if not thousands of kilometres. They can therefore be thought of as large flat structures in a shallow atmosphere. A weakly compressible atmosphere is assumed for both Earth-bound and Saturn simulations. The atmospheric fluid motion is subject to the Coriolis pseudo-force, due to atmospheres being in a non-inertial rotating reference frame. The simulations involve reducing the fully spherical nature of the atmosphere to a localised region, so that the commonly used 'tangent plane' approximations apply. The advantage of using 'tangent plane' approximations is that necessary spheroidal effects can be studied using Cartesian based equations. Three types of 'tangent plane' approximations are used, (i) the f-plane, where the Coriolis parameter is assumed constant over the entire region; (ii) the β-plane, where the Coriolis parameter varies linearly with latitude and (iii) the δ-plane, which is a high latitude approximation where quadratic effects of the Coriolis term are accounted for.

Large-scale low-pressure systems in the atmosphere are occasionally observed to possess Kelvin-Helmholtz fingers spiralling outwards, and an example is shown in this thesis. However, these structures are hundreds of kilometres long, so that they are necessarily affected strongly by non-linearity. They are evidently unstable and are commonly observed to dissipate after a few hours, and in rare cases may last for days. A model for this phenomenon is presented in this thesis, based on the usual f-plane equations of meteorology, assuming an atmosphere governed by the ideal gas law. Large-amplitude perturbations are accounted for, by retaining the equations in their non-linear forms, and these are then solved numerically using a spectral method. Finger formation is modelled as an initial perturbation to the n^{th} Fourier mode, and the numerical results show that the fingers grow in time, developing structures that depend on the particular mode. Results are

compared with predictions of the β-plane theory and there is close alignment with f-plane results at mid-latitudes. An idealized vortex in the northern hemisphere is considered, but the results are at least in qualitative agreement with an observation of a system in the southern hemisphere.

Vortices in the atmosphere are rarely observed to be singular entities. Thus the non-linear behaviour of interacting mid-latitude vortices is also investigated. The vortices studied are coupled binary systems and the high- or low-pressure in each vortex is modelled initially using an exponential function. Non-linear results in the f-plane approximation are discussed at mid-latitudes. It is found that the vortices do or do not interact, depending on their initial radii and the location of their centres. A scaling law is found numerically for the ratio of these two quantities, which determines whether interaction does occur at the approximate mid-latitude 43°N. An approximate rule has been developed, to generalize the scaling law to other latitudes.

Atmospheric vortices are rarely circular structures and have been observed to have a definite polygonal form. Saturn's North Polar Hexagon is an example of such a vortex, and was discovered by Godfrey [31] who pieced together map projections of images captured by the Voyager mission to unveil a hexagonal structure over the north pole of Saturn. This thesis attempts to answer whether or not a hexagonal structure can be formed through anti-cyclones impinging on the dominant eastward circumpolar flow and is in part based upon the proposed theory by Allison *et al.* [1] that the Hexagon may be the result of at least one impinging anti-cyclone perturbing a circumpolar jet centrally located around the 76°N latitude. A high-latitude δ-plane approximation is used to simulate the interaction between an initially circular circumpolar jet and at least one perturbing anti-cyclone. The simulations with one perturbing anti-cyclone failed to form a hexagonal structure; yet by including an additional anti-cyclone it was found that depending on the strength, location and radius of the perturbing anti-cyclones a hexagonal feature could develop. However, the longevity and drift rate of the actual Hexagon must be attributed to other factors not considered in this thesis.

Contents

List of Figures

List of Tables

Chapter 1

Introduction

The study of vortices in fluids has a rich history of research that continues to this day. This includes an array of applications from oceanographic, atmospheric and industrial problems. Vortices in fluids can be defined as strongly swirling coherent structures [67] or coherent regions of anomalous potential vorticity [51]. They form as a result of fluid rotation, shear and stratification.

The focus of this thesis is on the evolving behaviour of atmospheric vortices. Fluid motion in the atmosphere is subject to the Coriolis pseudo-force, due to the Earth's (or any other celestial body's) atmosphere being in a non-inertial reference frame. In such instances, the fluid motion is partially driven by the Coriolis pseudo-force. The continual rotation of the Earth (celestial body) plays a significant role in atmospheric dynamics, although the spherical nature of the Earth or any other rotating celestial body is often less important over scales smaller than global. In such cases, 'tangent plane' approximations are commonly used to simulate atmospheric phenomena as they simplify the full spheroidal equations without losing the general behaviour of the fluid system. The f-plane is the simplest and true 'tangent plane' approximation and is used when the effects of the Earth's rotation attributed to latitudinal change can be neglected; it assumes the Coriolis parameter is constant over the entire planar region and takes the value determined by the tangent point latitude. The influence of Earth's rotation varies with latitude and is approximated using the β-plane that includes an additional component that gives a measure of the rate of change in the Coriolis parameter f, denoted the β term. This approximation has the advantage of allowing for latitudinal variability of the Coriolis pseudo-force, whilst incorporating spherical effects that the f-plane ignores [70]. Rossby *et al.* [61] first developed the concept of the β-plane approximation in 1939. Surprisingly, it was not until the early 1960's when meteorological researchers such as

Phillips [58] and Lipps [48] began to legitimize the use of the β-plane approximation. Lipps [48] built on the work by Phillips [58] and outlined two specific conditions for which the β-plane approximation is valid for and emphasized that the conditions only hold in the mid-latitude regions.

Both the f-plane and β-plane approximations are used extensively in atmospheric fluid dynamics, but their validity is restricted to mid-latitude regions. Atmospheric vortices are not just confined to mid-latitude regions. Polar regions of celestial bodies also experience large-scale vortex behaviour. However, the commonly used f-plane and β-plane approximations are not valid to use in simulating atmospheric vortex behaviour in polar regions. In order to study high-latitude atmospheric Rossby waves Yang [78] proposed a δ-plane approximation. Similarly to the development of the β-plane, where the β term represents the rate of change in the Coriolis parameter f, the δ-plane (denoted γ-plane by Nof [57]) includes the latitudinal variation of β and thus allows for the quadratic variation in the Coriolis parameter around the polar regions, which was noted by LeBlond [46] in what is considered to be the first valid polar plane approximation technique. Nof [57] gives two sets of equations dependent on the tangent point latitude. The first set considers the tangent point to be located at the pole so that the linear variation term $\beta = 0$ and disappears entirely, resulting in the Coriolis parameter having solely quadratic variability. The second set of equations given by Nof [57] takes into account that not all polar approximations have the need for the pole to be the tangent point; in this case a simple coordinate transformation enables the now non-zero β term to be recovered so that the Coriolis parameter also has linear variation in latitude. A similar approach was used by Harlander *et al.* [34] to investigate flows near the poles with a poleward rigid boundary, thereby only having linear and quadratic change along the north-south y-axis. Unlike the β-plane approximation, higher-order approximations such as the δ-plane theories outlined by Yang [78], Nof [57] and Harlander *et al.* [34] can not be derived from spherical geographic coordinates. However, using a rotated geographic coordinate system Harlander [33] was able to derive a δ-plane model from spherical geometry.

Kelvin-Helmholtz flow is a classical problem in fluid mechanics, and it refers to the situation in which two horizontal fluid layers, acted on by gravity and separated by a narrow interface, move with different mean speeds. As a result, a shearing instability is present at the interface. Small disturbances therefore grow in time, and may eventually develop into "cat's eye" billows, which are large complicated overturning structures. The problem has been the subject of intense study,

and is described in the texts by Chandrasekhar [13] and Drazin and Reid [23].

Since Kelvin-Helmholtz flow is unstable, it is inevitable that non-linear effects become important within finite time, because the growing disturbance at the interface eventually becomes of sufficiently large amplitude that linearized descriptions of it no longer apply. Moore [54] showed that a curvature singularity is formed at the interface within finite time, in the classical Kelvin-Helmholtz flow in which viscosity is ignored, and Cowley *et al.* [19] gave an ingenious asymptotic argument to confirm this prediction. Numerical solutions of this problem are found to fail at about the critical time at which the curvature singularity is formed, but Krasny [41] overcame this difficulty using a "vortex blob" method, in which the interface was effectively replaced by a vortex sheet of finite width. His calculations could then proceed beyond the time of singularity formation at the interface, and at later times he obtained the rolled-up surfaces typical of Kelvin-Helmholtz instability. Nevertheless, the problem remains ill-conditioned, and Baker and Pham [5] demonstrated that different formulations of the "vortex blob" approach could lead to different solutions at later times.

The curvature singularity at the interface is a consequence of ignoring viscosity. When viscous effects are re-introduced into mathematical models of such unstable flows, the singularity is replaced with a small region of intense vorticity, and this is responsible for the interface rolling up to form over-hanging structures. This was demonstrated by Forbes [26] in the related Rayleigh-Taylor instability in which a heavy fluid overlies a lighter one. Chen and Forbes [15] included viscous effects in the classical Kelvin-Helmholtz flow and carried out a careful study of the behaviour of the curvature in the inviscid case, and likewise showed that, when viscosity is included, the singularity in curvature is replaced with a patch of interfacial vorticity that is ultimately responsible for the formation of over-turning "cat's eye" spirals.

Instabilities in cylindrical flow geometries have also been the subject of considerable recent interest. Matsuoka and Nishihara [50] considered an initially cylindrical patch of fluid that is disturbed by a shock, and they showed that several over-turning plumes can form in a ring around the originally circular interface. Similar unstable outflows were studied by Forbes [27] in a cylindrical Rayleigh-Taylor flow, in which a light fluid is ejected from a line source into a surrounding heavy fluid.

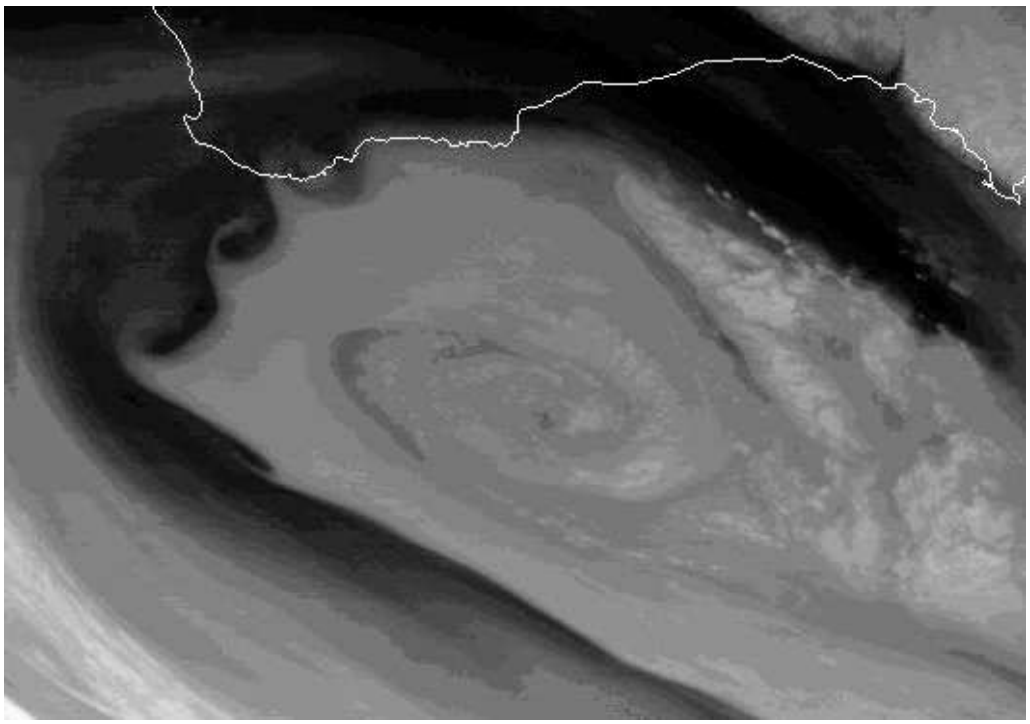

Figure 1.0.1: Satellite image originally processed by the Bureau of Meteorology from the geostationary meteorological satellite MTSAT-2 operated by the Japan Meteorological Agency, July 2, 2011 0323 GMT.

Instabilities can also occur at the cylindrical interface between two liquids, when either or both fluids undergo rotation. Crapper *et al.* [20] considered the stability of a cylindrical jet undergoing swirling motion with an additional velocity component directed along the axis of the cylinder. This was a linearized analysis in which disturbances to the interface were assumed small. However, Caflisch *et al.* [9] undertook a non-linear study of a rotating axi-symmetric jet with a line vortex present along its axis. Since the two fluids either side of the interface are moving with different mean angular speeds, a kind of rotational Kelvin-Helmholtz flow instability exists, and Caflisch *et al.* [9] found over-hanging plumes could develop along the jet. More recently, Forbes and Cosgrove [28] considered planar flow in which a line vortex is present up the z-axis of a cartesian coordinate system, but an initially cylindrical interface centred on the z-axis separated two fluids of possibly differing densities and angular speeds either side. They carried out a linearized inviscid analysis and demonstrated that Kelvin-Helmholtz type instabilities could occur in this cylindrical geometry, in a very similar manner to the classical planar situation discussed by Chandrasekhar [13, page 485]. Their large-amplitude inviscid results were also subject to the formation

of a curvature singularity at the interface within finite time, similar to the result of Moore [54] for planar flow. When viscous effects are included in the model, Forbes and Cosgrove [28] could obtain large-amplitude Kelvin-Helmholtz type fingers and billows arranged around the originally circular interface; however, strong mixing occurred, and as time progressed, some of the finger structures evidently even detached from the inner vortex.

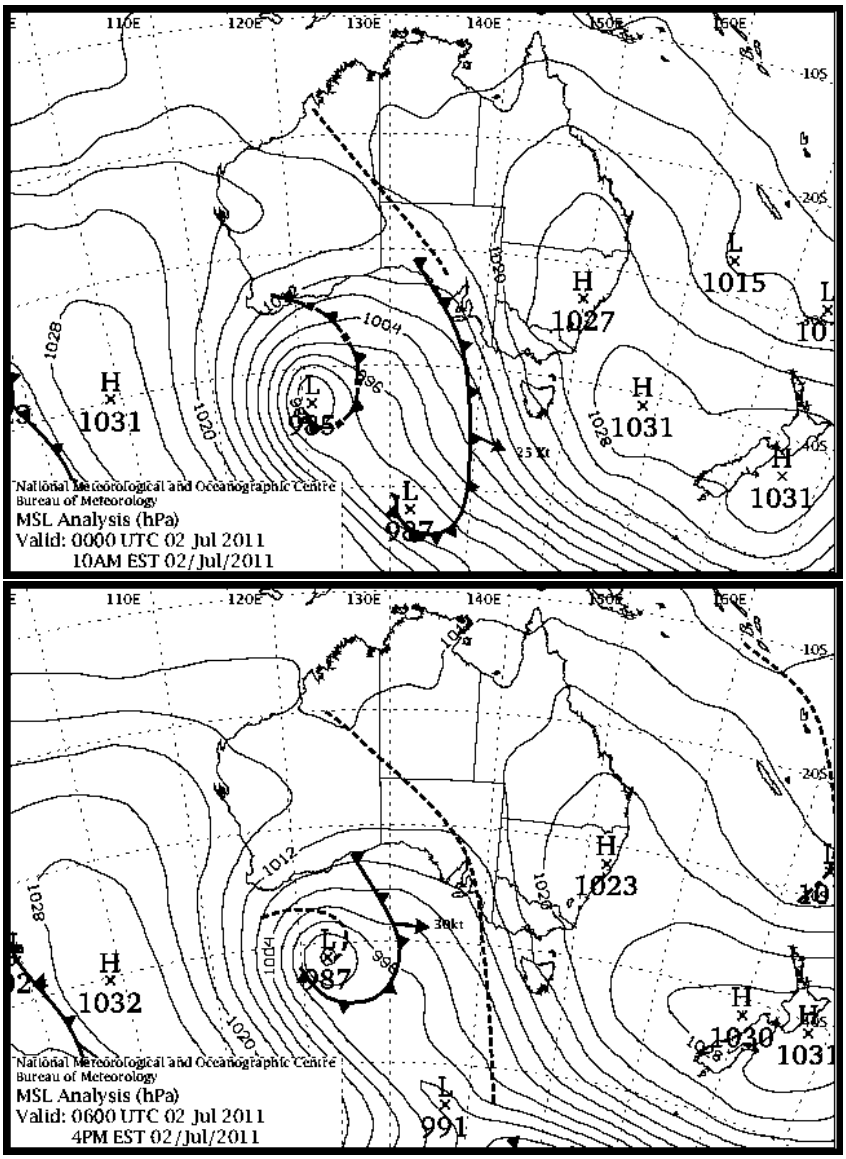

Figure 1.0.2: Mean sea-level pressure maps. Top: 0000 UTC 2 July 2011 and Bottom: 0600 UTC 2 July 2011. Printed with permission of the Australian Bureau of Meteorology.

It turns out that somewhat similar behaviour is occasionally encountered in meteorological

flows. One such example is presented in Figure 1.0.1. This flow occurred during July 2011, as a large low pressure system in the Great Australian Bight moved across the south-west corner of Western Australia; the outline of the coast of the continent is marked as a white line toward the top of this figure. This system rotated clockwise when viewed above from a satellite, and as it rotated, smaller curved fingers formed at the edge and moved around the system, starting at the south-east and moving up and around to the north-west (since this low pressure was situated in the southern hemisphere). The curved fingers are visible toward the upper left corner of this diagram, and although small relative to the overall atmospheric vortex, they nevertheless extend some hundreds of kilometres, so representing reasonably large-amplitude disturbances. These fingers were only present for about four hours and then disappeared. Figure 1.0.2 shows the mean sea-level pressure contours over continental Australia on July 2, 2011 at 0000 and 0600 UTC, spanning the time at which the finger formation had developed then dissipated. The low pressure system associated with the spiral finger structures can be seen to the south-east of the southern tip of Western Australia. These contour maps give an indication that the finger structures may be the result of the greater magnitude fluid velocity on the western side of the system, as indicated by the dense pressure contours to the west of the low pressure system associated with the finger structures.

Atmospheric vortices are not isolated singular entities. It is not unusual to see multiple vortices form within the same region. When two vortices form in close proximity they are referred to as binary systems and if they begin to interact this process is termed ‘binary interaction’ or ‘the Fujiwhara effect’, named after Fujiwhara because of his ground breaking work on interacting vortices in tank experiments [29, 30]. The North West Pacific is one such region where multiple tropical low pressures are often observed simultaneously [11]. In early October 2009 two typhoons formed in the Pacific Ocean to the south-east of Taiwan. An image of that binary system is provided in Figure 1.0.3 and shows the interaction between both Typhoons. Typhoon Parma is in the south-west quadrant and in the Typhoon Melor is in the eastern sector.

Figure 1.0.3: NASA image courtesy the MODIS Rapid Response Team at NASA GSFC, October 7, 2009. This image shows Typhoon Parma interacting with Typhoon Melor.

Due to Fujiwhara's insight binary interaction has been a major area of research over the last century. As well as tank experiments, binary interaction has been chronicled through observations and numerical modelling. The majority of such studies have involved tropical cyclones, as in the work of [11, 14, 44, 74, 76]. Brand [8] and Lander and Holland [45] used observational data of typhoons in the western North Pacific Ocean to analyse the interactive behaviour of binary tropical cyclones. Brand [8] took fifteen years ($1953 - 1967$) of data and under certain criteria found that there were 22 instances of binary tropical cyclone systems over this period. Brand concluded that the cyclones began to rotate about each other if the separation distance was less than 750 nm (nautical miles) and attraction occurred when within 400 nm.

A more comprehensive analysis of the interactive behaviour between binary tropical cyclones was presented by Lander and Holland [45] who used 44 years of data. In contrast to the Fujiwhara model where there is continual cyclonic rotation and mutual attraction, they found that a combination of interactions takes place. The cyclones approach in an anti-cyclonic orbit until they are

captured, followed by a period of cyclonic orbiting; then either they escape and move away or else they merge to become one. Dritschel and Waugh [24] categorised the interaction between binary vortices with uniform vorticity by considering the ratio of radii and separation distance. Their analysis of the interaction can be classified into (i) elastic interaction, (ii) partial straining-out, (iii) complete straining-out, (iv) partial merger and (v) complete merger.

The merger of binary systems has been extensively studied. Melander *et al.* [52] were the first to give insight as to the causes and conditions of merging vortices through the use of two complementary models. They considered a binary vortex system with like-signed vorticity regions and the results from both models were coupled to give a merger condition. A thorough examination of vortices in rotating fluids was carried out by Hopfinger and van Heijst [37]. They give a summary of the key findings of merging vortices, in particular a way of predicting when the merger of equally intense vortices will occur. In the past it was quite rare to observe a binary cyclonic system actually merge. The merger of Typhoon Pat and Ruth during September 1994 is believed to be the first documented case of such an event [44]. However, with more chaotic weather phenomena occurring with every passing year and the increased satellite coverage of the Earth over the past two decades the observed merger of cyclonic systems has increased. The merger of cyclone Zeb and Alex in late 1998 by way of Alex being completely strained out into a spiral band of Zeb [42] is another example. The eastern Pacific staged the merger of two tropical depressions, formerly tropical storm Henriette and Hurricane Gil. After three days of interaction they merged on 9 September 2001 [59]. The interaction of Typhoon No. 17 (T0917) and Typhoon No. 18 (T0918) occurred over the Philippines in late September 2009. The interaction evolved from elastic (where they rotate in a cyclonic orbit about each other) to partial merger, followed by partial straining out, and final separation to exhibit elastic interaction again [65]. The interactions observed in the work done by [42, 59, 65] displayed the five categories of binary interaction as defined by Dritschel and Waugh [24].

Ritchie and Holland [60] and Holland and Dietachmayer [35] proposed models that attempt to give insight into the observational findings of Lander and Holland [45]. Ritchie and Holland [60] used discrete vortex patches that were initially circular Rankine combined vortices to get a first-order approximation to observed atmospheric vortices. Their results indicated that if the vortices are comparable in strength and size, then either rapid merger ensues when the separation is less

than some critical distance, or else the vortices orbit about each other without merging when separation distances are larger. A derivation of the approximate critical distance for merger was given in terms of the ratio of strain and restoration processes [60, section 4(b)]. Holland and Dietachmayer [35] confirmed the findings of Ritchie and Holland [60] by considering a shallow-water model in spherical geometry. They studied not only the interaction between binary systems but also multiple vortex interaction, and in particular the interaction between two cyclones and one anti-cyclone with significantly reduced intensity (10% of the cyclones). Their simulations indicate that the anti-cyclone is sheared apart to the point of non-existence by the interaction processes of the binary cyclones and has virtually no effect on the merger of the cyclones.

The movement of the binary vortex systems induced by their interaction is also of considerable interest. Chan and Law [11] explored the interactive processes using a nondivergent barotropic model developed by Chan and Williams [12] which is governed by the conservation of absolute vorticity and includes the Coriolis parameter. The vortices are modelled in terms of a tangential wind profile in the form of an exponential function. The motion of the vortices is studied in two ways (i) with no background flow and (ii) in sheared flow and the f-plane and β-plane approximations are used for both. A comparison of the f-plane and β-plane solutions is given and their results show that mutual interaction between the vortices is virtually identical for both approximations. However, the β term moves the binary system to the north-west due to the well known β-drift. This in part confirmed the earlier work by Chang [14], who found that the β-drift also causes a more rapid merger of equally intense binary systems. However, for binary systems with a more intense system in the west, the β-drift induces separation of the systems. Although the f-plane approximation has certain limitations with respect to real world atmospheric simulations, Chan and Law [11] have shown that, when using the more atmospherically relevant β-plane approximation, the interactive processes are largely independent of β and thus the solutions obtained using the f-plane and β-plane are basically identical.

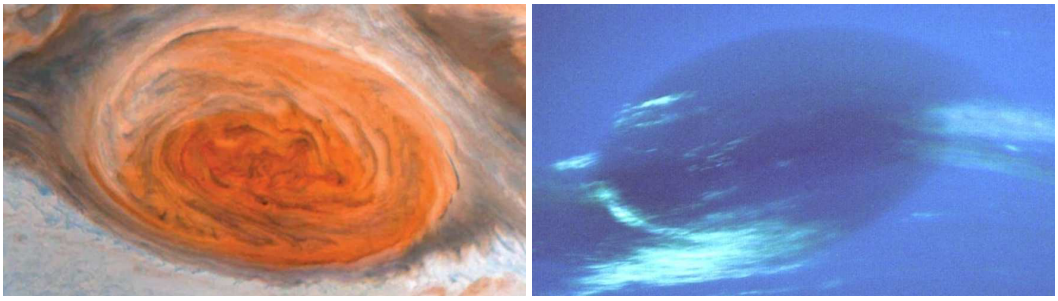

Figure 1.0.4: Left: The Great Red Spot (GRS) on Jupiter and Right: The Great Dark Spot (GDS) on Neptune.

Ziv and Alpert [79] considered binary interaction of extra-tropical cyclones at mid-latitude and subtropical areas in contrast to the works discussed above. Their study included analysing $17,313$ cyclone pairs over the domain $0° - 60°$N. An essential component to quantify their findings is what they define as the rotation factor (rotations per day of the binary system). For binary systems with separation distance less than 750 km they showed that for approximate latitudes $0° - 30°$N where anti-cyclones dominate, the rotation factor was negative, indicating anti-cyclonic relative rotation. Conversely, the rotation factor was positive, producing cyclonic relative rotation for latitudes greater than $30°$N.

Vortices in atmospheric fluids occur not only on Earth, but are also vivid features of other planetary environments. The Great Red Spot (GRS) on Jupiter shown in the left panel of Figure 1.0.4 is possibly the most famous and the lesser known Great Dark Spot (GDS) on Neptune illustrated in the right panel of Figure 1.0.4 and the North Polar Hexagon (NPH) on Saturn are just three examples within our Solar system. The North Polar Hexagon is of particular interest in this thesis due to its unconventional polygonal structure.

The Voyager space probes that were launched in 1977 heralded vast scientific insight into the study of the outer Solar system. Originally the objective was to obtain data on the atmospheric conditions of Jupiter and Saturn, their satellites and the rings of Saturn [66]. It was envisaged that the Voyager flight paths would enable observations of the north and south poles of Saturn's atmosphere. However, due to the south pole being in total darkness at the time, images of the south pole could not be captured [31]. The north polar images on the other hand revealed a hexagonal structure centred at the north pole. Godfrey [31] pieced together map-projections taken as Saturn rotated and thus was the first to identify Saturn's North Polar Hexagon. Figure 1.0.5 is the

sixth and final mosaic published in Godfrey's paper. Godfrey [31] also produced streamline maps that showed that there existed a hexagonal flow pattern about the pole, with a substantial counter-rotating vortex along one edge. It is also clear from these streamline plots that there are other counter-rotating vortices which were not visible, aligned along the other edges of the Hexagon.

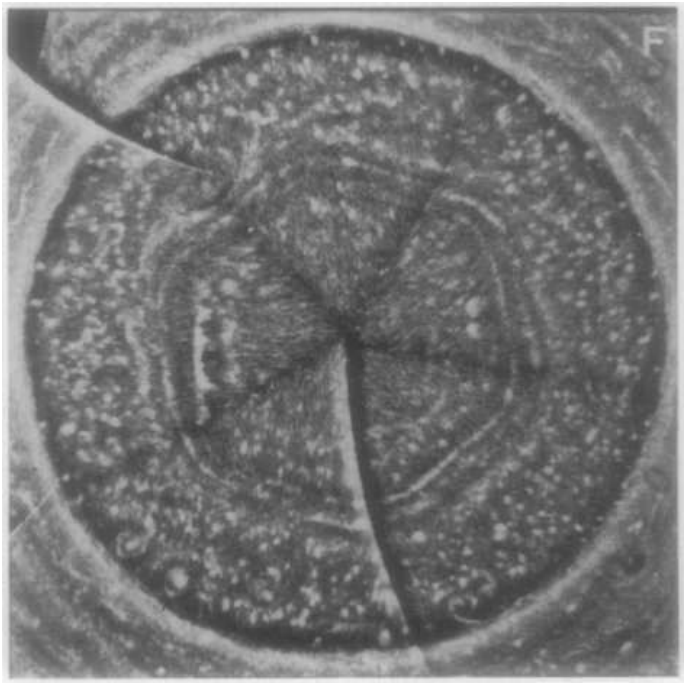

Figure 1.0.5: Composite map-projected images of Saturn's North Polar Hexagon as published by Godfrey [31] and reprinted with permission from Elsevier.

The Hexagon appears almost stationary with respect to the internal rotation of Saturn [32] and is ingrained in an eastward circumpolar jet of width 4° latitude. However, the cloud formations within the hexagonal structure were observed by the Voyager space craft to move with a velocity of approximately 100 ms^{-1} at the mid-point latitude of 76°N.

There has been some considerable work on interpreting the origin of the North Polar Hexagon on Saturn; Allison *et al.* [1] proposed that the Hexagon is the result of the eastward jet, in the form of a planetary Rossby wave being continually perturbed by at least one anti-cyclonic elliptical vortex to the south of the structure. This proposition is in part based on the fact that an anti-cyclone with approximate radius 3000 km is observed impinging on one edge of the Hexagon in the mosaic published by Godfrey [31] and thus has been of considerable interest and widely cited. Godfrey

[32] estimated that the visible vortex has a rotation rate of $-8.13 \pm 0.6 \times 10^{-9}$ rads s^{-1} with respect to a fixed meridian, in later publications the rotation rate of the once visible vortex is referred to as the drift rate. The drift rate calculated by Godfrey [32] corresponds to roughly $-0.040°$ per day using data captured over a 9 month period during 1980 and 1981.

Until the early 1990's it was not established whether the rotation rate estimated by Godfrey [32] was in fact representative of the actual movement of the vortex or just error that could be associated with the internal rotation rate of Saturn [10]. The Hubble Space Telescope (HST) observations in 1990 and 1991 confirmed that there is movement of the visible vortex relative to the rotation of Saturn. Caldwell *et al.* [10] coupled the data interpreted from the original Voyager images and the HST observations to form an 11-year baseline. It was found that over this longer period the vortex moved $-0.0569°$ per day.

The Hexagon and visible vortex were also observed over the period July 1990 to October 1991 using ground-based instruments [62]. Over this sixteen month period the vortex drifted longitudinally at a mean rate of $-0.0353°$ per day. This data was collated with the observational data used by Godfrey [32] to give another perspective into the long term motion of the vortex. The long term drift rate in this case was calculated to be $-0.0577°$ per day [62], nearly identical to that of the HST value calculated by Caldwell *et al.* [10]. Although the average drift rates of the visible vortex given by Godfrey [32], Caldwell *et al.* [10] and Sanchez-Lavega *et al.* [62] are relatively small with respect to Saturn's internal rotation, the short-term fluctuation is considerable, drifting upwards of $14°$ longitudinally at rates of approximately $1°$ per day, as well as latitudinal movement but on a much smaller scale [62].

Interestingly, Sanchez-Lavega *et al.* [62] raise the possibility that the vortex observed using ground-based technology in 1990 may be a different vortex than that captured by the Voyager spacecraft. This conclusion is based on knowing the longitude of the vortex at the time when the Voyager and 1990 images were captured and projecting forward in time using the respective short-term drift rates of $-0.040°$ [31] and $-0.0353°$ [62] per day. It was shown that the vortex would be in two distinct locations separated by approximately $60°$ in longitude, the angle spanned by a hexagon side. This therefore led Sanchez-Lavega *et al.* [62] to suggest that there might be at least two vortices centrally located along the edge of the Hexagon that may or may not be visible

at different times. This theory would coincide with the streamline maps produced by [31] and that of [1] who proposed possible multiple perturbing anti-cyclones.

Images captured by the visual-infrared mapping spectrometer (VIMS) on board the Cassini-Huygens Orbiter in 2006 [4], and more recently the first visible light images captured by the Imaging Science Subsystem (ISS) in 2009 [64] indicate that the Hexagon is a long-lived atmospheric vortex. However, these images indicate that the previously observed impinging anti-cyclone(s) in 1980 and 1990 have dissipated to non-existence, casting doubt over the Allison *et al.* [1] proposition. Although there is currently no visible anti-cyclonic vortex to the south of the Hexagon, there is a visible anti-cyclonic spot located in the interior of the Hexagon [56, 2], indicating anti-cyclonic phenomena occur on a regular basis to the north and south of the Hexagon. The hexagonal structure bounds a pole centred cyclonic vortex with speed upwards of 135 ms^{-1} [4, 2].

The VIMS imagery indicates that the clouds within the easterly flow have speeds in excess of 125 ms^{-1}, an increase of 25% from the observations of Voyager. These observed changes could be due to temporal variability and/or vertical shear [4]. The most recent observations suggest that the peak velocity within the Hexagon is around 119 ms^{-1} [2].

Rotating tank experiments have been used for simulating atmospheric jets that meander about a given latitude. An interesting and not uncommon result of such experiments is that various polygonal flow features form, depending on the type of forcing [68, 71, 72, 49, 38]. This type of experiment has given rise to alternative explanations of the origin of the North Polar Hexagon. In particular, laboratory experiments with fluids in rotating tanks in conjunction with a barotropic linear instability analysis of Saturn's zonal wind profile were used to infer that Saturn's Hexagon is the result of equilibrated wavemodes of the barotropic instability, with mode six being the preferred state on Saturn due to the location and strength of the eastward circumpolar jet [6]. Numerical simulations using the Explicit Planetary Isentropic-Coordinate (EPIC) model found that a stable hexagonal structure can result without forcing [55]. The EPIC simulations are in agreement with the experimental findings of Barbosa-Aguiar *et al.* [6] and the resulting hexagonal structure arises due to the formation of what is termed a 'vortex street', where there is an alignment of opposing vortices such that there exist a meandering jet separating them. In the case of the Saturn hexagon simulations there are six anti-cyclones slightly south of the six cyclones.

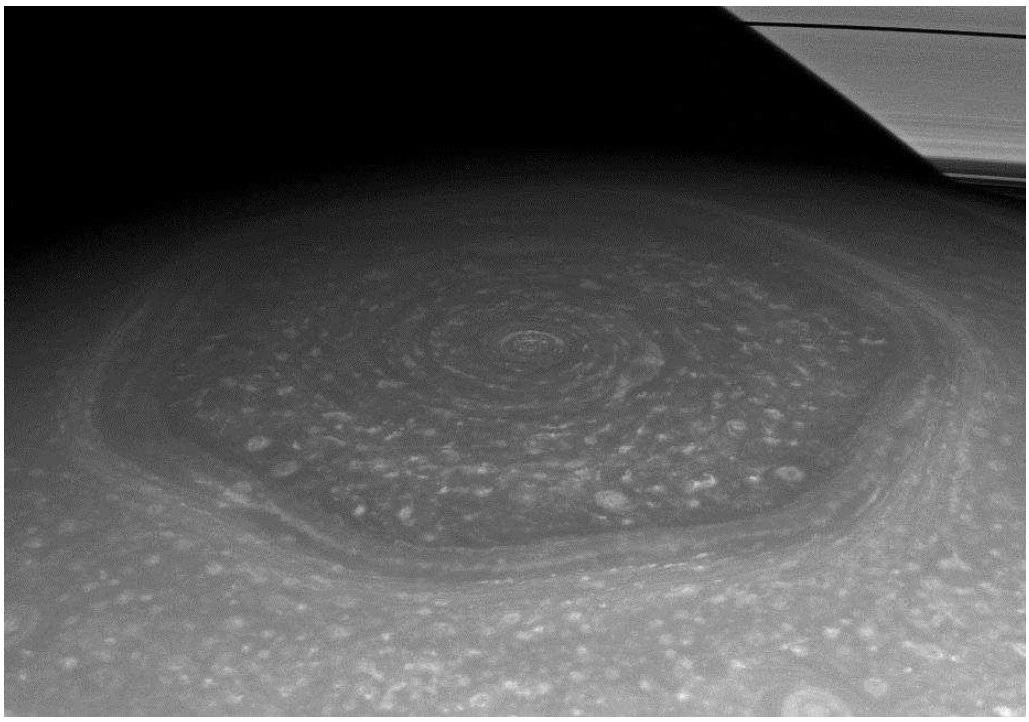

Figure 1.0.6: NASA/JPL-Caltech/Space Science Institute image captured by the Cassini spacecraft, November 27, 2012. This image shows Saturn's North Polar Hexagon along with its rings.

Although the experimental [6] and numerical [55] results produce hexagonal features as a bi-product of a 'vortex street', there remains doubt over the legitimacy of such a model producing the actual North Polar Hexagon on Saturn, due to the debate over the existence of large vortices being observed in the vicinity of the Hexagon region of Saturn [55, 63]. A visible 'vortex street' may not be apparent in the Cassini images [63], but it has been shown previously by analysing the original Voyager images that there was a visible anti-cyclone and several other non-visible anti-cyclonic regions aligned centrally along the southern side of the Hexagon edges [31], but the lack of cyclonic regions to the north exclude it from being the result of a 'vortex street'. The speed needed to propagate the 'vortex street' hexagon in the numerical simulations by Morales-Juberias *et al.* [55] would exceed the statistical bounds of measurements by Godfrey [31]. However, by considering small perturbations to an eastward Gaussian jet similar to that used Morales-Juberias *et al.* [55] a hexagon can result in the form of a shallow meandering jet which has comparable phase speed to the actual North Polar Hexagon [56].

The current non-existence of a perturbing anti-cyclone has for at least a decade now cast doubt over the original proposal of Allison *et al.* [1]. However, this does not necessarily mean that the former, highly visible spots impinging on the hexagonal edges did not influence its development initially, conversely the visible spots may have been the result of the Hexagon itself. It can not be denied that at the time of its discovery, the Hexagon had a significant counter-rotating vortex pushing on one edge. Without data prior to 1980 it is hard to say how long the spot was in existence. Maybe these vortices were enough to give the circumpolar jet the required perturbation similar to those given in the model used by Morales-Juberias *et al.* [56] so that the circumpolar current could evolve to form a hexagonal structure.

This thesis will consider numerical simulations on the evolution of atmospheric vortices using 'tangent plane' approximations. As remarked above, atmospheric vortices are not simply circular features. In particular this thesis will look at the formation of finger structures on the extremities of atmospheric vortices, similar in nature to those on the outer edges of the vortex shown in Figure 1.0.1; the interaction between two atmospheric vortices, comparable to the interacting typhoons in Figure 1.0.3; and a possible trigger mechanism for the development of the hexagonal structure over the north pole of Saturn, shown in Figure 1.0.6. The derivation of the governing equations and the justification of the mathematical formulation of the atmospheric flow problems considered in this thesis are detailed in Chapters 2 and 3 respectively. Chapter 4 is an expanded version of the article published in the *ANZIAM Journal* [16] 'The formation of large-amplitude fingers in atmospheric vortices' and seeks to undertake an analysis similar in some respects to that of Forbes and Cosgrove [28], in that moderately large-amplitude instabilities at the edge of a vortex system are of interest. However, the circulation does not arise from a line vortex at the centre of the system, but rather comes about through the Coriolis pseudo-acceleration due to the rotation of the Earth. Chapter 5 considers the interaction between binary mid-latitude atmospheric vortices with a particular focus on whether or not elastic interaction takes place. Unlike the majority of binary interaction studies, the elastic interaction of extra-tropical cyclones and anti-cyclones will be considered. This chapter is an extension of the paper 'Nonlinear behaviour of interacting mid-latitude atmospheric vortices' published in the *Journal of Engineering Mathematics* [17]; however, there is more evidence presented in this chapter to further enhance the results published in the associated article [17]. Although not correct, the theory of Allison *et al.* [1] and the multiple vortex conjecture discussed by Sanchez-Lavega *et al.* [62] raises some interesting questions

that seem to be ignored based solely on the fact that there is currently no impinging anti-cyclonic vortex to the south of the Hexagon. Chapter 6 seeks to determine whether or not a hexagonal feature can be formed by anti-cyclones perturbing an initially circular circumpolar jet. The vast literature discussing the North Polar Hexagon has not attempted to substantiate this component of the Allison *et al.* proposition through numerical or experimental reproduction and thus is a focus area of the thesis. This chapter is the foundation upon which the research article titled 'A δ-plane simulation of anti-cyclones perturbing circumpolar flows to form a transient north polar hexagon' published by *Monthly Notices of the Royal Astronomical Society* [18], is based.

Chapter 2

Equations of Atmospheric Flow

This chapter will outline the equations governing compressible, rotational, inviscid fluid flow for an inertial Cartesian coordinate based geometry. These equations will then be modified to allow for the fact that the Earth (and Saturn) and thus its atmosphere is continually rotating. The equations are then converted to spherical polar coordinates so that the spherical geometry of the atmosphere is taken into account. This thesis is focussed on using 'tangent plane' approximations to simulate atmospheric flow behaviours and therefore, the complicated spherical equations are simplified by projecting them onto a 'tangent plane'.

Fluid flow can be described in two different ways: (i) the Lagrangian approach and (ii) the Eulerian approach. The Lagrangian description considers the motion of a single fluid particle as it moves through space and time. The Eulerian description is a way of looking at fluid flow in terms of the patterns it creates, and so does not focus explicitly on particle motion. It is generally more useful in fluid mechanics. In this thesis, the fluid motion will be studied using the Eulerian equations, as the behaviour of the individual fluid particles in the atmosphere is of less interest than the volume of fluid as a whole. The equations of interest are the mass continuity equation, momentum equations for the respective velocity components, an energy equation in terms of temperature and the equation of state.

To relate the Lagrangian and Eulerian approaches of fluid motion, suppose that F is some property of the fluid; that is F depends on fluid particles as they move through space and time (Lagrangian). Then the particles' path in three dimensions is given by the position vector $\mathbf{r}(t)$, where $\mathbf{r}(t) = x(t)\underline{i} + y(t)\underline{j} + z(t)\underline{k}$. Thus from a Lagrangian perspective, a fluid property F depends

on particle location according to the relation $F = F(x(t), y(t), z(t), t)$. So the total rate of change of property F with respect to time is

$$\frac{dF}{dt} = \frac{\partial F}{\partial x}\frac{dx}{dt} + \frac{\partial F}{\partial y}\frac{dy}{dt} + \frac{\partial F}{\partial z}\frac{dz}{dt} + \frac{\partial F}{\partial t}. \tag{2.0.1}$$

From an Eulerian perspective equation (2.0.1) is called the material derivative, describing the change in the fluid property F following the motion, and is written

$$\frac{DF}{Dt} = \frac{\partial F}{\partial t} + \mathbf{q} \cdot (\nabla F), \tag{2.0.2}$$

where

$$\mathbf{q} = \frac{d\mathbf{r}}{dt} = \frac{dx}{dt}\mathbf{i} + \frac{dy}{dt}\mathbf{j} + \frac{dz}{dt}\mathbf{k} = u\mathbf{i} + v\mathbf{j} + w\mathbf{k} \tag{2.0.3}$$

is the velocity vector, ∇ is the standard differential operator and the operator

$$\frac{D}{Dt} \equiv \frac{\partial}{\partial t} + \mathbf{q} \cdot \nabla \tag{2.0.4}$$

is the derivative following the motion.

Reynolds' Transport Theorem is a fundamental theorem used in formulating the basic laws of fluid dynamics and describes the rate of change of a scalar field through some moving volume $\mathcal{V}(t)$. If ϕ is a scalar fluid property, then the rate of change of its volume integral can be shown to be

$$\frac{D}{Dt}\iiint_{\mathcal{V}(t)} \phi \; dV = \iiint_{\mathcal{V}(t)} \left[\frac{D\phi}{Dt} + \phi(\nabla \cdot \mathbf{q})\right] \; dV. \tag{2.0.5}$$

An in depth justification of equation (2.0.5) and its various forms are given in the text by Aris [3, pages 84–85]. Reynolds' Transport Theorem (2.0.5) is used to derive conservation laws for mass, momentum and energy. Expanding out the material derivative term in (2.0.5) and using the vector identity

$$\nabla \cdot (\phi\mathbf{q}) = \mathbf{q} \cdot \nabla\phi + \phi\,(\nabla \cdot \mathbf{q}), \tag{2.0.6}$$

then Reynolds' Transport Theorem (2.0.5) can also be written

$$\frac{D}{Dt}\iiint_{\mathcal{V}(t)} \phi \ dV = \iiint_{\mathcal{V}(t)} \left[\frac{\partial \phi}{\partial t} + \nabla \cdot (\phi \mathbf{q})\right] \ dV. \tag{2.0.7}$$

Investigations into electrostatics in the late 1700's and early 1800's gave rise to Gauss' Divergence Theorem. This theorem is a particularly important result used in fluid mechanics and enables a link between the flux through a surface and the divergence within a volume encased by the same surface [3, page 58]. Mathematically it is written as

$$\oiint_{\mathcal{S}(t)} \mathbf{F} \cdot \mathbf{n} \ dS = \iiint_{\mathcal{V}(t)} \nabla \cdot \mathbf{F} \ dV, \tag{2.0.8}$$

where $\mathbf{F}$ is a vector field and $\mathbf{n}$ is the outward normal unit vector of $\mathcal{S}(t)$. Consider $\mathbf{F} = \psi \mathbf{G}$, where $\mathbf{G}$ is any constant vector and ψ is a scalar property; then the Divergence Theorem (2.0.8) can be transformed to

$$\begin{aligned}
\oiint_{\mathcal{S}(t)} \psi \mathbf{G} \cdot \mathbf{n} \ dS &= \iiint_{\mathcal{V}(t)} \nabla \cdot (\psi \mathbf{G}) \ dV \\
&= \iiint_{\mathcal{V}(t)} (\mathbf{G} \cdot \nabla \psi + \psi (\nabla \cdot \mathbf{G})) \ dV \qquad \text{(by identity (2.0.6))}, \\
&= \iiint_{\mathcal{V}(t)} \mathbf{G} \cdot \nabla \psi \ dV, \qquad \text{(as } \mathbf{G} \text{ is a constant vector)}.
\end{aligned} \tag{2.0.9}$$

Writing $\mathbf{G} = g_1 \mathbf{i} + g_2 \mathbf{j} + g_3 \mathbf{k}$ and $\mathbf{n} = n_1 \mathbf{i} + n_2 \mathbf{j} + n_3 \mathbf{k}$, then the left hand side of equation (2.0.9) becomes

$$\begin{aligned}
\oiint_{\mathcal{S}(t)} \psi \mathbf{G} \cdot \mathbf{n} \ dS &= \oiint_{\mathcal{S}(t)} \psi (g_1 n_1 + g_2 n_2 + g_3 n_3) \ dS \\
&= g_1 \oiint_{\mathcal{S}(t)} \psi n_1 \ dS + g_2 \oiint_{\mathcal{S}(t)} \psi n_2 \ dS + g_3 \oiint_{\mathcal{S}(t)} \psi n_3 \ dS.
\end{aligned} \tag{2.0.10}$$

The right hand side of equation (2.0.9) is similarly transformed to give

$$\begin{aligned}
\iiint_{\mathcal{V}(t)} \mathbf{G} \cdot \nabla \psi \ dV &= \iiint_{\mathcal{V}(t)} \left(g_1 \frac{\partial \psi}{\partial x} + g_2 \frac{\partial \psi}{\partial y} + g_3 \frac{\partial \psi}{\partial z}\right) \ dV \\
&= g_1 \iiint_{\mathcal{V}(t)} \frac{\partial \psi}{\partial x} \ dV + g_2 \iiint_{\mathcal{V}(t)} \frac{\partial \psi}{\partial y} \ dV + g_3 \iiint_{\mathcal{V}(t)} \frac{\partial \psi}{\partial y} \ dV.
\end{aligned} \tag{2.0.11}$$

Equating the expansions from (2.0.10) and (2.0.11) gives

$$\oiint_{\mathcal{S}(t)} \psi\, n_1 \; dS = \iiint_{\mathcal{V}(t)} \frac{\partial \psi}{\partial x} \; dV, \tag{2.0.12}$$

$$\oiint_{\mathcal{S}(t)} \psi\, n_2 \; dS = \iiint_{\mathcal{V}(t)} \frac{\partial \psi}{\partial y} \; dV, \tag{2.0.13}$$

$$\oiint_{\mathcal{S}(t)} \psi\, n_3 \; dS = \iiint_{\mathcal{V}(t)} \frac{\partial \psi}{\partial z} \; dV. \tag{2.0.14}$$

Then it follows that the Divergence Theorem (2.0.8) can be written in the following alternate form

$$\begin{aligned}
\oiint_{\mathcal{S}(t)} \psi \mathbf{n} \; dS &= \left(\oiint_{\mathcal{S}(t)} \psi\, n_1 \; dS \right) \mathbf{i} + \left(\oiint_{\mathcal{S}(t)} \psi\, n_2 \; dS \right) \mathbf{j} + \left(\oiint_{\mathcal{S}(t)} \psi\, n_3 \; dS \right) \mathbf{k} \\
&= \left(\iiint_{\mathcal{V}(t)} \frac{\partial \psi}{\partial x} \; dV \right) \mathbf{i} + \left(\iiint_{\mathcal{V}(t)} \frac{\partial \psi}{\partial y} \; dV \right) \mathbf{j} + \left(\iiint_{\mathcal{V}(t)} \frac{\partial \psi}{\partial z} \; dV \right) \mathbf{k} \\
&= \iiint_{\mathcal{V}(t)} \left(\frac{\partial \psi}{\partial x} \mathbf{i} + \frac{\partial \psi}{\partial y} \mathbf{j} + \frac{\partial \psi}{\partial z} \mathbf{k} \right) \; dV \\
&= \iiint_{\mathcal{V}(t)} \nabla \psi \; dV.
\end{aligned} \tag{2.0.15}$$

2.1 Mass Equation

Since the fluid flow is being considered from an Eulerian perspective, it is essential that the mass of the fluid is conserved. To do this, consider an arbitrary volume $\mathcal{V}(t)$ of moving fluid, so the mass M of the fluid volume remains constant. The arbitrary volume can then be expressed as a volume integral with density, ρ in the form

$$M = \iiint_{\mathcal{V}(t)} \rho \; dV = \text{constant}. \tag{2.1.1}$$

Since the mass M is constant in the moving volume $\mathcal{V}(t)$, its derivative following the motion must be zero. Therefore

$$\frac{DM}{Dt} = \frac{D}{Dt} \iiint_{\mathcal{V}(t)} \rho \; dV = 0. \tag{2.1.2}$$

Applying Reynolds' Transport Theorem (2.0.5), equation (2.1.2) is equivalent to

$$\iiint_{\mathcal{V}(t)} \left[\frac{D\rho}{Dt} + \rho(\nabla \cdot \mathbf{q}) \right] \; dV = 0. \tag{2.1.3}$$

This equation holds for every arbitrary volume $\mathcal{V}(t)$, and thus gives

$$\frac{D\rho}{Dt} + \rho(\nabla \cdot \mathbf{q}) = 0 \tag{2.1.4}$$

at every point in the fluid. Equation (2.1.4) is known as the mass continuity equation and is satisfied everywhere in the fluid. Alternatively, using (2.0.4) and (2.0.6), (2.1.4) becomes

$$\frac{\partial \rho}{\partial t} + \nabla \cdot (\rho\, \mathbf{q}) = 0. \tag{2.1.5}$$

2.2 Momentum Equation

Newton's second Law states that $F = ma$, where F is the force, m is the mass and a is acceleration. Alternatively, the total force on a body is equal to the time derivative of linear momentum of the body. There are two types of forces that act on a fluid: (i) body forces, which act on every particle of fluid throughout the arbitrary volume $\mathcal{V}(t)$; and (ii) traction forces, which act on the surface $\mathcal{S}(t)$ of the volume $\mathcal{V}(t)$. Let the body force per unit mass be $\mathbf{f}$ and then the total body force on $\mathcal{V}(t)$ can be expressed as

$$\text{Total body force } = \iiint_{\mathcal{V}(t)} \rho\, \mathbf{f}\ dV. \tag{2.2.1}$$

Viscous fluids support shear forces on the surface of a volume of fluid and thus are ignored when considering inviscid fluid flow. The traction forces acting on the surface of $\mathcal{V}(t)$ are pressure forces normal to surface $\mathcal{S}(t)$ and are represented as a closed surface integral of the form

$$\text{Total traction force } = \oiint_{\mathcal{S}(t)} -p\, \mathbf{n}\ dS, \tag{2.2.2}$$

where p is the pressure and $\mathbf{n}$ is the normal vector to the surface $\mathcal{S}(t)$. The momentum $\mathbf{P}$ of the volume $\mathcal{V}(t)$ is the product of its mass, as defined by (2.1.1) and its velocity $\mathbf{q}$ to give

$$\mathbf{P} = \iiint_{\mathcal{V}(t)} \rho\, \mathbf{q}\ dV. \tag{2.2.3}$$

The conservation of momentum in an arbitrary moving volume $\mathcal{V}(t)$ can be related in terms of the time derivative of equation (2.2.3) being equal to the sum of the total body force (2.2.1) and the total traction force (2.2.2). This results in the vector equation

$$\frac{D}{Dt}\iiint_{\mathcal{V}(t)} \rho\,\mathbf{q}\ dV = \iiint_{\mathcal{V}(t)} \rho\,\mathbf{f}\ dV + \oiint_{\mathcal{S}(t)} -p\,\mathbf{n}\ dS. \tag{2.2.4}$$

Gauss' Divergence Theorem in its alternate form given by equation (2.0.15) can be used to transform closed surface integrals into volume integrals, so that equation (2.2.2) equates to

$$\oiint_{\mathcal{S}(t)} -p\,\mathbf{n}\ dS = \iiint_{\mathcal{V}(t)} -\nabla p\ dV, \tag{2.2.5}$$

and (2.2.5) can be used to write the vector equation (2.2.4) in the more convenient form

$$\frac{D}{Dt}\iiint_{\mathcal{V}(t)} \rho\,\mathbf{q}\ dV = \iiint_{\mathcal{V}(t)} [\rho\,\mathbf{f} - \nabla p]\ dV. \tag{2.2.6}$$

Now consider the i^{th} component of the vector equation (2.2.6). The i^{th} component is

$$\frac{D}{Dt}\iiint_{\mathcal{V}(t)} \rho\,q_i\ dV = \iiint_{\mathcal{V}(t)} \left[\rho\,f_i - \frac{\partial p}{\partial x_i}\right] dV. \tag{2.2.7}$$

Equation (2.2.7) is transformed using Reynolds' Transport Theorem (2.0.5) to give

$$\iiint_{\mathcal{V}(t)} \left[\frac{\partial}{\partial t}(\rho\,q_i) + \nabla\cdot(\rho\,q_i\,\mathbf{q})\right] dV = \iiint_{\mathcal{V}(t)} \left[\rho\,f_i - \frac{\partial p}{\partial x_i}\right] dV. \tag{2.2.8}$$

It follows then that

$$\frac{\partial}{\partial t}(\rho\,q_i) + \nabla\cdot(\rho\,q_i\,\mathbf{q}) = \rho\,f_i - \frac{\partial p}{\partial x_i} \tag{2.2.9}$$

at each point, as the volume $\mathcal{V}(t)$ is arbitrary. A more favourable representation of (2.2.9) is achieved by expanding the left hand side to get

$$\frac{\partial \rho}{\partial t}\,q_i + \rho\frac{\partial q_i}{\partial t} + q_i\nabla\cdot(\rho\,\mathbf{q}) + \rho\,\mathbf{q}\cdot\nabla q_i = \rho\,f_i - \frac{\partial p}{\partial x_i}. \tag{2.2.10}$$

The mass conservation condition (2.1.5) simplifies (2.2.10) to

$$\rho\left[\frac{\partial q_i}{\partial t} + \mathbf{q}\cdot\nabla q_i\right] + \frac{\partial p}{\partial x_i} = \rho\,f_i. \tag{2.2.11}$$

Dividing through by ρ, the vectorised form of equation (2.2.11) becomes

$$\frac{\partial \mathbf{q}}{\partial t} + (\mathbf{q}\cdot\nabla)\,\mathbf{q} + \frac{1}{\rho}\nabla p = \mathbf{f}. \tag{2.2.12}$$

Alternatively (2.2.12) can be written in terms of the derivative following the motion as

$$\frac{D\mathbf{q}}{Dt} + \frac{1}{\rho}\nabla p = \mathbf{f}. \tag{2.2.13}$$

The equations (2.2.12) and (2.2.13) are Euler's equation of motion for a compressible gas.

2.3 Energy Equation

One of the fundamental laws of physics is that energy must be conserved. For an arbitrary volume of fluid $\mathcal{V}(t)$, the energy principle states that the rate of increases of energy in volume $\mathcal{V}(t)$ must equal the sum of: (i) rate of addition of external heat and (ii) the rate of work done on volume $\mathcal{V}(t)$. Let the rate of heat addition, per unit mass, be q_h and therefore the total rate of heat addition on $\mathcal{V}(t)$ can be defined as

$$\text{Total rate of heat addition } = \iiint_{\mathcal{V}(t)} \rho\, q_h \; dV. \tag{2.3.1}$$

Suppose that the thermodynamic heat energy per unit mass in the fluid is e (latent heat per mass), where

$$e = c_v T, \tag{2.3.2}$$

c_v is the specific heat at a constant volume and T is the temperature in degrees Kelvin ($^\circ K$). The kinetic energy per unit mass is $\frac{1}{2}|\mathbf{q}|^2 = \frac{1}{2}(\mathbf{q}\cdot\mathbf{q})$. Thus the energy per unit mass is $e + \frac{1}{2}|\mathbf{q}|^2$. Then,

$$\text{Total energy in } \mathcal{V}(t) \; = \iiint_{\mathcal{V}(t)} \rho\left(e + \frac{1}{2}|\mathbf{q}|^2\right) \; dV. \tag{2.3.3}$$

The rate of work done on $\mathcal{V}(t)$ is due to both the body force per unit mass $\mathbf{f}$ on $\mathcal{V}(t)$ and surface force per unit mass on $\mathcal{S}(t)$. It follows then from (2.2.1) and (2.2.2) respectively, that the total rate of work done by body forces on $\mathcal{V}(t)$ is

$$\iiint_{\mathcal{V}(t)} \rho\, \mathbf{f}\cdot\mathbf{q} \; dV, \tag{2.3.4}$$

and the total rate of work done by surface forces is

$$\oiint_{\mathcal{S}(t)} -p\,\mathbf{n}\cdot\mathbf{q}\ \ dS. \tag{2.3.5}$$

Applying Gauss' Divergence Theorem (2.0.8) to (2.3.5) gives

$$\oiint_{\mathcal{S}(t)} -p\,\mathbf{n}\cdot\mathbf{q}\ \ dS = \iiint_{\mathcal{V}(t)} -\nabla\cdot(p\,\mathbf{q})\ \ dV, \tag{2.3.6}$$

thus, mathematically the energy principle becomes

$$\frac{D}{Dt}\iiint_{\mathcal{V}(t)} \rho\left(e+\frac{1}{2}|\mathbf{q}|^2\right)\ \ dV = \iiint_{\mathcal{V}(t)} \left[\rho\, q_h + \rho\,\mathbf{f}\cdot\mathbf{q} - \nabla\cdot(p\,\mathbf{q})\right]\ \ dV. \tag{2.3.7}$$

Applying Reynolds' Transport Theorem (2.0.5), equation (2.3.7) is transformed to

$$\iiint_{\mathcal{V}(t)} \left[\frac{\partial}{\partial t}\left\{\rho\left(e+\frac{1}{2}|\mathbf{q}|^2\right)\right\} + \nabla\cdot\left\{\rho\left(e+\frac{1}{2}|\mathbf{q}|^2\right)\mathbf{q}\right\}\right]\ \ dV = \iiint_{\mathcal{V}(t)} \left[\rho\, q_h + \rho\,\mathbf{f}\cdot\mathbf{q} - \nabla\cdot(p\,\mathbf{q})\right]\ \ dV. \tag{2.3.8}$$

The volume $\mathcal{V}(t)$ is arbitrary, giving

$$\frac{\partial}{\partial t}\left\{\rho\left(e+\frac{1}{2}|\mathbf{q}|^2\right)\right\} + \nabla\cdot\left\{\rho\left(e+\frac{1}{2}|\mathbf{q}|^2+\frac{p}{\rho}\right)\mathbf{q}\right\} = \rho\,(q_h + \mathbf{f}\cdot\mathbf{q}) \tag{2.3.9}$$

at each point in the fluid. Equation (2.3.9) can be expressed in many forms. A convenient form arises by using the mass equation (2.1.4) and the momentum equation (2.2.12) to 'split off' the purely mechanical part of the energy to give

$$\rho\frac{De}{Dt} - \frac{p}{\rho}\frac{D\rho}{Dt} = \rho q_h. \tag{2.3.10}$$

Combining equations (2.3.2) and (2.3.10) and simplifying with the use of equation (2.1.4) results in a single equation for the temperature T in the form

$$\rho c_v\frac{DT}{Dt} + p(\nabla\cdot\mathbf{q}) = \rho q_h. \tag{2.3.11}$$

The form (2.3.10) is essentially the first law of thermodynamics for a system in equilibrium (see Liepmann & Roshko [47, page 189]).

2.4 Equation of State

This study will look at atmospheric fluids that are governed by the ideal gas law, and thus the equation of state is a important governing equation. It has been shown experimentally for a dry gas at constant pressure, the temperature T ($^\circ K$) and the volume are proportional [69, page 217]. That is

$$V \propto T, \quad \text{(Charles' Law)}. \tag{2.4.1}$$

Also, it has been observed that, at constant temperature T, the pressure is inversely proportional to the volume it occupies [69, page 217]. Therefore, per unit mass, the pressure is proportional to the density . That is

$$p \propto \rho, \quad \text{(Boyle's Law)}. \tag{2.4.2}$$

It follows from (2.4.1) and (2.4.2) that

$$p\,V = n\,R\,T, \tag{2.4.3}$$

where V is the volume of gas, n is the number of moles of gas present and R is the universal gas constant and has the value of $R = 8.314$ J/mol.K for all gases. Equation (2.4.3) is known as the ideal gas law [73, page 508]. The total number of moles n, of gas present is equal to the mass of the gas, m, divided by the molar mass, M, such that

$$n = \frac{m}{M}. \tag{2.4.4}$$

The density of the gas can be expressed as

$$\rho = \frac{m}{V}, \tag{2.4.5}$$

and thus by equations (2.4.4) and (2.4.5), the ideal gas law equation (2.4.3) is transformed such that

$$p = \frac{\rho\,R\,T}{M} = \rho\,R_s\,T \tag{2.4.6}$$

The term R_s in equation (2.4.6) is the specific gas constant and is the ratio $\frac{R}{M}$. Depending on the context, the specific gas constant is often denoted R. This notation will be used throughout this thesis and therefore the equation of state is

$$p = \rho R T. \tag{2.4.7}$$

2.5 Rotating Coordinate System Equations

Sections (2.1) – (2.4) have outlined the derivation of the basic equations of motion for a compressible gas. This thesis investigates the evolution of atmospheric vortices, and thus the equations need to allow for the fact that the Earth (or any other celestial body) is rotating. Suppose $(\hat{x}, \hat{y}, \hat{z})$ are fixed inertial cartesian coordinates and (x, y, z) rotate with the Earth. The angular velocity is $\boldsymbol{\Omega} = \Omega \hat{\mathbf{k}}$, where Ω is a constant. Figure 2.5.1 shows the layout of the inertial and rotating coordinate systems.

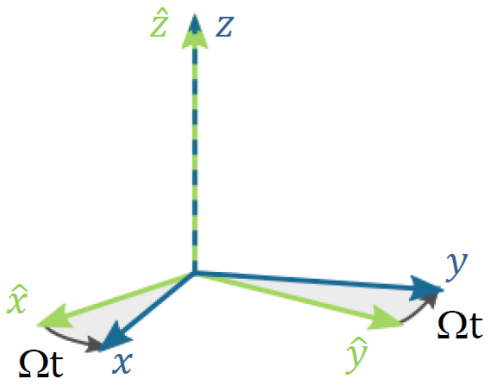

Figure 2.5.1: Definition sketch of the fixed inertial $(\hat{x}, \hat{y}, \hat{z})$ and rotating (x, y, z) coordinate systems.

The two coordinate systems are related by:

$$\begin{cases} x = \hat{x} \cos \Omega t + \hat{y} \sin \Omega t \\ y = -\hat{x} \sin \Omega t + \hat{y} \cos \Omega t \\ z = \hat{z} \end{cases} \tag{2.5.1}$$

Similarly, the unit vectors in the two coordinate systems are related by:

$$\begin{cases} \mathbf{i} = \hat{\mathbf{i}}\cos\Omega t + \hat{\mathbf{j}}\sin\Omega t \\ \mathbf{j} = -\hat{\mathbf{i}}\sin\Omega t + \hat{\mathbf{j}}\cos\Omega t \\ \mathbf{k} = \hat{\mathbf{k}} \end{cases} \tag{2.5.2}$$

The Lagrangian perspective gives the position vector of a particle in the atmosphere in the form

$$\mathbf{r} = \hat{x}\,\hat{\mathbf{i}} + \hat{y}\,\hat{\mathbf{j}} + \hat{z}\,\hat{\mathbf{k}} \quad \text{(inertial frame)} \tag{2.5.3}$$

$$= x\,\mathbf{i} + y\,\mathbf{j} + z\,\mathbf{k} \quad \text{(rotating frame).} \tag{2.5.4}$$

Deriving equations governing the flow within a rotating system requires two different coordinates: (i) absolute and (ii) relative. Absolute coordinates are with respect to the inertial coordinates and will be shown with subscript 'a'. Relative coordinates are with respect to rotating coordinates and have no subscripts. Given that the relative coordinate system is rotating, the time derivative of the position vector $\mathbf{r}$ will be different if viewed from the two coordinate systems. Mathematically, this is represented as

$$\begin{aligned} \left(\frac{d\mathbf{r}}{dt}\right)_a &= \frac{d\hat{x}}{dt}\hat{\mathbf{i}} + \frac{d\hat{y}}{dt}\hat{\mathbf{j}} + \frac{d\hat{z}}{dt}\hat{\mathbf{k}} \\ &= \frac{dx}{dt}\mathbf{i} + \frac{dy}{dt}\mathbf{j} + \frac{dz}{dt}\mathbf{j} + x\frac{d\mathbf{i}}{dt} + y\frac{d\mathbf{j}}{dt} + z\frac{d\mathbf{k}}{dt}. \end{aligned} \tag{2.5.5}$$

From (2.5.2) it follows that $\dfrac{d\mathbf{k}}{dt} = \dfrac{d\hat{\mathbf{k}}}{dt} = 0$ and

$$\begin{aligned} x\frac{d\mathbf{i}}{dt} + y\frac{d\mathbf{j}}{dt} &= x\Omega\,\mathbf{j} - y\Omega\,\mathbf{i} \\ &= \Omega\,\mathbf{k} \times (x\,\mathbf{i} + y\,\mathbf{j} + z\,\mathbf{k}) \\ &= \boldsymbol{\Omega} \times \mathbf{r}. \end{aligned} \tag{2.5.6}$$

The time derivative of the position vector in relative coordinates is

$$\frac{d\mathbf{r}}{dt} = \frac{dx}{dt}\mathbf{i} + \frac{dy}{dt}\mathbf{j} + \frac{dz}{dt}\mathbf{k}. \tag{2.5.7}$$

Thus (2.5.5) becomes

$$\left(\frac{d\mathbf{r}}{dt}\right)_a = \frac{d\mathbf{r}}{dt} + \boldsymbol{\Omega} \times \mathbf{r} \tag{2.5.8}$$

and

$$\mathbf{q}_a = \mathbf{q} + \boldsymbol{\Omega} \times \mathbf{r}. \tag{2.5.9}$$

In order to write down the equations of motion as seen by an Earth-bound observer, the mass (2.1.4), momentum (2.2.12) and energy (2.3.11) equations must be converted from absolute coordinates to coordinates that are rotating with the Earth. This requires the following three theorems:

Theorem 2.5.1. *The gradient of a scalar function, F, is equal in both coordinate systems. Then*

$$\hat{\nabla} F = \nabla F.$$

Theorem 2.5.2. *The derivative (following the motion) of a scalar function, F, has the same form in both coordinate systems, that is*

$$\left(\frac{DF}{Dt}\right)_a = \frac{DF}{Dt},$$

and

Theorem 2.5.3. *If* $\mathbf{A}$ *is a vector function. Then*

$$\left(\frac{D\mathbf{A}}{Dt}\right)_a = \frac{D\mathbf{A}}{Dt} + \boldsymbol{\Omega} \times \mathbf{A}.$$

Further discussion of these results may be found in the text by Vallis [70, Chapter 2].

The acceleration of a body is not measured to be the same in the rotating and fixed inertial frames, and thus we need a formula for the acceleration in the rotating frame. This is

$$\begin{aligned}
\left(\frac{D\mathbf{q}_a}{Dt}\right)_a &= \frac{D\mathbf{q}_a}{Dt} + \boldsymbol{\Omega} \times \mathbf{q_a} \\
&= \frac{D}{Dt}(\mathbf{q} + \boldsymbol{\Omega} \times \mathbf{r}) + \boldsymbol{\Omega} \times (\mathbf{q} + \boldsymbol{\Omega} \times \mathbf{r}) \quad \text{(by Theorem (2.5.3))} \\
&= \frac{D\mathbf{q}}{Dt} + \frac{D}{Dt}(\boldsymbol{\Omega} \times \mathbf{r}) + \boldsymbol{\Omega} \times \mathbf{q} + \boldsymbol{\Omega} \times (\boldsymbol{\Omega} \times \mathbf{r}) \\
&= \frac{D\mathbf{q}}{Dt} + \frac{D\boldsymbol{\Omega}}{Dt} \times \mathbf{r} + \boldsymbol{\Omega} \times \frac{D\mathbf{r}}{Dt} + \boldsymbol{\Omega} \times \mathbf{q} + \boldsymbol{\Omega} \times (\boldsymbol{\Omega} \times \mathbf{r}).
\end{aligned} \tag{2.5.10}$$

Given that

$$\frac{D\mathbf{r}}{Dt} \equiv \frac{d\mathbf{r}}{dt} \equiv \mathbf{q}$$

and that the relative coordinate system rotates at a constant rate, then (2.5.10) simplifies further to

$$\left(\frac{D\mathbf{q}_a}{Dt}\right)_a = \frac{D\mathbf{q}}{Dt} + 2\boldsymbol{\Omega} \times \mathbf{q} + \boldsymbol{\Omega} \times (\boldsymbol{\Omega} \times \mathbf{r}). \tag{2.5.11}$$

Now that there is a way of relating vector quantities in the two different coordinate systems, consider the momentum equation (2.2.13). In absolute coordinates equation (2.2.13) is expressed as

$$\left(\frac{D\mathbf{q}_a}{Dt}\right)_a + \frac{1}{\rho}\hat{\nabla} p = \mathbf{f}. \tag{2.5.12}$$

In relative coordinates, the equation (2.5.12) becomes

$$\frac{D\mathbf{q}}{Dt} + \frac{1}{\rho}\nabla p = \mathbf{f} - 2\boldsymbol{\Omega} \times \mathbf{q} - \boldsymbol{\Omega} \times (\boldsymbol{\Omega} \times \mathbf{r}). \tag{2.5.13}$$

The respective pseudo-forces, $2\boldsymbol{\Omega} \times \mathbf{q}$ and $\boldsymbol{\Omega} \times (\boldsymbol{\Omega} \times \mathbf{r})$, are known as the Coriolis force and centrifugal force. It is common to absorb the centrifugal force term into the body force term $\mathbf{f}$. In fact, for meteorology, gravity is the body force term $\mathbf{f}$ which is directed towards the centre of the Earth. Conversely, the centrifugal force is directed outward from the centre of the Earth. Therefore the centrifugal force modifies the gravity force to reflect its true influence.

In summary, the equations of motion for the rotating Earth (celestial body) are the mass equation

$$\frac{D\rho}{Dt} + \rho(\nabla \cdot \mathbf{q}) = 0, \tag{2.5.14}$$

the momentum equation

$$\frac{D\mathbf{q}}{Dt} + 2\boldsymbol{\Omega} \times \mathbf{q} + \frac{1}{\rho}\nabla p = \mathbf{f}, \tag{2.5.15}$$

the energy equation

$$\rho c_v \frac{DT}{Dt} + p(\nabla \cdot \mathbf{q}) = \rho q_h. \tag{2.5.16}$$

and the equation of state

$$p = \rho RT. \tag{2.5.17}$$

2.6 Spherical Coordinate System Equations

The surface of most celestial bodies are oblate spheroids due to the rotation causing an expansion around the equator. It is then appropriate to approximate the surface as a sphere, and thus it is convenient to write the equations (2.5.14) – (2.5.17) in spherical polar coordinates, with longitude λ, latitude ϕ and distance from the centre of the celestial body r. However, the usual mathematical definition of spherical polar coordinates, where the polar angle is measured from a fixed zenith direction, so that the polar angles are in the interval $0° < \phi < 180°$ will not be used. The latitudinal extent on Earth is measured such that the range is from $\phi = -90°$ at the south pole to $\phi = 90°$ at the north pole. This choice of latitudinal range makes the Coriolis force work out more conveniently. Figure 2.6.1 is a definition sketch of the spherical polar geometry used throughout this thesis.

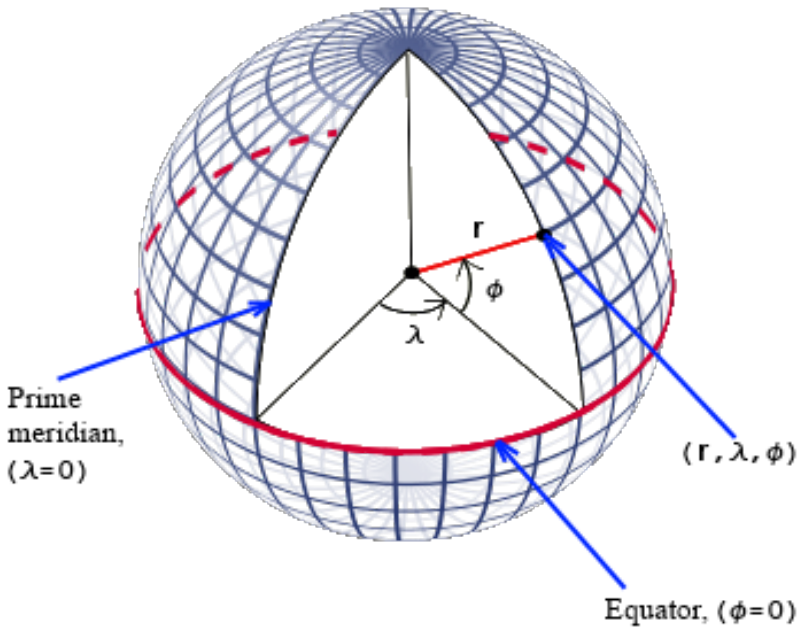

Figure 2.6.1: Definition sketch of the spherical polar geometry used throughout this thesis, with non-standard $\phi \in [-90°, 90°]$.

Cartesian and spherical polar coordinates are related by:

$$\begin{cases} x = r\,\cos\phi\,\cos\lambda \\ y = r\,\cos\phi\,\sin\lambda \\ z = r\,\sin\phi \end{cases} \tag{2.6.1}$$

So the position vector of a particle in the atmosphere (2.5.4) is

$$\mathbf{r} = r\,\cos\phi\,\cos\lambda\,\mathbf{i} + r\,\cos\phi\,\sin\lambda\,\mathbf{j} + r\,\sin\phi\,\mathbf{k}. \tag{2.6.2}$$

To calculate the unit vectors $\mathbf{e}_r$, $\mathbf{e}_\lambda$, $\mathbf{e}_\phi$ in the spherical coordinate directions (r, λ, ϕ), scale factors h_r, h_λ, h_ϕ are needed for the three coordinate directions, such that

$$\frac{\partial \mathbf{r}}{\partial r} = h_r\,\mathbf{e}_r, \quad \frac{\partial \mathbf{r}}{\partial \lambda} = h_\lambda\,\mathbf{e}_\lambda, \quad \frac{\partial \mathbf{r}}{\partial \phi} = h_\phi\,\mathbf{e}_\phi. \tag{2.6.3}$$

By comparing the appropriate partial derivative of (2.6.2) to the corresponding equations in (2.6.3) it follows that

$$\begin{cases} h_r = \left|\dfrac{\partial \mathbf{r}}{\partial r}\right| = 1 \\ \mathbf{e}_r = \cos\phi\,\cos\lambda\,\mathbf{i} + \cos\phi\,\sin\lambda\,\mathbf{j} + \sin\phi\,\mathbf{k}, \end{cases} \tag{2.6.4}$$

$$\begin{cases} h_\lambda = \left|\dfrac{\partial \mathbf{r}}{\partial \lambda}\right| = r\,\cos\phi \\ \mathbf{e}_\lambda = -\sin\lambda\,\mathbf{i} + \cos\lambda\,\mathbf{j}, \end{cases} \tag{2.6.5}$$

and

$$\begin{cases} h_\phi = \left|\dfrac{\partial \mathbf{r}}{\partial \phi}\right| = r \\ \mathbf{e}_\phi = -\sin\phi\,\cos\lambda\,\mathbf{i} - \sin\phi\,\sin\lambda\,\mathbf{j} + \cos\phi\,\mathbf{k}. \end{cases} \tag{2.6.6}$$

Inverting the spherical unit vectors, the Cartesian unit vectors in terms of the spherical unit vectors are

$$\begin{cases} \mathbf{i} = \cos\lambda\,\cos\phi\,\mathbf{e}_r - \sin\lambda\,\mathbf{e}_\lambda - \cos\lambda\,\sin\phi\,\mathbf{e}_\phi \\ \mathbf{j} = \sin\lambda\,\cos\phi\,\mathbf{e}_r + \cos\lambda\,\mathbf{e}_\lambda - \sin\lambda\,\sin\phi\,\mathbf{e}_\phi \\ \mathbf{k} = \sin\phi\,\mathbf{e}_r + \cos\phi\,\mathbf{e}_\phi \end{cases} \tag{2.6.7}$$

The spherical polar velocity vector is defined as

$$\mathbf{q} = u_r\mathbf{e}_r + u_\lambda\mathbf{e}_\lambda + u_\phi\mathbf{e}_\phi. \tag{2.6.8}$$

The Coriolis force component of equation (2.5.15) is converted using (2.6.7) and (2.6.8) so that

$$\begin{aligned} 2\boldsymbol{\Omega}\times\mathbf{q} &= 2\Omega\mathbf{k}\times\mathbf{q} \\ &= 2\Omega\left[-u_\lambda\cos\phi\,\mathbf{e}_r + (u_r\cos\phi - u_\phi\sin\phi)\,\mathbf{e}_\lambda + u_\lambda\sin\phi\,\mathbf{e}_\phi\right]. \end{aligned} \tag{2.6.9}$$

The gradient of a scalar function F, such as density ρ or temperature T in this non-standard spherical system is

$$\nabla F = \frac{\partial F}{\partial r}\,\mathbf{e}_r + \frac{1}{r\cos\phi}\,\frac{\partial F}{\partial\lambda}\,\mathbf{e}_\lambda + \frac{1}{r}\,\frac{\partial F}{\partial\phi}\,\mathbf{e}_\phi \tag{2.6.10}$$

and

$$\mathbf{q}\cdot\nabla F = u_r\frac{\partial F}{\partial r} + \frac{u_\lambda}{r\cos\phi}\,\frac{\partial F}{\partial\lambda} + \frac{u_\phi}{r}\,\frac{\partial F}{\partial\phi}. \tag{2.6.11}$$

The material derivative of a scalar function in spherical polar coordinates has the same form as equation (2.0.2). However, the material derivative of a vector function is much more complicated in spherical coordinates, and it is best to split it up in the form

$$\begin{aligned} \frac{D\mathbf{q}}{Dt} &= \frac{\partial\mathbf{q}}{\partial t} + (\mathbf{q}\cdot\nabla)\,\mathbf{q} \\ &= \frac{\partial\mathbf{q}}{\partial t} + \frac{1}{2}\nabla(\mathbf{q}\cdot\mathbf{q}) - \mathbf{q}\times(\nabla\times\mathbf{q}). \end{aligned} \tag{2.6.12}$$

After a considerable amount of algebra, it follows then from (2.6.12) that

$$\frac{D\mathbf{q}}{Dt} = \left(\frac{Du_r}{Dt} - \frac{u_\phi^2 + u_\lambda^2}{r} \right) \mathbf{e}_r + \left(\frac{Du_\lambda}{Dt} + \frac{u_r u_\lambda - u_\phi u_\lambda \tan\phi}{r} \right) \mathbf{e}_\lambda + \left(\frac{Du_\phi}{Dt} + \frac{u_r u_\phi - u_\lambda^2 \tan\phi}{r} \right) \mathbf{e}_\phi. \tag{2.6.13}$$

Lastly, the divergence of the velocity vector is given by

$$\nabla \cdot \mathbf{q} = \frac{1}{r^2} \frac{\partial (r^2 u_r)}{\partial r} + \frac{1}{r \cos\phi} \frac{\partial u_\lambda}{\partial \lambda} + \frac{1}{r \cos\phi} \frac{u_\phi \cos\phi}{\partial \phi}. \tag{2.6.14}$$

The governing equations in spherical polar coordinates are just an extension of those shown in the previous section 2.5. The form of the mass equation (2.5.14), energy equation (2.5.16) and equation of state (2.5.17) are unchanged apart from coordinate system itself. However, the momentum equation (2.5.15) is now split into three components, one each for the spherical components. It is important to recognise that the body force $\mathbf{f}$ is gravity and is directed towards the centre of the Earth, thus $\mathbf{f} = -g\,\mathbf{e}_r$. The r-component of the momentum equation is

$$\frac{Du_r}{Dt} - \frac{u_\phi^2 + u_\lambda^2}{r} - 2\Omega u_\lambda \cos\phi + \frac{1}{\rho} \frac{\partial p}{\partial r} = -g. \tag{2.6.15}$$

The λ- and ϕ- components are

$$\frac{Du_\lambda}{Dt} + \frac{u_r u_\lambda - u_\phi u_\lambda \tan\phi}{r} + 2\Omega(u_r \cos\phi - u_\phi \sin\phi) + \frac{1}{\rho} \frac{1}{r \cos\phi} \frac{\partial p}{\partial \lambda} = 0 \tag{2.6.16}$$

and

$$\frac{Du_\phi}{Dt} + \frac{u_r u_\phi + u_\lambda^2 \tan\phi}{r} + 2\Omega u_\lambda \sin\phi + \frac{1}{\rho} \frac{1}{r} \frac{\partial p}{\partial \phi} = 0 \tag{2.6.17}$$

respectively. These extend the results in the text by Batchelor [7, page 601] to include Coriolis effects.

2.7 Tangent Plane Equations

The equations (2.5.14), (2.5.16), (2.5.17) and (2.6.15) – (2.6.17) are an arduous system of equations to solve, in particular with regards to the momentum equations. A common technique is

to simplify the equations by projecting from the surface of the spherical Earth, onto a 'tangent plane'. The tangent plane is commonly defined in terms of Cartesian coordinates so that the y-axis is pointing North, x- axis is pointing East and the z-axis is pointing outward from the centre of the spherical body through the tangent point which doubles as the origin of the 'tangent plane'. The geometry of a 'tangent plane' is illustrated in Figure 2.7.1.

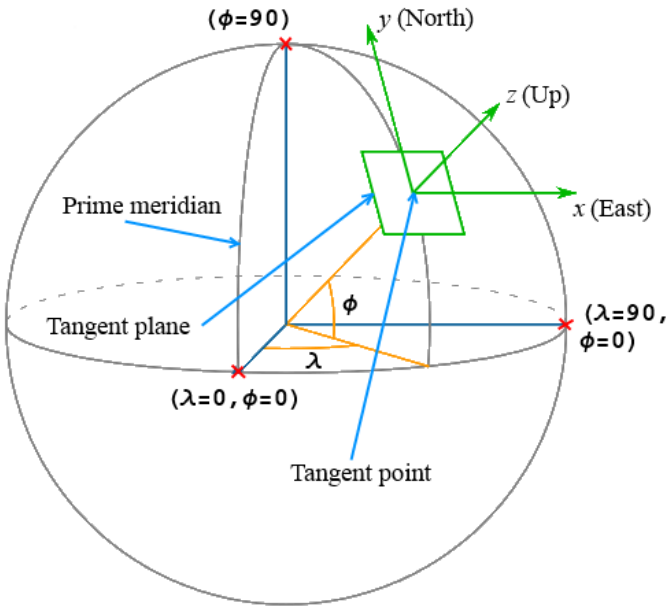

Figure 2.7.1: Definition sketch of the tangent plane geometry with x-,y- and z- axis defined to be pointing East, North and outwards respectively.

In this Cartesian system the velocity vector $\mathbf{q} = u\mathbf{i} + v\mathbf{j} + w\mathbf{k}$. This simplification assumes

$$\begin{aligned} \mathbf{e}_\lambda &\equiv \mathbf{i} \qquad \mathbf{e}_\phi \equiv \mathbf{j} \qquad \mathbf{e}_r \equiv \mathbf{k} \\ u &\equiv u_\lambda \qquad v \equiv u_\phi \qquad w \equiv u_r \end{aligned} \tag{2.7.1}$$

The spherical coordinate, r, is a good approximation for the radius of the Earth, r_e, thus $r \approx r_e$. Simple circular geometry gives

$$\begin{aligned} \Delta y &\approx r_e \, \Delta\phi \\ \therefore \frac{\Delta p}{\Delta y} &\approx \frac{1}{r_e} \frac{\Delta p}{\Delta \phi} \end{aligned} \tag{2.7.2}$$

and

$$\begin{aligned} \Delta x &\approx (r_e \cos\phi)\,\Delta\lambda \\ \therefore \frac{\Delta p}{\Delta x} &\approx \frac{1}{r_e \cos\phi}\,\frac{\Delta p}{\Delta\lambda}. \end{aligned} \tag{2.7.3}$$

Using the approximations given by (2.7.1) – (2.7.3), together with $r \approx r_e$, the momentum equations (2.6.15) – (2.6.17) become

$$\frac{Du}{Dt} + \frac{uw - uv\tan\phi}{r_e} + 2\Omega(w\cos\phi - v\sin\phi) + \frac{1}{\rho}\,\frac{\partial p}{\partial x} = 0, \tag{2.7.4}$$

$$\frac{Dv}{Dt} + \frac{vw + u^2\tan\phi}{r_e} + 2\Omega u\sin\phi + \frac{1}{\rho}\,\frac{\partial p}{\partial y} = 0 \tag{2.7.5}$$

and

$$\frac{Dw}{Dt} - \frac{u^2 + v^2}{r_e} - 2\Omega u\cos\phi + \frac{1}{\rho}\,\frac{\partial p}{\partial z} = -g. \tag{2.7.6}$$

For example, this system may be found in the text by Vallis [70, page 61].

The simplified momentum component equations (2.7.4) – (2.7.6) are further streamlined by the assumption that the vertical wind-speed component w is small compared to the horizontal components u and v. Furthermore, since the radius of the Earth r_e is large, terms involving the inverse $\dfrac{1}{r_e}$ will be small. Also, it is known that gravity g and $\dfrac{1}{\rho}\,\dfrac{\partial p}{\partial z}$ are large. Then the momentum equations become approximately

$$\frac{Du}{Dt} - fv + \frac{1}{\rho}\,\frac{\partial p}{\partial x} \approx 0, \tag{2.7.7}$$

$$\frac{Dv}{Dt} + fu + \frac{1}{\rho}\,\frac{\partial p}{\partial y} \approx 0, \tag{2.7.8}$$

and

$$\frac{1}{\rho}\,\frac{\partial p}{\partial z} \approx -g, \tag{2.7.9}$$

where $f = 2\Omega \sin \phi$ and is known as the Coriolis parameter. These equations are derived in the text by Vallis [70, pages 66–67]. The governing equations for atmospheric fluid flow on a projected tangential Cartesian coordinate system are (2.5.14), (2.5.16), (2.5.17) and (2.7.7) – (2.7.9).

Chapter 3

Mathematical Formulation

This chapter will outline the mathematical formulation of the problems to be solved. Numerical simulations on the evolution of atmospheric vortices using 'tangent plane' approximations are of interest. In particular, three topics will be simulated in depth. They are (i) Finger structures on the boundary of an atmospheric vortex; (ii) Interaction of mid-latitude atmospheric vortices; and (iii) Anti-cyclones perturbing circumpolar flows to form a transient north polar hexagon. Captured images of the three vortex phenomena occurring in nature can be seen in Figures 1.0.1, 1.0.3 and 1.0.6 respectively. These images are the motivation for the work in this thesis. Depending on the actual phenomenon being simulated, different 'tangent plane' approximations are required to achieve reliable numerical solutions to the actual atmospheric behaviour.

3.1 Dimensional Equations

Large-scale atmospheric vortices typically have diameters of hundreds if not thousands of kilometres, but are relatively shallow in depth and so they can be thought of a large flat structures. Therefore the vertical structure and the effects of gravity will not be considered. The governing equations for the numerical simulations carried out in this thesis are firstly the mass conservation equation (2.5.14) in the expanded form

$$\frac{\partial \rho}{\partial t} + u\frac{\partial \rho}{\partial x} + v\frac{\partial \rho}{\partial y} + \rho\left(\frac{\partial u}{\partial x} + \frac{\partial v}{\partial y}\right) = 0. \tag{3.1.1}$$

Next, the momentum equations (2.7.7) and (2.7.8) for the u and v velocity components, respectively, are expanded to give

$$\frac{\partial u}{\partial t} + u\frac{\partial u}{\partial x} + v\frac{\partial u}{\partial y} - fv + \frac{1}{\rho}\frac{\partial p}{\partial x} = 0, \tag{3.1.2}$$

$$\frac{\partial v}{\partial t} + u\frac{\partial v}{\partial x} + v\frac{\partial v}{\partial y} + fu + \frac{1}{\rho}\frac{\partial p}{\partial y} = 0. \tag{3.1.3}$$

Finally, it will be assumed that there will be no addition of heat per unit mass by external heat sources, that is $q_h = 0$. This leads to the energy equation (2.5.16) becoming

$$\frac{\partial T}{\partial t} + u\frac{\partial T}{\partial x} + v\frac{\partial T}{\partial y} + \frac{p}{\rho c_v}\left(\frac{\partial u}{\partial x} + \frac{\partial v}{\partial y}\right) = 0. \tag{3.1.4}$$

The mass (3.1.1), momentum (3.1.2), (3.1.3) and energy (3.1.4) equations are time derivative equations. For consistency, the equation of state (2.5.17) will now be expressed in the form

$$\frac{\partial p}{\partial t} = \frac{\partial(\rho R T)}{\partial t} = R\left[T\frac{\partial \rho}{\partial t} + \rho\frac{\partial T}{\partial t}\right]. \tag{3.1.5}$$

Alternatively, using equations (3.1.1) and (3.1.4), the time derivative equation of state (3.1.5) for pressure is

$$\begin{aligned}\frac{\partial p}{\partial t} = &-RT\left[u\frac{\partial \rho}{\partial x} + v\frac{\partial \rho}{\partial y} + \rho\left(\frac{\partial u}{\partial x} + \frac{\partial v}{\partial y}\right)\right] \\ &- R\rho\left[u\frac{\partial T}{\partial x} + v\frac{\partial T}{\partial y} + \frac{p}{\rho c_v}\left(\frac{\partial u}{\partial x} + \frac{\partial v}{\partial y}\right)\right].\end{aligned} \tag{3.1.6}$$

3.2 'Tangent Plane' Approximations

It is common when studying fluid flow in the atmosphere and/or ocean to use a 'tangent plane' approximation, particularly when the flow of interest is smaller than global, in which case the complicated spherical effects can be ignored. Fluid motion in the atmosphere is subject to the Coriolis pseudo-force, due to the Earth (or any other celestial body with an atmosphere) being in a non-inertial rotating reference frame. The Coriolis parameter at latitude ϕ is given by

$$f = 2\Omega \sin\phi \text{ rad s}^{-1}, \tag{3.2.1}$$

where Ω is the angular velocity of the celestial body. The celestial bodies of interest in this thesis are Earth and Saturn. The sidereal rotation period of the Earth is 23.9345 hours [75] and so the Earth's angular velocity takes the value

$$\Omega_e = \frac{2\pi}{23.9345 \times 3600} = 7.292 \times 10^{-5} \text{ rad s}^{-1}. \tag{3.2.2}$$

Using the Saturnian system III coordinates [75], the sidereal rotation period of Saturn is taken to be 10.656 hours and therefore Saturn's angular velocity is

$$\Omega_s = \frac{2\pi}{10.656 \times 3600} = 1.638 \times 10^{-4} \text{ rad s}^{-1}. \tag{3.2.3}$$

Atmospheric fluid behaviour varies considerably over the latitudinal domain and to account for such change there are three common 'tangent plane' approximations that are used in atmospheric fluid dynamics. These are the f-plane, β-plane and δ-plane approximations. The f-plane and β-plane approximations are often used for mid latitude studies [11, 16, 48, 70] whereas the δ-plane approximation by definition is more appropriate for polar region behaviour [34, 33, 46, 57, 78].

3.2.1 f-Plane Approximation

The f-plane approximation is the most simple approximation used in atmospheric fluid dynamics, and it assumes that the Coriolis parameter f is constant over a 'tangent plane' of interest. The spherical nature of a celestial body can be somewhat complicated when considering fluid flow over a localised region of a celestial body and thus using the simpler Cartesian representation is the most convenient approach. Thus the f-plane is a Cartesian based coordinate system with the x-axis defined to be pointing east and the y-axis points north (see Figure 2.7.1) and is a true 'tangent plane'. The origin is located at the tangent point at a given latitude ϕ_0. The value of the Coriolis parameter for the f-plane is determined using the latitude of the tangent point in equation (3.2.1), so that

$$f = 2\Omega \sin \phi_0 \text{ rad s}^{-1}. \tag{3.2.4}$$

Latitudes on a celestial body increase in magnitude away from the equator to their maximum absolute values at the poles. The latitudinal domain for the Northern Hemisphere is 0° at the equator to 90° north and 0° to 90° south for the Southern Hemisphere. However, computationally the Northern Hemisphere has latitudes ranging from 0° to 90° and −90° to 0° in the Southern Hemisphere. It follows then that the Coriolis parameter is positive ($f > 0$) and negative ($f < 0$) in the Northern and Southern Hemispheres respectively.

3.2.2 β-Plane Approximation

In reality there is considerable latitudinal variation of the Coriolis parameter and thus depending on the requirements of the simulation, this latitudinal variation may need to be taken into account. The β-plane approximation makes the assumption that the Coriolis parameter f varies linearly with latitude and enables the study of important dynamical interactions of the spheroidal atmosphere, without the complex spherical geometry. To derive the Coriolis parameter for the β-plane, consider equation (3.2.1) in the form

$$f = 2\Omega \sin(\phi_0 + \phi - \phi_0). \tag{3.2.5}$$

Representing f as a truncated Taylor series yields the following

$$f = 2\Omega \sin\phi_0 + 2\Omega(\phi - \phi_0)\cos\phi_0 + O(\phi - \phi_0)^2. \tag{3.2.6}$$

In Cartesian coordinates $y \approx r(\phi - \phi_0) = r\Delta\phi$, where r is the radius of the celestial body. Therefore the Coriolis parameter for the β-plane takes the form

$$f = f_0 + \beta y, \tag{3.2.7}$$

where f_0 is defined by the constant Coriolis parameter for the f-plane (3.2.1) and β is the rate of change of f and is given by

$$\beta = \frac{2\Omega}{r}\cos\phi_0 \text{ rad s}^{-1}\text{m}^{-1}. \tag{3.2.8}$$

The influence of the β term is more pronounced closer to the equator and is termed the β-effect. The β-plane has the x- and y-axes oriented east and north respectively in the same manner as the

f-plane approximation.

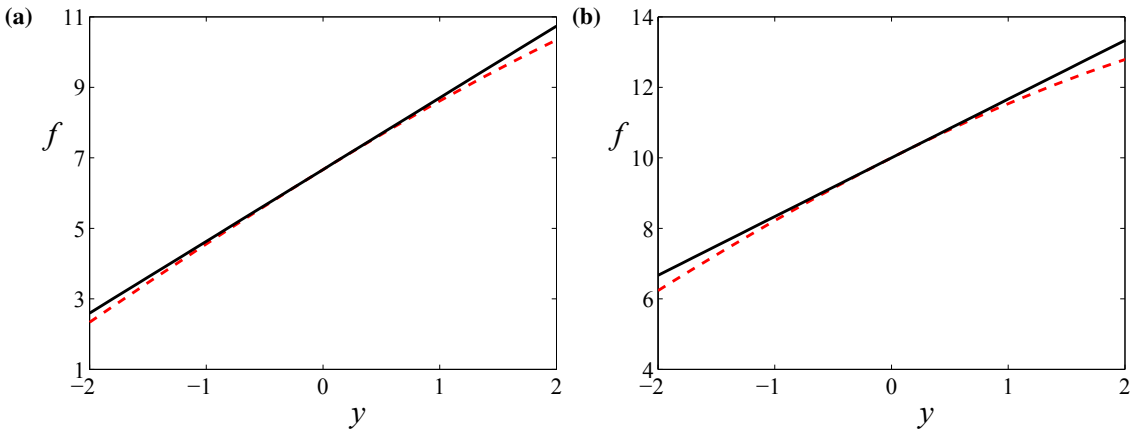

Figure 3.2.1: Variation of the Coriolis parameter as a function of latitude on the β-plane with (a) $\phi_0 = 27.2°$ and (b) $\phi_0 = 43.3°$. Red dashed line is the 'true' Coriolis variation and the solid black line represents the Coriolis parameter values for the β-plane approximation.

To give an indication of the variation in the Coriolis parameter f with latitude compared to the value assigned using the β-plane approximation, Figure 3.2.1 shows plots of the Coriolis parameter value against latitude (in the form of the y-coordinate). The variability between the 'true' Coriolis parameter value given by equation (3.2.1) and the β-plane approximation value defined by (3.2.7) with tangent point latitudes of $\phi_0 = 27.2°$N and $\phi_0 = 43.3°$N are shown respectively in Figures 3.2.1(a) and 3.2.1(b). These figures have used the β-plane representations (3.2.7) and (3.2.8) in their dimensionless form (refer to Section 3.3). The tangent point latitude corresponds to $y = 0$, the solid black line represents the β-plane values and the dashed red line is the 'true' Coriolis variation. Although not perfect, there is close agreement between the 'true' and approximate Coriolis parameter values over this domain.

3.2.3 δ-Plane Approximation

The δ-plane approximation is an approximation where the Coriolis parameter varies quadratically in space and is used to approximate fluid flow over the polar regions of a celestial body. The tangent point is $\phi_0 = \pm 90°$ depending on the pole of interest. The derivation is similar to that of the β-plane approximation and uses (3.2.5), but now f is truncated to fourth order, in the form

$$f = 2\Omega \sin\phi_0 + 2\Omega\Delta\phi \cos\phi_0 - \frac{2\Omega(\Delta\phi)^2 \sin\phi_0}{2} - \frac{2\Omega(\Delta\phi)^3 \cos\phi_0}{3!} + O(\Delta\phi)^4. \tag{3.2.9}$$

At the North pole $\phi_0 = 90°$, $\sin\phi_0 = 1$ and $\cos\phi_0 = 0$ simplifying (3.2.9) to

$$f = 2\Omega - \Omega(\Delta\phi)^2 + O(\Delta\phi)^4, \tag{3.2.10}$$

In Cartesian coordinates $\sqrt{x^2 + y^2} \approx r\Delta\phi$ giving the Coriolis parameter for the δ-plane in the Northern hemisphere as

$$f = 2\Omega - \delta(x^2 + y^2) \tag{3.2.11}$$

where

$$\delta = \frac{\Omega}{r^2} \text{ rad s}^{-1}\text{m}^{-2}. \tag{3.2.12}$$

The Coriolis parameter for the δ-plane in the Southern hemisphere is the negative of (3.2.11) and is given by

$$f = -2\Omega + \delta(x^2 + y^2). \tag{3.2.13}$$

However, this representation of the Coriolis parameter is never used in this thesis and its formulation is stated here only in the interest of completeness.

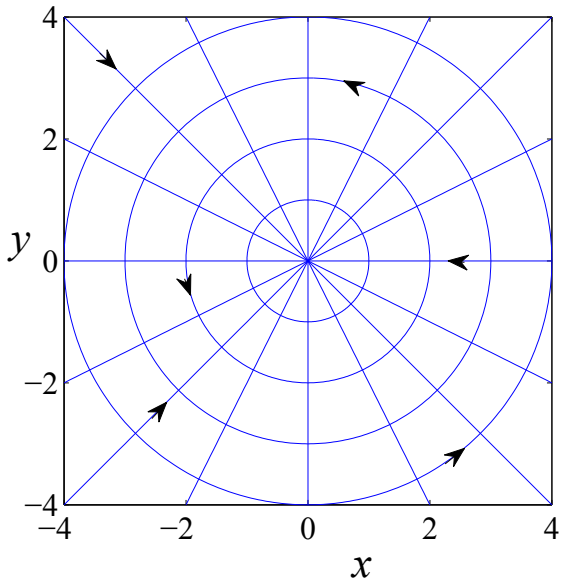

Figure 3.2.2: Geometric sketch of dimensionless δ-plane with north and east directional arrows.

The δ-plane with tangent point $\phi_0 = 90°\text{N}$ has the unique characteristic that the magnitude of Coriolis parameter decreases away from the pole, which is the origin of the 'tangent plane'. Unlike the f-plane and β-plane, the x- and y-axes are not oriented to the east and north respectively. The easterly direction is defined to be pointing anti-clockwise around circles of equal latitude with centres located at the origin, and the northerly direction is the ray from any (x, y) coordinate terminating at the pole. A geometric sketch of the dimensionless δ-plane is given in Figure 3.2.2, with boundary $-4 < x < 4$, $-4 < y < 4$. The arrows along the rays going through the origin show the northerly direction and the arrows on the circles show the easterly direction. It is important to note that the β-plane and δ-plane approximations don't describe dynamics on a hypothetical 'tangent plane' and only take the name from the analogous f-plane approximation. From equation (3.2.11), the δ-theory clearly represents the Coriolis term near the pole as an approximate paraboloid.

Throughout this thesis the celestial bodies of interest are the Earth and Saturn depending on what phenomenon is being simulated. The radius of the Earth is taken to be $r = 6.371 \times 10^6$ m and the radius of Saturn is taken to be $r = 5.8232 \times 10^7$ m. These radii values are the volumetric mean radius of the celestial body of interest [75].

The f-plane and β-plane approximations have been used extensively over the last century and

thus need little justification of their use in this thesis. However, the δ-plane approximation is not as well known and seems to be rather flexible in its definition; the only consistency is that the Coriolis parameter varies quadratically in space. The δ-plane approximation used in this thesis and outlined above is conveniently setup to be used over quite a large area of a celestial body. This is enabled due to the tangent point of the δ-plane being the pole itself. Using a tangent point that is not the pole limits the computational domain of the δ-plane as the pole would create an inflexible boundary of the δ-plane [34].

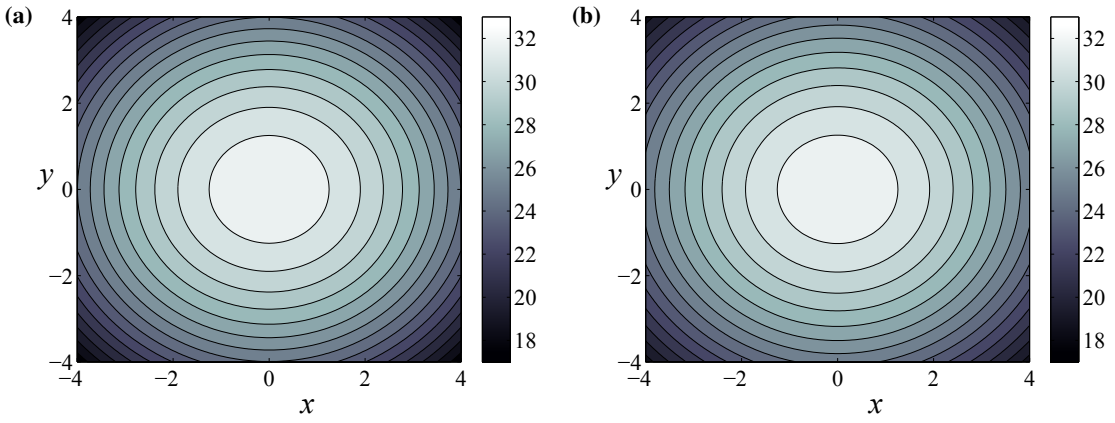

Figure 3.2.3: Pressure contour plots of the Coriolis parameter values over the north pole of Saturn using (a) δ-plane f values and (b) 'true' f values.

The f-plane and β-plane approximate the 'true' value of the Coriolis parameter (3.2.1) with a zeroth and first order Taylor series representation respectively. The validity of the results obtained by using the f-plane and β-plane approximations depend on factors such as the tangent point latitude, extent of the 'tangent plane' and the phenomenon being simulated and are discussed in depth later in Chapters 4 and 5. The approximate Coriolis parameter f obtained by using the polar δ-plane approximation as defined by (3.2.11) is virtually identical to that of the 'true' Coriolis parameter f given by (3.2.1), and this is illustrated in Figures 3.2.3(a) and 3.2.3(b) respectively in the form of contour diagrams. These two figures are essentially identical in appearance with maximum values of $f \approx 33$ at the poles and decreasing radially. These diagrams have used the angular velocity of Saturn (3.2.3) in its dimensionless form (refer to Section 3.3).

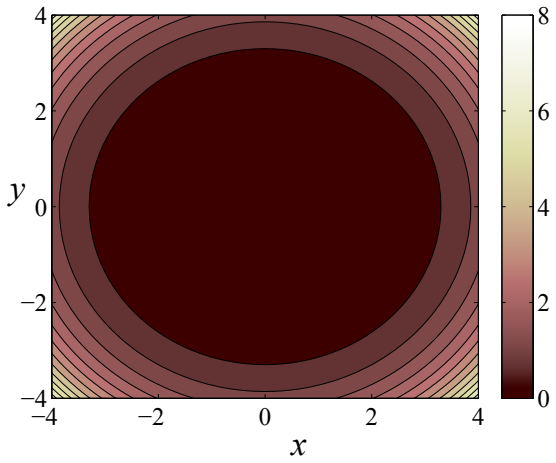

Figure 3.2.4: Contour diagram of the approximation error. The scale gives the percentage relative error (3.2.14) in the δ-plane assumption.

To determine a quantitative value of the error between the the 'true' and approximate values of the Coriolis parameters given by equations (3.2.1) and (3.2.11), Figure 3.2.4 shows the contours of the relative error given as a percentage of the 'true' Coriolis value in the form

$$Er(x,y) = \frac{2\Omega\sin\phi - 2\Omega + \delta(x^2+y^2)}{2\Omega\sin\phi} \times 100. \tag{3.2.14}$$

It can be seen from Figure 3.2.4 that, over the circular region of radius approximately four, there is less than one percent difference between the 'true' value and that given by the δ-plane value.

3.3 Dimensionless Parameters

The numerical simulations depicted in this thesis use a two-dimensional Cartesian coordinate system. For the f-plane and β-plane approximations this is a rectangular xy-plane that is tangent to a given point on a celestial body, where the x-axis is defined to be pointing east and the y-axis points north. The origin is located at the tangent point at a given latitude ϕ_0 on the surface of the celestial body. For the δ-plane approximation the orientation of the orthogonal x- and y-axes is arbitrary with respect to the origin at the pole, $\phi_0 = 90°$. However, for all three approximations the left and right sides of the 'tangent plane' are situated at $x = -L$ and $x = L$ respectively, and the top and bottom are located at $y = H$ and $y = -H$ respectively.

It is convenient to scale the problem so that all quantities, variables and equations are dimensionless. The time scale is τ, the approximate number of seconds in one day (10^5 s). The lengths are scaled relative to A. For simulations associated with Earth $A = 10^6$ m and for Saturn $A = 10^7$ m, the approximate side length of the hexagonal feature over the pole. Therefore the speed scale is A/τ, 10 ms^{-1} for Earth and 100 ms^{-1} for Saturn. The density and temperature scales are chosen to be the background density ρ_0 and background temperature T_0, respectively. Pressure is referenced to the quantity $\rho_0 R T_0$, in which R is the gas constant and takes the values of $R = 287.04$ J Kg^{-1} K^{-1} on Earth and $R = 4016.43$ J Kg^{-1} K^{-1} on Saturn. The problem then is found to be dependent on four dimensionless constant parameters,

$$\lambda = \frac{L}{A}, \quad \omega = \frac{H}{A}, \quad \gamma = \frac{c_p}{c_v}, \quad \nu_E = \frac{\tau^2 R T_0}{A^2}, \tag{3.3.1}$$

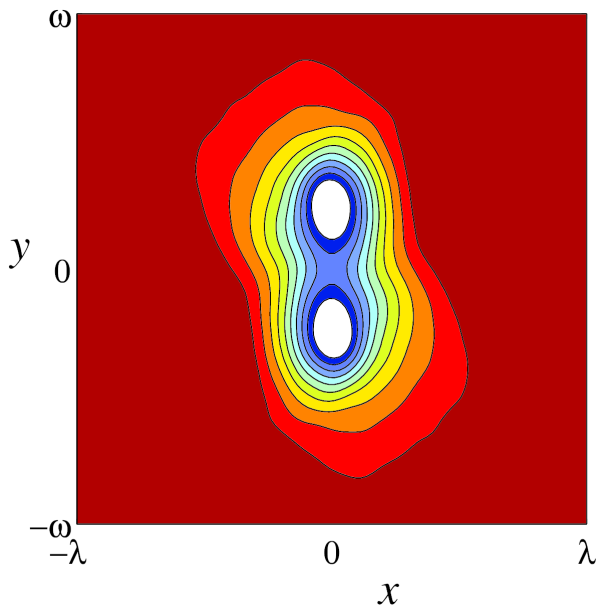

Figure 3.3.1: Sketch of dimensionless 'tangent plane' with $\lambda = \omega = 6$. The contours have been taken from an actual solution of an interacting binary low pressure system with initial eyes located at $(x, y) = (\pm 1, \pm 1)$, pressure differential $\mu_1 = \mu_2 = 0.1$ and $\sigma_1 = \sigma_2 = \sqrt{2}$ at time $t = 1.2$.

and five further parameters

$$\tilde{f} = f\tau, \quad \tilde{\beta} = \beta A \tau, \quad \tilde{\delta} = \delta A^2 \tau, \quad \tilde{\Omega} = \Omega \tau, \quad Ro_T = \frac{1}{f\tau} \tag{3.3.2}$$

that describe aspects of the Coriolis force due to the rotation of a celestial body.

The first two constants λ and ω in the system (3.3.1) represent the dimensionless half-width and half-length of the 'tangent plane', respectively. The constant $\gamma = c_p/c_v$ is the ratio of specific heats, where c_p is the specific heat at a constant pressure and c_v is the specific heat at a constant volume (For an ideal gas, $c_p - c_v = R$). The constant parameter ν_E is a type of inverse Eckert number, which is a ratio of kinetic energy and enthalpy [39, page 255]. A definition sketch of the dimensionless 'tangent plane' is given in Figure 3.3.1.

The constant $\tilde{f}$ in system (3.3.2) is the non-dimensional Coriolis parameter. The second parameter $\tilde{\beta}$ is the dimensionless rate of change of f with latitude, and is of interest only in the β-plane description of the flow. The third parameter $\tilde{\delta}$ is the dimensionless form of the second derivative of the Coriolis parameter with respect to latitude, and is only used in the δ-plane approach. The fourth parameter $\tilde{\Omega}$ is the dimensionless angular velocity and takes the values of 7.292 and 16.38 for Earth and Saturn simulations respectively. The last parameter Ro_T is the Rossby number defined in terms of time scales, as defined by Vallis [70, page 85]. It describes the ratio of inertial to Coriolis force and is the inverse of the dimensionless Coriolis parameter $\tilde{f}$.

3.4 Dimensionless Equations

As the 'tangent plane' is non-dimensionalized, the governing equations of fluid flow in the atmosphere derived in Chapter 2 must also be non-dimensionalized. The governing equations are non-dimensionalized using the following quantities

$$\begin{aligned} \tilde{x} &= \frac{x}{A}, \qquad \tilde{y} = \frac{y}{A}, \qquad \tilde{u} = \frac{u\tau}{A}, \qquad \tilde{v} = \frac{v\tau}{A} \\ \tilde{t} &= \frac{t}{\tau}, \qquad \tilde{\rho} = \frac{\rho}{\rho_0}, \qquad \tilde{T} = \frac{T}{T_0}, \qquad \tilde{p} = \frac{p}{\rho_0 R T_0} \end{aligned} \tag{3.4.1}$$

Recall the mass continuity equation (3.1.1)

$$\frac{\partial \rho}{\partial t} + u\frac{\partial \rho}{\partial x} + v\frac{\partial \rho}{\partial y} + \rho\left(\frac{\partial u}{\partial x} + \frac{\partial v}{\partial y}\right) = 0.$$

The following is an example of how to non-dimensionalize terms of the governing equations outlined in Section 3.1. Using the dimensionless quantities (3.4.1), the first term of equation (3.1.1)

$$\begin{aligned}\frac{\partial \rho}{\partial t} &= \frac{\partial(\rho_0 \tilde{\rho})}{\partial t} \\ &= \rho_0 \frac{\partial \tilde{\rho}}{\partial t} \\ &= \rho_0 \left(\frac{\partial \tilde{\rho}}{\partial \tilde{t}} \frac{\partial \tilde{t}}{\partial t} \right) \\ &= \frac{\rho_0}{\tau} \frac{\partial \tilde{\rho}}{\partial \tilde{t}}. \end{aligned} \tag{3.4.2}$$

Following a similar approach to how the time derivative of density (3.4.2) was obtained, the fully non-dimensional form of the mass continuity equation (3.1.1) is

$$\frac{\partial \tilde{\rho}}{\partial \tilde{t}} + \tilde{u} \frac{\partial \tilde{\rho}}{\partial \tilde{x}} + \tilde{v} \frac{\partial \tilde{\rho}}{\partial \tilde{y}} + \tilde{\rho} \left(\frac{\partial \tilde{u}}{\partial \tilde{x}} + \frac{\partial \tilde{v}}{\partial \tilde{y}} \right) = 0. \tag{3.4.3}$$

The dimensionless momentum equations are

$$\frac{\partial \tilde{u}}{\partial \tilde{t}} + \tilde{u} \frac{\partial \tilde{u}}{\partial \tilde{x}} + \tilde{v} \frac{\partial \tilde{u}}{\partial \tilde{y}} - \tilde{f} \tilde{v} + \frac{\nu_E}{\tilde{\rho}} \frac{\partial \tilde{p}}{\partial \tilde{x}} = 0, \tag{3.4.4}$$

$$\frac{\partial \tilde{v}}{\partial \tilde{t}} + \tilde{u} \frac{\partial \tilde{v}}{\partial \tilde{x}} + \tilde{v} \frac{\partial \tilde{v}}{\partial \tilde{y}} + \tilde{f} \tilde{u} + \frac{\nu_E}{\tilde{\rho}} \frac{\partial \tilde{p}}{\partial \tilde{y}} = 0, \tag{3.4.5}$$

A complete derivation of the non-dimensionalization of the momentum equation (3.1.2) that results in equation (3.4.4) is outlined in Appendix A. The non-dimensionalization of the momentum equations is the most complicated; however, they are simplified through the use of the inverse Eckert number ν_E. The dimensionless representation of the energy equation is of the form

$$\frac{\partial \tilde{T}}{\partial \tilde{t}} + \tilde{u} \frac{\partial \tilde{T}}{\partial \tilde{x}} + \tilde{v} \frac{\partial \tilde{T}}{\partial \tilde{y}} + (\gamma - 1) \frac{\tilde{p}}{\tilde{\rho}} \left(\frac{\partial \tilde{u}}{\partial \tilde{x}} + \frac{\partial \tilde{v}}{\partial \tilde{y}} \right) = 0, \tag{3.4.6}$$

and

$$\begin{aligned}\frac{\partial \tilde{p}}{\partial \tilde{t}} = &-\tilde{T} \left[\tilde{u} \frac{\partial \tilde{\rho}}{\partial \tilde{x}} + \tilde{v} \frac{\partial \tilde{\rho}}{\partial \tilde{y}} + \tilde{\rho} \left(\frac{\partial \tilde{u}}{\partial \tilde{x}} + \frac{\partial \tilde{v}}{\partial \tilde{y}} \right) \right] \\ &- \tilde{\rho} \left[\tilde{u} \frac{\partial \tilde{T}}{\partial \tilde{x}} + \tilde{v} \frac{\partial \tilde{T}}{\partial \tilde{y}} + (\gamma - 1) \frac{\tilde{p}}{\tilde{\rho}} \left(\frac{\partial \tilde{u}}{\partial \tilde{x}} + \frac{\partial \tilde{v}}{\partial \tilde{y}} \right) \right]. \end{aligned} \tag{3.4.7}$$

is the dimensionless time derivative equation of state, as the dimensionless form of (2.5.17) collapses to

$$\tilde{p} = \tilde{\rho}\,\tilde{T}. \tag{3.4.8}$$

For convenience, from here onwards the tildes on the non-dimensionalized equations (3.4.3) – (3.4.7) will be omitted, except for the constants that describe aspects of the Coriolis force given by (3.3.2). The two-dimensional compressible fluid equations (3.4.3) – (3.4.7) are used on the 'tangent plane', to reflect the fact that the horizontal length scales are far greater than the vertical heights. This is not a shallow-water approximation since the "top" of the atmosphere is not modelled explicitly. Instead, the variables used here are are essentially depth-averaged quantities, with weak tangential compressibility included to account for these effects. This extends the approach of Meunier *et al.* [53] who also used planar equations, but assumed an incompressible fluid. Allowing the fluid to have compressibility in the lateral coordinate gives the same physical degree of freedom as classical shallow-water theories. This is similar to the analogy that exists between flow of an incompressible fluid in an elastic-walled pipe, and that of a compressible fluid in a rigid pipe [43, 25].

Chapter 4

Large-amplitude finger structures in atmospheric vortices

Large-scale low pressure systems in the atmosphere are occasionally observed to posses Kelvin-Helmholtz fingers, and an example is shown in Figure 1.0.1. However, these structures are hundreds of kilometres long, so they are necessarily affected strongly by non-linearity. They are evidently unstable and are observed to dissipate after a few hours, and rare cases may last a few days.

This chapter will discuss and undertake an analysis similar in some respects to that of Forbes and Cosgrove [28], in that moderately large-amplitude instabilities at the edge of a vortex system are of interest. In the present problem, however, the circulation does not arise from a line vortex at the centre of the system, but rather comes about through the Coriolis pseudo-acceleration due to the rotation of the Earth. A real life example of a similar phenomenon is shown in Figure 1.0.1. A model for this phenomenon is presented here, based on the usual f-plane equations of meteorology, assuming an atmosphere governed by the ideal gas law. Large-amplitude perturbations are accounted for, by retaining the equations in their non-linear forms, and these are then solved numerically using a spectral method. Finger formation is modelled as an initial perturbation to the n-th Fourier mode, and the numerical results show that the fingers grow in time, developing structures that depend on the particular mode. Results are presented and discussed, and are also compared with the predictions of the β-plane theory, in which changes of the Coriolis acceleration with latitude are included. An idealized vortex in the northern hemisphere is considered, but the results are at least in qualitative agreement with an observation of such systems in the southern

hemisphere.

The mathematical conditions imposed and the numerical method used to simulate the formation of large-amplitude finger structures on the edges of atmospheric vortices are discussed. The mathematical conditions of interest are (i) boundary conditions, (ii) initial conditions and (iii) assumed atmospheric conditions.

The motivation for this analysis is the image of the low pressure system shown in Figure 1.0.1. The vortex was approximately located at 36°S latitude and the unusual fingers on the outer edges only lasted for a short while, less than four hours. The advantage of considering such a phenomenon located at this approximate latitude is that both the f-plane and β-plane approximations are valid choices [48]. Thus in simulating the formation of finger structures on the outer edges of such an atmospheric vortex, both the f-plane and β-plane approximations will be used and a detailed comparison of the results will be discussed. It will be shown that at mid-latitudes the f-plane and β-plane theories are in close agreement, but for mid-low latitudes the β-effect is noticeable. This is predominantly due to the increased difference between the fluid velocity approximated by the f-plane and β-plane at the same latitude for the lower tangent point latitude $\phi_0 = 27.2°$. For mid-latitude regions the f-plane and β-plane velocities at a given latitude are of the same order of magnitude for the selected geometric domain of the chosen tangent planes. In contrast, the f-plane and β-plane speeds in the mid-low latitude case are an order of magnitude larger in the β theory at the Southern boundary region (refer to Table 4.1 in the results section of this chapter).

4.1 Boundary Conditions

The atmospheric boundary conditions for the problems are determined by considering time independent, steady state behaviour. It can be shown that apart from the tropical regions the flow of atmospheric fluid is essentially geostrophic [36, page 30]. It follows then that it is reasonable to assume that the atmospheric flow is initially geostrophic and this assumption is made here. Thus the material derivative terms in the governing momentum equations (3.4.4) and (3.4.5) can be ignored so that these two equations simplify, approximately, to

$$u_s(x,y) = -\frac{\nu_E}{f\rho_s}\frac{\partial p_s}{\partial y} = -\frac{\nu_E Ro_T}{\rho_s}\frac{\partial p_s}{\partial y}, \tag{4.1.1}$$

$$v_s(x,y) = \frac{\nu_E}{f\rho_s}\frac{\partial p_s}{\partial x} = \frac{\nu_E Ro_T}{\rho_s}\frac{\partial p_s}{\partial x}, \tag{4.1.2}$$

for the respective zonal and meridional velocity components and the subscript s just indicates the steady component of the variable in question. The observed finger structure phenomenon was a large low-pressure system in the Great Australian Bight (see Figure 1.0.2) and so this will be modelled using an exponential function of the form

$$p_s(x,y) = 1 - \mu \exp[-(x^2 + y^2)], \tag{4.1.3}$$

where μ is a constant that gives the maximum pressure change over the flow region. The atmosphere will be assumed to be initially isothermal and so the initial constant temperature in dimensionless form is simply

$$T_s(x,y) = 1. \tag{4.1.4}$$

The steady pressure (4.1.3) and constant temperature (4.1.4) must satisfy the equation of state (3.4.8) and thus the steady density ρ_s must have the same form as the steady pressure

$$\rho_s(x,y) = 1 - \mu \exp[-(x^2 + y^2)] = p_s(x,y) = G(x,y). \tag{4.1.5}$$

The tangent plane dimensions are set up so that the flow on the outer edges of the tangent plane has minimal influence on the flow in the centre of the tangent plane where the finger structure phenomenon is located. The steady equations (4.1.1) – (4.1.5) must hold on the edges at $x = \pm\lambda$ and $y = \pm\omega$ of the tangent plane and these equations will double as the boundary conditions to the fully non-linear flow problem.

4.2 Spectral Solution Method

A spectral solution is sought for the five variables that are needed in order to solve the problem. The variables for pressure p, density ρ, temperature T, zonal velocity u and meridional velocity

v are expressed as the sum of a steady time-independent background flow component and a fully unsteady time dependent component in the form

$$p(x,y,t) = p_s(x,y) + p_u(x,y,t), \tag{4.2.1}$$

$$\rho(x,y,t) = \rho_s(x,y) + \rho_u(x,y,t), \tag{4.2.2}$$

$$T(x,y,t) = T_s(x,y) + T_u(x,y,t), \tag{4.2.3}$$

$$u(x,y,t) = u_s(x,y) + u_u(x,y,t), \tag{4.2.4}$$

$$v(x,y,t) = v_s(x,y) + v_u(x,y,t). \tag{4.2.5}$$

The steady background components denoted with the subscript s, are given by equations (4.1.1) – (4.1.5). As the steady background components double as the boundary conditions for the problem, the unsteady time dependent components must equal zero on the boundaries $x = \pm\lambda$ and $y = \pm\omega$. Thus the fully non-linear representation of the variables is

$$u(x,y,t) = -\frac{\nu_E Ro_T}{G(x,y)}\frac{\partial G}{\partial y} + \sum_{m=1}^{\infty}\sum_{n=1}^{\infty} A_{mn}(t)\sin\left(\frac{m\pi(x+\lambda)}{2\lambda}\right)\sin\left(\frac{n\pi(y+\omega)}{2\omega}\right), \tag{4.2.6}$$

$$v(x,y,t) = \frac{\nu_E Ro_T}{G(x,y)}\frac{\partial G}{\partial x} + \sum_{m=1}^{\infty}\sum_{n=1}^{\infty} B_{mn}(t)\sin\left(\frac{m\pi(x+\lambda)}{2\lambda}\right)\sin\left(\frac{n\pi(y+\omega)}{2\omega}\right), \tag{4.2.7}$$

$$p(x,y,t) = G(x,y) + \sum_{m=1}^{\infty}\sum_{n=1}^{\infty} P_{mn}(t)\sin\left(\frac{m\pi(x+\lambda)}{2\lambda}\right)\sin\left(\frac{n\pi(y+\omega)}{2\omega}\right), \tag{4.2.8}$$

$$\rho(x,y,t) = G(x,y) + \sum_{m=1}^{\infty}\sum_{n=1}^{\infty} R_{mn}(t)\sin\left(\frac{m\pi(x+\lambda)}{2\lambda}\right)\sin\left(\frac{n\pi(y+\omega)}{2\omega}\right), \tag{4.2.9}$$

$$T(x,y,t) = 1 + \sum_{m=1}^{\infty}\sum_{n=1}^{\infty} T_{mn}(t)\sin\left(\frac{m\pi(x+\lambda)}{2\lambda}\right)\sin\left(\frac{n\pi(y+\omega)}{2\omega}\right). \tag{4.2.10}$$

In the equations (4.2.8) and (4.2.9) the function $G(x, y)$ is given by (4.1.5) and its partial derivatives with respect to x and y are used in equations (4.2.7) and (4.2.6), respectively. The time dependent Fourier coefficients $A_{mn}(t)$, $B_{mn}(t)$, $P_{mn}(t)$, $R_{mn}(t)$ and $T_{mn}(t)$ are to be determined.

Using the representation (4.2.9), the mass equation (3.4.3) can be rearranged so that

$$\frac{\partial \rho}{\partial t} = \sum_{m=1}^{\infty}\sum_{n=1}^{\infty} R'_{mn}(t)\sin\left(\frac{m\pi(x+\lambda)}{2\lambda}\right)\sin\left(\frac{n\pi(y+\omega)}{2\omega}\right) = -F_1(x, y, t), \tag{4.2.11}$$

where

$$F_1(x, y, t) = u\frac{\partial \rho}{\partial x} + v\frac{\partial \rho}{\partial y} + \rho\left(\frac{\partial u}{\partial x} + \frac{\partial v}{\partial y}\right). \tag{4.2.12}$$

The function $F_1(x, y, t)$ is simply the non-linear terms in the mass equation (3.4.3). Following a similar approach to that used by Forbes [26], a system of ordinary differential equations is derived for the Fourier coefficients, $R_{mn}(t)$. The equation (4.2.11) is decomposed spectrally by multiplying by basis functions and integrating over the region of the tangent plane $-\lambda < x < \lambda$, $-\omega < y < \omega$. Then

$$\begin{aligned}\int_{-\lambda}^{\lambda}\int_{-\omega}^{\omega}\sum_{m=1}^{\infty}\sum_{n=1}^{\infty} R'_{mn}(t)\sin\left(\frac{m\pi(x+\lambda)}{2\lambda}\right)\sin\left(\frac{k\pi(x+\lambda)}{2\lambda}\right)\sin\left(\frac{n\pi(y+\omega)}{2\omega}\right)\sin\left(\frac{l\pi(y+\omega)}{2\omega}\right)dydx \\ = -\int_{-\lambda}^{\lambda}\int_{-\omega}^{\omega} F_1(x, y, t)\sin\left(\frac{k\pi(x+\lambda)}{2\lambda}\right)\sin\left(\frac{l\pi(y+\omega)}{2\omega}\right)dydx\end{aligned} \tag{4.2.13}$$

but the orthogonality relations for trigonometric functions result in

$$\int_{-\lambda}^{\lambda}\sin\left(\frac{m\pi(x+\lambda)}{2\lambda}\right)\sin\left(\frac{k\pi(x+\lambda)}{2\lambda}\right)dx = \begin{cases}\lambda, & \text{if } m = k; \\ 0, & \text{if } m \neq k.\end{cases} \tag{4.2.14}$$

and

$$\int_{-\omega}^{\omega}\sin\left(\frac{n\pi(y+\omega)}{2\omega}\right)\sin\left(\frac{l\pi(y+\omega)}{2\omega}\right)dy = \begin{cases}\omega, & \text{if } n = l; \\ 0, & \text{if } n \neq l.\end{cases} \tag{4.2.15}$$

Therefore equation (4.2.13) is simplified using the results given by (4.2.14) and (4.2.15) to give the system of ordinary differential equations

$$R'_{kl}(t) = \frac{-1}{\lambda\omega}\int_{-\lambda}^{\lambda}\int_{-\omega}^{\omega} F_1(x,y,t)\sin\left(\frac{k\pi(x+\lambda)}{2\lambda}\right)\sin\left(\frac{l\pi(y+\omega)}{2\omega}\right)dydx$$
$$\text{for } k = 1, 2, ..., M, \text{ and } l = 1, 2, ..., N. \tag{4.2.16}$$

This procedure is replicated to derive systems of ordinary differential equations for the remaining Fourier coefficients, $A_{mn}(t)$, $B_{mn}(t)$, $P_{mn}(t)$, and $T_{mn}(t)$. In the interests of brevity they will only be stated here. The momentum equations (3.4.4), (3.4.5) give rise to the system of differential equations

$$\begin{aligned} A'_{kl}(t) = {} & \frac{\nu_E}{\lambda\omega}\int_{-\lambda}^{\lambda}\int_{-\omega}^{\omega}\frac{1}{G(x,y)}\frac{\partial G}{\partial x}\sin\left(\frac{k\pi(x+\lambda)}{2\lambda}\right)\sin\left(\frac{l\pi(y+\omega)}{2\omega}\right)dydx \\ & \frac{-1}{\lambda\omega}\int_{-\lambda}^{\lambda}\int_{-\omega}^{\omega} F_2(x,y,t)\sin\left(\frac{k\pi(x+\lambda)}{2\lambda}\right)\sin\left(\frac{l\pi(y+\omega)}{2\omega}\right)dydx \\ & + \tilde{f}B_{kl}(t) \qquad \text{for } k = 1, 2, ..., M, \text{ and } l = 1, 2, ..., N, \end{aligned} \tag{4.2.17}$$

$$\begin{aligned} B'_{kl}(t) = {} & \frac{\nu_E}{\lambda\omega}\int_{-\lambda}^{\lambda}\int_{-\omega}^{\omega}\frac{1}{G(x,y)}\frac{\partial G}{\partial y}\sin\left(\frac{k\pi(x+\lambda)}{2\lambda}\right)\sin\left(\frac{l\pi(y+\omega)}{2\omega}\right)dydx \\ & \frac{-1}{\lambda\omega}\int_{-\lambda}^{\lambda}\int_{-\omega}^{\omega} F_3(x,y,t)\sin\left(\frac{k\pi(x+\lambda)}{2\lambda}\right)\sin\left(\frac{l\pi(y+\omega)}{2\omega}\right)dydx \\ & - \tilde{f}A_{kl}(t) \qquad \text{for } k = 1, 2, ..., M, \text{ and } l = 1, 2, ..., N, \end{aligned} \tag{4.2.18}$$

where $\tilde{f}$ is the non-dimensional constant Coriolis parameter as defined in system (3.3.2) for the f-plane approximation. The differentiated equation of state (3.4.7) yields

$$P'_{kl}(t) = \frac{-1}{\lambda\omega}\int_{-\lambda}^{\lambda}\int_{-\omega}^{\omega} F_4(x,y,t)\sin\left(\frac{k\pi(x+\lambda)}{2\lambda}\right)\sin\left(\frac{l\pi(y+\omega)}{2\omega}\right)dydx$$
$$\text{for } k = 1, 2, ..., M, \text{ and } l = 1, 2, ..., N. \tag{4.2.19}$$

Finally, the energy equation (3.4.6) results in the system

$$T'_{kl}(t) = \frac{-1}{\lambda\omega}\int_{-\lambda}^{\lambda}\int_{-\omega}^{\omega} F_5(x,y,t)\sin\left(\frac{k\pi(x+\lambda)}{2\lambda}\right)\sin\left(\frac{l\pi(y+\omega)}{2\omega}\right)dydx$$
$$\text{for } k = 1, 2, ..., M, \text{ and } l = 1, 2, ..., N. \tag{4.2.20}$$

In these expressions, the non-linear terms

$$F_2(x,y,t) = u\frac{\partial u}{\partial x} + v\frac{\partial u}{\partial y} + \frac{\nu_E}{\rho}\frac{\partial p}{\partial x}, \tag{4.2.21}$$

$$F_3(x,y,t) = u\frac{\partial v}{\partial x} + v\frac{\partial v}{\partial y} + \frac{\nu_E}{\rho}\frac{\partial p}{\partial y}, \tag{4.2.22}$$

$$F_5(x,y,t) = u\frac{\partial T}{\partial x} + v\frac{\partial T}{\partial y} + (\gamma-1)\frac{p}{\rho}\left(\frac{\partial u}{\partial x} + \frac{\partial v}{\partial y}\right), \tag{4.2.23}$$

$$F_4(x,y,t) = T\,F_1(x,y,t) + \rho\,F_5(x,y,t) \tag{4.2.24}$$

have been defined for convenience, where $F_1(x,y,t)$ is given in equation (4.2.12). The equations (4.2.16) – (4.2.20) constitute a system of $5MN$ ordinary differential equations for the f-plane Fourier coefficients in the representations for the zonal velocity (4.2.6), the meridional velocity (4.2.7), the pressure (4.2.8), the density (4.2.9) and the temperature (4.2.10). A fourth-order Runge-Kutta method based on the Dormand-Prince $(4,5)$ pair [22] is used to solve the large system of differential equations by integrating the coefficients forward in time.

The variables for the zonal velocity u, meridional velocity v, pressure p, density ρ and temperature T for the β-plane approximation have the same form as for the f-plane and are represented by equations (4.2.6) – (4.2.10). However, the Fourier coefficients $A_{mn}(t)$, $B_{mn}(t)$, $P_{mn}(t)$, $R_{mn}(t)$, and $T_{mn}(t)$ will change. For the β-plane, the ordinary differential equations used to determine the Fourier coefficients $P_{mn}(t)$ (4.2.18), $R_{mn}(t)$ (4.2.19), and $T_{mn}(t)$ (4.2.20) are the same as for the f-plane. The equations for the coefficients $A_{mn}(t)$ and $B_{mn}(t)$ are the same as (4.2.17), (4.2.18), except that now the appropriate intermediate functions $F_2(x,y,t)$ and $F_3(x,y,t)$ are replaced by

$$F_6(x,y,t) = u\frac{\partial u}{\partial x} + v\frac{\partial u}{\partial y} - \tilde{\beta}yv + \frac{\nu_E}{\rho}\frac{\partial p}{\partial x},$$

$$F_7(x,y,t) = u\frac{\partial v}{\partial x} + v\frac{\partial v}{\partial y} + \tilde{\beta}yu + \frac{\nu_E}{\rho}\frac{\partial p}{\partial y},$$

respectively, to account for the additional term introduced by the dimensionless rate of change of the Coriolis parameter, $\tilde{\beta}$, defined in (3.3.2).

4.3 Initial Conditions

The initial conditions for the non-linear fluid flow in the f-plane and β-plane approximations were determined by assuming that the fluid flow was initially geostrophic and therefore its velocity was just the steady background velocity given by (4.1.1) and (4.1.2). This is achieved by setting $A_{mn}(0) = B_{mn}(0) = 0$ in equations (4.2.6) and (4.2.7). Similarly, initially the atmosphere is assumed to be isothermal so that the temperature is again just the steady background temperature $T = 1$ and thus $T_{mn}(0) = 0$ in equation (4.2.10). It then follows from equation (3.4.8) that the pressure p and density ρ are equal at $t = 0$. It has been shown in many studies of the classical instability problems such as Kelvin-Helmholtz flow [13, 15, 23] and Rayleigh-Taylor flow [26, 27] that disturbances in the interfacial region between two distinct fluids can grow in time. In this atmospheric vortex problem the initial pressure and density are disturbed by a sinusoidal or triangular wave perturbation to the interface between two distinctive regions of fluid. The sinusoidal perturbation is assumed to have the form

$$p(x, y, 0) = \rho(x, y, 0) = \begin{cases} 1, & \text{if } r > 1 + a\sin(n\theta); \\ 1 - \mu, & \text{if } r < 1 + a\sin(n\theta). \end{cases} \tag{4.3.1}$$

In equation (4.3.1) the variable μ is the maximum pressure drop, n is the perturbation mode, a is the perturbation amplitude and

$$r = \sqrt{x^2 + y^2}. \tag{4.3.2}$$

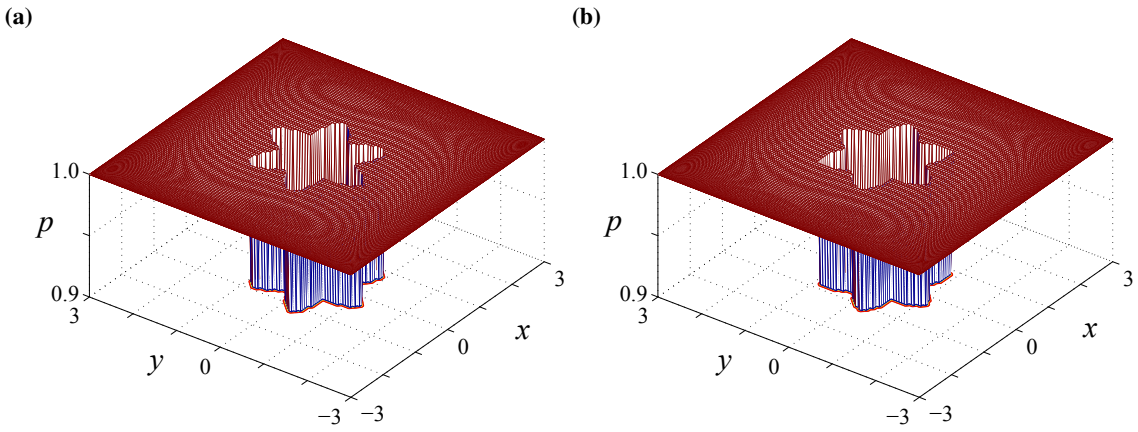

Figure 4.3.1: Sketch of 3-dimensional initial pressure and density profile with $a = 0.25$ for a mode 6 perturbation type (a) sinusoidal and (b) triangular.

Figure 4.3.1(a) shows a three-dimensional plot of the initial pressure and density profile using (4.3.1) for a mode six sinusoidal perturbation with amplitude $a = 0.25$ and pressure drop $\mu = 0.1$. The initial condition (4.3.1) is for a single mode perturbation. However, multi-modal functions are also considered using an initial pressure and density of the form

$$p(x, y, 0) = \rho(x, y, 0) = \begin{cases} 1, & \text{if } r > 1 + f(\theta); \\ 1 - \mu, & \text{if } r < 1 + f(\theta), \end{cases} \tag{4.3.3}$$

where $f(\theta)$ is a periodic perturbing function that can be expressed in terms of a multi-modal Fourier series. This has been done specifically to investigate the effects of a more complex, multi-mode initial condition. A multi-modal triangular wave perturbation will be of interest here. The triangular wave perturbation is given by

$$f(\theta) = \frac{8a}{\pi^2} \sum_{k=1}^{\infty} \frac{(-1)^{k+1} \sin[(2k-1)n\theta]}{(2k-1)^2}, \tag{4.3.4}$$

again n is the mode of the triangle wave and a is the amplitude.

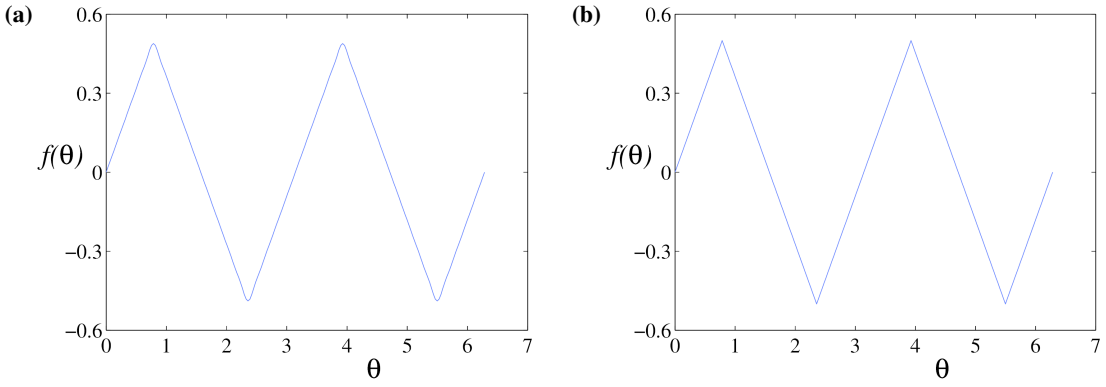

Figure 4.3.2: Mode 2 triangular wave plots of amplitude $a = 0.5$ using (a) a Fourier series and (b) an analytic representation.

The triangle wave representation (4.3.4) needs to be truncated beyond $k = 8$ Fourier modes for the series to converge to what could be interpreted as a sharp triangular wave. An example of a mode two representation truncated at $k = 9$ is shown in Figure 4.3.2(a). However, the Fourier representation of $f(\theta)$ can be expressed in the more convenient analytic form given by

$$f(\theta) = \frac{2a}{\pi}\left[\arcsin(\sin(n\theta))\right], \tag{4.3.5}$$

and is used to produce a comparative mode two representation that is illustrated in Figure 4.3.2(b). The analytic function (4.3.5) produces an exact triangular wave and is used in the simulations. Figure 4.3.1(b) shows a 3-dimensional plot of the initial pressure and density profile using (4.3.3) for a mode six triangular perturbation with amplitude $a = 0.25$ and pressure drop $\mu = 0.1$.

The Fourier coefficients for the initial pressure $P_{mn}(0)$ are determined by considering the Fourier series for the pressure (4.2.8) at time $t = 0$ so that

$$p(x, y, 0) = G(x, y) + \sum_{m=1}^{\infty}\sum_{n=1}^{\infty} P_{mn}(0)\sin\left(\frac{m\pi(x+\lambda)}{2\lambda}\right)\sin\left(\frac{n\pi(y+\omega)}{2\omega}\right), \tag{4.3.6}$$

and therefore

$$\sum_{m=1}^{\infty}\sum_{n=1}^{\infty} P_{mn}(0)\sin\left(\frac{m\pi(x+\lambda)}{2\lambda}\right)\sin\left(\frac{n\pi(y+\omega)}{2\omega}\right) = p(x, y, 0) - G(x, y). \tag{4.3.7}$$

In a similar manner to how the ordinary differential equations for the Fourier coefficients were derived, spectral decomposition of equation (4.3.7) gives

$$P_{mn}(0) = \frac{1}{\lambda\omega}\int_{-\lambda}^{\lambda}\int_{-\omega}^{\omega}[p(x,y,0) - G(x,y)]\sin\left(\frac{m\pi(x+\lambda)}{2\lambda}\right)\sin\left(\frac{n\pi(y+\omega)}{2\omega}\right)dydx. \tag{4.3.8}$$

The form of the Fourier coefficients $R_{mn}(0)$ for the density is identical, except that $p(x,y,0)$ is replaced with $\rho(x,y,0)$ in the integrand of equation (4.3.8). The quadratures are performed using the Gaussian integration routine provided by von Winckel [77].

4.4 Presentation of Results

The impetus for studying and simulating the formation of large-amplitude fingers in atmospheric vortices is shown in Figure 1.0.1. This formation occurred during July 2011, when a large ($\approx$ 1500 km in diameter) low-pressure system formed in the Great Australian Bight at an approximate latitude of 36°S. At this latitude it is suitable to use the f-plane and β-plane approximations, and a comparison of the results will be studied, in order to observe qualitative differences between both approximations. The Rossby numbers considered in this section will either be $Ro_T = 0.1$ or $Ro_T = 0.15$ and are either constant throughout the entire region of the f-plane approximation, or else take this value at $y = 0$ (corresponding to the tangent point latitude ϕ_0) for the β-plane approximation. These two Rossby numbers are chosen so that comparisons between mid-latitudes and mid-low latitude regions can be made. Also, at latitude $\phi = 36°$N where the phenomenon of interest was observed, the Rossby number takes the approximate value 0.12 which lies between the two Rossby numbers of choice. The Rossby number $Ro_T = 0.15$ corresponds to a tangent point at the mid-low latitude $\phi \approx 27.2°$N, and thus shows flow behaviour for mid-low latitude regions. The nature of mid-latitude fluid flow can be studied by considering Rossby number $Ro_T = 0.1$ which corresponds to a tangent point at the mid-latitude $\phi \approx 43.3°$N. As $Ro_T > 0$ we are looking at f-plane and β-plane approximations in the northern hemisphere. As the motivating vortex was the result of a low pressure region, the majority of results will be presented by means of pressure contour maps, as is common practice in meteorological charts.

Lipps [48] states that, for the β-plane approximation to be valid, then

$$Ro_T = \frac{1}{f\tau} = \frac{1}{\tilde{f}} \ll 1, \quad \tilde{\beta} = \beta A\tau \sim 1. \tag{4.4.1}$$

Clearly the first condition in (4.4.1) is met through the choice of Rossby numbers used in this study. For $Ro_T = 0.1$ and $Ro_T = 0.15$ the respective $\tilde{\beta}$ values are 1.667 and 2.036 and these are consistent with the second condition in (4.4.1).

The dimensionless half plane width and length will be $\lambda = 3$ and $\omega = 3$ respectively. The density scale was taken to be $\rho_0 = 1.213$ kg m^{-3}, the temperature scale was $T_0 = 290°$ K and therefore the pressure scale $\rho_0 RT_0 = 1$ atm $= 1.01 \times 10^5$ Pa. The ratio of specific heats is taken to be $\gamma = 1.4$ and the maximum dimensionless pressure drop is $\mu = 0.1$.

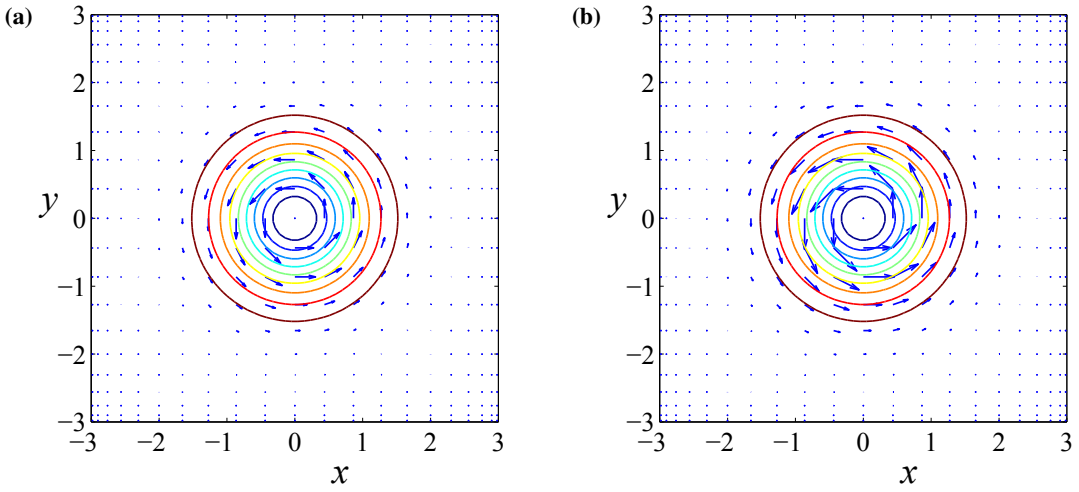

Figure 4.4.1: Steady pressure contour plots and quiver plots of steady velocity on the f-plane with Rossby numbers (a) $Ro_T = 0.1$ (b) $Ro_T = 0.15$.

Contour plots of the steady pressure p_s as defined by equation (4.1.3) together with quiver plots of the steady velocity components as defined by equations (4.1.1) and (4.1.2) for an f-plane approximation are shown in Figure 4.4.1. This figure depicts geostrophic balance, where the Coriolis effect and the pressure gradient force are equal. Figures 4.4.1(a) and 4.4.1(b) were produced using Rossby numbers $Ro_T = 0.1$ and $Ro_T = 0.15$ respectively. In the pressure contour plots, the blank outer region has pressure ranging from 0.99 to 1.00, the blank inner region has pressure in the range 0.90 to 0.91 and the visible contours have values that increase in increments of 0.01 from 0.91 to 0.99. In all subsequent contour plots in this section of the chapter, these contour values are used. The velocity for the f-plane approximation with $Ro_T = 0.15$ is exactly 50% larger than with $Ro_T = 0.1$, and this is illustrated in Figure 4.4.1, with the longer arrows in Fig-

ure 4.4.1(b) compared with Figure 4.4.1(a). In the Northern hemisphere, low pressure systems rotate in an anticlockwise direction, which has been confirmed by the quiver plot in these figures. A consequence of geostrophic flow is that the geostrophic velocity vector is parallel to lines where pressure is constant. This is also confirmed in both Figures 4.4.1(a) and 4.4.1(b) as the quivers are aligned tangentially to the contours of the steady pressure.

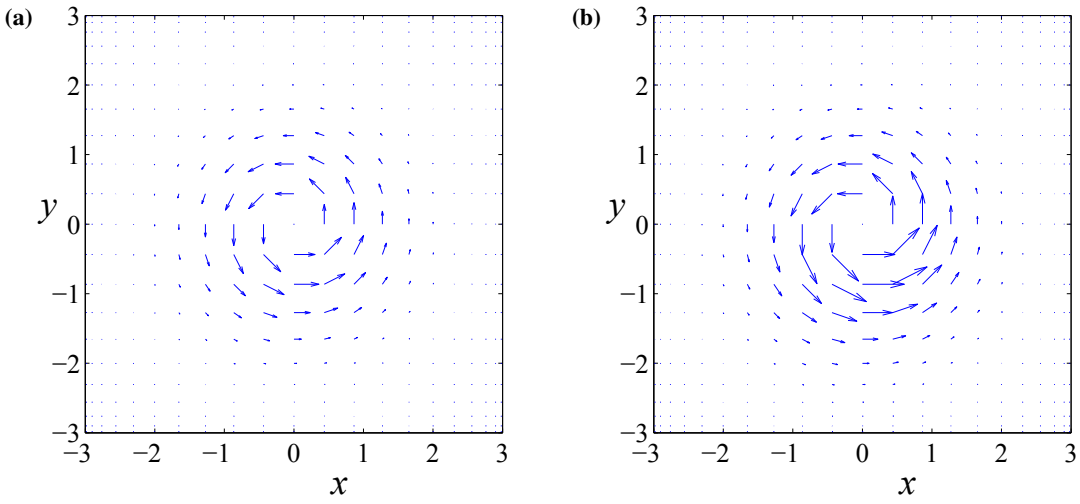

Figure 4.4.2: Steady velocity quiver plots on the β-plane with Rossby numbers (a) $Ro_T = 0.1$ (b) $Ro_T = 0.15$ on $y = 0$.

For the f-plane approximation the quivers are anti-symmetric about $y = 0$. However, this is not the case for the β-plane as the Rossby number varies as a function of latitude. The β-plane equivalent velocity plots for Figure 4.4.1 are shown in Figure 4.4.2. In this figure, the pressure contours have been omitted so the β-effect can be easily seen. In the case of the β-plane approximation, the Rossby number Ro_T increases towards the equator and so for the β-plane, the largest Rossby number occurs at $y = -3$ and the smallest at $y = 3$. This increase in Rossby number towards the equator is best illustrated by Figure 4.4.2(b) where $Ro_T = 0.15$ at $y = 0$. In the southern half of the figure the quivers are considerably longer than its northern counterpart due to the increased Rossby number, that is for $y \geq 0$, the quiver located at any coordinate (x, y) is smaller in magnitude than the corresponding quiver located at $(x, -y)$. Figure 4.4.2(a) also has larger velocities in the southern half compared to the northern half albeit not as identifiable.

When comparing the f-plane and β-plane approximations that have the same Rossby number at $y = 0$, the velocities at the same coordinate vary significantly. This is especially the case for the

Dimensionless fluid speed at $x = 0$				
Latitude Coordinate y	f-plane speed $Ro_T = 0.1$	β-plane speed $Ro_T = 0.1$ at $y = 0$	f-plane speed $Ro_T = 0.15$	β-plane speed $Ro_T = 0.15$ at $y = 0$
3.0	0.0070	0.0047	0.0105	0.0055
2.5	0.0929	0.0659	0.1394	0.0795
1.4	3.3746	2.7387	5.0619	3.5505
0.5	6.9020	6.3899	10.3530	9.0264
0	0.0000	0.0000	0.0000	0.0000
−0.5	6.9020	7.5034	10.3530	12.1353
−1.4	3.3746	4.3952	5.0619	8.8124
−2.5	0.0929	0.1579	0.1394	0.5661
−3.0	0.0070	0.0139	0.0105	0.1158

Table 4.1: Shows the dimensionless fluid velocity on the β-plane and f-plane for a selected number of latitude coordinates y, with $Ro_T = 0.1$ and $Ro_T = 0.15$ at $y = 0$.

larger Rossby number $Ro_T = 0.15$. In the southern half of the approximation regions the velocities for identical points are greater for the β-plane than for the f-plane and vice versa in the northern half. If $Ro_T = 0.15$ on $y = 0$ the velocities on the β-plane are approximately 11 times faster than those on the f-plane at the same southern latitude $y = -3$ and are about half the speed at the same northern latitude $y = 3$. Table 4.1 shows the dimensionless fluid speeds $\sqrt{u^2 + v^2}$ on the f-plane and β-planes for a selected number of y-coordinates, with $Ro_T = 0.1$ and $Ro_T = 0.15$ at $y = 0$. Here, u and v are the velocity components computed numerically from the representations (4.2.6) and (4.2.7). These results are the major influence on the differences observed between the f-plane and β-plane solutions.

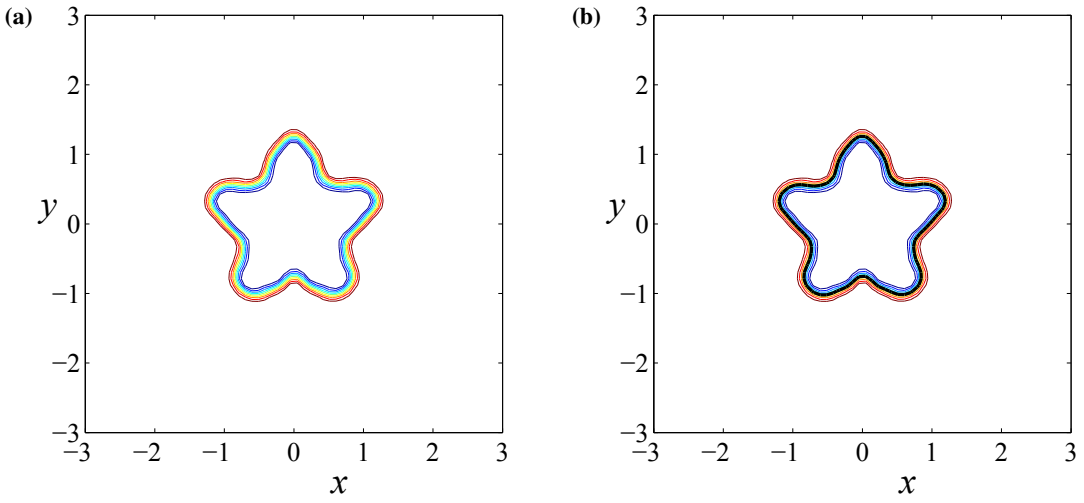

Figure 4.4.3: Pressure contour plots for a mode 5 perturbation and perturbation amplitude $a = 0.25$ at time $t = 0.001$ with (a) no interfacial pressure contour and (b) interfacial pressure contour $p = 0.95$.

In the fully non-linear solution, there are initially two distinct regions of pressure, one of low pressure ($p = 1 - \mu$) and one of a higher pressure ($p = 1$). Thus there is an initial discontinuity in the pressure, but as time progresses, this is gradually smoothed by compressibility. These two regions are separated by an interface, which is distinguished by a smooth but rapid change in pressure p, so that contours of this function are closely packed together in that zone. As the pressure difference between both regions is given by the maximum pressure drop μ, it makes sense to distinguish the boundary between both regions as the contour value of the average pressure. Therefore, the effective interface is defined to be the location of the pressure contour $p = 1 - \mu/2$. In our case where the pressure drop is $\mu = 0.1$, the interfacial pressure is the contour value $p = 0.95$. Figure 4.4.3(a) shows the pressure contours of a mode five perturbation with amplitude $a = 0.25$ at time $t = 0.001$. It can be seen that the pressure contours are tight, indicating the smooth but rapid change in pressure from the lowest value $p = 0.9$ to the highest $p = 1$. The interfacial pressure of this system is highlighted with a bold black line in Figure 4.4.3(b).

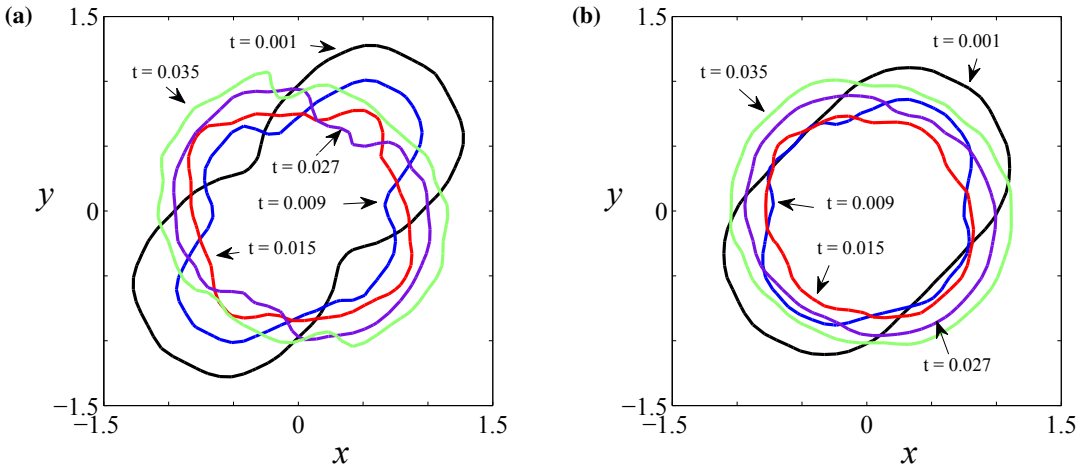

Figure 4.4.4: Interfacial pressure plot on the β-plane for a mode 2 perturbation with Rossby number $Ro_T = 0.15$ at times $t = 0.001, 0.009, 0.015, 0.027$ and 0.035 with perturbation amplitudes (a) $a = 0.5$ and (b) $a = 0.25$.

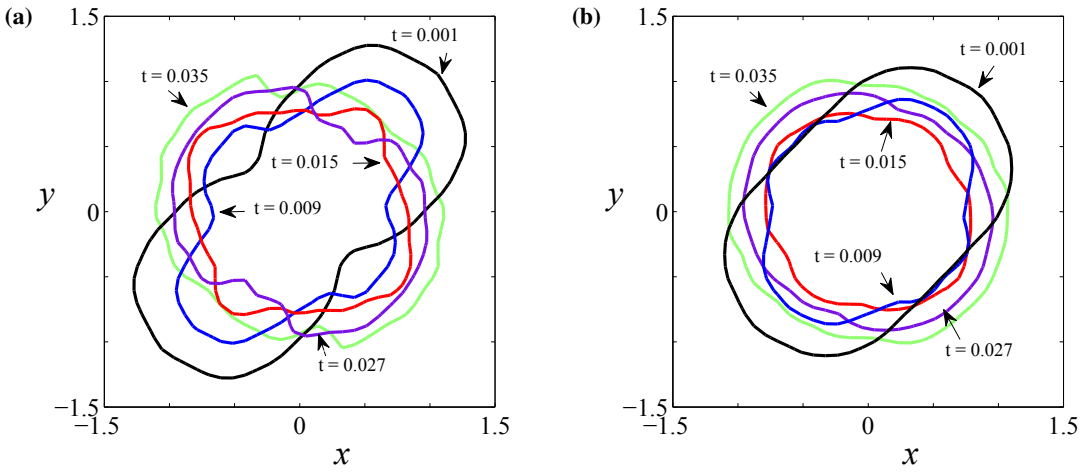

Figure 4.4.5: Interfacial pressure plot on the f-plane for a mode 2 perturbation with Rossby number $Ro_T = 0.15$ at times $t = 0.001, 0.009, 0.015, 0.027$ and 0.035 with perturbation amplitudes (a) $a = 0.5$ and (b) $a = 0.25$.

Numerous perturbation modes have been studied in this research together with perturbation amplitudes $a = 0.1$, $a = 0.25$ and $a = 0.5$. For all perturbation modes and amplitudes considered in this thesis, as time increases it is found that the pressure interface undergoes oscillations until it becomes essentially circular, suggesting it is approaching a geostrophic balance. The initial perturbation amplitude impacts on both the oscillation amplitudes and the time it takes for the pressure to reach its steady state. The larger the initial amplitude the greater the time to reach stability, and an example of this is illustrated in Figure 4.4.4.

Figure 4.4.4(a) shows the evolution of the interfacial pressure for a mode two perturbation with perturbation amplitude $a = 0.5$ and Rossby number $Ro_T = 0.15$ on $y = 0$ at times $t = 0.001$, 0.009, 0.015, 0.027 and 0.035 on the β-plane. At $t = 0.001$, the interface is elliptical in nature with the major axis oriented in a south-west to north-east direction and the minor axis is oriented in a south-east to north-west direction. As the time increases to $t = 0.035$ the interfacial pressure contour is almost circular apart from two dips in the north and south regions. In contrast the smaller perturbation amplitude $a = 0.25$ shown in Figure 4.4.4(b) has an essentially circular interfacial pressure contour at time $t = 0.015$ and beyond.

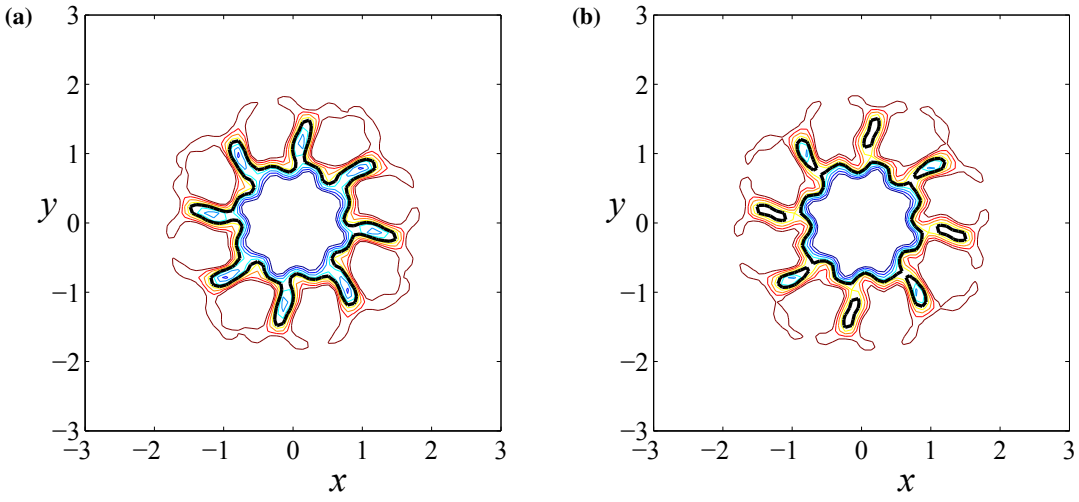

Figure 4.4.6: Pressure contour plots with interfacial pressure in bold for a mode 8 perturbation and perturbation amplitude $a = 0.5$ on the f-plane with $Ro_T = 0.15$ at time (a) $t = 0.014$ and (b) $t = 0.015$.

The corresponding f-plane interfacial pressure evolution of the parameters used in Figure 4.4.4 is depicted in Figure 4.4.5. The results of the f-plane and β-plane are similar for this mode two perturbation case; however, there is a much smoother transition to the stable circular shape, particularly in the south-east quadrant for the β-plane approximation. Once the interfacial pressure has evolved to the point where the initial perturbation amplitude has decayed to form a quasi-circular shape, the area encompassed by the interfacial contour increases with time. This is another indication that the initially smooth but rapid change in pressure is dissipating in time in an attempt to reach geostrophic balance. The interfacial pressure $p = 0.95$ is key in defining when finger formation has occurred. Finger formation is defined to be the greatest time at which the interfacial

pressure contour has one closed contour in the approximation region.

An example of when to determine the time to finger formation is given in Figure 4.4.6 which shows two consecutive time snaps of a mode eight pressure system of initial amplitude $a = 0.5$. At time $t = 0.014$ there is clearly only one closed interfacial pressure contour (Figure 4.4.6(a)) and at the next time step $t = 0.015$ (Figure 4.4.6(b)) there are nine closed interfacial contours indicating the finger formation has fully developed and begun to deteriorate. Thus for this configuration the time to finger formation is taken to be $t = 0.014$.

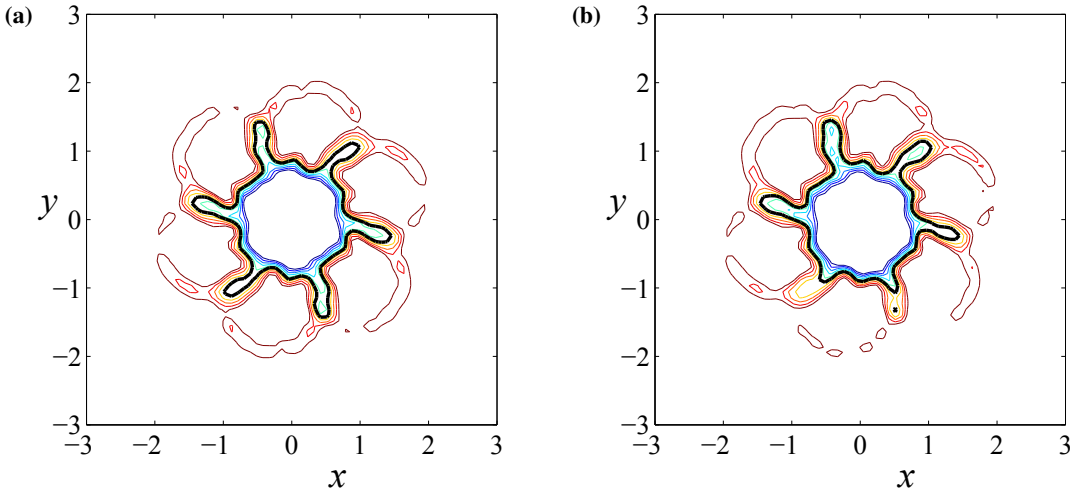

Figure 4.4.7: Pressure contour plots with interfacial pressure in bold for a mode 6 perturbation and perturbation amplitude $a = 0.5$ at time $t = 0.018$ for (a) f-plane with $Ro_T = 0.15$ and (b) β-plane with $Ro_T = 0.15$ on $y = 0$.

The predictions of the f-plane and β-plane models are contrasted in Figure 4.4.7. As the f-plane approximation uses a constant Coriolis parameter, the pressure contour plots exhibit rotational symmetry of order n about the origin of the plane, where n is the perturbation mode. This rotational symmetry is illustrated in Figure 4.4.7(a), which shows the pressure contours of a mode six perturbation with Rossby number $Ro_T = 0.15$ at time $t = 0.018$, from the f-plane equations. This is the time at which there is a clear finger structure on the outer rim of the pressure system.

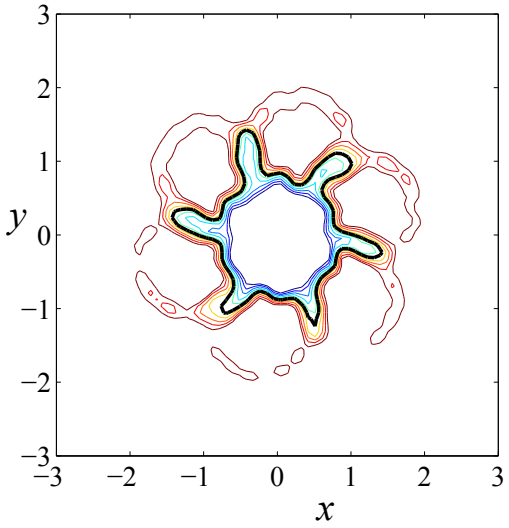

Figure 4.4.8: Pressure contour plot of a mode 6 finger formation on the β-plane with $a = 0.5$ and $Ro_T = 0.15$ on $y = 0$ at $t = 0.017$.

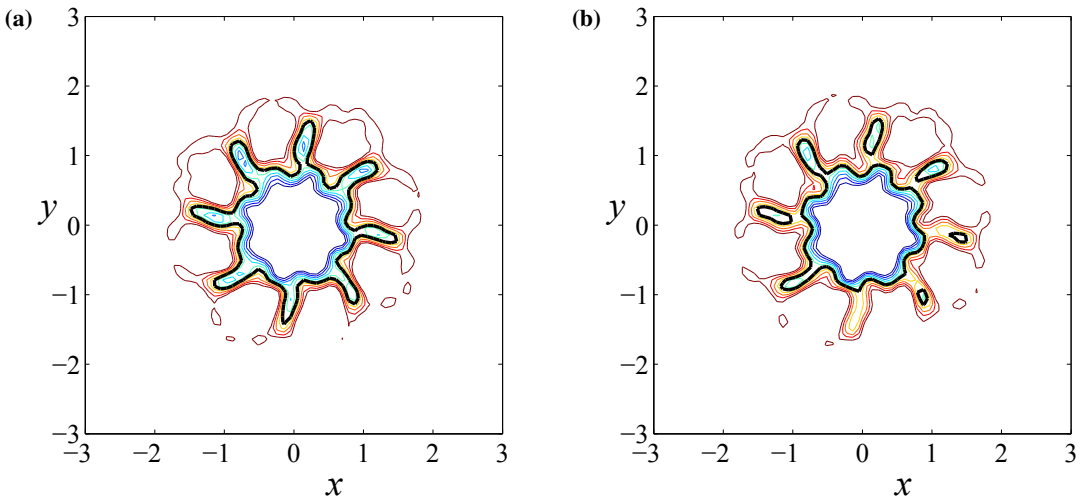

Figure 4.4.9: Pressure contour plots with interfacial pressure in bold for a mode 8 perturbation and perturbation amplitude $a = 0.5$ on the β-plane with $Ro_T = 0.15$ on $y = 0$ at time (a) $t = 0.014$ and (b) $t = 0.015$.

In contrast the β-plane approximation has a Coriolis parameter that varies linearly with latitude and consequently the pressure contour plots don't exhibit the rotational symmetry observed in the f-plane pressure plots. This lack of symmetry can be seen in Figure 4.4.7(b), which shows the pressure contour plots of the β-plane equivalent to Figure 4.4.7(a). The most noticeable differences occur in the northern region from $1 < y < 3$ and the southern region from $-3 < y < -1$. In the northern region the Rossby number $Ro_T < 0.15$ and thus the fluid speed is less than the

corresponding speed in the same region of the f-plane. This enables the pressure regions to maintain their profile and not disperse as easily. The opposite is true for the southern region, where the Rossby number $Ro_T > 0.15$ and therefore the speed of the fluid is greater than for the fluid on the f-plane in the same region. This greater speed enables the pressure to convect more rapidly on the β-plane and enables finger structures to form and deteriorate quicker. This can be seen in the southern half of Figure 4.4.7(b) where the finger structure observed for the f-plane is non-existent for the β-plane in this region. The isolated $p = 0.95$ contour indicates that the finger has broken off at this time for the β-plane. In fact, for this configuration, finger formation occurs at the earlier time $t = 0.017$, shown in Figure 4.4.8. The time itself is marginally less than for the f-plane but the finger length is considerably smaller. This result is consistent for all perturbation modes and amplitudes $a = 0.5$ and $a = 0.25$, with $Ro_T = 0.15$.

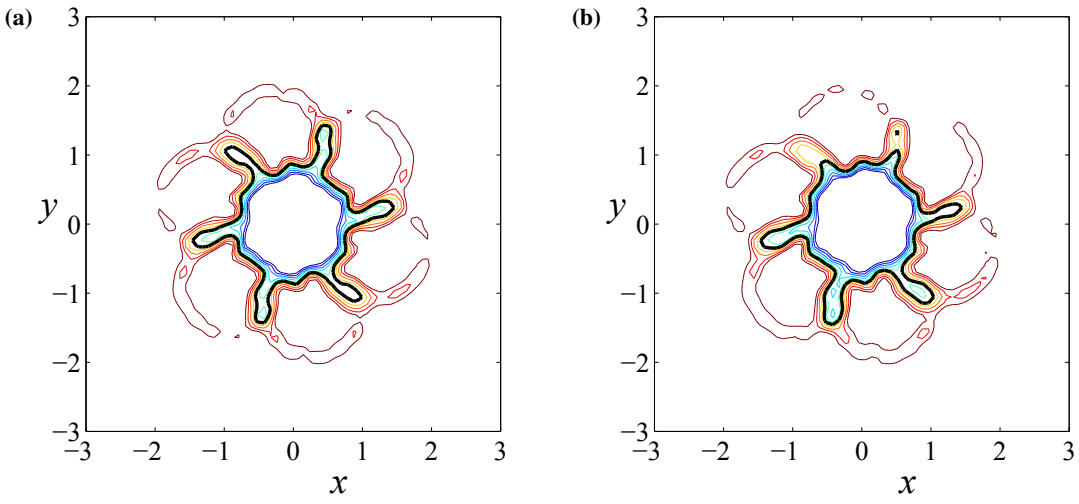

Figure 4.4.10: Southern hemisphere pressure contour plots with interfacial pressure in bold for a mode 6 perturbation and perturbation amplitude $a = 0.5$ at time $t = 0.018$ for (a) f-plane with constant Rossby number $Ro_T = -0.15$ and (b) β-plane with Rossby number $Ro_T = -0.15$ on $y = 0$.

The earlier formation and shortening of fingers induced by the β-effect is further illustrated in Figure 4.4.9(a) which is the β-plane match for Figure 4.4.6(a). For these mode eight scenarios the f-plane (Figure 4.4.6(a)) and β-plane (Figure 4.4.9(a)) fingers form at what seems to be the same time $t = 0.014$, contradicting the claim that the fingers form earlier on the β-plane; however, this is due to the time step interval chosen to produce the contour diagrams. In fact at the next time step $t = 0.015$ shown in Figure 4.4.9(b) the southern most finger tip has detached and entirely disap-

peared in the case of the β-plane simulation, compared to the isolated remnant left over from the f-plane equivalent shown by Figure 4.4.6(b). In the central region $-1 < y < 1$ where the Rossby number $Ro_T \approx 0.15$, the flow behaviour and pressure structure are almost identical as expected. The observed differences can be attributed to the β-effect, which indicates how fluid motion is affected by changes of the Coriolis parameter with respect to latitude. When $Ro_T = 0.15$ on $y = 0$, then the β-plane Rossby numbers increase from $Ro_T = 0.0783$ at $y = 3$ up to $Ro_T = 1.7834$ at $y = -3$.

The southern hemisphere equivalent to Figure 4.4.7 is presented in Figure 4.4.10. The f-plane depiction in Figure 4.4.10(a) as expected is rotationally symmetric; however, due to the opposing rotation of a low pressure system in the southern hemisphere the finger structures are spiralling out in an anti-clockwise direction as opposed to a clockwise direction shown in Figure 4.4.7(a). The magnitude of the Rossby number Ro_T increases as the magnitude of latitude decreases. This is why the observed finger structures are essentially non existent in the northern half of the β-plane shown in Figure 4.4.10(b). This is to be expected due to similar observation of the β-plane in the northern hemisphere in Figure 4.4.7(b) where the fingers were missing in southern region. This southern hemisphere simulation is shown for completeness only.

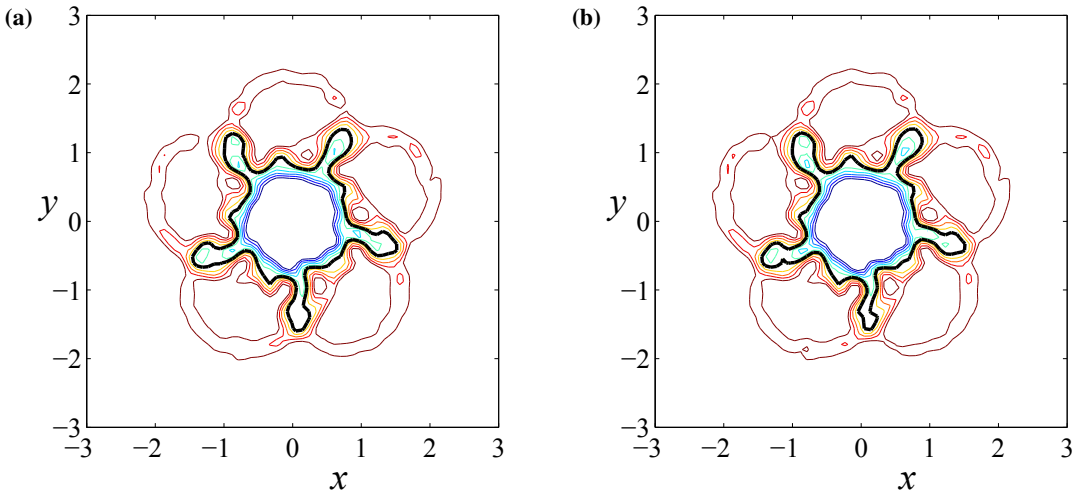

Figure 4.4.11: Pressure contour plots with interfacial pressure in bold for a mode 5 perturbation with perturbation amplitude $a = 0.5$ at time $t = 0.022$ for (a) f-plane with constant Rossby number $Ro_T = 0.1$ and (b) β-plane with Rossby number $Ro_T = 0.1$ on $y = 0$.

The β-effect is almost indistinguishable in the mid-latitude regions. If $Ro_T = 0.1$ on $y = 0$ then the β-plane approximation is almost identical to the f-plane approximation. Figures 4.4.11(a) and 4.4.11(b) are the respective pressure contour plots for an f-plane and β-plane approximation for a mode five perturbation with perturbation amplitude $a = 0.5$ at time $t = 0.022$. The only real differences between the f-plane and β-plane contour diagrams are the subtle changes in the pressure contour $p = 0.99$ in the south-east quadrant, the contour $p = 0.98$ in the south-west quadrant and the interfacial contour directed to the south and west.

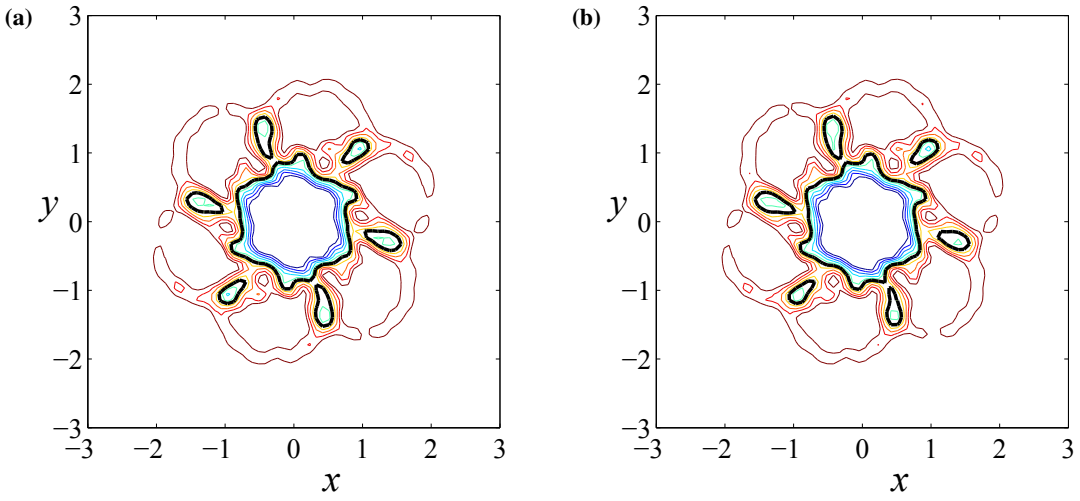

Figure 4.4.12: Pressure contour plots with interfacial pressure in bold for a mode 6 perturbation with perturbation amplitude $a = 0.5$ at time $t = 0.020$ for (a) f-plane with constant Rossby number $Ro_T = 0.1$ and (b) β-plane with Rossby number $Ro_T = 0.1$ on $y = 0$.

Further confirmation of the lack of influence the β-effect has on the simulations using the mid-latitude Rossby number $Ro_T = 0.1$ is illustrated in Figure 4.4.12. This figure shows the pressure structure just after the detachment of the primary finger growth for a mode six perturbation with amplitude $a = 0.5$. The f-plane and β-plane pressure plots in this figure are almost indistinguishable apart from the additional $p = 0.98$ contour dots and the marginally smaller in area detached finger tips in the southern region of the β-plane. This similarity of the contour maps depicted in Figures 4.4.11 and 4.4.12 can be explained by comparing the magnitudes of the change in Rossby number over the entire planar region. When $Ro_T = 0.1$ at $y = 0$, $Ro_T = 0.0667$ and $Ro_T = 0.2001$ at $y = 3$ and $y = -3$ respectively and therefore, the magnitude of the change in Rossby number over the region $-3 < y < 3$ is 0.1334 compared to 1.7051 for $Ro_T = 0.15$. This smaller range

in Rossby numbers for the β-plane approximation with $Ro_T = 0.1$ at $y = 0$ demonstrates that the velocity at any given point on the β-plane is of the same order as that on the f-plane for that given location. Therefore, significant differences between the two approximations would not be anticipated in mid-latitude regions.

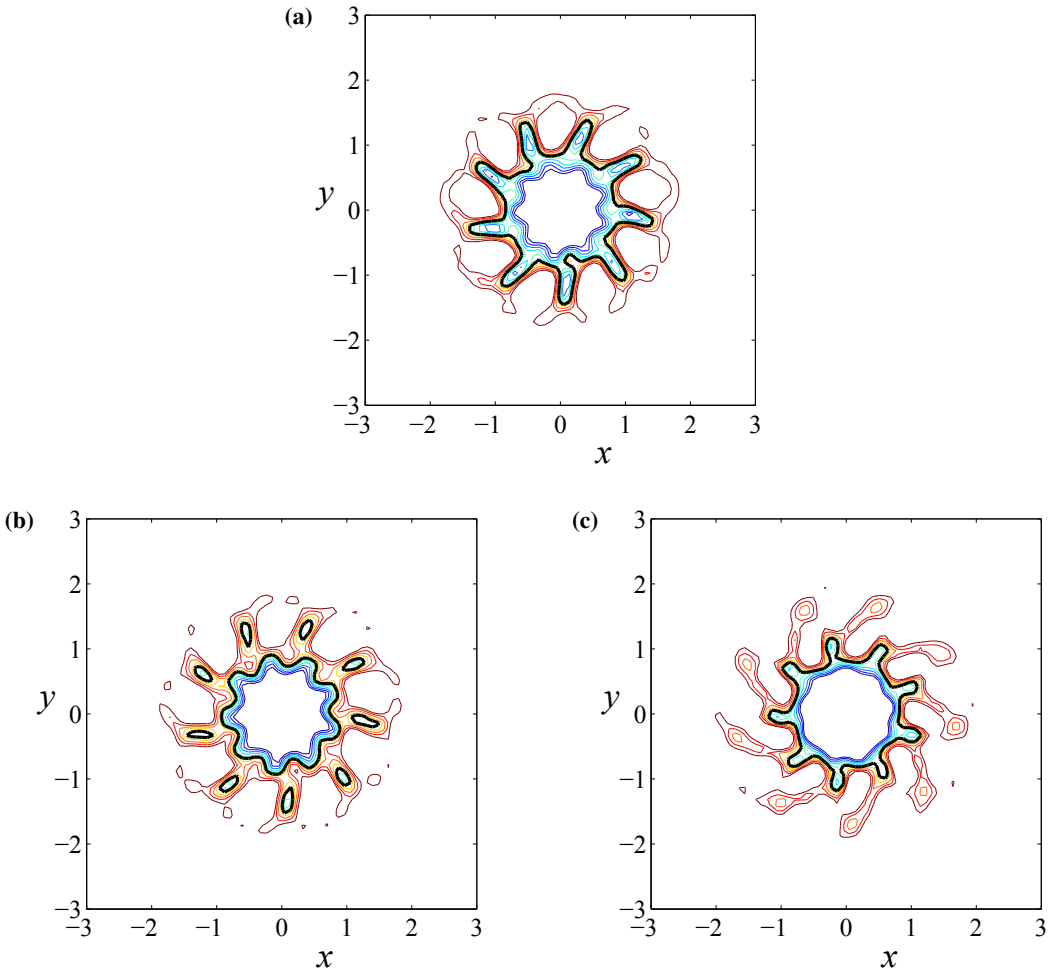

Figure 4.4.13: Pressure contour plots with interfacial contour in bold for a mode 9 perturbation with perturbation amplitude $a = 0.5$ and Rossby number $Ro_T = 0.15$ on the f-plane at times (a) $t = 0.012$, (b) $t = 0.014$ and (c) $t = 0.019$.

The continual anticlockwise rotation of the pressure system causes the finger structures to detach from the main system, resulting in pockets of low pressure ranging from $p = 0.94$ to $p = 0.97$. As expected, the number of these pressure regions correspond to the perturbation mode n. What was unexpected is that beyond the time at which the finger structures detached to form these lows, a new secondary finger structure started to form. This behaviour was observed for all perturbation

modes and amplitudes looked at in this study, provided that there existed a developed finger structure. This phenomenon is best illustrated using a mode nine perturbation and amplitude $a = 0.5$ with $Ro_T = 0.15$. For this configuration, fully formed finger structures occurred at $t = 0.012$ and fully developed secondary fingers were observed at time $t = 0.019$. The secondary finger growth is smaller in amplitude and emerges from the troughs between the initial finger growth. The initial and secondary finger formation is shown in Figures 4.4.13(a) and 4.4.13(c) respectively. Figure 4.4.13(b) shows the pressure contours at the intermediate time $t = 0.014$ between the formation of the two different finger structures and clearly shows the initial finger detachment. Once the secondary fingers separate from the main pressure system, there are no tertiary fingers formed and the fragments of the finger tips equilibrate with the surrounding pressure structure. This behaviour is replicated on the β-plane and in the interest of completeness the β-plane counterpart of Figure 4.4.13 is given in Figure 4.4.14.

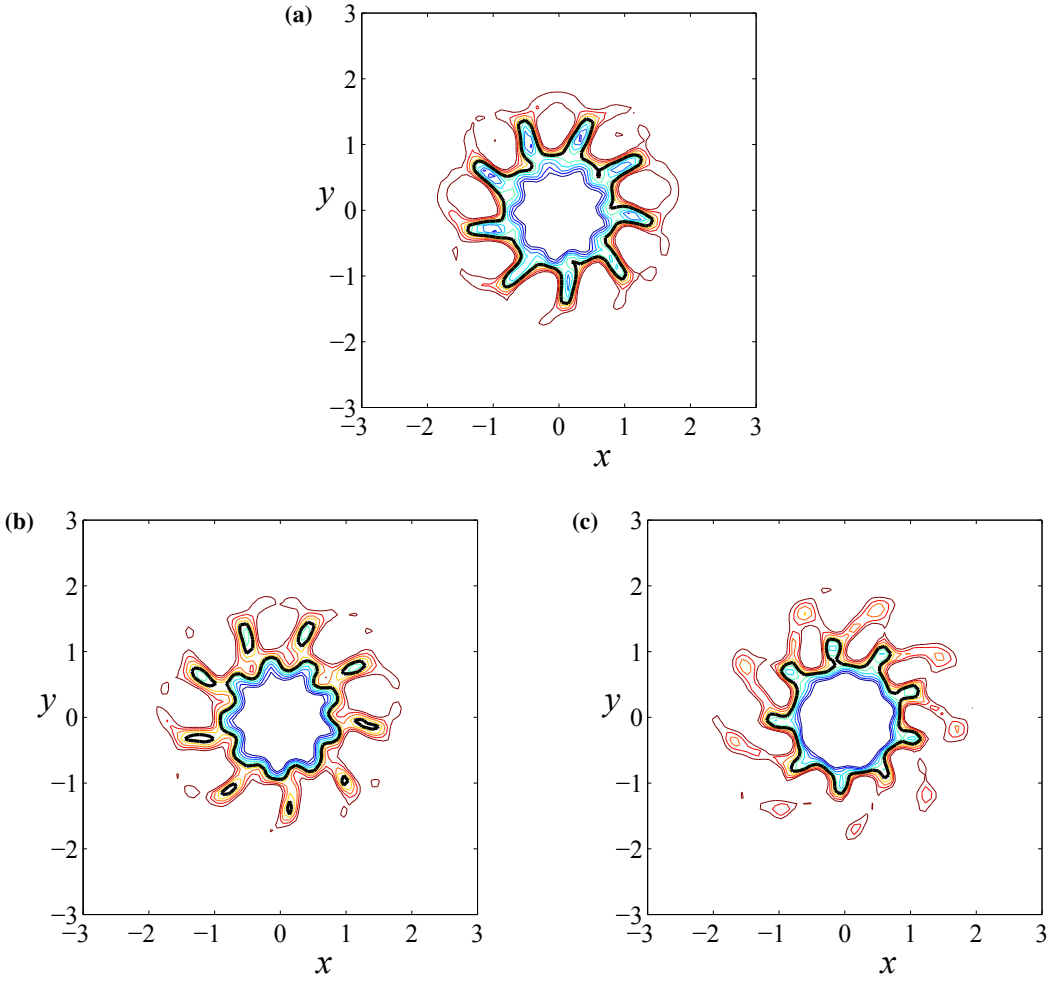

Figure 4.4.14: Pressure contour plots with interfacial contour in bold for a mode 9 perturbation with perturbation amplitude $a = 0.5$ and Rossby number $Ro_T = 0.15$ at $y = 0$ on the β-plane at times (a) $t = 0.012$, (b) $t = 0.014$ and (c) $t = 0.019$.

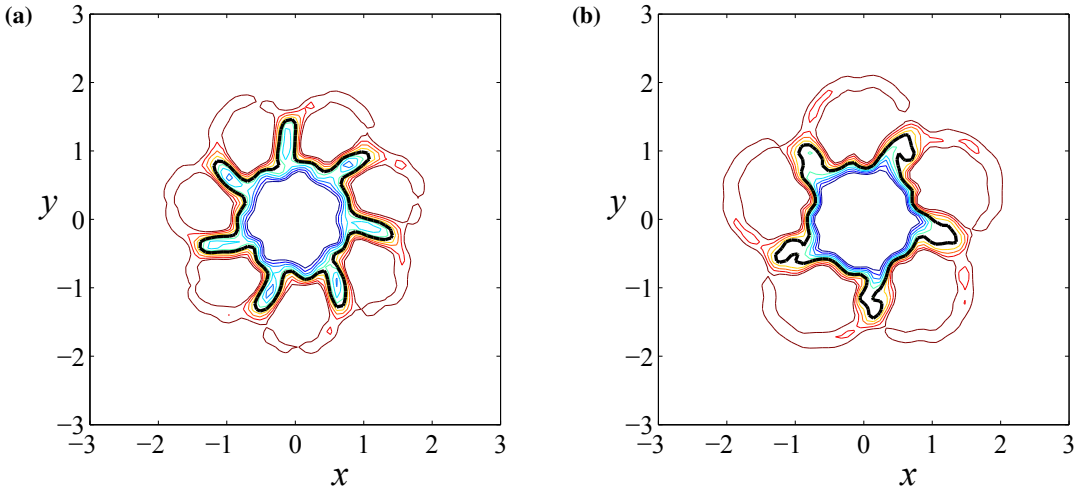

Figure 4.4.15: Pressure contour plots with interfacial contour in bold, perturbation amplitude $a = 0.5$ and $Ro_T = 0.15$ on the f-plane for a (a) mode 7 perturbation at time $t = 0.015$ and (b) mode 5 perturbation at time $t = 0.019$.

The resultant features and characteristics observed when $Ro_T = 0.15$ are similar for all perturbation modes considered in this thesis, although the times at which fully formed finger structures occur differ slightly. When the perturbation amplitude is the same, the time to finger formation is marginally increased as the perturbation mode decreases; this in part is shown in Figure 4.4.15. Finger structures have completely formed at time $t = 0.015$ for a mode seven perturbation (Figure 4.4.15(a)), compared to $t = 0.019$ for the decreased mode five perturbation (Figure 4.4.15(b)). Table 4.2 gives a summary of the time to finger primary finger formation for various perturbation modes with amplitude $a = 0.5$ using $Ro_T = 0.15$. Decreasing the Rossby number to $Ro_T = 0.1$ increases the time to develop primary finger structures when compared against the corresponding flows with $Ro_T = 0.15$. This is verified by comparing Figures 4.4.11(a) and 4.4.15(b).

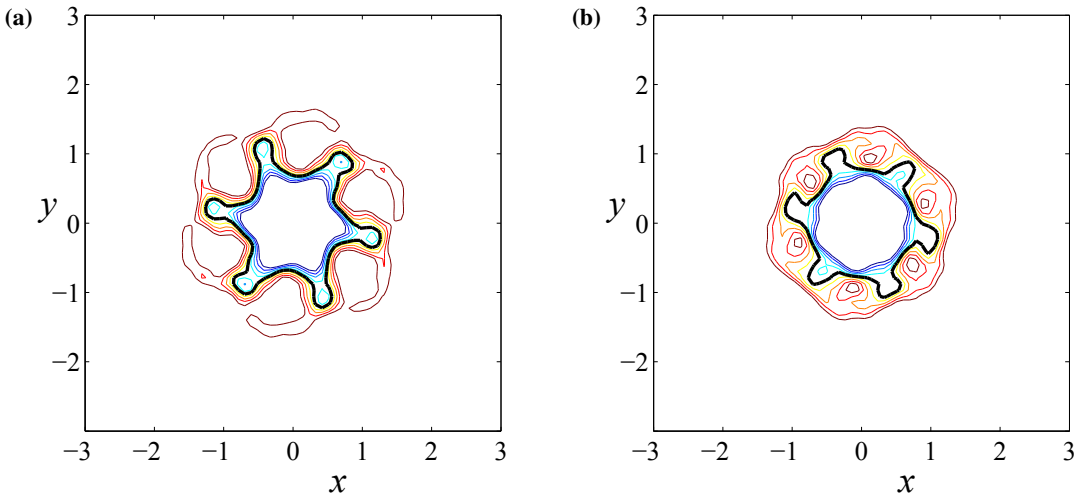

Figure 4.4.16: Pressure contour plots of a mode 6 perturbation with $Ro_T = 0.15$ on the f-plane including interfacial pressure in bold with (a) $a = 0.25$ at $t = 0.014$ and (b) $a = 0.10$ at $t = 0.009$

Changing the initial perturbation amplitude a also impacts on the formation of finger structures. If the initial amplitude of the perturbation was decreased to $a = 0.25$ then the time to finger formation also decreased. To illustrate this point Figure 4.4.16(a) shows the fully formed fingers for a mode six perturbation with reduced amplitude $a = 0.25$ at time $t = 0.014$, whereas for a mode six perturbation with amplitude $a = 0.5$ the fingers formed at $t = 0.018$, as presented in Figure 4.4.7(a). When the perturbation amplitude decreases further to $a = 0.1$, the well defined finger structures do not eventuate in this case. However, a formation of a slight 'knuckle' feature is observed and is shown in Figure 4.4.16(b).

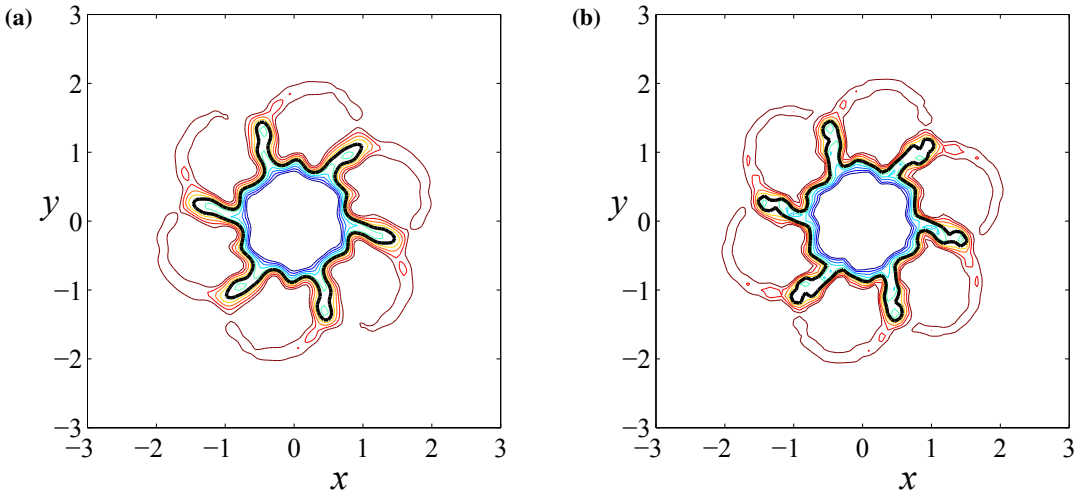

Figure 4.4.17: Pressure contour plots with interfacial pressure in bold for a mode 6 perturbation and perturbation amplitude $a = 0.5$ at time $t = 0.018$ on the f-plane with constant Rossby number $Ro_T = 0.15$ with (a) $M = N = 31$ and 151×151 grid and (b) $M = N = 41$ and 101×101 grid.

Solving problems using numerical methods introduces inaccuracies that need to be limited. It is essential that the numerical solution is accurate enough to produce reliable results. The contour plots presented above have used $M = N = 31$ Fourier coefficients and 101 grid points in each spatial variable. From a numerical viewpoint, the only role these grid points play is to evaluate the integral involving the non-linear terms $F_1(x, y, t)$ (equation (4.2.12)), and so on, and have no bearing on the numbers M and N of Fourier modes used. To justify using these values, different grid resolutions and truncations in the Fourier series representations were investigated. Increasing the grid size to 151×151 has no influence on the numerical solution. Figure 4.4.17(a) shows the contour map for the same parameters as in Figure 4.4.7(a) except that a grid of 151×151 points is used. Besides the minor changes in the outermost contour $p = 0.99$, the contour diagram 4.4.17(a) is almost indistinguishable from that of Figure 4.4.7(a). The numerical solution for increased Fourier modes of $M = N = 41$ is shown in Figure 4.4.17(b). By direct comparison with Figure 4.4.7(a) it can be concluded that introducing higher Fourier modes suggests that our numerical solution when $M = N = 31$ with 101×101 grid points has converged, as there are only small scale changes in the tips of the finger structures.

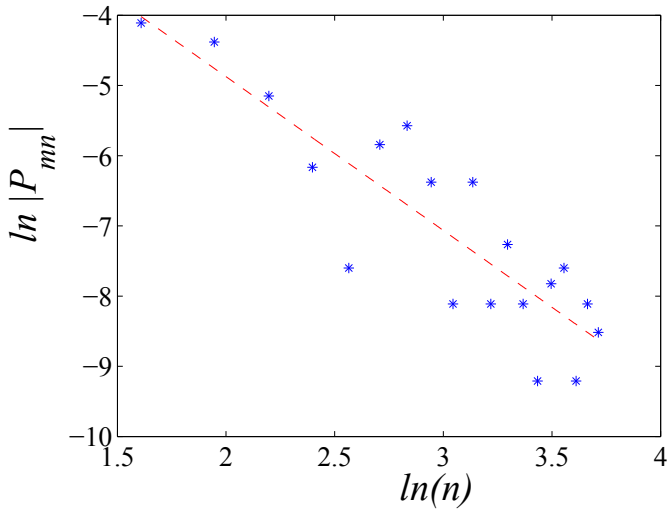

Figure 4.4.18: Log – log plot of the Fourier coefficients $P_{mn}(t)$ for the pressure variable with $M = N = 41$ at time $t = 0.020$ for $m = 1$. Dashed red line is the line of best fit with slope equal to negative 2.16.

Furthermore, an analysis of the Fourier coefficients with increasing mode number n has been undertaken, by fitting a straight line on a log – log plot. This reveals that the coefficients decay approximately like n^{-2}. An example log – log plot for $|P_{mn}(t)|$ is shown in Figure 4.4.18, for the case $m = 1$ at time $t = 0.020$. In this instance, every second coefficient is zero and so has been omitted; the first few coefficients are also not shown, since it is only the later ones that are of interest. The coefficients are drawn with (blue) asterisks, and the (red) dashed line is the 'best fit' line, with slope -2.16.

All the simulations so far have consisted of a single mode perturbation of sinusoidal profile. However, considering an initial pressure and density of the form given by equation (4.3.3) the initial perturbation takes the form of a multi-modal Fourier series, in the form of a triangle wave. The multi-modal nature arises in how the triangular wave is defined in terms of the Fourier sine series given by equation (4.3.4). A mode two triangular wave ($n = 2$) with amplitude $a = 0.5$ transforms (4.3.4) such that

$$f(\theta) = \frac{16}{\pi^2} \sum_{k=1}^{\infty} \frac{(-1)^{k+1} \sin[(4k-2)\theta]}{(4k-2)^2}. \tag{4.4.2}$$

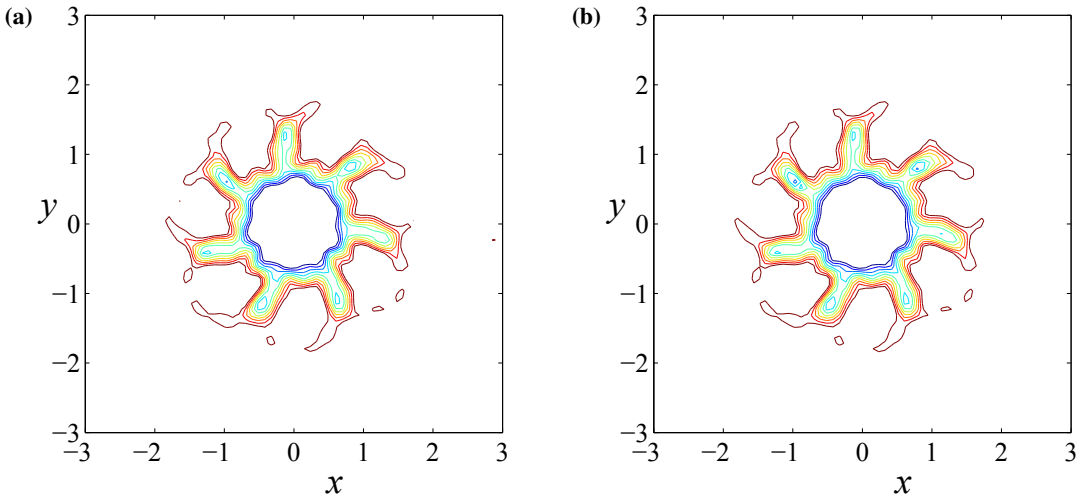

Figure 4.4.19: Pressure contour plots for a mode 7 perturbation with perturbation amplitude $a = 0.5$ on the f-plane with $Ro_T = 0.15$ at time $t = 0.015$ using (a) a sinusoidal perturbation and (b) a triangular perturbation truncated at $k = 3$.

The equation (4.4.2) was used to produce Figure 4.3.2(a), with $k = 9$ truncation, and thus is multi-modal with modes $4k - 2$, $k \in \mathbb{N}$. It is evident from Figure 4.3.2 that truncating beyond $k = 9$, the higher modes have little influence over the general shape of the triangular wave in its initial state. In fact, although not shown in Figure 4.3.2, the higher order truncation terms only significantly influence and sharpen the tips of the triangle wave. Figure 4.4.19 shows the pressure contours of a mode seven triangular perturbation of initial amplitude $a = 0.5$ at time $t = 0.015$. Figures 4.4.19(a) and 4.4.19(b) were respectively generated using the analytic equation (4.3.5) and the Fourier representation (4.3.4) with truncation $k = 3$. Interestingly, both triangular wave interpretations essentially produces the same output, suggesting that the higher order modes needed for the Fourier series interpretation of the triangular wave have marginal impact on the overall flow characteristics when compared to the analytic function results.

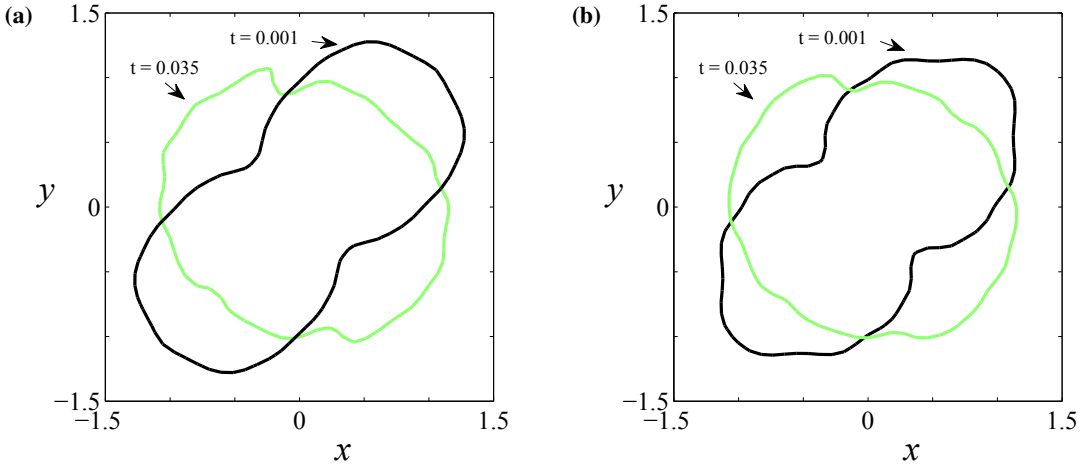

Figure 4.4.20: Interfacial pressure plot on the β-plane with perturbation amplitude $a = 0.5$ and Rossby number $Ro_T = 0.15$ at times $t = 0.001$ and 0.035 for a (a) Mode 2 perturbation and (b) Multi-mode perturbation with $m = 2$.

Finger formation times for perturbation amplitude $a = 0.5$		
Mode number	Sinusoidal perturbation	Triangle perturbation
5	0.019	0.017
6	0.018	0.017
7	0.015	0.015
8	0.014	0.013
9	0.012	0.012
10	0.011	0.010

Table 4.2: Shows the time to finger formation for selected sinusoidal and triangular perturbation modes with $a = 0.5$ and $Ro_T = 0.15$.

The results from applying a multi-modal perturbation (4.3.3) with (4.3.4) are similar to those achieved using a sinusoidal perturbation (4.3.1). Figure 4.4.20(a) shows the interfacial pressure on the β-plane for a mode two perturbation at times $t = 0.001$ and $t = 0.035$ and there is close resemblance to a multi-mode perturbation when $n = 2$ (mode two triangular wave) at the same times shown in Figure 4.4.20(b). The higher modes seem to smooth out the interfacial contours as time increases. When a triangular wave perturbation is used, the time to finger formation either decreases slightly or remains the same when compared to a sinusoidal perturbation. A summary of the time to finger formation for sinusoidal and triangular wave perturbation of amplitude $a = 0.5$

on the f-plane with $Ro_T = 0.15$ is shown in Table 4.2.

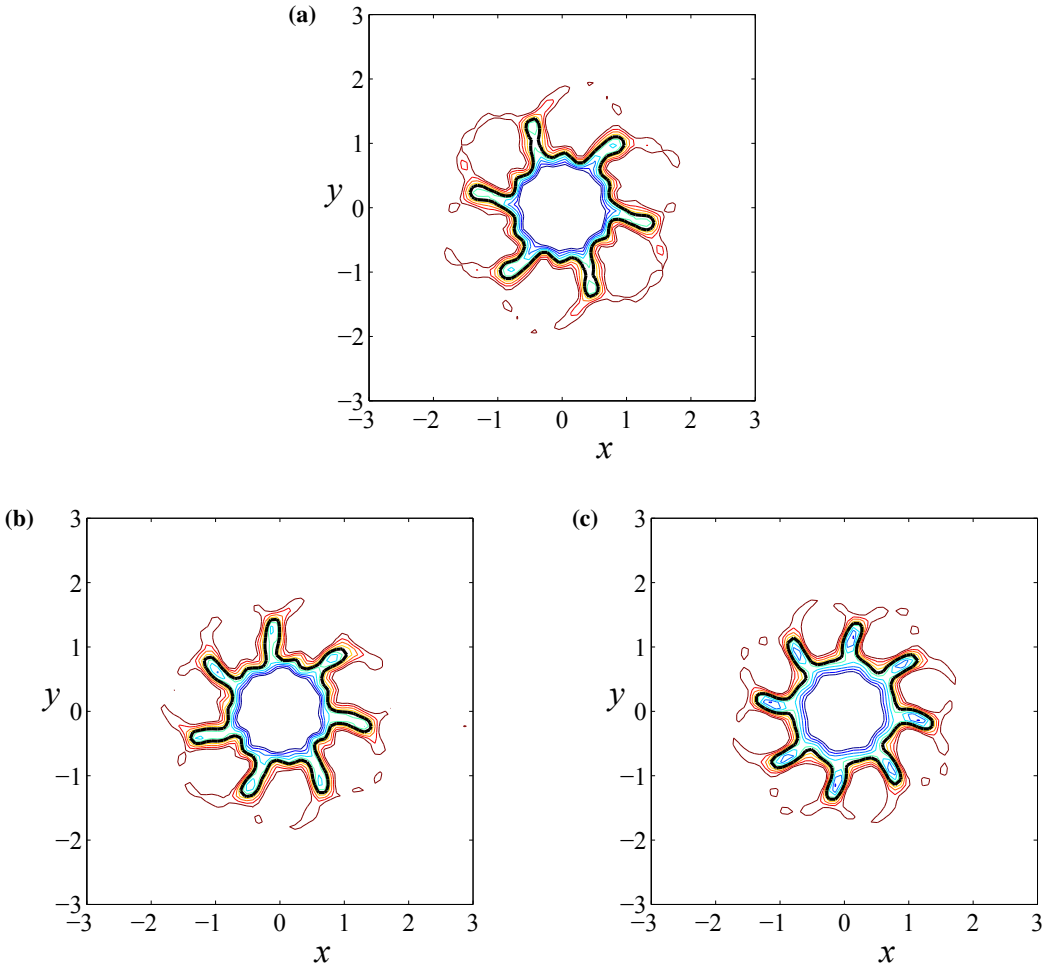

Figure 4.4.21: Pressure contour plots with triangle wave perturbation of amplitude $a = 0.5$ and $Ro_T = 0.15$ on the f-plane for a (a) mode 6, $t = 0.017$, (b) Mode 7, $t = 0.015$ and (c) Mode 8, $t = 0.013$.

Contour plots of when fingers have formed for triangular modes six, seven and eight of amplitude $a = 0.5$ are given in Figures 4.4.21(a), (b) and (c) respectively. A direct comparison with their sinusoidal counterparts in Figures 4.4.7(a), 4.4.15(a) and 4.4.6(a) shows that the structures are virtually identical apart from differing times at which finger structures formed in the case of the mode six and eight simulations.

4.5 Discussion

The results of the finger formations predominantly concentrated on the structure of large-scale vortices in the Earth's atmosphere that initially have a perturbed sinusoidal structure. However, simulations were also run with an initial triangle wave perturbation which can be interpreted as a multi-modal perturbation, contrasting the singular mode of the sinusoidal perturbation. As time passes, these perturbations grow, die out and even regrow to form wave-like fingers. The aim was firstly to look at what conditions are most favourable for these perturbations to grow and form large-scale finger formations on the outer edges of the pressure system. Secondly, the role of the f-plane and β-plane approximations on finger development has been studied. In the f-plane approximation, the Coriolis acceleration is assumed to be constant; whereas it varies with latitude in the β-plane theory. The greatest difference between both approximations is seen at the extremities of the planes. This is to be expected as the β-effect is more noticeable further away from the f-plane tangent latitude.

The observation data that initially inspired the work in this thesis shows the fingers spiralling out and travelling in the same direction as the system's rotation, owing to the fluid velocity being greater on the outer edges of the pressure system (see Figure 1.0.1), particularly on the western side of the pressure system as indicated in Figure 1.0.2 by the dense pressure contours to the west of the low-pressure system. However, as shown in this thesis, the fingers spiral out in the opposite direction to the system's rotation as the fluid velocity is largest in the centre of the simulated pressure systems used here, and thus leaves the finger tips trailing behind.

By considering the Rossby numbers $Ro_T = 0.1$ and $Ro_T = 0.15$, the focus has been directed on the accuracy of the approximation models in the mid-latitude and mid-low latitude regions. If $Ro_T = 0.1$, then the origin of the approximation for both the f-plane and β-plane is located along the latitude $\phi \approx 43.3°$N corresponding to a mid-latitude region. The mid-low latitude of $\phi \approx 27.2°$N is the tangent point latitude for simulations involving $Ro_T = 0.15$. In the mid-latitude simulations the results for both the f-plane and β-plane are almost identical. At lower latitudes the β-effect is more pronounced due to the greater range of the Rossby numbers. Therefore, it is concluded that in mid-latitude regions the f-plane is sufficiently accurate to be able to ignore the β-effect, whereas in the mid-low latitude regions the β-effect is significant and thus the β term

must be included in the Coriolis parameter. At the mid-low latitude considered in this thesis, the initial finger formation occurred consistently earlier with shorter length for the β-plane simulations compared to those on the f-plane. This quicker development time can only be attributed to the increased β-effect.

The time to initial finger formation is taken to be the latest time at which the interfacial pressure contour $p = 0.95$ has one closed contour. Beyond this time, the weakly compressible atmosphere and physical rotation of the system cause the finger tips to detach and form pockets of low pressure that dissipate in time as secondary finger structures form. The secondary fingers emerge from the troughs of the primary finger growth. The time at which secondary finger structures occur is taken to be when there is again one closed contour of the interfacial pressure contour. The amplitude of the secondary fingers is substantially smaller than the initial finger length and thus no significant tertiary fingers develop.

The initial condition for pressure has a substantial impact on the subsequent development of the finger formations on the outer regions of the pressure system. Several perturbation modes have been investigated throughout this thesis. The higher the perturbation mode, the more pronounced is the finger structure formed. This was especially the case for the largest perturbation amplitude of $a = 0.5$. For the lowest perturbation amplitude $a = 0.1$ the development of fingers was non-existent. The results of using an initial triangle wave perturbation which happens to be multi-modal are similar to those achieved using a sinusoidal perturbation. The higher modes in the triangle wave structure seem to smooth out the interfacial contours as time increases and the time to finger formation either decreases slightly or remains the same when compared to the purely sinusoidal perturbations.

The original motivation for this research as seen in Figure 1.0.1 was a low pressure system in the southern hemisphere. However, the majority of results presented here are of a low pressure system in the northern hemisphere, apart from Figure 4.4.10 which is the result of a southern hemisphere ($f < 0$ and $Ro_T < 0$) simulation. The results from the opposite hemispheres are identical, except for the fact that they are reflected about the centre line $y = 0$.

The evolution of a perturbed single low-pressure system was of interest in this chapter. This

raises the question of how such vortices in the mid-latitude regions would interact when in close proximity to another, and this is the topic of the next chapter.

Chapter 5

Non-linear behaviour of interacting mid-latitude atmospheric vortices

Non-linear behaviour of interacting large-scale atmospheric vortices is considered in this chapter. These vortices are approximately fifteen kilometres high and can have diameters of hundreds if not thousands of kilometres, and thus can be treated as large flat structures. The vortices studied are coupled binary systems, in the form of mid-latitude atmospheric vortices. Although not mid-latitude vortices, a captured satellite image of interacting atmospheric vortices is shown in Figure 1.0.3. If atmospheric vortices interact, their interactive behaviour at any given time can be categorised into one of five well defined interactive processes [24]: (i) elastic interaction, (ii) partial straining-out, (iii) complete straining-out, (iv) partial merger and (v) complete merger. Unlike a majority of binary interaction studies, where the focus is on the inelastic interactions ((ii)–(v)), the focus of this section is on whether or not elastic interaction takes place. Khain *et al.* [40] state that elastic interaction occurs when the vortices interact without any significant change in their intensity and structure. Mid-latitude vortices have been largely overlooked in the binary interaction field and thus the current problem will examine the elastic interaction of extra-tropical cyclones and anti-cyclones and give some insight into this somewhat neglected area of binary interaction.

In the current problem, the air is weakly compressible, and the fluid motion is subject to the Coriolis pseudo-force, due to the Earth being in a non-inertial rotating reference frame. The high or low pressure in each vortex is modelled initially using an exponential function. The results from Chapter 4 have shown that, at the mid-latitude tangent point $\phi = 43.3°$N considered here,

the f-plane approximation is sufficiently accurate, particularly when the velocity near the tangent plane boundaries is basically zero in magnitude. Furthermore, the interactive processes between vortices when using the β-plane are virtually identical to those on the simplified f-plane [11]; however, there is a nett movement of the centre of interaction due to the β-drift. As the overall movement of the coupled binary system as a sole entity is of little interest in this chapter, the f-plane approximation will be used to investigate the interaction of extra-tropical cyclones and anti-cyclones at mid-latitudes. It is found that the vortices do or do not interact, depending on the initial radii and location of their centres. A scaling law is found numerically for the ratio of these two quantities, which determines whether interaction does occur.

Similar to the numerical method used for developing large-amplitude finger structures, discussed in Chapter 4, a spectral method is presented, for obtaining accurate numerical solutions. However, there are substantial differences to the current spectral technique to that outlined previously. In Chapter 4, the evolution of the finger structures was partly driven by the initial perturbations that had a smooth but rapid change in pressure. The formations that occurred were the result of the perturbations equilibrating with the background geostrophic flow. In contrast, the current chapter has no added perturbing feature influencing the pressure structure and/or resulting flow. Apart from the initial pressure structure, the resultant pressure variation as time evolves is in most part due to the 'Fujiwhara effect' and interactive processes. As a result, some of the mathematical conditions differ from those outlined in the previous chapter and thus are detailed accordingly.

5.1 Background Flow

The background flow is determined by ignoring time dependent variations in the five variables. The geometry of the of the f-plane used in simulating interacting mid-latitude vortices is chosen such that the the important flow induced by the interactive process occurs in the centre of the 'tangent plane', bounded by an approximate region similar to that used for the finger structure simulations in Chapter 4. This enables the boundary values and near boundary values of the variables to be independent of time and spatial variation, thus approximated by constants. Non-dimensionalized variables are again used, as discussed in Chapter 3, and the isothermal atmospheric assumption suggests that the background temperature must be

$$T_b(x, y) = 1. \tag{5.1.1}$$

It follows then from (3.4.8) that the background values of pressure and density are

$$p_b(x, y) = 1 \ ; \ \rho_b(x, y) = 1. \tag{5.1.2}$$

The geostrophic zonal and meridional velocity components are dependent on the spatial derivatives of pressure. Near the boundaries the pressure is approximately constant and thus the background velocity components are

$$u_b(x, y) = -\frac{\nu_E Ro_T}{\rho_b(x, y)} \frac{\partial p_b(x, y)}{\partial y} = 0, \tag{5.1.3}$$

$$v_b(x, y) = \frac{\nu_E Ro_T}{\rho_b(x, y)} \frac{\partial p_b(x, y)}{\partial x} = 0. \tag{5.1.4}$$

5.2 Spectral Solution Method

The five dependent variables pressure p, density ρ, temperature T, zonal velocity component u and the meridional velocity component v are written as the sum of a near boundary background component and an evolving component dependent on time. Therefore

$$p(x, y, t) = p_b(x, y) + p_u(x, y, t) = 1 + p_u(x, y, t), \tag{5.2.1}$$

$$\rho(x, y, t) = \rho_b(x, y) + \rho_u(x, y, t) = 1 + \rho_u(x, y, t), \tag{5.2.2}$$

$$T(x, y, t) = T_b(x, y) + T_u(x, y, t) = 1 + T_u(x, y, t), \tag{5.2.3}$$

$$u(x, y, t) = u_b(x, y) + u_u(x, y, t) = u_u(x, y, t), \tag{5.2.4}$$

$$v(x, y, t) = v_b(x, y) + v_u(x, y, t) = v_u(x, y, t). \tag{5.2.5}$$

The near-boundary background components as indicated with the subscript b, are given by the equations (5.1.1), (5.1.2), (5.1.3) and (5.1.4). The fully non-linear time dependent forms of the variables are expressed as

$$p(x,y,t) = 1 + \sum_{m=1}^{\infty}\sum_{n=1}^{\infty} P_{mn}(t)F_m(x)G_n(y), \tag{5.2.6}$$

$$\rho(x,y,t) = 1 + \sum_{m=1}^{\infty}\sum_{n=1}^{\infty} R_{mn}(t)F_m(x)G_n(y), \tag{5.2.7}$$

$$T(x,y,t) = 1 + \sum_{m=1}^{\infty}\sum_{n=1}^{\infty} T_{mn}(t)F_m(x)G_n(y), \tag{5.2.8}$$

$$u(x,y,t) = \sum_{m=1}^{\infty}\sum_{n=1}^{\infty} A_{mn}(t)F_m(x)G_n(y), \tag{5.2.9}$$

$$v(x,y,t) = \sum_{m=1}^{\infty}\sum_{n=1}^{\infty} B_{mn}(t)F_m(x)G_n(y). \tag{5.2.10}$$

The aim is to solve for the five sets of time-dependent coefficients $P_{mn}(t)$, $R_{mn}(t)$, $T_{mn}(t)$, $A_{mn}(t)$ and $B_{mn}(t)$.

It is first necessary to choose appropriate basis functions $F_m(x)$ and $G_n(y)$ in the representations (5.2.6) – (5.2.10), given that the governing equations (3.4.3) – (3.4.7) are to be solved over the rectangular portion of the f-plane $-\lambda < x < \lambda$, $-\omega < y < \omega$. An obvious choice is to impose Dirichlet conditions on the unsteady components of the variables in (5.2.6) – (5.2.10), of the form

$$p(\pm\lambda, y, t) = 0 \ ; \ p(x, \pm\omega, t) = 0, \tag{5.2.11}$$

$$\rho(\pm\lambda, y, t) = 0 \ ; \ \rho(x, \pm\omega, t) = 0, \tag{5.2.12}$$

$$T(\pm\lambda, y, t) = 0 \ ; \ T(x, \pm\omega, t) = 0, \tag{5.2.13}$$

$$u(\pm\lambda, y, t) = 0 \ ; \ u(x, \pm\omega, t) = 0, \tag{5.2.14}$$

$$v(\pm\lambda, y, t) = 0 \ ; \ v(x, \pm\omega, t) = 0. \tag{5.2.15}$$

Employing such boundary conditions makes the near boundary background components (5.1.1) – (5.1.4) the exact boundary values for the problem. This leads to the familiar set of basis functions

$$F_m(x) = \sin\left(\frac{m\pi(x+\lambda)}{2\lambda}\right) \ ; \ G_n(y) = \sin\left(\frac{n\pi(y+\omega)}{2\omega}\right). \tag{5.2.16}$$

It has been found, however, that a spectral representation based on the functions in equation (5.2.16) produces waves in the solution that are reflected off the (artificial) boundaries of the f-plane and cause the pressure systems to pulse in an unrealistic manner and is discussed later in section 5.4. The oscillations in the pressure systems are reduced by limiting the influence of the artificial wave reflection. This is achieved by using Robin (absorbing) boundary conditions, which act as an insulator; they are a linear combination of the values of a variable and the values of its normal derivative on the tangent plane boundary. For this problem the Robin boundary conditions are of the general form

$$S_u = -\kappa\frac{\partial S_u}{\partial n} \quad \text{on } x = \pm\lambda,\ y = \pm\omega, \tag{5.2.17}$$

where S_u is the unsteady time-dependent component of the given variable, the normal derivative is $\partial S_u/\partial n = \nabla S_u \cdot \mathbf{n}$ and $\mathbf{n}$ is the outward unit normal vector at the boundary. The coefficient κ is an absorption constant. At $x = \lambda$ the time dependent components can be written

$$S_u(\lambda, y, t) = \sum_{m=1}^{\infty}\sum_{n=1}^{\infty} S_{mn}(t)F_m(\lambda)G_n(y), \tag{5.2.18}$$

where $S_{mn}(t)$ corresponds to the associated Fourier coefficient. The normal derivative at $x = \lambda$ is

$$\begin{aligned}\frac{\partial S}{\partial n} &= \nabla S \cdot \mathbf{i} \\ &= \sum_{m=1}^{\infty}\sum_{n=1}^{\infty} S_{mn}(t)F'_m(\lambda)G_n(y).\end{aligned} \tag{5.2.19}$$

It follows from the Robin boundary condition (5.2.17) that at $x = \lambda$

$$\sum_{m=1}^{\infty}\sum_{n=1}^{\infty} S_{mn}(t)F_m(\lambda)G_n(y) = -\kappa\sum_{m=1}^{\infty}\sum_{n=1}^{\infty} S_{mn}(t)F'_m(\lambda)G_n(y), \tag{5.2.20}$$

thus, from (5.2.20)

$$F_m(\lambda) = -\kappa F'_m(\lambda). \tag{5.2.21}$$

Similarly at $x = -\lambda$

$$F_m(-\lambda) = \kappa F'_m(-\lambda). \tag{5.2.22}$$

For consistency the basis functions for the Robin boundary value problem must recover the existing basis functions (5.2.16) for the Dirichlet problem when $\kappa = 0$. For this to occur, the x-directed basis function $F_m(x)$ and its derivative $F'_m(x)$ will have the respective forms

$$F_m(x) = A\cos(\alpha_m(x+\lambda)) + \sin(\alpha_m(x+\lambda)), \tag{5.2.23}$$

and

$$F'_m(x) = -\alpha_m A\sin(\alpha_m(x+\lambda)) + \alpha_m\cos(\alpha_m(x+\lambda)), \tag{5.2.24}$$

where A is a constant. It follows from equations (5.2.23) and (5.2.24) that (5.2.21) is expanded to give

$$\begin{aligned} F_m(\lambda) &= A\cos(2\alpha_m\lambda) + \sin(2\alpha_m\lambda) \\ &= \alpha_m\kappa A\sin(2\alpha_m\lambda) - \alpha_m\kappa\cos(2\alpha_m\lambda) = -\kappa F'_m(\lambda). \end{aligned} \tag{5.2.25}$$

and (5.2.22) becomes

$$F_m(-\lambda) = A = \alpha_m\kappa = \kappa F'_m(-\lambda). \tag{5.2.26}$$

Substituting equation (5.2.26) transforms (5.2.25) so that

$$\alpha_m\kappa\cos(2\alpha_m\lambda) + \sin(2\alpha_m\lambda)) = \alpha_m^2\kappa^2\sin(2\alpha_m\lambda) - \alpha_m\kappa\cos(2\alpha_m\lambda). \tag{5.2.27}$$

The equations (5.2.23), (5.2.26) and (5.2.27) are used to determine the basis functions that satisfy the Robin boundary conditions (5.2.17), and although not shown here an identical approach is used to derive the y-directed forms. Thus the basis functions are taken to be

$$F_m(x) = \alpha_m \kappa \cos(\alpha_m(x+\lambda)) + \sin(\alpha_m(x+\lambda)), \tag{5.2.28}$$

$$G_n(y) = \beta_n \kappa \cos(\beta_n(y+\omega)) + \sin(\beta_n(y+\omega)), \tag{5.2.29}$$

in which the constants α_m and β_n are the respective solutions to the transcendental equations

$$\sin(2\alpha_m\lambda) = \alpha_m\kappa[-2\cos(2\alpha_m\lambda) + \alpha_m\kappa\sin(2\alpha_m\lambda)], \tag{5.2.30}$$

$$\sin(2\beta_n\omega) = \beta_n\kappa[-2\cos(2\beta_n\omega) + \beta_n\kappa\sin(2\beta_n\omega)]. \tag{5.2.31}$$

The derivation of the y-directed basis function equations (5.2.29) and (5.2.31) follow the exact same process as the x-directed equations (5.2.28) and (5.2.30).

Notice that, if $\kappa = 0$ then $\alpha_m = m\pi/2\lambda$ in equations (5.2.28) and (5.2.30) and $\beta_n = n\pi/2\omega$ in (5.2.29) and (5.2.31). So the previous basis functions (5.2.16) for the Dirichlet boundary conditions are recovered in the non-absorbing limit $\kappa \to 0$. However, when $\kappa \neq 0$ the transcendental equations (5.2.30), (5.2.31) are solved using Newton's method to determine the constants α_m and β_n. To find appropriate initial guesses for these constants, for use in Newton's method, perturbation theory to first order in κ was employed to give the initial estimates

$$\alpha_m^{(0)} = \frac{m\pi}{2\lambda}\left(1 - \frac{\kappa}{\lambda}\right),$$
$$\beta_n^{(0)} = \frac{n\pi}{2\omega}\left(1 - \frac{\kappa}{\omega}\right).$$

The spectral solution is therefore given by the representations (5.2.6) – (5.2.10), with basis functions (5.2.28), (5.2.29) and constants determined from the transcendental equations (5.2.30), (5.2.31).

The time-dependent coefficients $A_{mn}(t)$, $B_{mn}(t)$, $P_{mn}(t)$, $R_{mn}(t)$ and $T_{mn}(t)$ are now determined from the governing equations. Using the non-linear representation (5.2.7), the mass equation (3.4.3) can be expressed

$$\frac{\partial \rho}{\partial t} = \sum_{m=1}^{\infty}\sum_{n=1}^{\infty} R'_{mn}(t)F_m(x)G_n(y) = -F_1(x,y,t), \tag{5.2.32}$$

where the function $F_1(x,y,t)$ represents the non-linear terms in the mass equation (3.4.3) and is given by (4.2.12). It is necessary to derive a system of ordinary differential equations for the time

dependent Fourier coefficients, $R_{mn}(t)$. The equation (5.2.32) is decomposed by multiplying by the basis functions $F_k(x)$ and $G_l(y)$ in (5.2.28) and (5.2.29), and integrating over the domain of the tangent plane. This results in

$$\int_{-\lambda}^{\lambda}\int_{-\omega}^{\omega}\sum_{m=1}^{\infty}\sum_{n=1}^{\infty}R'_{mn}(t)F_k(x)G_l(y)F_m(x)G_n(y)\,dydx = -\int_{-\lambda}^{\lambda}\int_{-\omega}^{\omega}F_1(x,y,t)F_k(x)G_l(y)\,dydx \tag{5.2.33}$$

However, unlike the Dirichlet boundary value problem basis functions (5.2.16), the basis functions for the Robin boundary problem (5.2.28), (5.2.29) fail to result in a convenient orthogonality relationship when multiplied and integrated, and therefore the integrals involving the product of similar basis functions do not collapse and simplify. Thus (5.2.33) is expressed as

$$\sum_{m=1}^{M}\sum_{n=1}^{N}\mathbf{Q}_{klmn}R'_{mn}(t) = \overline{R_{kl}} \quad \text{for } k = 1, 2, ..., M, \text{ and } l = 1, 2, ..., N, \tag{5.2.34}$$

where

$$\mathbf{Q}_{klmn} = \int_{-\lambda}^{\lambda}\int_{-\omega}^{\omega}F_k(x)G_l(y)F_m(x)G_n(y)\,dydx \tag{5.2.35}$$

and

$$\overline{R_{kl}} = -\int_{-\lambda}^{\lambda}\int_{-\omega}^{\omega}F_1(x,y,t)F_k(x)G_l(y)\,dydx. \tag{5.2.36}$$

To solve (5.2.34), the constants $\overline{R_{kl}}$ are stored in an $(MN \times 1)$ vector, and the matrix $\mathbf{Q}_{klmn}$ is then represented as an $(MN \times MN)$ matrix, and the linear equations then solved for $R'_{mn}(t)$ at each time t. The ordinary differential equations for the remaining Fourier coefficients, $A_{mn}(t)$, $B_{mn}(t)$, $P_{mn}(t)$, and $T_{mn}(t)$ are derived in a similar manner and thus will only be stated here. The momentum equations (3.4.4) and (3.4.5) result in the respective systems

$$\sum_{m=1}^{M}\sum_{n=1}^{N}\mathbf{Q}_{klmn}\left[A'_{mn}(t) - \tilde{f}\,B_{mn}(t)\right] = \overline{A_{kl}} = -\int_{-\lambda}^{\lambda}\int_{-\omega}^{\omega}F_2(x,y,t)F_k(x)G_l(y)\,dydx, \tag{5.2.37}$$

$$\sum_{m=1}^{M}\sum_{n=1}^{N}\mathbf{Q}_{klmn}\left[B'_{mn}(t) + \tilde{f}\,A_{mn}(t)\right] = \overline{B_{kl}} = -\int_{-\lambda}^{\lambda}\int_{-\omega}^{\omega}F_3(x,y,t)F_k(x)G_l(y)\,dydx, \tag{5.2.38}$$

where $\tilde{f}$ is the dimensionless constant Coriolis parameter given in system (3.3.2) for the f-plane approximation. The energy equation (3.4.6) gives

$$\sum_{m=1}^{M}\sum_{n=1}^{N}\mathbf{Q}_{klmn}T'_{mn}(t) = \overline{T_{kl}} = -\int_{-\lambda}^{\lambda}\int_{-\omega}^{\omega}F_5(x,y,t)F_k(x)G_l(y)\,dydx. \tag{5.2.39}$$

The final system comes from the differentiated equation of state (3.4.7) and takes the form

$$\sum_{m=1}^{M}\sum_{n=1}^{N}\mathbf{Q}_{klmn}P'_{mn}(t) = \overline{P_{kl}} = -\int_{-\lambda}^{\lambda}\int_{-\omega}^{\omega}F_4(x,y,t)F_k(x)G_l(y)\,dydx. \tag{5.2.40}$$

The right hand sides of equations (5.2.37) – (5.2.40) are identical to equation (5.2.36), except that the non-linear function $F_1(x,y,t)$ is replaced with the previously defined non-linear terms given by equations (4.2.21) – (4.2.24). The equations (5.2.37) – (5.2.40) are solved in a similar manner to (5.2.34). The constants $\overline{R_{kl}}$, $\overline{A_{kl}}$, $\overline{B_{kl}}$, $\overline{T_{kl}}$ and $\overline{P_{kl}}$ are not to be confused with the Fourier coefficients $R_{mn}(t)$, $A_{mn}(t)$, $B_{mn}(t)$, $T_{mn}(t)$, and $P_{mn}(t)$.

5.3 Initial Conditions

The initial conditions are determined in a similar manner to those derived for the finger structures problem as shown in the previous Chapter 4. The atmosphere is initially isothermal, with constant dimensionless temperature

$$T(x,y,0) = 1, \tag{5.3.1}$$

and this is achieved by setting $T_{mn}(0) = 0$ in equation (5.2.8).

Due to equation (5.3.1) having to satisfy the dimensionless equation of state (3.4.8), the initial pressure and density have the same form and each will be modelled using an exponential function of the form

$$p(x,y,0) = 1 - E(x,y) = \rho(x,y,0) \tag{5.3.2}$$

where

$$E(x,y) = \mu_1 \exp\left[-\left(\frac{(x+L)^2+(y+L)^2}{\sigma_1^2}\right)\right] + \mu_2 \exp\left[-\left(\frac{(x-L)^2+(y-L)^2}{\sigma_2^2}\right)\right] \tag{5.3.3}$$

and μ_k for $k = 1, 2$ are constants that give the pressure difference from background pressure $p = 1$. If $\mu_k < 0$ this produces high-pressure systems and low-pressure systems when $\mu_k > 0$

and $(x, y) = \pm(L, L)$ are the initial eye locations of the pressure systems. The initial radii of the pressure systems are given by σ_k for $k = 1, 2$. The subscripts $k = 1$ and $k = 2$ refer to the pressure systems originally in the south-west and north-east quadrants of the f-plane respectively. Logically, there are three different scenarios for binary interaction, (i) two low-pressure systems, (ii) two high-pressure systems or (iii) a combination of both. This leads to four types of binary interactions that will be considered. A binary system that contains only low-pressure systems will be called an LL-binary system, whereas an HH-binary system consists of two high-pressure systems. These may also be referred to as non-mixed binary systems. We will also consider mixed systems, where there is both a high- and a low-pressure system present. The initial locations for the two pressure systems will always be in the south-west and north-east quadrants. If we have a low-pressure system in the south-west quadrant then we call this an LH-binary system and an HL-binary system if there is a high in the south-west quadrant. A three-dimensional plot of the initial pressure and density profile for an LL-binary, HH-binary, LH-binary and HL-binary system is shown in Figure 5.3.1(a), (b), (c) and (d) respectively. In these figures, the eyes of the systems are located at $L = \sqrt{2}$, and the radius of each system is $\sigma_1 = \sigma_2 = 1$.

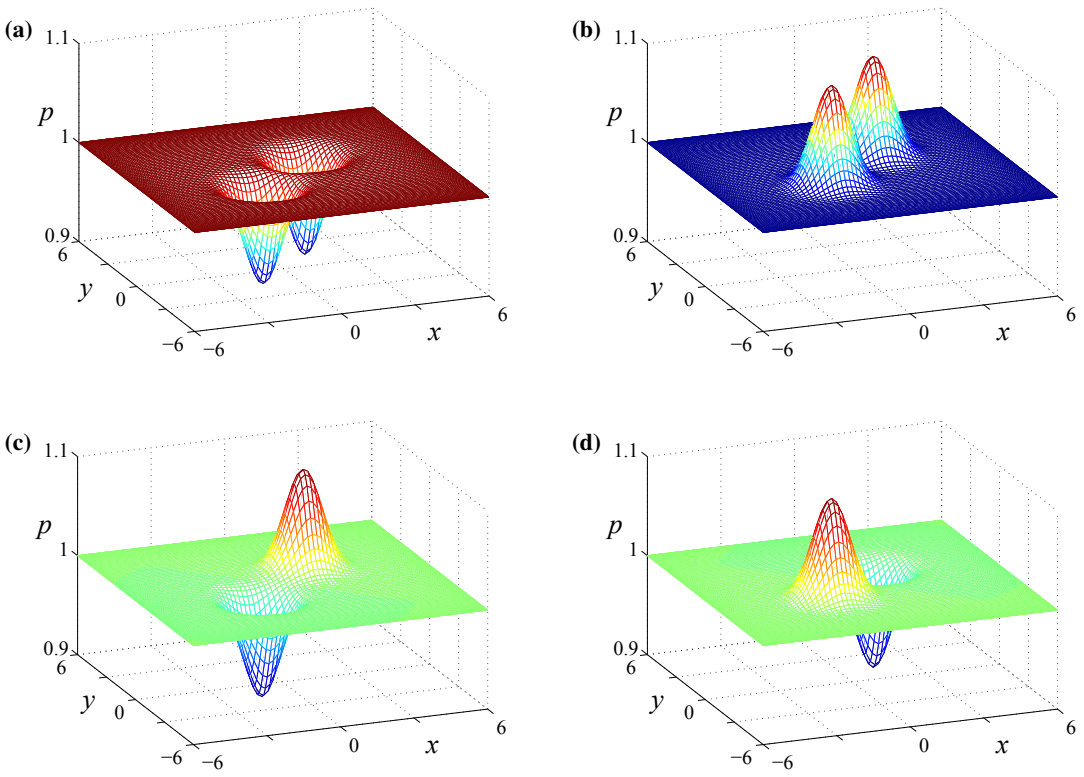

Figure 5.3.1: Sketch of four 3-dimensional initial binary pressure systems centred at $L = \sqrt{2}$ and $\sigma_1 = \sigma_2 = 1.0$ for (a) LL-binary system with $\mu_1 = \mu_2 = 0.1$, (b) HH-binary system with $\mu_1 = \mu_2 = -0.1$, (c) LH-binary system with $\mu_1 = 0.1$ and $\mu_2 = -0.1$ and (d) HL-binary system with $\mu_1 = -0.1$ and $\mu_2 = 0.1$.

Spectral decomposition is used to find the initial values for the Fourier coefficients $P_{mn}(0)$ and $R_{mn}(0)$ for the pressure and density components. This leads to the equation

$$\sum_{m=1}^{M}\sum_{n=1}^{N}\mathbf{Q}_{klmn}P_{mn}(0) = I_{kl}, \tag{5.3.4}$$

where $\mathbf{Q}_{klmn}$ is defined by (5.2.35) and

$$I_{kl} = -\int_{-\lambda}^{\lambda}\int_{-\omega}^{\omega}E(x,y)F_k(x)G_l(y)\,dydx, \tag{5.3.5}$$

in which $E(x,y)$ is defined by (5.3.3). The matrix equation (5.3.4) is solved for the initial coefficients $P_{mn}(0)$. The initial coefficients $R_{mn}(0)$ are identical in this non-dimensionalization, so $R_{mn}(0) = P_{mn}(0)$.

The material derivative terms in equations (3.4.4) and (3.4.5) are neglected when assuming geostrophic flow, so that the initial zonal and meridional velocity simplify approximately to

$$u(x, y, 0) = -\frac{\nu_E Ro_T}{\rho(x, y, 0)} \frac{\partial p(x, y, 0)}{\partial y}, \tag{5.3.6}$$

$$v(x, y, 0) = \frac{\nu_E Ro_T}{\rho(x, y, 0)} \frac{\partial p(x, y, 0)}{\partial x}. \tag{5.3.7}$$

The initial Fourier coefficients for the zonal velocity component $A_{mn}(0)$ and meridional velocity component $B_{mn}(0)$ are similarly determined by substituting in place of $P_{mn}(0)$ in equation (5.3.4) and the exponential term $-E(x, y)$ in equation (5.3.5) is replaced with $u(x, y, 0)$ as defined by (5.3.6) when solving for $A_{mn}(0)$ and $v(x, y, 0)$ given by (5.3.7) when determining $B_{mn}(0)$.

5.4 Presentation of Results

In Chapter 4 the behaviour of a single atmospheric vortex was of interest. A further extension to atmospheric vortex behaviour is to look at how they interact when in close proximity to another vortex. A particular research focus has been the study of when two atmospheric vortices interact and merge. However, it is quite uncommon for two atmospheric vortices to merge considering how many actually interact. In fact, the merger of Typhoons Pat and Ruth is said to be the first documented case of merging vortices in the atmosphere [44]. The merger condition for atmospheric vortices has been extensively studied, but little has been done on what Dritschel and Waugh [24] term elastic interaction. Elastic interaction occurs when coupled vortices interact with minimal changes to their structure and intensity [40]. The satellite image shown in Figure 1.0.3 shows Typhoons Parma and Melor interacting elastically. This Chapter investigates binary interaction in terms of elastic interaction. It is found that the vortices interact or not, dependent on their initial radii and the location of their centres. A scaling law is found numerically for the ratio of these two quantities, that determines whether interaction occurs.

More often than not, the major focus of binary interaction research has been focussed on tropical cyclones and typhoons. Very few interaction studies have considered atmospheric vortices in the mid-latitude regions where the time scale Rossby number $Ro_T = 0.1$. The density ρ_0, temperature T_0 and pressure p_0 scales are the same as for the finger structure simulations, as well as the ratio of specific heats γ. However, the dimensionless half-width and half-length are chosen to be $\lambda = \omega = 6$ respectively, unless specified otherwise. This domain was chosen initially to minimise the effects of the false reflections from the numerical boundaries, and this is discussed in more

detail later (see Figures 5.4.7 and 5.4.8). In the results that follow, it will be seen that most of the important features of the flow occur only in the approximate dimensionless zone $-3 < x < 3$, $-3 < y < 3$. It was shown in Chapter 4 and subsequent article by Cosgrove and Forbes [16] that at the latitude of interest, 43.3°N ($Ro_T = 0.1$), β-plane effects are small over such a region. Furthermore, Chan and Law [11] concluded that the relative movement due to interaction of binary systems using the f-plane and β-plane approximations are almost identical, even with the increased β term value given by the lower tangent point latitude of 15°N. The findings of Cosgrove and Forbes [16] together with those of Chan and Law [11] lead to the f-plane approximation being used here. It must be said that if the flow of interest extended to the boundaries of the full domain $-6 < x < 6$, $-6 < y < 6$, the spheroidal effects of the Earth would have to be taken into account and the f-plane approximation would not be a valid choice. However, this is not the case in the simulations that follow.

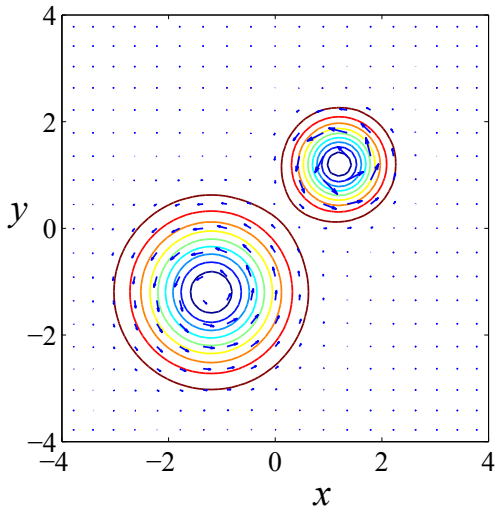

Figure 5.4.1: Initial pressure contour plots and quiver plots of initial velocity with eyes located at $L = 1.2$ and radii $\sigma_1 = 1.2$ and $\sigma_2 = 0.7$.

Solutions will be given for different eye locations and initial radii of the systems. In all examples shown in this chapter the eyes are initially symmetrically located at $(x, y) = \pm(L, L)$ and for convenience will simply be denoted L from here on, as the value of L is used in what is defined as the interaction ratio, I_r, given later by equation (5.4.1). These initial locations are a highly idealised situation that would rarely be observed in the atmosphere. However, this symmetry can be achieved by a simple transformation of the coordinate system; this is one advantage of using

the f-plane approximation. The maximum absolute change in pressure is $\mu_k = 0.1$ for $k = 1, 2$. The initial radii of the pressure systems are given by σ_k for $k = 1, 2$. If σ is stated alone without subscripts, then this is the radius of both systems. The subscript k is the locator of the initial pressure system. If $k = 1$ then the pressure system is originally located in the south-west quadrant and when $k = 2$, this refers to the system in the north-east quadrant. The Rossby number $Ro_T = 0.1$ is used throughout and corresponds to a tangent point at the mid-latitude $\phi \approx 43.3°$N. The initial radius of the system gives an indication of its intensity; the smaller the radius, the more-intense the system. Figure 5.4.1 illustrates this and shows an LL-binary system with unequal radii. The pressure system in the north-east quadrant has radius $\sigma_2 = 0.7$ and is the more-intense as indicated by the longer velocity vector arrows than those associated with the pressure system in the south-west, which has radius $\sigma_1 = 1.2$.

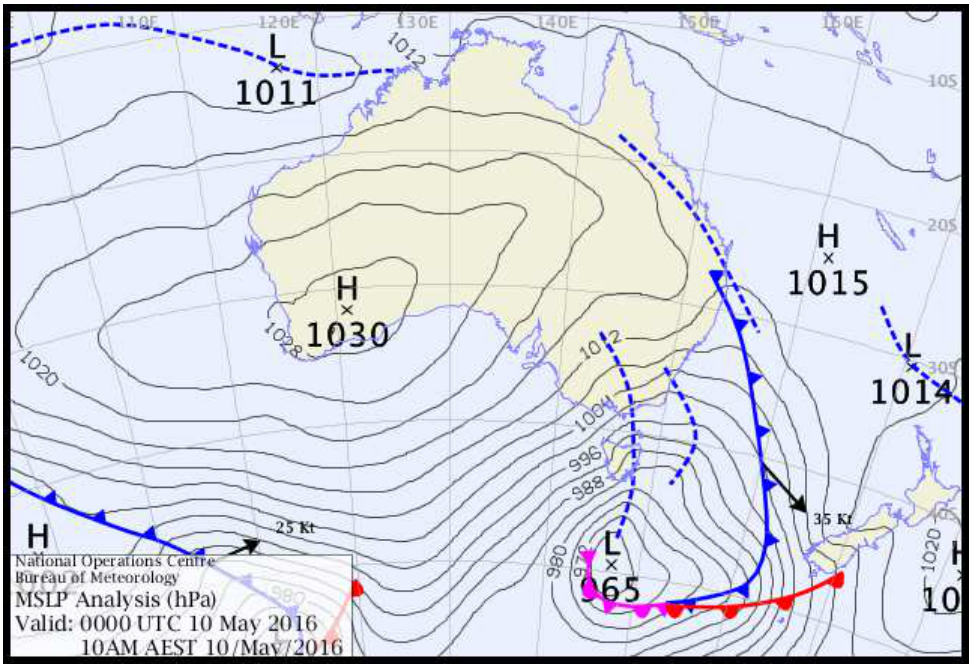

Figure 5.4.2: Mean sea-level pressure map, 0000 UTC 10 May 2016. Printed with permission of the Australian Bureau of Meteorology.

In the results that follow the radii of the individual systems will be as large as $\sigma = \sqrt{2}$ (≈ 1400 km). This might seem extreme, but extra-tropical cyclones and anti-cyclones in the mid-latitude regions commonly have this magnitude radius. Extra-tropical systems with large-scale radii are commonly observed in the mid-latitude regions around Australia. In early May 2016 a continental sized high-pressure system formed over Australia. A mean sea-level pressure map of this event,

courtesy of the Bureau of Meteorology, is shown in Figure 5.4.2. The highest pressure of 1030 hPa occurred in the south-west region of Western Australia and the 1020 hPa contour spanned the approximate region 102°E – 142°E longitudinally and 25°S – 41°S latitudinally. This mean sea-level pressure map also shows a rather large low-pressure system directly south of Tasmania with an approximate radius of 7° latitude.

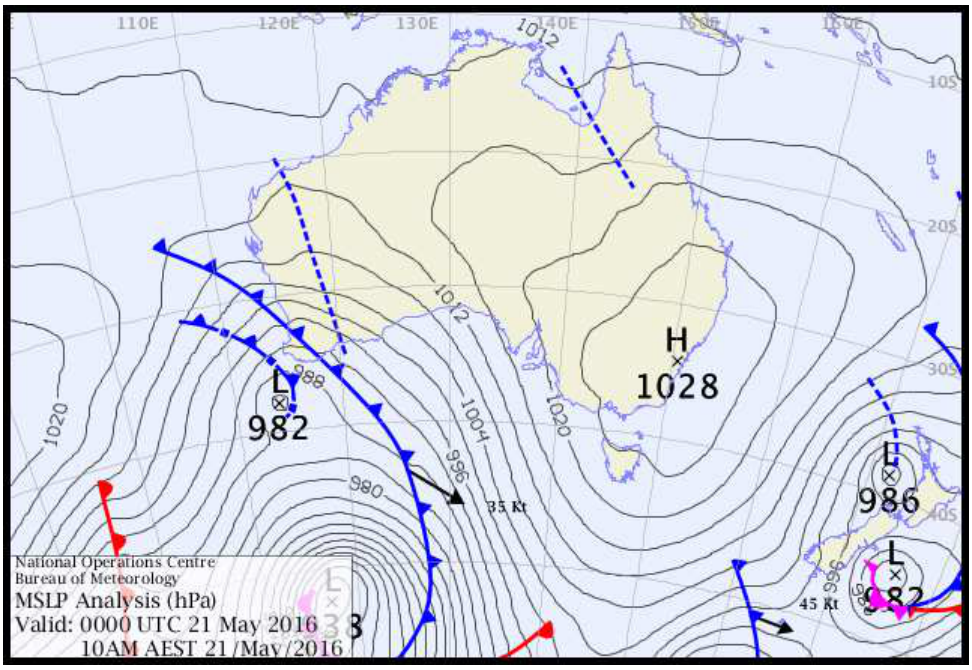

Figure 5.4.3: Mean sea-level pressure map, 0000 UTC 21 May 2016. Printed with permission of the Australian Bureau of Meteorology.

Another example of similar events shown in Figure 5.4.2 is illustrated in Figure 5.4.3. This mean sea-level pressure map shows the extra-tropical systems 11 days later than those shown in Figure 5.4.2. There is a dominant high-pressure system with its eye over the central coast of New South Wales. However, this figure is included because it shows a low-pressure system in the south-west quadrant with conservative radius of 10° latitude ($\approx$ 1100 km). What is evident from the two Figures 5.4.2 and 5.4.3 is that the contours of the high-pressure systems are sparse and the contours of the low-pressure systems are densely compacted together. In the simulated results that follow the contour diagrams exhibit this exact structure.

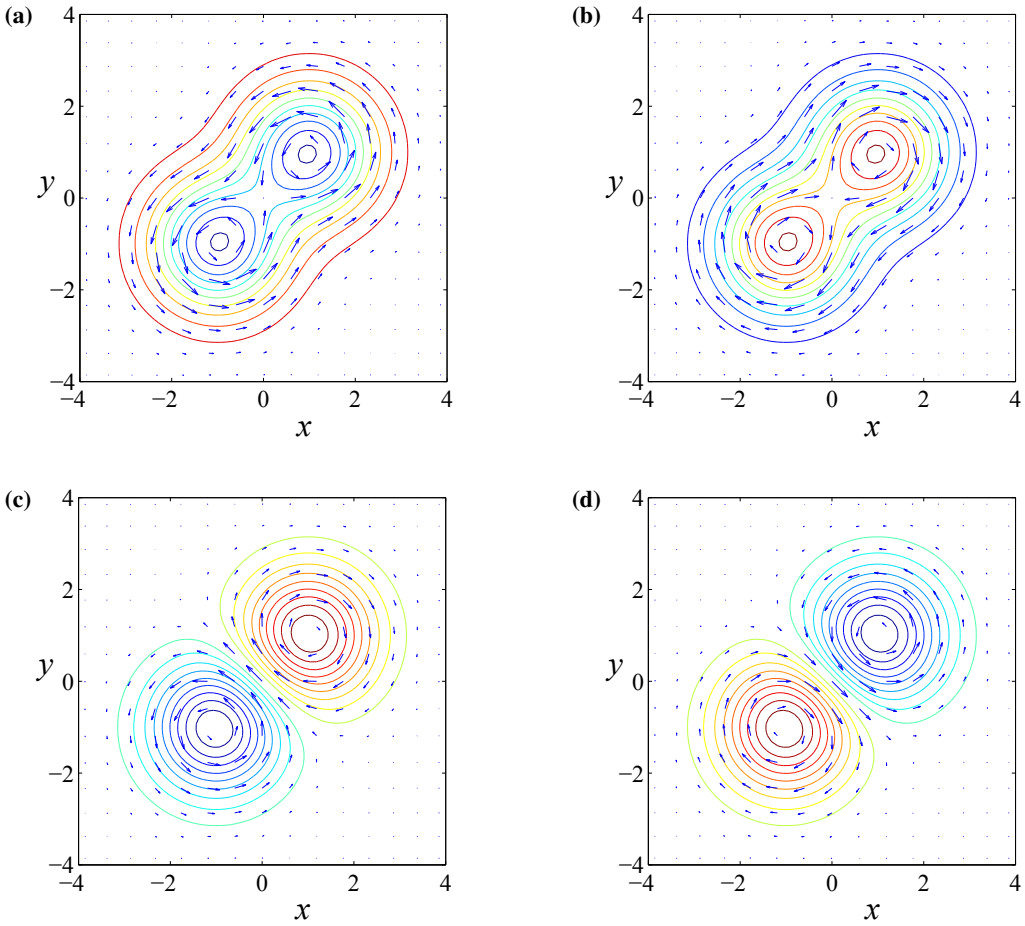

Figure 5.4.4: Initial pressure contour plots and quiver plots of initial velocity with eyes located at $L = 1$ and radius $\sigma = \sqrt{2}$ for an (a) LL-binary system, (b) HH-binary system, (c) LH-binary system and (d) HL-binary system.

As an indicator of the initial flow behaviour, contour plots of the initial pressure $p(x, y, 0)$ as defined by equation (5.3.2) composed with quiver plots of the initial velocity components given by equations (5.3.6) and (5.3.7) are shown in Figure 5.4.4. This figure illustrates geostrophic balance, where the pressure gradient force is equal to the Coriolis effect. They also verify that the geostrophic velocity vector is tangential to lines of constant pressure. Figures 5.4.4(a) and 5.4.4(b) show the initial flow pattern for the non-mixed LL-binary system and HH-binary system respectively. Conversely, the two mixed binary systems LH and HL are displayed in Figures 5.4.4(c) and 5.4.4(d). In all these subfigures the blank outer region has dimensionless pressure $p = 1$. The respective eye pressures for the low- and high-systems take the values $p = 0.9$ and $p = 1.1$. The visible contours either increase or decrease in increments of 0.01 from the eye out, so that for the low-pressure systems the contours range from 0.91 – 0.99 and 1.09 – 1.01 for the high-pressure

systems. High-pressure systems rotate in a clockwise direction in the northern hemisphere and vice versa for a low-pressure system, which is confirmed by the quiver plots in these figures.

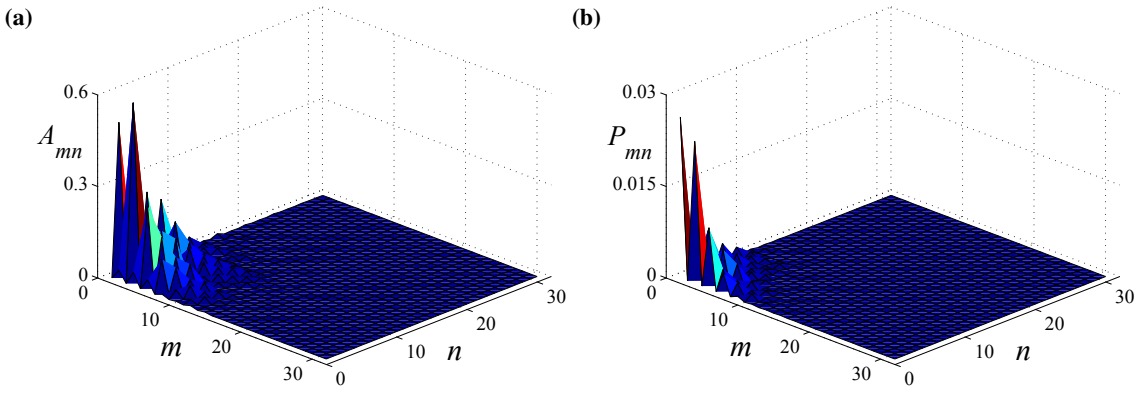

Figure 5.4.5: Absolute value of the Fourier coefficients at time $t = 0.80$ for (a) $A_{mn}(t)$ and (b) $P_{mn}(t)$.

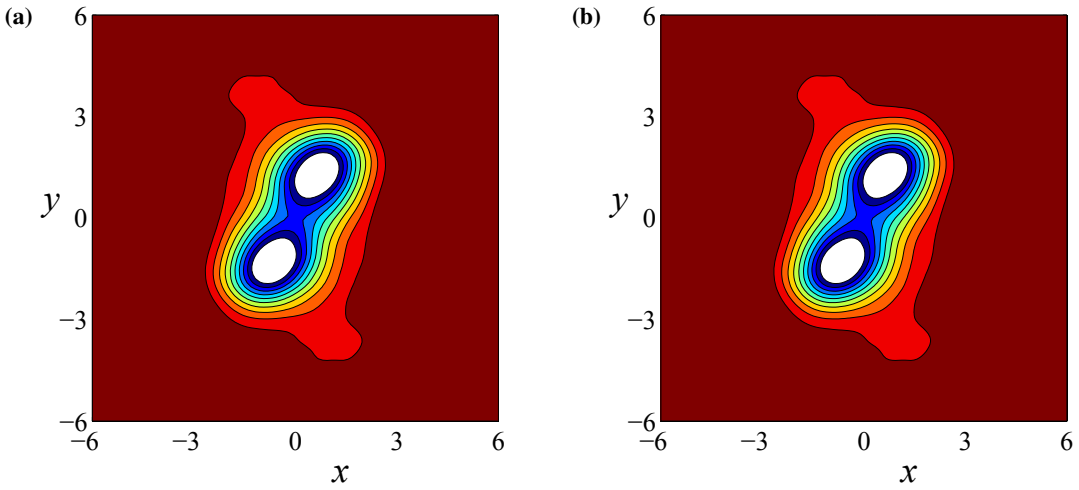

Figure 5.4.6: Pressure contour plots of an LL-binary system with $L = 1$ and $\sigma = \sqrt{2}$ at time $t = 0.50$ for a spatial grid of (a) 151 points and (b) 201 points.

To guarantee convergence of the numerical solutions $M = N = 31$ Fourier coefficients and 151 grid points were used in each spatial variable. Figure 5.4.5(a) shows the decay of the time dependent Fourier coefficients for the zonal velocity u at time $t = 0.80$ for a particular simulation and reveals that beyond $M = N = 15$ Fourier coefficients, their magnitude is essentially zero, suggesting higher Fourier modes have very little impact on the numerical solutions. Furthermore, the Fourier coefficients for the pressure p for the same simulation are given in Figure 5.4.5(b) which

also illustrates that beyond $M = N = 13$, their magnitude is very close to zero. Although not shown here the Fourier coefficients for the other variables show similar characteristics. Changing the grid resolution to greater than 151×151 points results in solutions that are indistinguishable from each other. Thus using an increased spatial sample has no influence on the numerical solutions and an example is shown in Figures 5.4.6(a) and 5.4.6(b) with grid points 151 and 201, respectively.

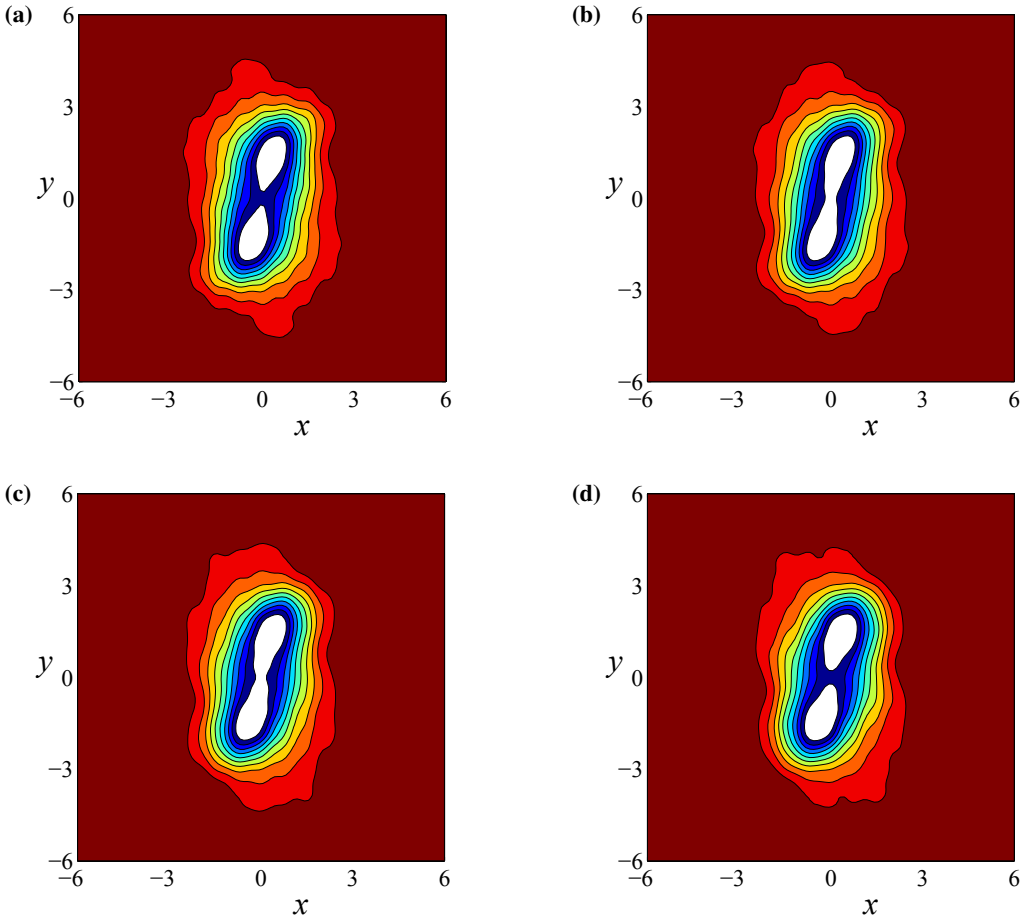

Figure 5.4.7: Pressure contour plots of pulsing behaviour for an LL- binary system with Dirichlet boundary conditions, initial eyes at $L = 1$ and radius $\sigma = \sqrt{2}$ at time (a) $t = 0.78$, (b) $t = 0.79$, (c) $t = 0.80$ and (d) $t = 0.81$.

Initially the computational boundary was chosen to be $-6 < x < 6$, $-6 < y < 6$ with important flow features constrained to an inner domain of $-3 < x < 3$, $-3 < y < 3$ so that the f-plane is still a valid approximation to use. However, as mentioned previously in Section 5.2, using the Dirichlet boundary conditions (5.2.11) – (5.2.15) causes the pressure systems to pulse in an unrealistic

manner, due to reflections off the artificial boundaries. This oscillatory behaviour is demonstrated in Figure 5.4.7 which shows a sequence of four times for an LL-binary system with $L = 1$ and $\sigma = \sqrt{2}$. At time $t = 0.78$, Figure 5.4.7(a), there are two distinct tear drop shaped low-pressure systems pinching in at the origin of the plane. The next two time steps shown in subfigures (b) and (c) indicate merging of the binary system as there is only one closed contour of pressure $p = 0.90$. Figure 5.4.7(d) shows the binary system at time $t = 0.81$ where separation of the lowest pressure region has occurred to form two disjoint regions of pressure $p = 0.90$. This false behaviour increased with time due to waves propagating outward and reflecting back off the artificial tangent plane boundaries. However, for greater times there was no further merger.

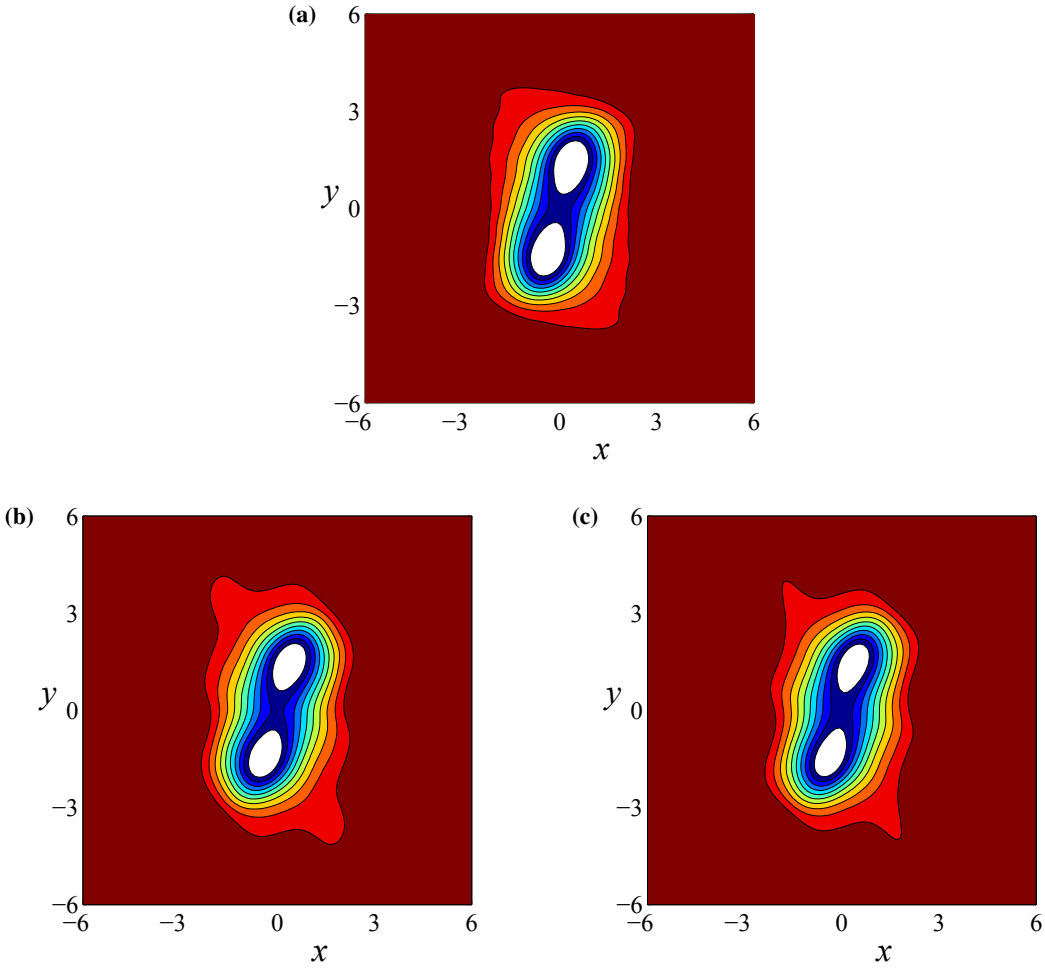

Figure 5.4.8: Pressure contour plots for an LL-binary system with initial eye locations at $L = 1$, $\sigma = \sqrt{2}$ at time $t = 0.80$ for (a) Dirichlet BCs, cropped at $\lambda = \omega = 6$ (b) Robin BCs with $\kappa = 0.75$ and (c) Robin BCs with $\kappa = 1.0$

To obtain a more realistic flow behaviour the boundaries were extended from $\lambda = \omega = 6$ out to

$\lambda = \omega = 9$ and the Dirichlet boundary conditions were kept so that the artificial reflections would take longer to affect the flow pattern. The LL-binary system parameters were otherwise kept exactly the same as for Figure 5.4.7. The results of doing this can be seen in Figure 5.4.8(a) which shows the pressure contours at $t = 0.80$. Although the computational boundary was extended, Figure 5.4.8(a) has been cropped at $\lambda = \omega = 6$ so that a comparison to Figure 5.4.7(c) can be made. Clearly the oscillatory behaviour at this time is far less than observed previously as there are now two distinct pressure systems, compared to the merger in Figure 5.4.7(c). However, as time increases the pulsing of the system is still observed with these extended boundaries, but prior to this happening it is a reasonable indicator of the true flow pattern at time $t = 0.80$.

The extended boundaries stopped the merger of the pressure systems, but the pulsing of the pressure systems continued up to time $t = 2.0$. A constructed movie created using the contour diagrams over the time interval $0 \leq t \leq 2$ shows waves propagating outwards and bouncing back off the artificial tangent plane boundaries resulting in an unrealistic amplification of the pressure. The waves moving away from the centre of the pressure systems are inevitable, but the reflections back can be minimised and absorbed to some extent by using Robin boundary conditions. Figure 5.4.8(a) was used as a baseline to determine what is the most appropriate absorption constant κ to use for the Robin boundary conditions (5.2.17). After trying numerous absorption constant values it was found that $\kappa = 0.75$ and $\kappa = 1.0$ matched most closely to what was observed for the extended boundaries. The respective $\kappa = 0.75$ and $\kappa = 1.0$ results are shown in Figures 5.4.8(b) and 5.4.8(c). For $\kappa = 0.75$ the width and length of the pressure region $p = 0.9$ is more aligned to that of the expanded Dirichlet boundary problem shown in Figure 5.4.8(a).

At early times the Dirichlet boundary problem aligns well with the Robin boundary problem using $\kappa = 0.75$. Three-dimensional surface plots of the Dirichlet and Robin boundary value problem at time $t = 0.01$ are shown in Figure 5.4.9 for comparison. In this figure the parameters are the same as those used in Figure 5.4.8. Figures 5.4.9(a) and 5.4.9(b) are the respective Dirichlet and Robin boundary problems. Apart from the slight interference near the corners of the tangent plane region for the Dirichlet representation, these figures are basically identical at this early time.

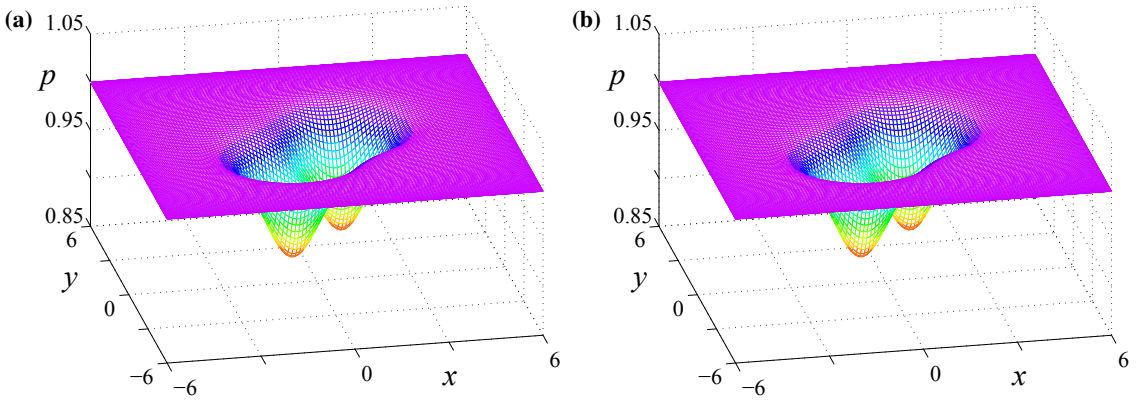

Figure 5.4.9: 3-dimensional pressure plot of an LL-binary system at the early time $t = 0.01$ with $\sigma = \sqrt{2}$, $L = 1$ and (a) Dirichlet BCs and (b) Robin BCs with $\kappa = 0.75$.

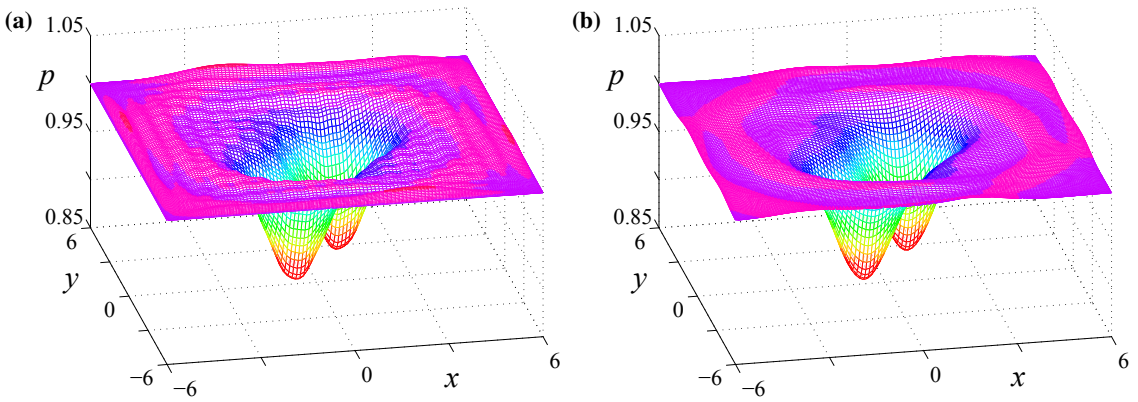

Figure 5.4.10: 3-dimensional pressure plot of an LL-binary system at the early time $t = 0.15$ with $\sigma = \sqrt{2}$, $L = 1$ and (a) Dirichlet BCs and (b) Robin BCs with $\kappa = 0.75$.

The close resemblance of the three-dimensional surface plots for the Dirichlet and Robin boundary conditions is maintained up to the approximate time of $t = 0.15$, depending on the configuration of the initial LL-binary system. At this time the Dirichlet solution shown in Figure 5.4.9(a) has evolved so that there is considerable rippling caused by the outward propagating waves being reflected back with a phase shift of 180°, and this is shown in Figure 5.4.10(a). The observed ripples coincide with the Fourier modes of the numerical simulation. The Robin boundary equivalent is illustrated in Figure 5.4.10(b) and shows the effect of the absorbing boundary. The outward travelling waves are still noticeable; however, there is evidence of the artificial boundary absorbing the outward travelling wave by way of smoothing out the contour surface near the

outer regions of the tangent plane.

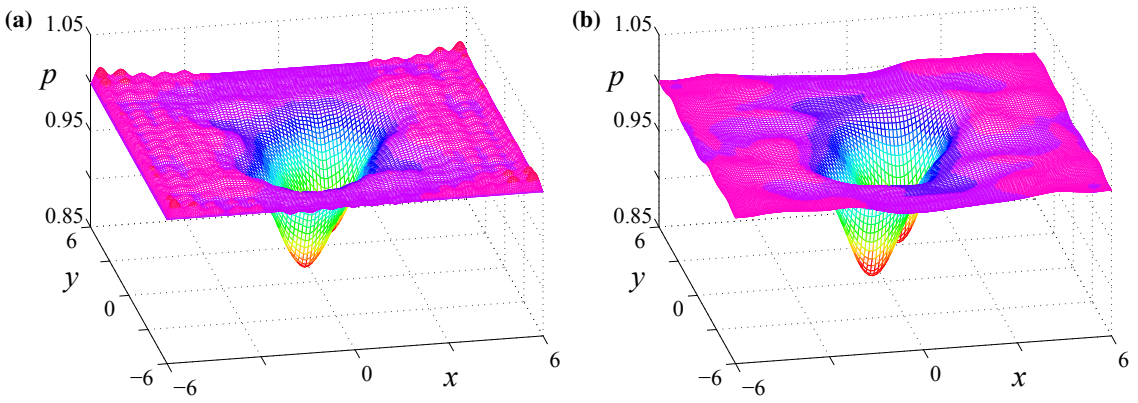

Figure 5.4.11: 3-dimensional pressure plot of an LL-binary system at the later time $t = 0.50$ with $\sigma = \sqrt{2}$, $L = 1$ and (a) Dirichlet BCs and (b) Robin BCs with $\kappa = 0.75$.

As time increases the Dirichlet boundary-induced high-frequency rippling is magnified as more outward travelling waves and the now reflected inward travelling waves coalesce at later times. This coalescence is demonstrated in Figure 5.4.11(a) and is a snap shot of the pressure surface at time $t = 0.50$. The full effect of the absorbing boundary conditions is best illustrated at later times where the pulsing caused by the Dirichlet boundary conditions starts to take hold. There is quite dramatic smoothing of the contour surface at time $t = 0.50$ when the absorbing conditions are used. This effect is shown in Figure 5.4.11(b). There is clear evidence from the contour diagram 5.4.8 and the three-dimensional surface plots of pressure 5.4.9, 5.4.10 and 5.4.11 that the Robin boundary conditions with $\kappa = 0.75$ are inhibiting reflections off the artificial boundaries. For this reason, all subsequent pressure contour diagrams will use Robin boundary conditions with $\kappa = 0.75$ and the region with $\lambda = \omega = 6$.

It must be stressed here that at no stage do we suggest that the (artificial) boundaries at $\lambda = \omega = 9$ used in Figure 5.4.8(a) represent physical reality over that entire domain, not even $\lambda = \omega = 6$. As discussed previously, using the tangent point latitude $\phi_0 = 43.3°$N, the f-plane approximation is only valid over a domain corresponding roughly to $-3 < x < 3$, $-3 < y < 3$. The only reason for considering these extended boundaries in Figure 5.4.8(a) is to eliminate false reflections off the boundaries over the time interval of interest, and thus to benchmark appropriate values of the absorption coefficient κ in Figures 5.4.8(b) and 5.4.8(c).

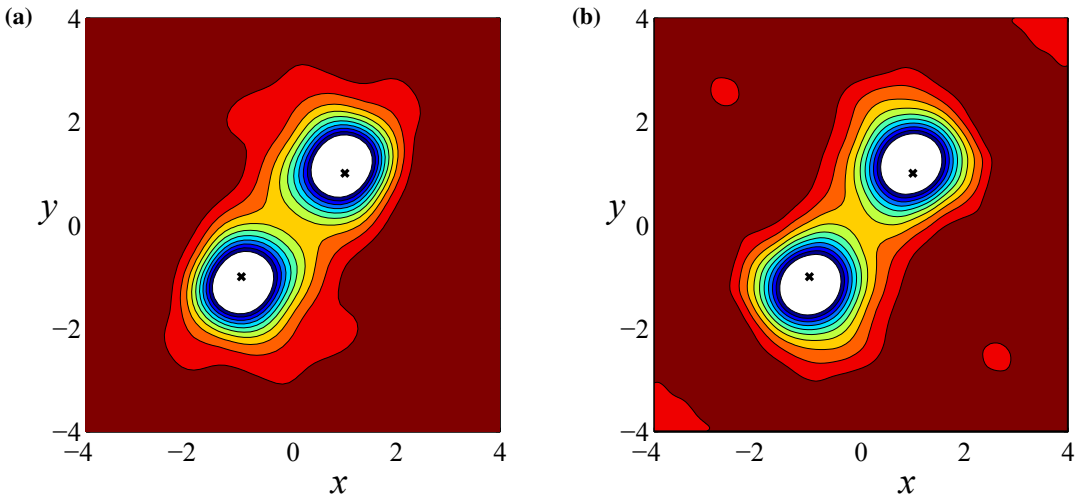

Figure 5.4.12: Pressure contour plots of an LL-binary system with $L = 1$ and $\sigma = 1$ at time $t = 0.45$ for (a) $\lambda = \omega = 6$ and (b) $\lambda = \omega = 4$. **Crosses** indicate initial positions of the eyes of the vortices.

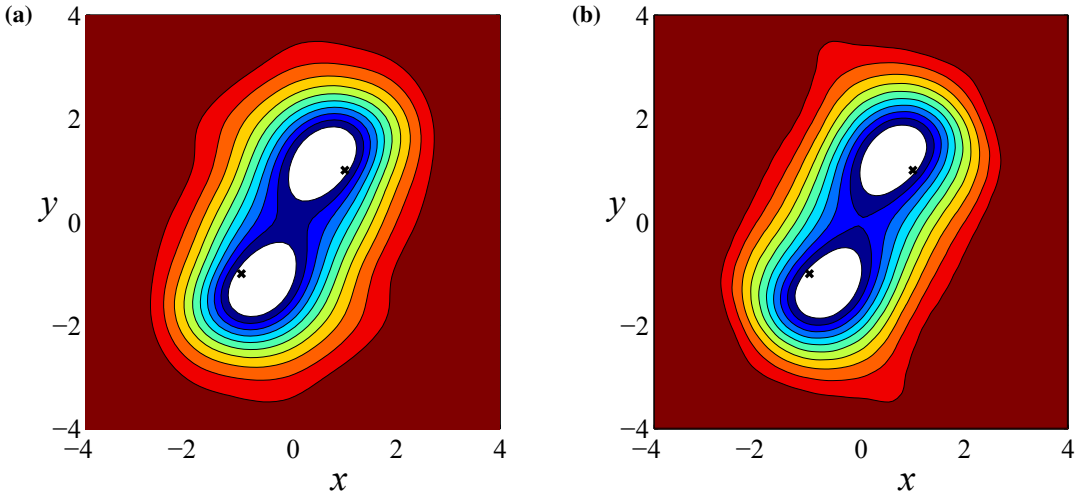

Figure 5.4.13: Pressure contour plots of an LL-binary system with $L = 1$ and $\sigma = \sqrt{2}$ at time $t = 0.45$ for (a) $\lambda = \omega = 6$ and (b) $\lambda = \omega = 4$. **Crosses** indicate initial positions of the eyes of the vortices.

To illustrate further the fact that the constant Coriolis parameter f, coupled with the absorbing boundary condition is valid to use over the region with $\lambda = \omega = 6$, Figure 5.4.12 shows pressure contour plots of an LL-binary system with $L = 1$ and $\sigma = 1$ at time $t = 0.45$. Figure 5.4.12(a) was computed with $\lambda = \omega = 6$ but cropped at $\lambda = \omega = 4$ so a direct comparison can be made with Figure 5.4.12(b) which was simulated with $\lambda = \omega = 4$. It can be seen that there is little difference

between the flow feature of interest in the two diagrams except that there is some interference caused by reflections off the boundary in the $\lambda = \omega = 4$ case. The region around the eye of the low-pressure system, which is of the most importance in these simulations, has minimal difference in the overall movement and pressure structure in both cases, suggesting that the interaction process are in agreement. There is even closer resemblance in Figures 5.4.13(a) and 5.4.13(b) which has the increased initial radii of $\sigma = \sqrt{2}$. The small bold crosses in Figures 5.4.12 and 5.4.13 indicate the locations of the centres of the vortices at the initial time $t = 0$.

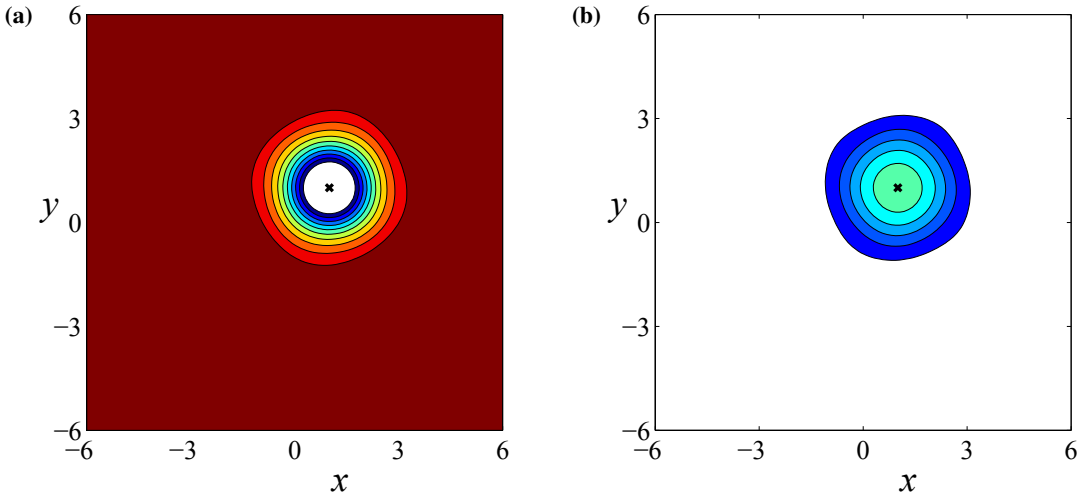

Figure 5.4.14: Pressure contour plots of a single pressure system located at $(x, y) = (1, 1)$ at time $t = 0.45$ with $\sigma = \sqrt{2}$ of type (a) Low and (b) High. **Crosses** indicate initial positions of the eyes of the vortices.

The results in this section will focus on the interaction or lack thereof between binary pressure systems in the mid-latitude regions. Figures 5.4.14(a) and 5.4.14(b) respectively show the pressure structure at $t = 0.45$ (approximately 12.5 hours in dimensional time) for a single low-pressure system and a single high-pressure system. Both figures had their pressure system eye located initially at $(x, y) = (1, 1)$ with radius $\sigma = \sqrt{2}$. As a result of the singular system there is no mechanism for interaction besides the limited reflections off the artificial boundaries. These figures are used as the defining structure of what results when negligible or no interaction occurs. The low-pressure system has maintained its pressure differential of $p = 0.9$ –1.0, whereas the high-pressure has diffused over time, indicated by the drop in maximum pressure down to $p = 1.05$ from the initial maximum of $p = 1.1$. Moreover, the eyes of the pressure systems are essentially at their initial locations, indicating that no movement of the system has occurred.

Regions of high pressure (locally) push toward lower pressure regions. Thus the structure of the low pressure in Figure 5.4.14(a) is maintained through pressure pushing towards the centre. By contrast, the high pressure region in Figure 5.4.14(b) pushes outwards towards its lower-pressure surrounding fluid, and so it dissipates more rapidly. The mean sea-level pressure diagrams shown in Figures 5.4.2 and 5.4.3 have constant pressure differential (4 hPa) between two adjacent contours. A clear feature of the two mean sea-level pressure figures is that the contours associated with the high-pressure regions are sparse and spread out. Conversely, the low-pressure zones have contours that are densely compacted. The contours for the simulated low- and high-pressure systems in Figure 5.4.14 exhibit identical characteristics to observed atmospheric behaviour, and this feature is confirmed repeatedly in all the subsequent pressure contour diagrams in this results section of the chapter.

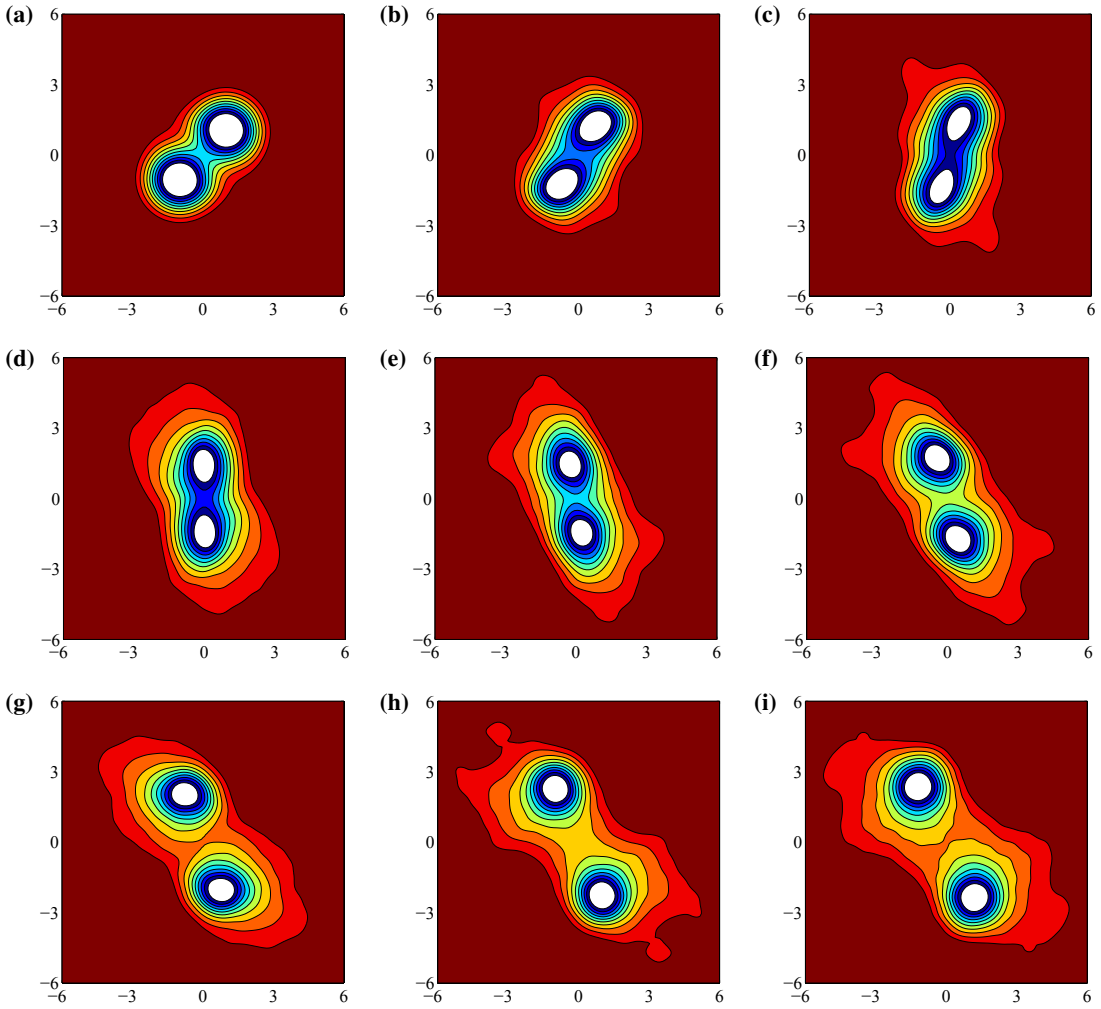

Figure 5.4.15: Pressure contour plots showing the evolution of the interaction of an LL-binary system with $L = 1$ and $\sigma = \sqrt{2}$ at times (a) $t = 0.05$, (b) $t = 0.40$, (c) $t = 0.80$, (d) $t = 1.20$, (e) $t = 1.60$, (f) $t = 2.00$, (g) $t = 2.40$, (h) $t = 2.80$ and (i) $t = 3.20$.

Interaction causes the binary systems to move and/or rotate about each other. If interaction occurs, an LL-binary system will rotate in an anti-clockwise direction until the vortices become sufficiently separated and then move away from each other. This anti-clockwise rotation and subsequent movement away is demonstrated in Figure 5.4.15 which shows the evolution of the interaction processes of an LL-binary system with each vortex having radius $\sigma = \sqrt{2}$ and eyes located at $L = 1$ initially. Figure 5.4.15(a) is the contour map at the early time $t = 0.05$ and Figure 5.4.15(i) is at the latest time $t = 3.20$ (which corresponds to about 3.5 days). The intermediate times $t = 0.40, 0.80, 1.20, 1.60, 2.00, 2.40$ and 2.80 are shown in Figures 5.4.15(b) – 5.4.15(h) respectively. The interaction of an HH-binary system will induce clockwise rotation but the pressure

systems disperse as time increases. In fact, for all binary systems that contain high-pressure zones the pressure diffuses as time increases. In contrast, low-pressure systems maintain their pressure structure over time.

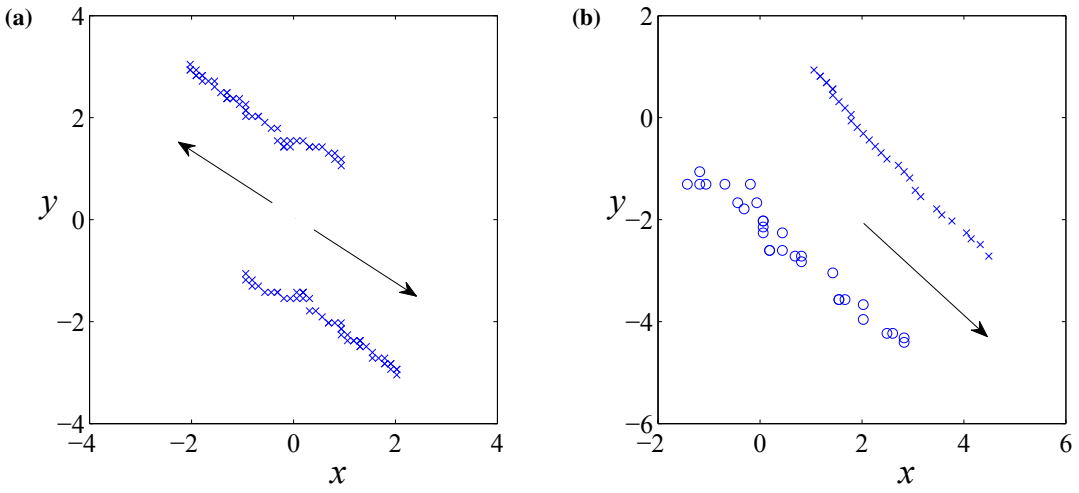

Figure 5.4.16: Tracking plots of the eyes of two different binary systems initially located at $L = 1$ with $\sigma = \sqrt{2}$ for (a) LL-binary system, $t \in [0, 5]$ and (b) HL-binary system, $t \in [0, 3]$. **Crosses** and **circles** correspond to low and high-pressures, respectively.

The rotational interaction shown in Figure 5.4.15 is also illustrated in Figure 5.4.16(a) which shows the movement of the low-pressure systems by tracking the position of the eyes that were initially at $L = 1$ over the time $t = 0-5$. There is clear anti-clockwise rotation of the binary system for approximately 60° and then movement away from each other to the north-west and south-east. A possible explanation for this behaviour is that the initial influence each system has over the other has lessened to the point where mutual rotation about one another is overcome by the rotation and momentum of the individual systems, causing the systems to move apart. A mixed binary system will move perpendicular to the line joining the initial eye locations. Figure 5.4.16(b) shows the eye locations over the time interval $0 \leq t \leq 3$, for an HL-binary system with the eyes initially located at $L = 1$ and with $\sigma = \sqrt{2}$. The crosses and the open circles are the locations of the low- and high-pressure eyes respectively. There is clear movement to the south-east. However, the movement of the high-pressure eye is not as smooth as those for the low-pressure system. This is due to the high-pressure system diffusing over time. The diffusion of high-pressure and movement towards the south-east is illustrated in Figure 5.4.17 which shows the evolving nature of an interacting HL-binary system with $L = 1$ and $\sigma = \sqrt{2}$ over $0 < t \leq 0.75$. At the early time $t = 0.01$,

shown in Figure 5.4.17(a), there is a well defined pressure structure with equal magnitude $\mu = 0.1$ change from background pressure in both the low- and high-pressure systems. Figure 5.4.17(b) is the contour diagram at time $t = 0.15$. At this time the, high-pressure has diffused down from $p = 1.10$ to $p = 1.05$, and this high-pressure value is maintained over the time steps $t = 0.30$, 0.45, 0.60 and 0.75; the respective contour plots for these time values are shown in Figures 5.4.17(c) through (f) respectively.

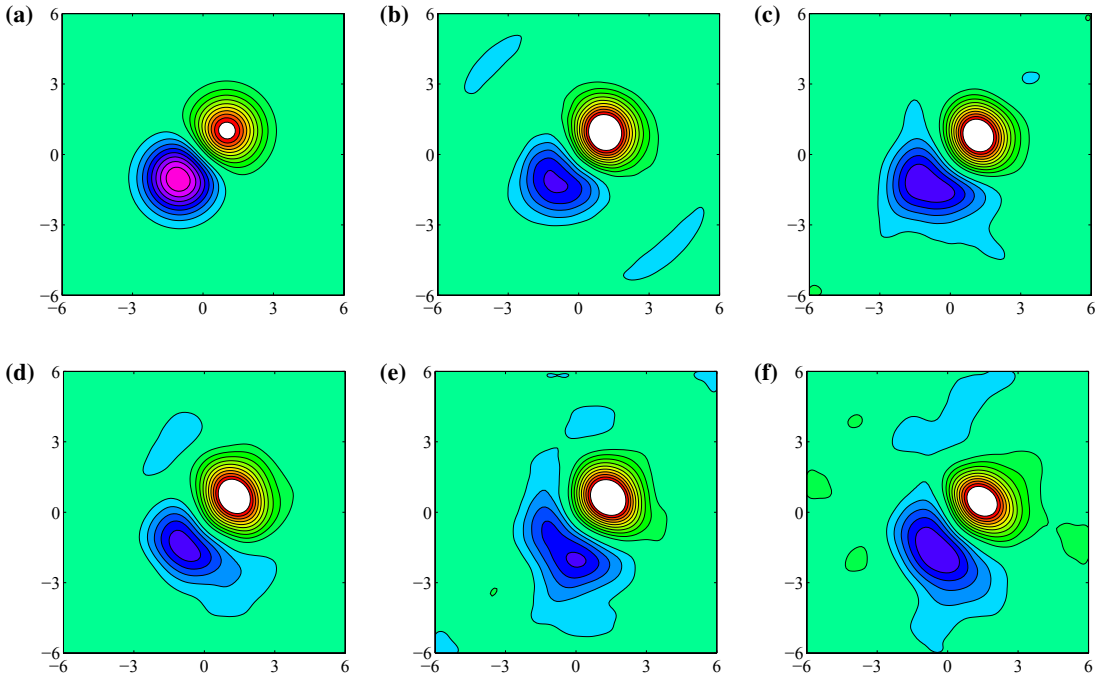

Figure 5.4.17: Pressure contour plots showing the evolution of the interaction of an HL-binary system with $L = 1$ and $\sigma = \sqrt{2}$ at times (a) $t = 0.01$, (b) $t = 0.15$, (c) $t = 0.30$, (d) $t = 0.45$, (e) $t = 0.60$ and (f) $t = 0.75$.

To determine a quantitative prediction of when interaction occurs, numerous binary-system configurations were simulated with equal radii $\sigma_1 = \sigma_2$ and unequal radii $\sigma_1 \neq \sigma_2$. It was found that interaction is dependent on eye location L and average radius $\sigma = \dfrac{\sigma_1 + \sigma_2}{2}$ for sensible σ_1, $\sigma_2 > 0$. Thus the interaction ratio is defined as

$$I_r = \frac{\sigma}{L}. \tag{5.4.1}$$

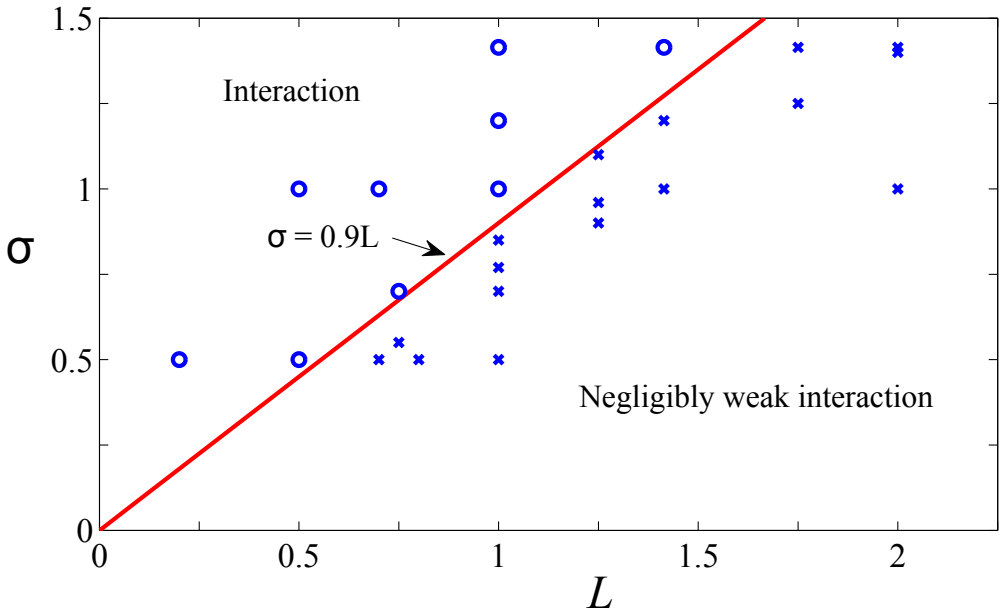

Figure 5.4.18: Sketch of the interaction regions for binary systems in an (L, σ) parameter plane. The **circles** indicate configurations in which interaction occurred and the **crosses** when interaction did not occur.

Figure 5.4.18 shows a plot of σ versus L for all configurations simulated, in an (L, σ) parameter plane. The circles indicate when interaction occurred and the crosses when no interaction was observed. The straight line $\sigma = 0.9L$ represents the approximate boundary between interacting and non-interacting systems. The region marked 'Negligibly weak interaction', refers to values of σ and L at which the vortices are too weak to influence each other significantly and their ratio as defined by (5.4.1) is less than 0.9. Conversely, the region marked 'Interaction' is where the interaction ratio, $I_r \geq 0.9$, and the vortices have influence over each other.

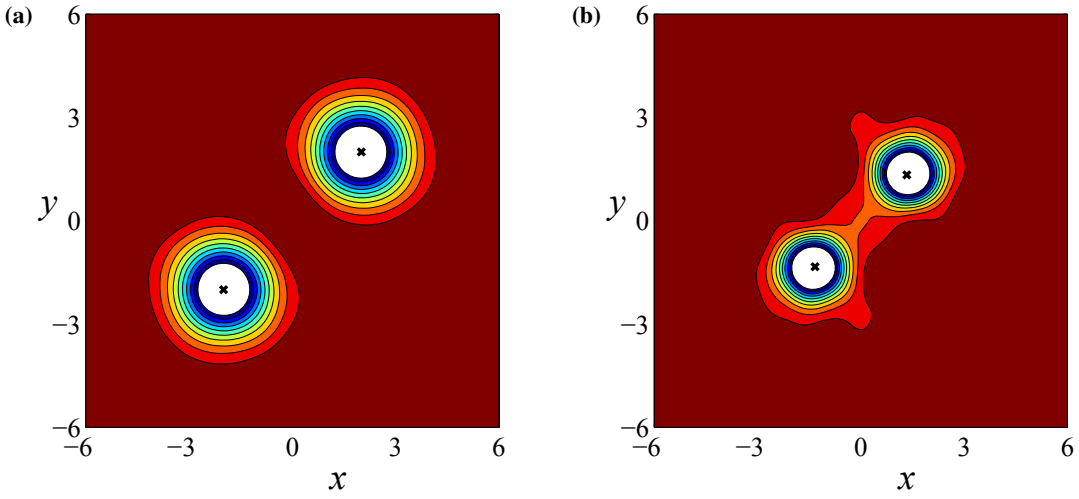

Figure 5.4.19: Pressure contour plots of negligibly weak interacting LL-binary systems at time $t = 0.45$ with (a) $I_r = 0.7$ ($\sigma = 1.4$, $L = 2$) and (b) $I_r = 0.75$ ($\sigma = 1$, $L = 4/3$). **Crosses** indicate initial positions of the eyes of the vortices.

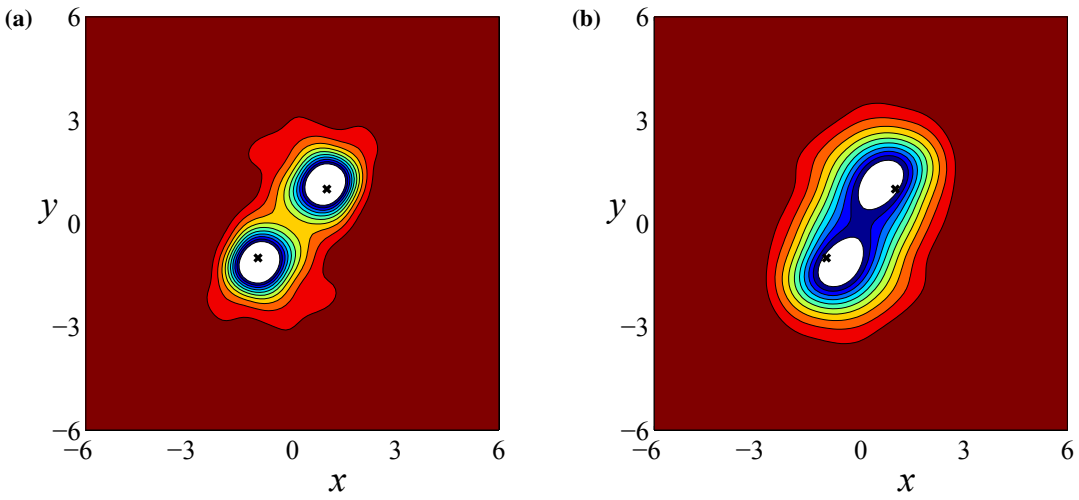

Figure 5.4.20: Pressure contour plots of interacting LL-binary systems at time $t = 0.45$ with (a) $I_r = 1$ ($\sigma = 1$, $L = 1$) and (b) $I_r = \sqrt{2}$ ($\sigma = \sqrt{2}$, $L = 1$). **Crosses** indicate initial positions of the eyes of the vortices.

Interaction is defined to occur when there is clear movement of one system caused by the other at time $t = 0.45$. The interaction of an LL-binary system is negligible if the pressure systems have their initial eye located centrally at time $t = 0.45$, as indicated in Figure 5.4.14(a). Figures 5.4.19(a) with $I_r = 0.7$ and 5.4.19(b) with $I_r = 0.75$ are indicative of non-interactive LL-binary systems. These figures clearly show inconsequential interaction, as the initial eyes of the pressure system shown with bold crosses are in the centre of the existing low-pressure region at

this time.

For an LL-binary system, evidence of interaction is when each system is rotating about each other. Two LL-binary system configurations in which interaction has occurred are shown in Figure 5.4.20. The interaction ratios are $I_r = 1$ and $I_r = \sqrt{2}$ for Figures 5.4.20(a) and 5.4.20(b) respectively. Both clearly show that the initial eye locations are no longer in the centre of the lows associated with the rotating binary systems.

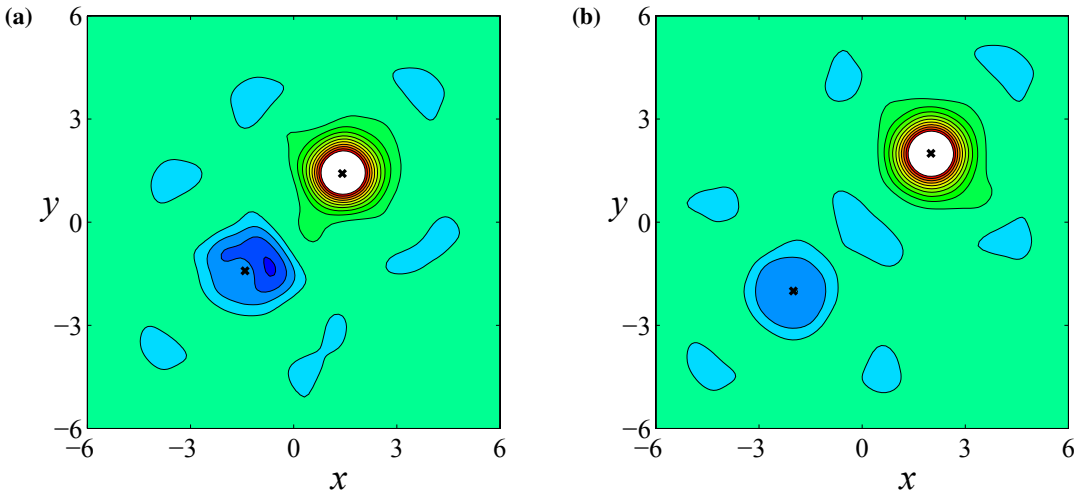

Figure 5.4.21: Pressure contour plots of negligibly interacting HL-binary systems at time $t = 0.45$ with (a) $I_r = 1/\sqrt{2}$ ($\sigma = 1$, $L = \sqrt{2}$) and (b) $I_r = 0.5$ ($\sigma = 1$, $L = 2$). **Crosses** indicate initial positions of the eyes of the vortices.

As shown in Figure 5.4.14(b), high-pressure systems have the tendency to dissipate as time increases. Due to this dissipation of high-pressure, interaction of a mixed HL- or an LH-binary system is determined by the movement of the associated low-pressure system. The dissipation of high-pressure is clearly evident at time $t = 0.45$ in Figure 5.4.21, which shows the non-interaction of an HL-binary system with $I_r = 1/\sqrt{2}$ in Figure 5.4.21(a) and $I_r = 0.5$ in Figure 5.4.21(b). In both of these figures the high-pressure systems range from $p = 1.00 - 1.04$ and $p = 1.00 - 1.02$ respectively, down from their original pressure range $p = 1.00 - 1.10$, whereas the low-pressure systems have maintained their pressure differential of $p = 0.90 - 1.00$. The low-pressure systems have not moved laterally as their initial eye locations are still centred, which is suggestive of negligibly weak or no interaction.

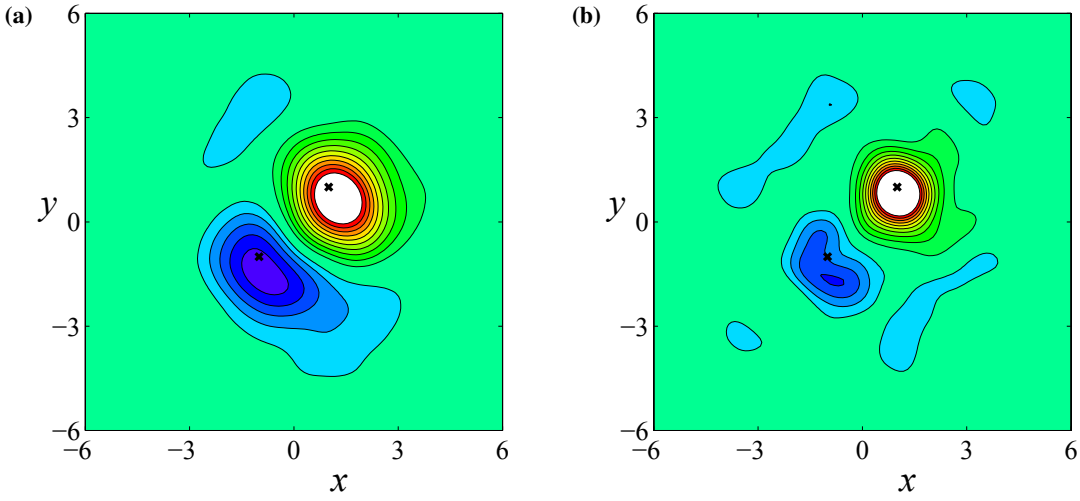

Figure 5.4.22: Pressure contour plots of interacting HL-binary systems at time $t = 0.45$ with (a) $I_r = \sqrt{2}$ ($\sigma = \sqrt{2}$, $L = 1$) and (b) $I_r = 1$ ($\sigma = 1$, $L = 1$). **Crosses** indicate initial positions of the eyes of the vortices.

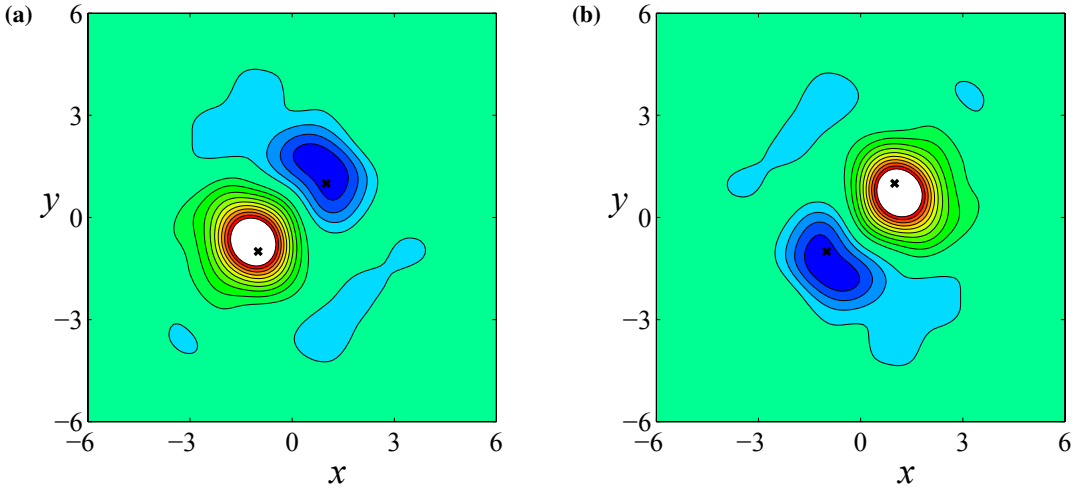

Figure 5.4.23: Pressure contour plots of mixed binary systems at $t = 0.45$ with $\sigma = 1.2$ and $L = 1$ for (a) LH-binary system and (b) HL-binary system. **Crosses** indicate initial positions of the eyes of the vortices.

When interaction of an HL-binary system eventuates, the dissipation of the high pressure is less dramatic than that observed in an non-interactive system and this is shown in Figure 5.4.22 with $I_r = \sqrt{2}$ and $I_r = 1$. When $I_r = \sqrt{2}$ in Figure 5.4.22(a) the high-pressure ranges from $p = 1.00 - 1.05$. For $I_r = 1$, high-pressure is in the range 1.00 to 1.04 and is illustrated in 5.4.22(b). For an interactive HL-binary system, there is overall movement to the south-east with the low-pressure system retaining its structure. Conversely, an LH-binary system has nett movement to

the north-west when interaction occurs. The opposing nett movements of an LH-binary system and an HL-binary system are demonstrated in Figure 5.4.23. In this figure the interaction ratio is $I_r = 1.2$ with $\sigma = 1.2$ and $L = 1$. The LH-binary system illustrated in Figure 5.4.23(a) is migrating north-west and the movement of the equivalent HL-binary system is to the south-east as shown in Figure 5.4.23(b). As expected due to the f-plane having constant Coriolis parameter each subfigure is rotationally symmetric of order two when compared.

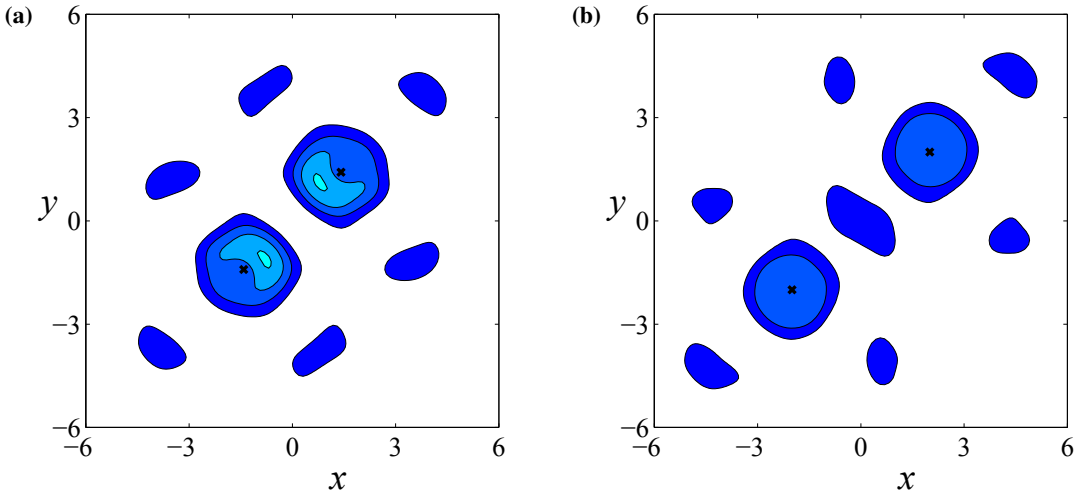

Figure 5.4.24: Pressure contour plots of negligibly interacting HH-binary systems at time $t = 0.45$ with (a) $I_r = 1/\sqrt{2}$ ($\sigma = 1$, $L = \sqrt{2}$) and (b) $I_r = 0.5$ ($\sigma = 1$, $L = 2$). **Crosses** indicate initial positions of the eyes of the vortices.

The interaction of an HH-binary system is the most difficult to determine, as both systems are dissipating in time. Interaction of an HH-binary system is defined to occur when the high-pressure diffuses to form one closed region of intermediate pressure ($1.01 \leq p \leq 1.09$) that rotates in a clockwise direction. The non-interaction of HH-binary systems is illustrated in Figure 5.4.24. Here the pressure systems are still located about their initial eye locations, and although the high-pressure has diffused in a clockwise direction as indicated by the extremely small regions of highest pressure to the north-east and south-west of the initial eyes, there isn't a closed pressure region of intermediate value. Figure 5.4.24(a) shows the non-interaction when $I_r = 1/\sqrt{2}$ with highest pressure region $p = 1.04$ to the north-east and south-west of the initial eye locations and Figure 5.4.24(b) has highest pressure region $p = 1.02$ and $I_r = 0.5$.

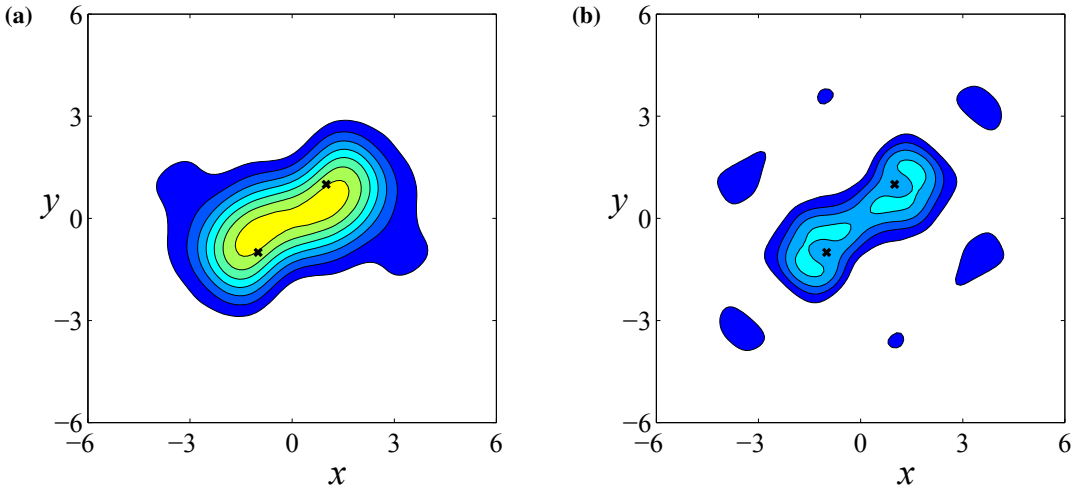

Figure 5.4.25: Pressure contour plots of interacting HH-binary systems at time $t = 0.45$ with (a) $I_r = \sqrt{2}$ ($\sigma = \sqrt{2}$, $L = 1$) and (b) $I_r = 1$ ($\sigma = 1$, $L = 1$). **Crosses** indicate initial positions of the eyes of the vortices.

Examples of interactive HH-binary systems are illustrated in Figures 5.4.25(a) with $I_r = \sqrt{2}$ and 5.4.25(b) with $I_r = 1$. In these examples, when $I_r = \sqrt{2}$ it can be seen that there is one region of intermediate pressure $p = 1.07$ that is rotating in a clockwise direction from the initial eye locations; similarly, the dispersion of pressure when $I_r = 1$ has formed a single region of mid-pressure $p = 1.03$, with additional pressure $p = 1.04$ rotating about the initial eyes.

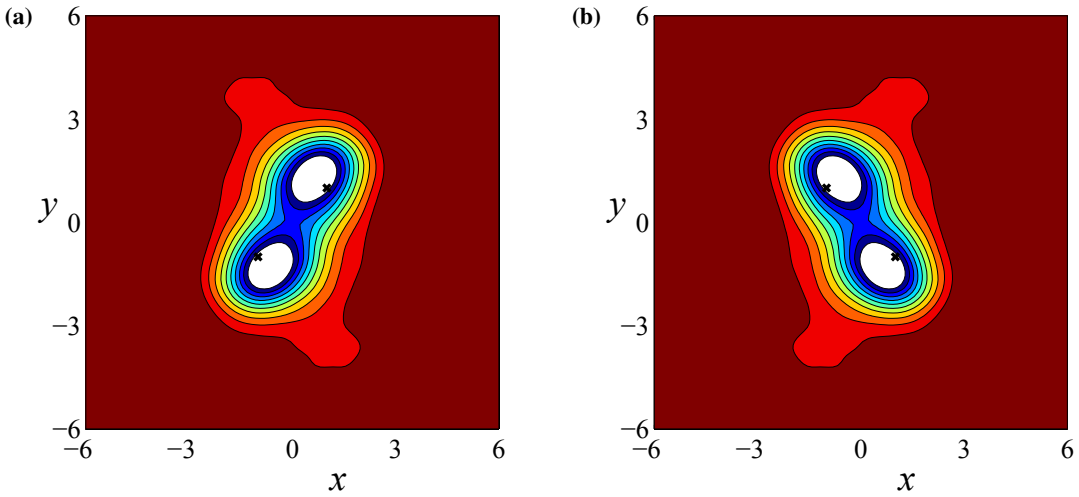

Figure 5.4.26: Pressure contour plots for an LL-binary system with $I_r = \sigma = \sqrt{2}$ at time $t = 0.50$ for the (a) northern hemisphere with $Ro_T = 0.1$ and (b) southern hemisphere with $Ro_T = -0.1$. **Crosses** indicate initial positions of the eyes of the vortices.

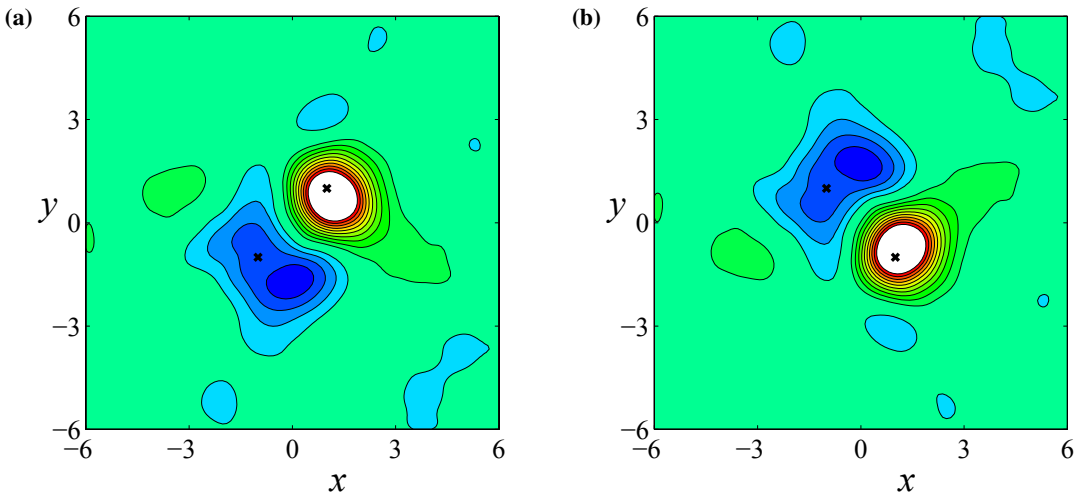

Figure 5.4.27: Pressure contour plots for an HL-binary system with $I_r = \sigma = 1.2$ at time $t = 0.50$ for the (a) northern hemisphere with $Ro_T = 0.1$ and (b) southern hemisphere with $Ro_T = -0.1$. **Crosses** indicate initial positions of the eyes of the vortices.

All the contour diagrams above have focussed on flow behaviour in the northern hemisphere. A thorough examination of this topic must include southern hemisphere simulations, although brief. The value of the Coriolis parameter f is determined by an odd function centred at the equator (see equation (3.2.1)). In the northern hemisphere simulations the initial eye locations are given by the value L so that their location initially is $(x, y) = \pm(L, L)$. The same geometric set-up in the southern hemisphere requires the initial location of the eyes to be $(x, y) = \pm(L, -L)$ because of the odd symmetry in the latitudinal y-coordinate. Unsurprisingly, the southern hemisphere simulations of non-mixed binary systems rotate in the opposite directions to those observed in the northern hemisphere cases. Figure 5.4.26(a) and 5.4.26(b) are the respective northern and southern hemisphere plots at time $t = 0.50$ with $\sigma = \sqrt{2}$ and $L = 1$, and in particular it can be seen that the LL-binary system in the southern hemisphere has rotated clockwise as opposed to the anti-clockwise rotation observed in the northern hemisphere case. Each subfigure of Figure 5.4.26 is the exact reflection about the x-axis.

Figure 5.4.27 shows the contrasting nett movement of an HL-binary system in the northern and southern hemispheres. In this figure the interaction ratio is $I_r = 1.2$ and the radii of the initial pressure systems is $\sigma = 1.2$. In the northern hemisphere, Figure 5.4.27(a), the nett movement is to the south-east. However, in the southern hemisphere, due to opposing rotation of equiva-

lent systems and the change in sign of the Coriolis parameter, the southern hemisphere HL-binary systems move in a north-east direction, as shown in Figure 5.4.27(b). Again, each subfigure of Figure 5.4.27 is symmetric about the x-axis. Although not shown here, an LH-binary system will move to the south-west in the southern hemisphere compared to the north-west in the northern hemisphere.

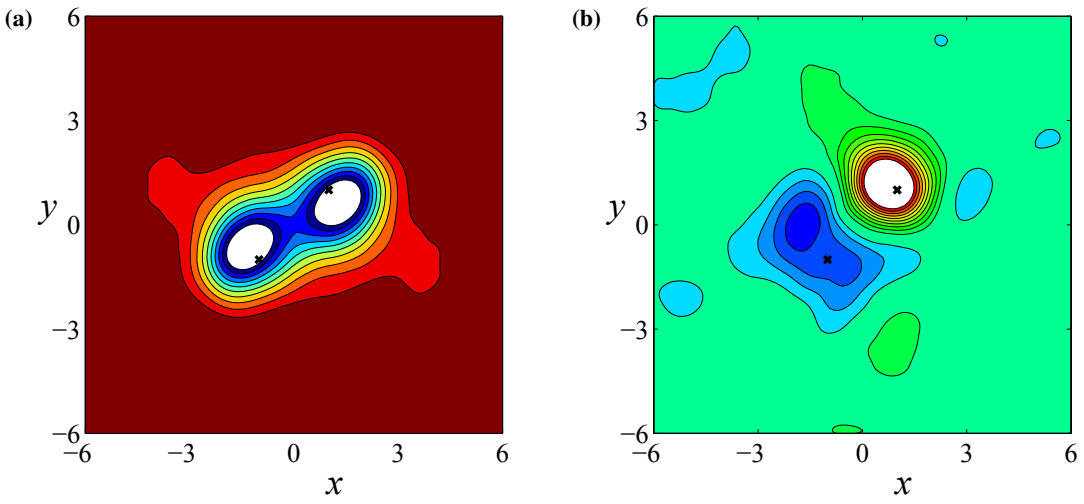

Figure 5.4.28: Pressure contour plots of southern hemisphere simulations with initial eyes located at $(x, y) = \pm(L, L)$ at time $t = 0.50$ for an (a) LL-binary system with $I_r = \sqrt{2}$ ($\sigma = \sqrt{2}$, $L = 1$) and (b) HL-binary system with $I_r = 1.2$ ($\sigma = 1.2$, $L = 1$). **Crosses** indicate initial positions of the eyes of the vortices.

Having the initial eyes located at $(x, y) = \pm(L, L)$ in the southern hemisphere produces contour maps that are the inverse of the northern hemisphere simulations, in the sense that they are reflected about the line $y = x$. Examples of this are shown in Figure 5.4.28. The contour map shown in Figure 5.4.28(a) was simulated with the same parameters used in Figure 5.4.26(b) apart from the initial eyes being located at $(x, y) = \pm(L, L)$. This subfigure is the exact reflection about $y = x$ of Figure 5.4.26(a). Similarly, Figure 5.4.28(b) is the perfect image of Figure 5.4.27(a) about $y = x$.

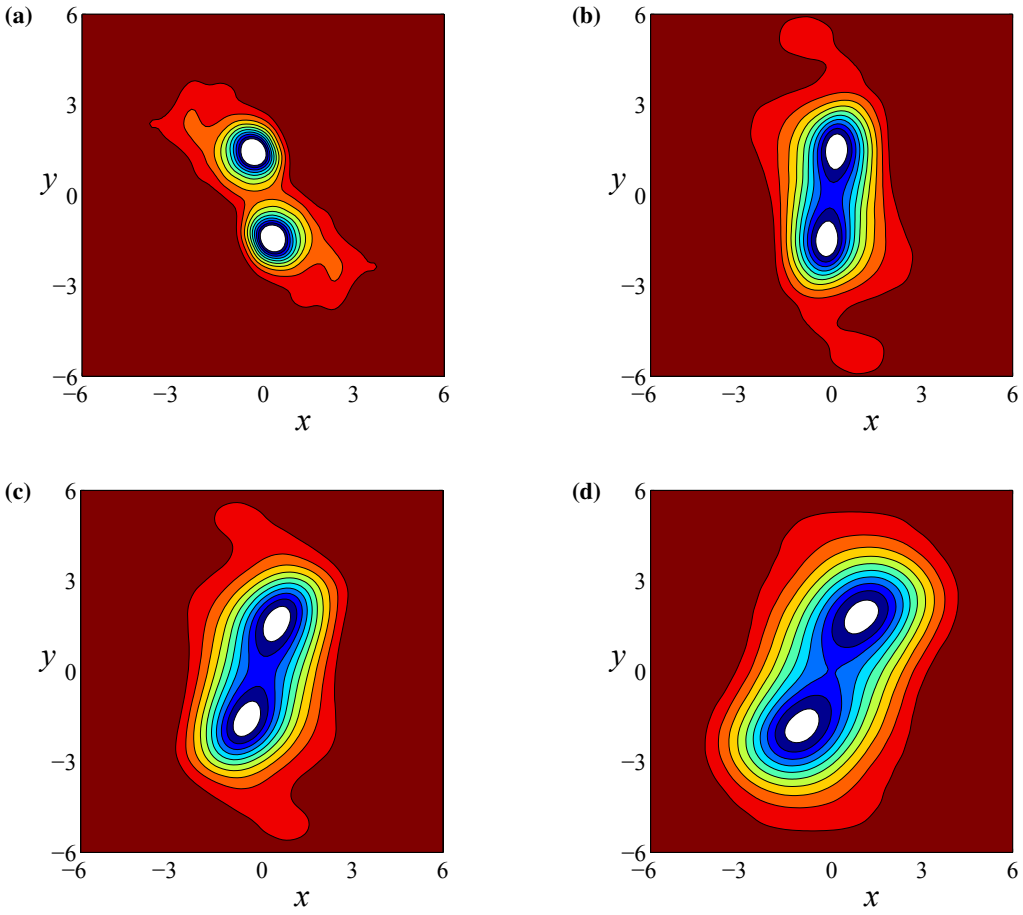

Figure 5.4.29: Contour plots of an LL-binary system with interaction ratio $I_r = \sqrt{2}$ at time $t = 1.00$ with (a) $\sigma = 1$ and $L = 1/\sqrt{2}$, (b) $\sigma = \sqrt{2}$ and $L = 1$, (c) $\sigma = 1.2\sqrt{2}$ and $L = 1.2$ and (d) $\sigma = 3/\sqrt{2}$ and $L = 3/2$.

Keeping the interaction ratio constant and changing the initial radii of the pressure systems gives an insight into the effect intensity of a single pressure system has on the rotation of binary systems. The smaller the initial radius of the pressure system the more-intense, as seen by the magnitude of the quivers in Figure 5.4.1. Decreasing the radii of the systems requires the location of the binary systems to be closer to each other to keep the interaction ratio constant. Figure 5.4.29 shows four separate LL-binary systems all with interaction ratio $I_r = \sqrt{2}$ at time $t = 1$. The most intense binary system shown in Figure 5.4.29(a) has rotated by approximately 58° from its initial position along the line $y = x$. Similarly, the next most intense system system illustrated in Figure 5.4.29(b) has rotational displacement of approximately 41° followed by a rotation of 27° in Figure 5.4.29(c). The least intense system shown in Figure 5.4.29(d) has rotated 17°. Therefore an LL-binary system with the same interaction ratio will have greater rotational displacement than another if the distance between the initial eye location is less than the other; that is, the further

apart the initial eyes the less rotation about each other.

Rotational displacement		
σ_1	σ_2	Rotation of intense system
$\sqrt{2}$	$\sqrt{2}$	30°
$\sqrt{2}+0.1$	$\sqrt{2}-0.1$	33°
$\sqrt{2}+0.2$	$\sqrt{2}-0.2$	37°
$\sqrt{2}+0.3$	$\sqrt{2}-0.3$	38°
$\sqrt{2}+0.4$	$\sqrt{2}-0.4$	43°
$\sqrt{2}+0.5$	$\sqrt{2}-0.5$	44°
$\sqrt{2}+0.6$	$\sqrt{2}-0.6$	46°
$\sqrt{2}+0.7$	$\sqrt{2}-0.7$	49°
$\sqrt{2}+0.8$	$\sqrt{2}-0.8$	54°

Table 5.1: Rotational displacement of the more-intense system for an LL-binary with $I_r = \sqrt{2}$, $L = 1$ at time $t = 0.80$.

Following on from what is shown in Figure 5.4.29 where the radius σ and initial eye locations L are selectively chosen so that the interaction ratio I_r remains identical. The question then is, what if the interaction ratio and the initial eye location are kept the same but the radii of the vortices are altered so that the average radius is identical? Table 5.1 shows various LL-binary system configurations in which the interaction ratio $I_r = \sqrt{2}$ with $L = 1$ and thus the average radius of the pressure systems is $\sigma = \sqrt{2}$. As the radius of the more-intense system decreased, the rotational displacement of the more-intense system increased, similar to what was shown in Figure 5.4.29. This in part confirms what Dong and Neumann [21] found when the separation distance was less than 650 km for binary cyclones. However, for our model the same results are achieved for all separation distances when interaction takes place. Conversely, the less-intense system rotated less as the radius is increased.

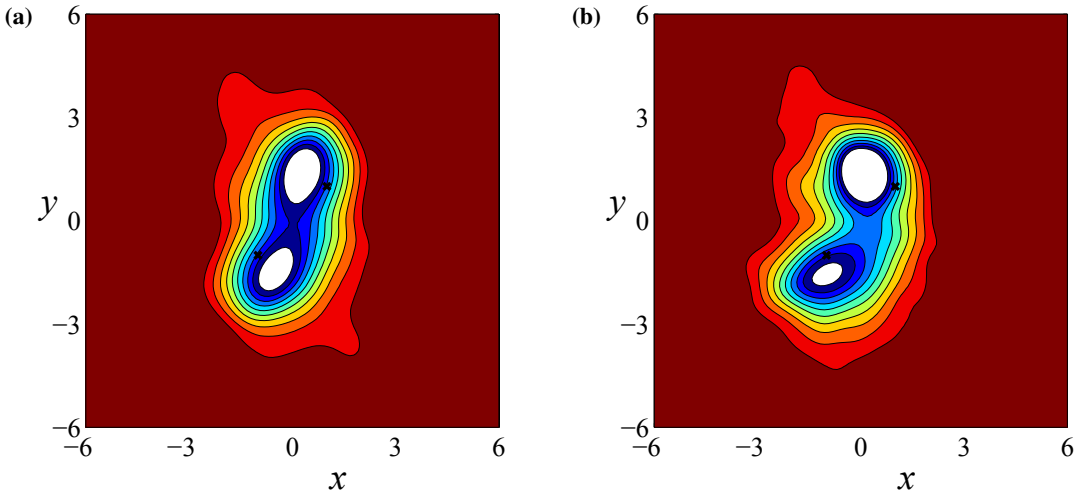

Figure 5.4.30: Pressure contour plots of an LL-binary system at time $t = 0.80$ with $I_r = \sqrt{2}$ and $L = 1$ for radii (a) $\sigma_1 = \sqrt{2} + 0.1$ and $\sigma_2 = \sqrt{2} - 0.1$ and (b) $\sigma_1 = \sqrt{2} + 0.4$ and $\sigma_2 = \sqrt{2} - 0.4$. **Crosses** indicate initial positions of the eyes of the vortices.

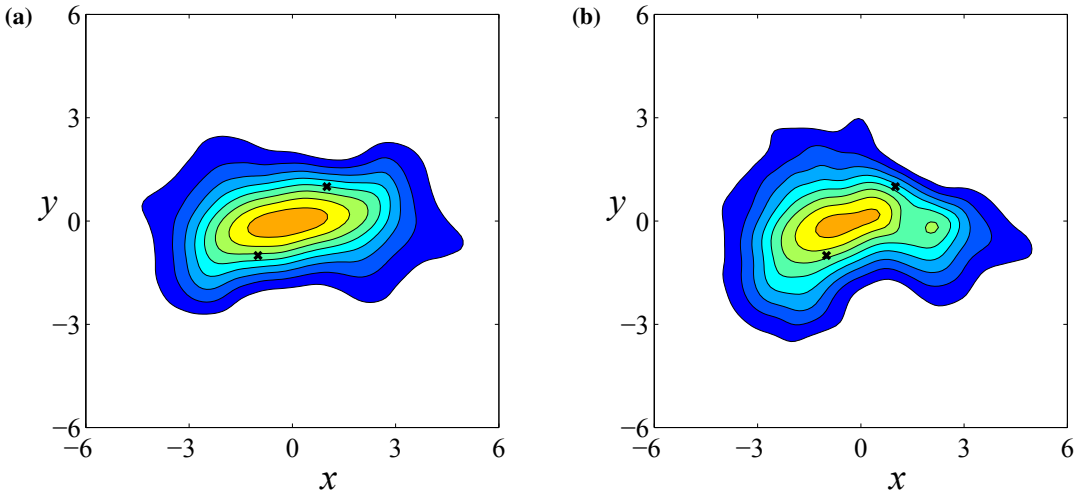

Figure 5.4.31: Pressure contour plots of an HH-binary system at time $t = 0.80$ with $I_r = \sqrt{2}$ and $L = 1$ for radii (a) $\sigma_1 = \sqrt{2} + 0.1$ and $\sigma_2 = \sqrt{2} - 0.1$ and (b) $\sigma_1 = \sqrt{2} + 0.4$ and $\sigma_2 = \sqrt{2} - 0.4$. **Crosses** indicate initial positions of the eyes of the vortices.

Examples of LL-binary systems with unequal intensities are shown in Figure 5.4.30. In this figure the interaction ratio is $I_r = \sqrt{2}$ and $L = 1$ and in each subfigure the more intense system is initially in the north-east quadrant. Figure 5.4.30(a) illustrates an LL-binary system with radii $\sigma_1 = \sqrt{2} + 0.1$ and $\sigma_2 = \sqrt{2} - 0.1$ at time $t = 0.80$. The rotation of the more intense vortex is approximately 33° from its initial location and its core has increased in area. Figure 5.4.30(b) shows

the effect of decreasing the radius of the intense system and increasing the radius of the other system to $\sigma_2 = \sqrt{2} - 0.4$ and $\sigma_1 = \sqrt{2} + 0.4$ respectively. The more-intense system rotates even further to approximately 43° and the core increases in area. In addition, the core of the less-intense system has rotated about its axis due to the influence of the intense system. Figure 5.4.31 shows the evolution of HH-binary systems with interaction ratio $I_r = \sqrt{2}$ and $L = 1$ with unequal radii and is the HH-binary system equivalent to Figure 5.4.30. The results of the HH-binary system are similar to those of the LL-binary system in that the more intense the individual system, the greater is the rotational displacement from its initial location. This fact is most evident in Figure 5.4.31(b) where the more-intense system has a radius of $\sigma_2 = \sqrt{2} - 0.4$ compared to $\sigma_2 = \sqrt{2} - 0.1$ in Figure 5.4.31(a).

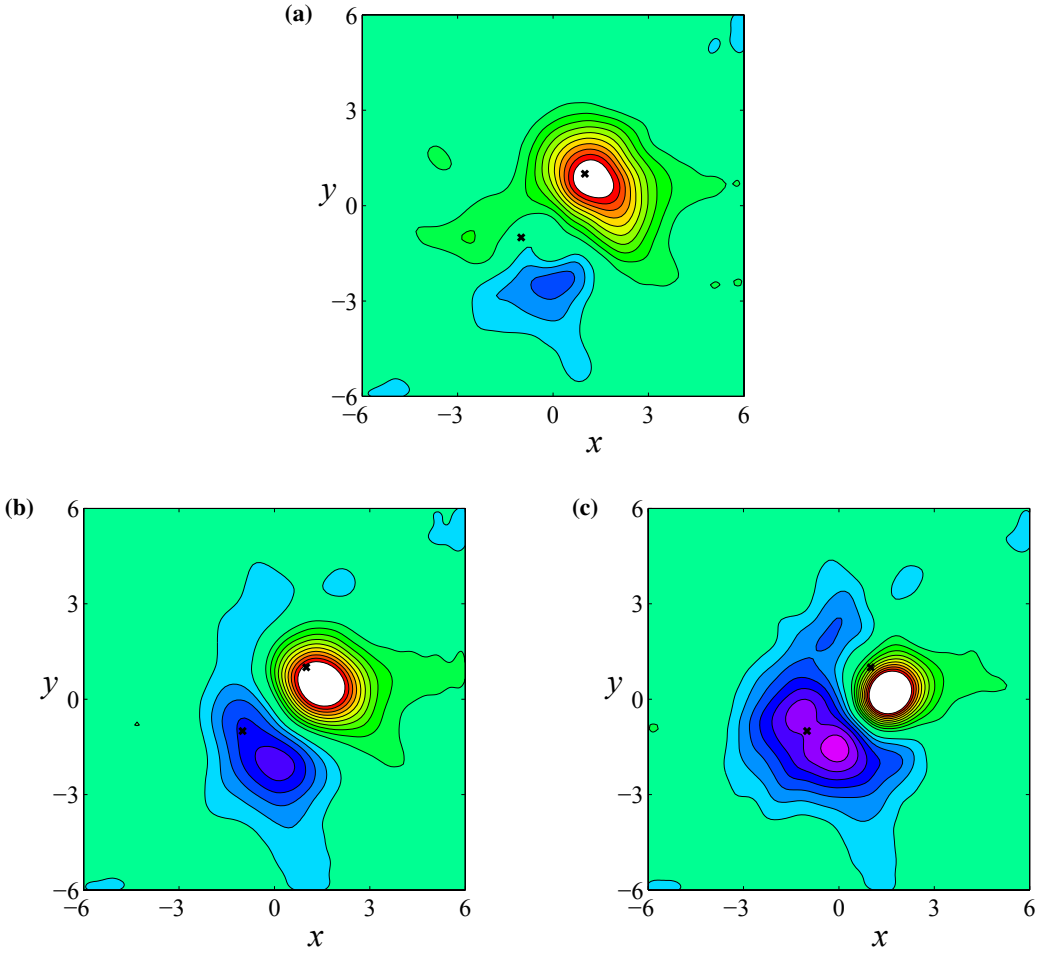

Figure 5.4.32: Contour plots of an HL-binary system with interaction ratio $I_r = \sqrt{2}$ and $L = 1$ at time $t = 0.80$ with initial low-pressure radius (a) $\sigma_2 = \sqrt{2} + 0.4$, (b) $\sigma_2 = \sqrt{2}$ and (c) $\sigma_2 = \sqrt{2} - 0.4$. **Crosses** indicate initial positions of the eyes of the vortices.

Figure 5.4.32 shows three different configurations of an HL-binary system with interaction ratio $I_r = \sqrt{2}$, initial eye locations at $L = 1$ at time $t = 0.80$. This figure highlights the effect of changing the intensity of a low-pressure system within a mixed binary system. When the low-pressure system is less intense with larger radius of $\sigma_2 = \sqrt{2} + 0.4$, shown in Figure 5.4.32(a) the movement away from its initial location is less than for the increasing intensity low-pressure regions shown in Figures 5.4.32(b) with $\sigma = \sqrt{2}$ and 5.4.32(c) with $\sigma_2 = \sqrt{2} - 0.4$. As a consequence of the intensity of the low increasing, the intensity of the high must decrease to maintain the constant interaction ratio. The greater the intensity of the high-pressure zone the more rapid the loss of pressure structure. This is evident from the reduced density of high-pressure contours in Figure 5.4.32. Initially the most intense high-pressure region shown in Figure 5.4.32(a) has pressure contours ranging from $p = 1.00 - 1.03$ and the respective contour ranges for Figures 5.4.32(b) and 5.4.32(c) are 1.00 – 1.05 and 1.00 – 1.07.

The results above have been obtained using Rossby number $Ro_T = 0.1$ which corresponds to a tangent point latitude $\phi \approx 43.3°$N. It has been shown throughout this section that the radius of the system is the determining factor of its intensity. By considering the geostrophic velocity representations (5.3.6) and (5.3.7) it is possible to relate the interaction ratio formulation (5.4.1) for different tangent point latitudes. A way of achieving this is to determine at what initial radius are the geostrophic speeds when $Ro_T = 0.1$ the same as for some pressure system with the same pressure differential $\mu = 0.1$ at a different latitude. Suppose that at some other latitude the Rossby number is $Ro_{T2} \neq 0.1$ and at that latitude the initial radius of the pressure system is σ_r. Then equating the geostrophic speeds gives

$$Ro_{T2}\frac{\mu \exp[-r^2/\sigma_r^2]}{1-\mu \exp[-r^2/\sigma_r^2]} = Ro_T\frac{\mu \exp[-r^2/\sigma^2]}{1-\mu \exp[-r^2/\sigma^2]}, \tag{5.4.2}$$

where $r^2 = x^2 + y^2$. Evaluating the expression (5.4.2) at $r = \sigma$, it can be shown that the initial radius σ when $Ro_T = 0.1$ can be written in terms of the initial radius σ_r when $Ro_T \neq 0.1$ in the form

$$\sigma = \sigma_r \eta, \tag{5.4.3}$$

where η is a function of the ratio of the Rossby numbers in the form

$$\eta = \sqrt{\ln\left[\exp\left(\frac{Ro_{T2}}{Ro_T}\right) + \mu\left(1 - \left(\frac{Ro_{T2}}{Ro_T}\right)\right)\right]}. \tag{5.4.4}$$

To validate equation (5.4.3) there is a need to cross reference with known binary system behaviour. Figure 5.4.18 gives an indication of the boundary between interactive ($I_r \geq 0.9$) and negligibly weak interaction ($I_r < 0.9$) zones and thus testing equation (5.4.3) against binary systems with $I_r > 1$ where there is considerable interaction, $I_r = 1$ where there is slight interaction and $I_r < 0.9$ where unobservable interaction occurs are the most appropriate choices. Consider a new tangent point latitude $\phi \approx 27.2°$N which is sufficiently separated from the standard tangent point latitude $\phi \approx 43.3°$N. The mid-low latitude $\phi \approx 27.2°$N equates to a Rossby number $Ro_{T2} = 0.15$. Substituting $Ro_T = 0.1$ and $Ro_{T2} = 0.15$ into equation (5.4.4) gives $\eta \approx 1.22$.

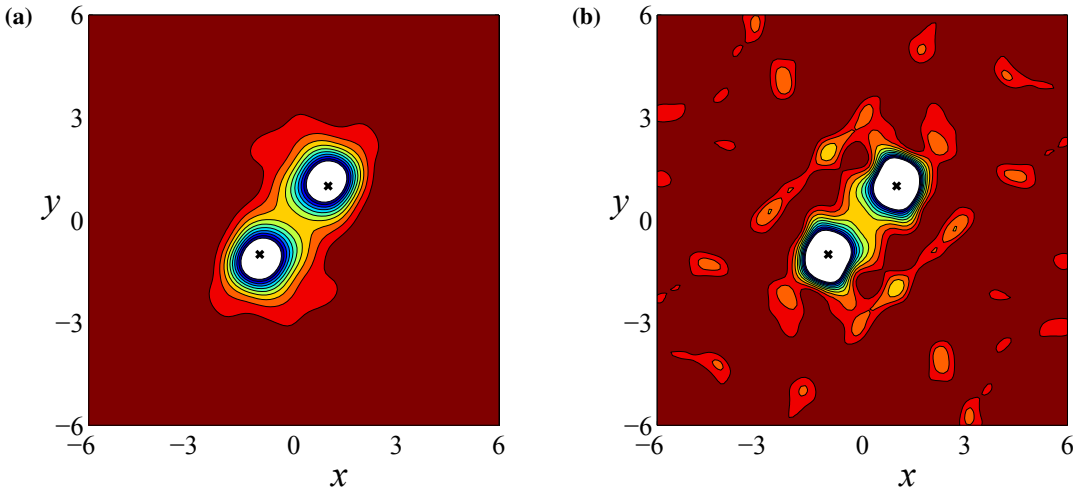

Figure 5.4.33: Pressure contour plots of an LL-binary system with $L = 1$ at time $t = 0.45$ with (a) $Ro_T = 0.1$, $\sigma = 1$ and (b) $Ro_T = 0.15$, $\sigma_r \approx 0.82$. **Crosses** indicate initial positions of the eyes of the vortices.

Recall Figure 5.4.20(a) which showed an interactive LL-binary system with $\sigma = 1$, $L = 1$ and thus an interaction ratio $I_r = 1$. This is a prime example of slight interaction and is reproduced in Figure 5.4.33(a) for ease of comparison. The lower latitude equivalent where $Ro_{T2} = 0.15$ is given in Figure 5.4.33(b) and by equation (5.4.3) the initial radius is $\sigma_r \approx 0.82$. As expected from an interaction ratio of $I_r = 1$ there is modest movement of the pressure systems in both these figures. Apart from the deformation of the low-pressure systems, the moderate movement is similar for the two different Rossby numbers in Figure 5.4.33.

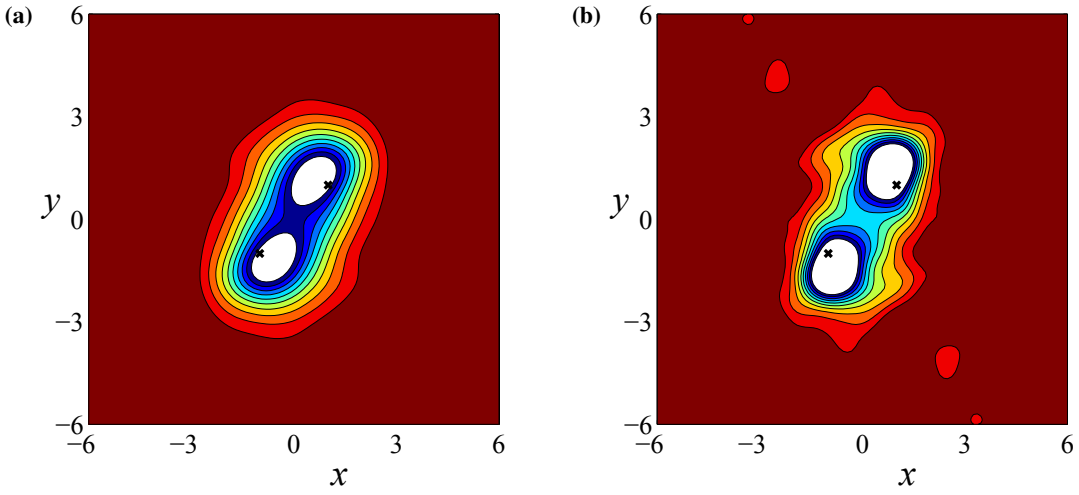

Figure 5.4.34: Pressure contour plots of an LL-binary system with $L = 1$ at time $t = 0.45$ with (a) $Ro_T = 0.1$, $\sigma = \sqrt{2}$ and (b) $Ro_T = 0.15$, $\sigma_r \approx 1.16$. **Crosses** indicate initial positions of the eyes of the vortices.

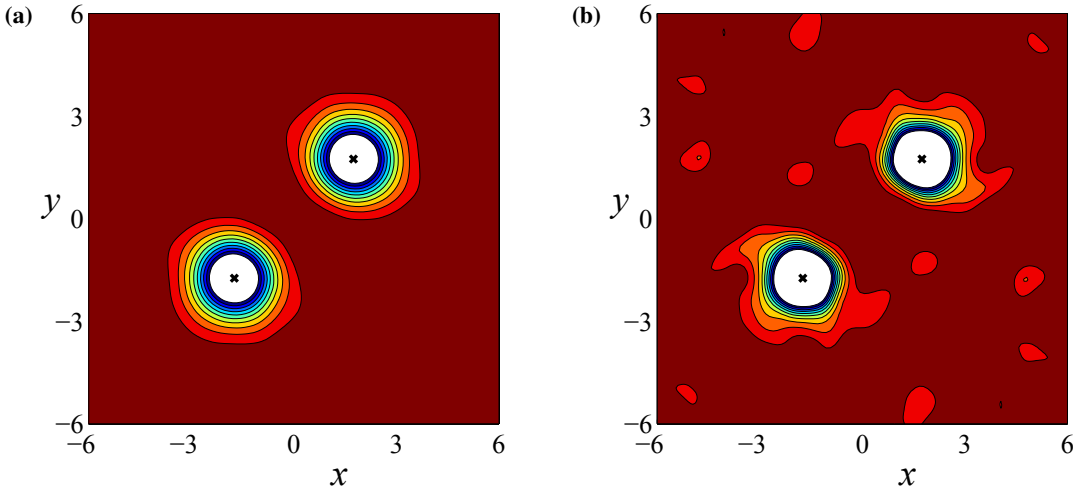

Figure 5.4.35: Pressure contour plots of an LL-binary system with $L \approx 1.74$ at time $t = 0.45$ with (a) $Ro_T = 0.1$, $\sigma = 1.22$ and (b) $Ro_T = 0.15$, $\sigma_r \approx 1$. **Crosses** indicate initial positions of the eyes of the vortices.

If the interaction ratio is greater than one, for example $I_r = \sqrt{2}$, illustrated in Figure 5.4.20(b) and again in Figure 5.4.34(a), there is clear movement of the binary system at time $t = 0.45$. This figure has initial pressure systems located at $L = 1$ of radii $\sigma = \sqrt{2}$ with $Ro_T = 0.1$. At the lower latitude of $\phi \approx 27.2°$N where $Ro_T = 0.15$ the comparable radius σ_r is approximately 1.16. The contour map of this scenario is given in Figure 5.4.34(b), and the rotation of the binary system induced by the interaction at this lower latitude is comparable to that of the corresponding LL-

binary system centred about the mid-latitude 43.3°N shown in Figure 5.4.34(a).

It has been well established that no observable interaction takes place when $I_r = 0.7$. For ease of converting between the different Rossby numbers consider an LL-binary system at the mid-latitude 43.3°N with $\sigma = 1.22$ and $L \approx 1.74$ so that the interaction ratio is $I_r \approx 0.7$ at time $t = 0.45$ shown in Figure 5.4.35(a). As expected the low-pressure systems are still centrally located about the initial eyes (indicated by bold crosses). The convenient choice of $\sigma = 1.22$ in this figure makes the equivalent radius using $Ro_{T2} = 0.15$ having the value $\sigma_r \approx 1$. The pressure contours of this simulation are given in Figure 5.4.34(b). In both these figures there is no indication of significant movement caused by the influence of the other system. Figures 5.4.33 – 5.4.35 have illustrated how equation (5.4.3) can be used to approximate within a sensible degree of accuracy, whether or not pressure systems will interact when located around latitudes where $Ro_T \neq 0.1$.

5.5 Discussion

The interaction of atmospheric vortices has been an intensive area of research, particularly, the interaction of tropical cyclones, hurricanes and typhoons. However, the interaction of large-scale binary systems in terms of extra-tropical cyclones and extra-tropical anti-cyclones has had considerably less interest. Such vortices form in the mid-latitude regions of Earth and thus the f-plane approximation with a tangent point latitude of $\phi \approx 43.3$°N giving a time scale Rossby number of $Ro_T = 0.1$ was used. The f-plane approximation is used as the interaction of binary systems along approximately the same latitude was of interest. However, the coordinate geometry is rotated 45° and absorbing boundary conditions are used to help minimise reflections off the artificial tangent plane boundaries. The binary systems could be in one of four different configurations, an LL-binary system, HH-binary system, LH-binary system or an HL-binary system. Depending on the initial locations and radii of the binary systems, interaction takes place or it does not. Interaction is defined to have occurred when there is clear movement of one system caused by the other at time $t = 0.45$ (approximately 12.5 hours in dimensional time). It was found that interaction took place if the ratio of the average radius σ to initial eye location L was greater than or equal to 0.9 ($I_r \geq 0.9$). For this model the low-pressure systems preserved their pressure differential as time increased. In contrast, the high-pressure systems diffuse over time and lose their pressure charac-

teristics. The resulting pressure contour diagrams, as time increases, reflect the real world mean sea-level pressure diagrams, in that low-pressure systems have densely compacted contours and high-pressure systems have sparse and spread out contours.

If interaction occurs, an LL-binary system will rotate in an anticlockwise direction in the northern hemisphere until such a time at which its vortices begin to move apart. The contour maps are rotationally symmetric about the origin for equally intense systems. As the vortices studied in this thesis use the same pressure differential, the intensity is related to the initial radius of the system. The greater the radius the less intense is the vortex. When the radius of each vortex is different, the rotation of the binary system is not symmetric about the origin. This is illustrated in Figure 5.4.30, for a LL system, and similar results have also been obtained for HH binary pairs (see Figure 5.4.31). Keeping the interaction ratio and initial eye locations constant and changing the radii of the systems so that the average radius is the same, the more-intense vortex (smaller radius) rotates faster whilst the less-intense one (larger radius) rotates slower about the origin. For these non-mixed binary systems the rotation is in the opposite direction in the southern hemisphere.

For mixed binary systems (HL and LH) in the northern hemisphere with equal radius the interaction causes the systems to move perpendicular to the line joining the initial eye locations. For an HL-binary system the movement is to the south-east, and to the north-west for an LH-binary system. Changing the intensity of the low-pressure system in these configurations whilst maintaining a constant interaction ratio and separation distance has basically the same effect as for the LL-binary system. Increasing the intensity of the low-pressure by decreasing the radius produces greater movement of the pressure system to the south-east for an HL-binary system and for an LH-binary system the movement is further in the north-west direction. However, in both cases the less intense the high-pressure system, the smaller the loss in the pressure differential. In the southern hemisphere the initial eye location used was $(x, y) = \pm(L, -L)$ to reflect the fact that the Coriolis parameter exhibits odd function characteristics in the latitudinal y-coordinate. With this geometry the mixed binary systems move north-east and south-west for the respective HL- and LH-binary systems in the southern hemisphere.

The interaction of an HH-binary system is somewhat different to binary systems involving a low-pressure system. The interaction produces a region of intermediate pressure in the range

$p = 1.01 - 1.09$ depending on the loss of pressure structure associated with high-pressure systems. The intermediate pressure region will then rotate in a clockwise (anti-clockwise) direction in the northern (southern) hemisphere. Similarly to the LL-binary systems, the contour maps of the HH-binary systems are rotationally symmetric about the origin for equally intense systems. When the intensities of the high-pressure systems are different, the more-intense vortex will have greater rotational displacement about the origin, together with greater pressure dissipation, than its binary partner.

An approximate rule has been developed, to generalize the scaling law from Figure 5.4.18 to other latitudes, by calculating the effective radii at the standard latitude $\phi = 43.3°$N, for which the Rossby number is $Ro_T = 0.1$. This conversion is given in equations (5.4.2) – (5.4.4). Figure 1.0.3 shows two typhoons at an approximate latitude of $\phi = 20°$N, for which the Rossby number is $Ro_T = 0.2$. At this latitude $\sigma = 1.41\sigma_r$ by (5.4.3) and (5.4.4). From Figure 1.0.3, it is estimated very approximately that the interaction ratio I_r in equation (5.4.1) is about 1.17 after allowing for differences in latitude (20°N), suggesting that the two vortices would interact, as indeed was the case.

This chapter has developed a way of determining when mid-latitude vortices located at approximately 43°N may or may not interact with each other. The interaction is determined by considering the value of the interaction ratio given by equation (5.4.1). The interaction ratio can be modified to give an indication of whether or not binary vortices would interact when located about other mid-latitude locations. It has been proposed that the interaction between atmospheric vortices can perturb vortices in close proximity and produce vortices that have clearly defined straight edges, resulting in polygonal shaped vortices. This is the focus of the next chapter.

Chapter 6

A δ-plane simulation of anti-cyclones perturbing circumpolar flows to form a transient north polar hexagon

Saturn's North Polar Hexagon was discovered by Godfrey [31] who pieced together map projections of images captured by the Voyager mission to unveil a hexagonal feature over the geographic north pole of Saturn. The Hexagon is a long lived structure that continues to this day; its origin has been the topic of interest for the last few decades and several theories have been suggested [1, 55, 56]. This chapter attempts to give insight into a possible trigger mechanism for such a unique structure to arise and answer whether or not a hexagonal feature can result due to the influence of encroaching anti-cyclones. This research is based upon the proposed theory by Allison *et al.* [1] that the Hexagon may be the result of at least one impinging anti-cyclone to the south perturbing a circumpolar jet centrally located at the approximate latitude of 76°N. There is also a smaller retrograde circumpolar flow at 69°N.

The location of the flow feature of interest prohibits the use of the commonly used f-plane and β-plane approximations. In contrast a high-latitude δ-plane approximation will be used to simulate the spheroidal effects of polar flow and the interaction between an initially circular circumpolar jet and at least one perturbing anti-cyclone. A Gaussian profile function will represent the predominant eastward circumpolar current and the smaller magnitude westward flow to the south. The perturbing anti-cyclones are initially expressed as offset high-pressure regions mod-

elled with an exponential function. It will be shown that depending on strength, location and radius of the perturbing anti-cyclones a hexagonal feature can develop. However, the longevity of the actual North Polar Hexagon must be attributed to other factors not considered in this chapter.

6.1 Background Polar Flow

Godfrey [31] was the first to give an indication of the magnitude of the atmospheric fluid velocities on Saturn. Figure 6.1.1 was first published by Godfrey [31] in 1988 and shows the zonal velocity variation with latitude. The horizontal axis gives the value of the zonal velocity and the vertical axis is the northern latitudes in degrees. This figure was derived by careful analysis of the ground breaking composite map-projected images that were used to reveal the Hexagon for the first time in its entirety (see Figure 1.0.5). The Hexagon itself is embedded within an eastward polar jet spanning the latitudes 74° – 78°, with peak velocity of approximately 100 ms^{-1} at 76°, whilst Baines [4] suggests it could be as high as 125 ms^{-1}. This increase has been attributed to temporal variability and/or vertical shear. The most recent observations captured using the Imaging Science Subsystem onboard the Cassini spacecraft indicate that the peak velocity within the Hexagon is around 119 ms^{-1} [2]. Along the extremities of the Hexagon the velocity drops considerably to less than 20 ms^{-1}. At the approximate latitude of 69° the velocity is about -20 ms^{-1}, indicating a moderate westward jet to the south. These extremes of the velocity profile are paramount when deciding the initial velocities of the numerical simulations. The velocity profile given by Godfrey [31] will be the basis for the time-independent steady background flow component of the non-linear representations given later. This is in contrast to the techniques used in Chapters 4 and 5 where the velocity components were derived using the initial pressure profile function.

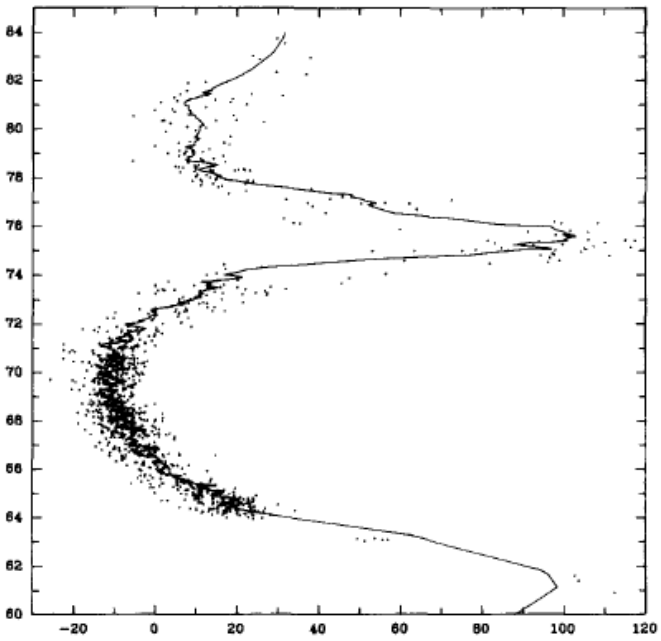

Figure 6.1.1: Zonal velocity profile determined by tracking clouds as published by Godfrey [31], latitude along the vertical axis and velocity along the horizontal axis. Reprinted with permission from Elsevier.

Due to the scaling of the problem, 1° in latitude is approximately equal to a dimensionless distance of 0.1. The scale velocity is 100 ms^{-1} and therefore the dimensionless velocity is peaked at 1 . To model the eastward travelling polar jet, the velocity components will take the form

$$u_e(x,y) = -C_0\, y\, \exp\left[-C_1\left(\sqrt{x^2+y^2}-1.4\right)^2\right], \tag{6.1.1}$$

$$v_e(x,y) = C_0\, x\, \exp\left[-C_1\left(\sqrt{x^2+y^2}-1.4\right)^2\right], \tag{6.1.2}$$

where the constants C_0 and C_1 are to be determined. The constant 1.4 in the equations (6.1.1) and (6.1.2) is the approximate dimensionless distance from the origin of the δ-plane to the latitude 76°N and is an indicator of where the velocity of the eastward jet is at its maximum.

The slower moving westward flow has similar form to that of the eastward flow components, such that

$$u_w(x,y) = C_2\, y\, \exp\left[-C_3\left(\sqrt{x^2+y^2}-2.1\right)^2\right], \tag{6.1.3}$$

$$v_w(x,y) = -C_2\, x\, \exp\left[-C_3\left(\sqrt{x^2+y^2} - 2.1\right)^2\right]. \tag{6.1.4}$$

The westward flow is maximised at latitude 69°N and thus the constant 2.1 is the approximate dimensionless distance from the origin of the δ-plane. Like C_0 and C_1, the value of the constants C_2 and C_3 are to determined. The background flow components are simply the sums of the easterly (subscript e) and westerly (subscript w) jet components, thereby giving the background velocity components in the form

$$\begin{aligned} u_b(x,y) = &-C_0\, y\, \exp\left[-C_1\left(\sqrt{x^2+y^2} - 1.4\right)^2\right] \\ &+ C_2\, y\, \exp\left[-C_3\left(\sqrt{x^2+y^2} - 2.1\right)^2\right], \end{aligned} \tag{6.1.5}$$

$$\begin{aligned} v_b(x,y) = &\, C_0\, x\, \exp\left[-C_1\left(\sqrt{x^2+y^2} - 1.4\right)^2\right] \\ &- C_2\, x\, \exp\left[-C_3\left(\sqrt{x^2+y^2} - 2.1\right)^2\right]. \end{aligned} \tag{6.1.6}$$

Approximate zonal velocity at latitudes of interest, interpolated from Figure 6.1.1		
Latitude (°N)	Dimensionless radius from pole	Dimensionless velocity (ms^{-1})
78	1.2	0.20
76	1.4	1.00
74	1.6	0.20
73	1.7	0.10
72	1.8	0.00
71	1.9	−0.10
69	2.1	−0.20
67	2.3	−0.10
66	2.4	0.00

Table 6.1: Shows the approximate non-dimensional zonal velocity on Saturn for latitudes of interest in terms of radii from the north pole.

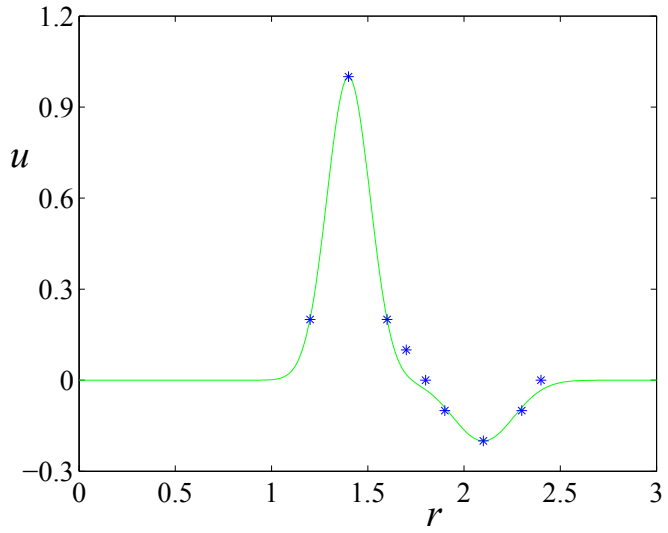

Figure 6.1.2: Curve fitted zonal velocity profile. The blue asterisks are the data points given in Table 6.1.

The flow region of interest is bounded within the latitudes 66°N and 80°N and encompasses the North Polar Hexagon. Outside of this region the background velocity will take the dimensionless value of zero. Table 6.1 gives the approximate non-dimensional zonal velocity at various latitudes of interest. The values in this table were interpolated from Figure 6.1.1 and are used in the curve fitting procedure to determine the constants C_0, C_1, C_2 and C_3 so that the background flow had similar characteristics to the zonal velocity profile published by Godfrey [31] and reprinted in Figure 6.1.1. The values of the velocity constants that are used in this chapter are taken to be $C_0 \approx 0.7$, $C_1 = 40$, $C_2 \approx 0.1$ and $C_3 = 20$. The constants C_0 and C_2 are effective amplitude values for the exponential terms and thus $C_0 = \frac{1}{1.4}$ and $C_2 = \frac{0.2}{2.1}$ and the constants C_1 and C_3 are dilation factors of the peaks in the exponential representations. Figure 6.1.2 shows a plot of the curve fitted representation of the zonal velocity published by Godfrey [31] in dimensionless form, with u representing the zonal velocity and r is the radius from the pole. The blue asterisks are the data values given in Table 6.1.

Pressure and temperature in the atmosphere of Saturn increase towards the centre of the planet. To accommodate for the variation with depth, the atmosphere will not be assumed to be isothermal, but isopycnal. This assumption contrasts with the previous finger formation (Chapter 4) and binary interaction (Chapter 5) mathematical assumptions. The isopycnal assumption leads to the initial and background density having the constant dimensionless value

$$\rho_b(x,y) = 1 = \rho(x,y,0). \tag{6.1.7}$$

The dimensionless equation of state (3.4.8) must be satisfied and therefore it follows from equation (6.1.7) that the background pressure and temperature are initially equal. Assuming that the velocity components above are essentially geostrophic then

$$u_b(x,y) = -\frac{\nu_E}{f\rho_b(x,y)}\frac{\partial p_b(x,y)}{\partial y} = -\frac{\nu_E}{f}\frac{\partial p_b(x,y)}{\partial y}, \tag{6.1.8}$$

$$v_b(x,y) = \frac{\nu_E}{f\rho_b(x,y)}\frac{\partial p_b(x,y)}{\partial x} = \frac{\nu_E}{f}\frac{\partial p_b(x,y)}{\partial x}. \tag{6.1.9}$$

Alternatively equations (6.1.8) and (6.1.9) can be re-arranged to isolate the partial derivatives of pressure in the form

$$\frac{\partial p_b(x,y)}{\partial y} = -\frac{u_b(x,y)f}{\nu_E}, \tag{6.1.10}$$

$$\frac{\partial p_b(x,y)}{\partial x} = \frac{v_b(x,y)f}{\nu_E}. \tag{6.1.11}$$

To get a representation for the background pressure, equation (6.1.10) is integrated with respect to y to give

$$p_b(x,y) = -\int \frac{u_b(x,y)f}{\nu_E}\,dy + F(x), \tag{6.1.12}$$

Substituting the background component $u_b(x,y)$ given by equation (6.1.5) into (6.1.12) gives

$$\begin{aligned} p_b(x,y) = {} & \frac{C_0}{\nu_E}\int yf\exp\left[-C_1\left(\sqrt{x^2+y^2}-1.4\right)^2\right]dy \\ & -\frac{C_2}{\nu_E}\int yf\exp\left[-C_3\left(\sqrt{x^2+y^2}-2.1\right)^2\right]dy + F(x). \end{aligned} \tag{6.1.13}$$

Letting $\xi = \sqrt{x^2+y^2}$, the background pressure representation given by (6.1.13) becomes

$$\begin{aligned} p_b(x,y) = {} & \frac{C_0}{\nu_E}\int \xi f\exp\left[-C_1\left(\xi-1.4\right)^2\right]d\xi \\ & -\frac{C_2}{\nu_E}\int \xi f\exp\left[-C_3\left(\xi-2.1\right)^2\right]d\xi + F(x). \end{aligned} \tag{6.1.14}$$

The background pressure is radially symmetric and thus can be expressed in the alternate form

$$p_b(x,y) = \frac{C_0}{\nu_E}\int_0^{\xi} rf\exp\left[-C_1\,(r-1.4)^2\right]\,dr - \frac{C_2}{\nu_E}\int_0^{\xi} rf\exp\left[-C_3\,(r-2.1)^2\right]\,dr + F(x), \tag{6.1.15}$$

where r is a variable radius from the north pole. The integration of a partial derivative with respect to y resulted in the integration 'constant' being a function $F(x)$ which has to be determined. Differentiating equation (6.1.15) with respect to x gives

$$\begin{aligned}\frac{\partial p_b}{\partial x} &= \frac{C_0}{\nu_E}xf\exp\left[-C_1\left(\sqrt{x^2+y^2}-1.4\right)^2\right] \\ &\quad - \frac{C_2}{\nu_E}xf\exp\left[-C_1\left(\sqrt{x^2+y^2}-2.1\right)^2\right] + \frac{dF}{dx} \\ &= \frac{v_b(x,y)f}{\nu_E} + \frac{dF}{dx}.\end{aligned} \tag{6.1.16}$$

A direct comparison of the equations given by (6.1.16) and (6.1.11) results in $\frac{dF}{dx} = 0$, which implies the integration function $F(x)$ is a constant and thus the background pressure and temperature take the form

$$\begin{aligned}p_b(x,y) &= \frac{C_0}{\nu_E}\int_0^{\xi} rf\exp\left[-C_1\,(r-1.4)^2\right]\,dr \\ &\quad - \frac{C_2}{\nu_E}\int_0^{\xi} rf\exp\left[-C_3\,(r-2.1)^2\right]\,dr + \mathcal{K} \\ &= T_b(x,y).\end{aligned} \tag{6.1.17}$$

The background pressure and temperature representation (6.1.17) is generated using both Gaussian profile functions for the eastward and westward circumpolar jets. If the westward flow is excluded, then the background pressure and temperature have the alternate form

$$p_b(x,y) = \frac{C_0}{\nu_E}\int_0^{\xi} rf\exp\left[-C_1\,(r-1.4)^2\right]\,dr + \mathcal{D} = T_b(x,y). \tag{6.1.18}$$

The constants $\mathcal{K}$ and $\mathcal{D}$ are specifically chosen so that the pressure and temperature take the values $p_b(x,y) = 1$ and $T_b(x,y) = 1$, respectively, on the boundaries of the δ-plane.

6.2 Perturbation Flow

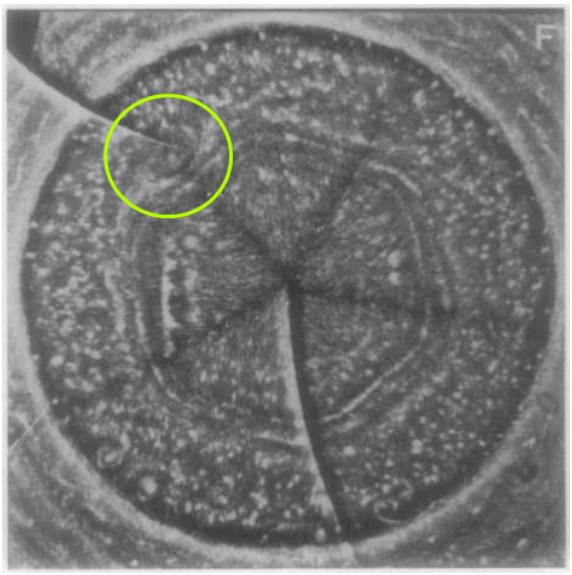

Figure 6.2.1: Composite map-projected images of Saturn's North Polar Hexagon as published by Godfrey [31] and reprinted with permission from Elsevier. Contains additional highlighting of the prominent anti-cyclone.

It has been suggested by Allison *et al.* [1] that the Hexagonal structure over the pole of Saturn may be the result of at least one perturbing anti-cyclone. The aforementioned perturbing anti-cyclone can be seen in the top left quadrant of Figure 6.2.1. Analysis of the map projections used to generate Figure 6.2.1 enabled streamline maps to be produced. At the time they showed the presence of multiple anti-cyclones around the same latitude centred between the vertices of the Hexagon [31], although not visible. Ground based and Hubble Space Telescope observations gathered over the period 1990–1991 also showed a large visible anti-cyclone to the south of the Hexagon. However, a comparison of the visible anti-cyclone measured in the Voyager images (see Figure 6.2.1) to those of ground based observations over the period 1990–1991 led Sanchez-Lavega to theorise that the visible anti-cyclone observed in 1990 may in fact be different to the one observed previously [62], and that there might be at least two anti-cyclonic vortices, that may be visible at different times, located along different edges of the Hexagon.

The claim by Allison *et al.* [1] appears not to have been investigated thoroughly in the literature. For this reason, the effects of perturbing anti-cyclone(s) will be simulated to infer whether or not anti-cyclones could be a possible trigger mechanism for the formation of the North Polar

Hexagon on Saturn. The perturbing anti-cyclones are modelled using high-pressure systems. A single perturbing anti-cyclone has the form

$$p_p(x,y) = \mu \exp\left[\frac{-((x-M)^2 + (y-M)^2)}{\sigma^2}\right] = T_p(x,y), \tag{6.2.1}$$

where μ is the increase in pressure from background, σ is the radius of the anti-cyclone and $(x,y) = (M,M)$ is the initial location of the eye of the perturbing system. Binary perturbations will also be considered and in such a case the perturbing pressure systems are defined by

$$\begin{aligned} p_p(x,y) = \mu_1 \exp&\left[\frac{-((x-M)^2 + (y-M)^2)}{\sigma_1^2}\right] \\ + \mu_2 \exp&\left[\frac{-((x+M)^2 + (y+M)^2)}{\sigma_2^2}\right] = T_p(x,y). \end{aligned} \tag{6.2.2}$$

Similarly, the rise in pressure is given by μ_1 and μ_2 and the radii of each pressure system are σ_1 and σ_2. The initial locations of the anti-cyclones are the cartesian coordinates $\pm(M,M)$. A direct result of the equation of state (3.4.8) and the isopycnal assumption is that the perturbing density must take the form

$$\rho_p(x,y) = 1. \tag{6.2.3}$$

The velocity components of the atmospheric flow induced by the anti-cyclones are geostrophic representations

$$u_p(x,y) = -\frac{\nu_E}{f}\frac{\partial p_p(x,y)}{\partial y}, \tag{6.2.4}$$

$$v_p(x,y) = \frac{\nu_E}{f}\frac{\partial p_b(x,y)}{\partial x}. \tag{6.2.5}$$

6.3 Spectral Solution Method

Similar to the finger structures and interacting vortices simulations in Chapters 4 and 5, a spectral solution is determined using both Dirichlet and Robin boundary conditions and a comparison of both approaches is discussed in the results section 6.5. The dependent variables pressure p,

temperature T, density ρ and the x- and y-directed velocity components u and v are expressed as the sum of background component, perturbation component and a time-dependent component and thus written

$$p(x, y, t) = p_b(x, y) + p_p(x, y) + p_u(x, y, t), \tag{6.3.1}$$

$$\rho(x, y, t) = \rho_b(x, y) + \rho_p(x, y) + \rho_u(x, y, t), \tag{6.3.2}$$

$$T(x, y, t) = T_b(x, y) + T_p(x, y) + T_u(x, y, t), \tag{6.3.3}$$

$$u(x, y, t) = u_b(x, y) + u_p(x, y) + u_u(x, y, t), \tag{6.3.4}$$

$$v(x, y, t) = v_b(x, y) + v_p(x, y) + v_u(x, y, t). \tag{6.3.5}$$

The subscripts b indicate the background component in equations (6.1.7) – (6.1.9) and (6.1.17). The perturbation components identified by the subscripts p are given by equations (6.2.1) or (6.2.2) for the pressure and temperature depending on whether one or two perturbing anti-cyclones are in effect, and also (6.2.3), (6.2.4) and (6.2.5). Apart from the constants in background flow components of the pressure, temperature and density, the time and spatial dependent components can be absorbed into one component dependent upon time for each of the variables. Thus the fully non-linear terms (6.3.1) – (6.3.5) have the same form as those used in the interacting vortices simulations of Chapter 5, and are respectively written

$$p(x, y, t) = 1 + \sum_{m=1}^{\infty} \sum_{n=1}^{\infty} P_{mn}(t) F_m(x) G_n(y), \tag{6.3.6}$$

$$\rho(x, y, t) = 1 + \sum_{m=1}^{\infty} \sum_{n=1}^{\infty} R_{mn}(t) F_m(x) G_n(y), \tag{6.3.7}$$

$$T(x, y, t) = 1 + \sum_{m=1}^{\infty} \sum_{n=1}^{\infty} T_{mn}(t) F_m(x) G_n(y), \tag{6.3.8}$$

$$u(x,y,t) = \sum_{m=1}^{\infty}\sum_{n=1}^{\infty} A_{mn}(t)F_m(x)G_n(y), \tag{6.3.9}$$

$$v(x,y,t) = \sum_{m=1}^{\infty}\sum_{n=1}^{\infty} B_{mn}(t)F_m(x)G_n(y). \tag{6.3.10}$$

The spectral method used in Chapters 4 and 5 involved re-arranging the governing equations where applicable, so that the time-dependent and linear terms were expressed as the sum of the non-linear components. However, since carrying out that work, it was subsequently found that equally reliable results could be obtained simply by isolating only the time-dependent and spatial components. This makes the analysis and coding simpler to undertake, for both the Dirichlet and Robin type boundary conditions, and is discussed in the following.

6.3.1 Dirichlet Conditions

The basis functions $F_m(x)$ and $G_n(y)$ are chosen so that the Dirichlet conditions which are imposed on the unsteady time-dependent components take the form

$$p(\pm\lambda, y, t) = 0 \; ; \; p(x, \pm\omega, t) = 0 \tag{6.3.11}$$

for the pressure and similarly for the remaining series terms. This leads to the familiar sinusoidal basis functions

$$F_m(x) = \sin\left(\frac{m\pi(x+\lambda)}{2\lambda}\right) \; ; \; G_n(y) = \sin\left(\frac{n\pi(y+\omega)}{2\omega}\right). \tag{6.3.12}$$

The Fourier series representation of the pressure (6.3.6) and the governing mass equation (3.4.3) are coupled such that

$$\frac{\partial\rho}{\partial t} = \sum_{m=1}^{\infty}\sum_{n=1}^{\infty} R'_{mn}(t)\, F_m(x)\, G_n(y) = -F_1(x,y,t), \tag{6.3.13}$$

where

$$F_1(x,y,t) = u\frac{\partial \rho}{\partial x} + v\frac{\partial \rho}{\partial y} + \rho\left(\frac{\partial u}{\partial x} + \frac{\partial v}{\partial y}\right). \tag{6.3.14}$$

The function $F_1(x,y,t)$ is also defined by equation (4.2.12) and represents the spatial terms in the mass equation (3.4.3). The ordinary differential equation for the Fourier coefficients is

$$R'_{kl}(t) = \frac{-1}{\lambda\omega}\int_{-\lambda}^{\lambda}\int_{-\omega}^{\omega} F_1(x,y,t)F_k(x)G_l(y)\,dydx$$
$$\text{for } k = 1,2,....,M, \text{ and } l = 1,2,....,N, \tag{6.3.15}$$

and is the result of multiplying by the similar basis functions $F_k(x)$, $G_l(y)$ and integrating over the region of the δ-plane. The system of ordinary differential equations for the Fourier coefficients $R_{kl}(t)$ is identical to that of equation (4.2.16) in the finger structure formulations and the function $F_1(x,y,t)$ is as defined by (4.2.12). Similarly, the Fourier coefficients $P_{kl}(t)$ and $T_{kl}(t)$ are determined by using the equations (4.2.19) and (4.2.20) with respective internal functions $F_4(x,y,t)$ and $F_5(x,y,t)$ given by the equations (4.2.24) and (4.2.23).

Previously, the derivation of the ordinary differential equation system for the Fourier coefficients $A_{mn}(t)$ and $B_{mn}(t)$ used in the x- and y-directed momentum equations has involved separating the linear and non-linear terms. However, considering the time-dependent component separately, the corresponding system of equations for the Fourier coefficients are simplified without loss of numerical accuracy; in fact, they produced identical results. The expanded forms of the x- and y-directed momentum equation on the δ-plane are

$$\frac{\partial u}{\partial t} + u\frac{\partial u}{\partial x} + v\frac{\partial u}{\partial y} - \left(2\tilde{\Omega} + \tilde{\delta}(x^2+y^2)\right)v + \frac{\nu_E}{\rho}\frac{\partial p}{\partial x} = 0, \tag{6.3.16}$$

$$\frac{\partial v}{\partial t} + u\frac{\partial v}{\partial x} + v\frac{\partial v}{\partial y} + \left(2\tilde{\Omega} + \tilde{\delta}(x^2+y^2)\right)u + \frac{\nu_E}{\rho}\frac{\partial p}{\partial y} = 0. \tag{6.3.17}$$

Thus using the spectral representations of the velocity components (6.3.9) and (6.3.10) gives

$$\frac{\partial u}{\partial t} = \sum_{m=1}^{\infty}\sum_{n=1}^{\infty} A'_{mn}(t)F_m(x)G_n(y) = -F_A(x,y,t), \tag{6.3.18}$$

$$\frac{\partial v}{\partial t} = \sum_{m=1}^{\infty}\sum_{n=1}^{\infty} B'_{mn}(t)F_m(x)G_n(y) = -F_B(x,y,t), \tag{6.3.19}$$

where

$$F_A(x,y,t) = u\frac{\partial u}{\partial x} + v\frac{\partial u}{\partial y} - \left(2\tilde{\Omega} + \tilde{\delta}(x^2+y^2)\right)v + \frac{\nu_E}{\rho}\frac{\partial p}{\partial x}, \tag{6.3.20}$$

$$F_B(x,y,t) = u\frac{\partial v}{\partial x} + v\frac{\partial v}{\partial y} + \left(2\tilde{\Omega} + \tilde{\delta}(x^2+y^2)\right)u + \frac{\nu_E}{\rho}\frac{\partial p}{\partial y}. \tag{6.3.21}$$

The functions $F_A(x,y,t)$ and $F_B(x,y,t)$ represent the spatial terms in the momentum equations (6.3.16) and (6.3.17) respectively. Decomposing spectrally results in the significantly simpler forms of the equations

$$A'_{kl}(t) = \frac{-1}{\lambda\omega}\int_{-\lambda}^{\lambda}\int_{-\omega}^{\omega} F_A(x,y,t)F_k(x)G_l(y)\,dydx$$
$$\text{for } k = 1,2,....,M, \text{ and } l = 1,2,....,N, \tag{6.3.22}$$

$$B'_{kl}(t) = \frac{-1}{\lambda\omega}\int_{-\lambda}^{\lambda}\int_{-\omega}^{\omega} F_B(x,y,t)F_k(x)G_l(y)\,dydx$$
$$\text{for } k = 1,2,....,M, \text{ and } l = 1,2,....,N, \tag{6.3.23}$$

These simpler forms of the momentum equations involve solely the desired differentiated coefficients on their left-hand sides. By contrast, equations (4.2.17) and (4.2.18) used for the finger structure simulations and equations (5.2.37) and (5.2.38) for the binary interaction problems gave coupled systems involving both sets of the coefficients $A_{mn}(t)$ ($A_{kl}(t)$) and $B_{mn}(t)$ ($B_{kl}(t)$) simultaneously.

6.3.2 Robin Conditions

Following on from the results in simulating interacting vortices, it was originally thought that the best approach for simulating the interaction of a large polar vortex in the form of a low-pressure system with at least one, albeit, considerably smaller radius perturbing anti-cyclone was to use Robin boundary conditions to absorb the false reflections off the boundary of the δ-plane. The boundary conditions are given by (5.2.17) and the equations (5.2.28) and (5.2.29) are the required basis functions $F_m(x)$ and $G_n(y)$ that satisfy the boundary conditions. The evaluations of the Fourier coefficients $R_{mn}(t)$, $T_{mn}(t)$ and $P_{mn}(t)$ are identical to those outlined in Chapter 5 and are respectively given by (5.2.34), (5.2.39) and (5.2.40). However, isolating the time-dependent and

spatially varying terms makes the matrix equations for the Fourier coefficients $A_{mn}(t)$ and $B_{mn}(t)$ less complicated than the associated equations (5.2.37) and (5.2.38) for the interacting vortex problem. The matrix equations are

$$\sum_{m=1}^{M}\sum_{n=1}^{N}\mathbf{Q}_{klmn}A'_{mn}(t) = -\int_{-\lambda}^{\lambda}\int_{-\omega}^{\omega}F_A(x,y,t)F_k(x)G_l(y)\,dydx, \tag{6.3.24}$$

$$\sum_{m=1}^{M}\sum_{n=1}^{N}\mathbf{Q}_{klmn}B'_{mn}(t) = -\int_{-\lambda}^{\lambda}\int_{-\omega}^{\omega}F_B(x,y,t)F_k(x)G_l(y)\,dydx, \tag{6.3.25}$$

where $\mathbf{Q}_{klmn}$, $F_A(x,y,t)$ and $F_B(x,y,t)$ are defined by (5.2.35), (6.3.20) and (6.3.21), respectively. The equations (6.3.24) and (6.3.25) are solved in a similar manner to equation (5.2.34).

6.4 Initial Conditions

The Saturn model used here requires the atmosphere to be initially isopycnal with constant dimensionless density represented by equation (6.1.7). This is simply achieved by setting $R_{mn}(0) = 0$ in equation (6.3.7). A direct consequence of the initial isopycnal atmosphere is that the initial pressure and temperature are identical and take the form

$$p(x,y,0) = 1 + H(x,y) = T(x,y,0), \tag{6.4.1}$$

where $H(x,y)$ is conveniently defined as a slightly modified sum of the background and perturbation components for the pressure and temperature. When both the eastward and westward jets together with two perturbing anti-cyclones are included in the initial flow the function $H(x,y)$ takes the form

$$\begin{aligned}H(x,y) = {}& \frac{C_0}{\nu_E}\int_0^{\xi} rf\exp\left[-C_1\,(r-1.4)^2\right]dr - \frac{C_2}{\nu_E}\int_0^{\xi} rf\exp\left[-C_3\,(r-2.1)^2\right]dr \\ & + \mu_1\exp\left[\frac{-((x-M)^2+(y-M)^2)}{\sigma_1^2}\right] + \mu_2\exp\left[\frac{-((x+M)^2+(y+M)^2)}{\sigma_2^2}\right] + \mathcal{S}.\end{aligned} \tag{6.4.2}$$

If both jets and only one perturbation is of interest then $H(x,y)$ is given by

$$\begin{aligned}H(x,y) = {}& \frac{C_0}{\nu_E}\int_0^{\xi} rf\exp\left[-C_1\,(r-1.4)^2\right]dr - \frac{C_2}{\nu_E}\int_0^{\xi} rf\exp\left[-C_3\,(r-2.1)^2\right]dr \\ & + \mu\exp\left[\frac{-((x-M)^2+(y-M)^2)}{\sigma^2}\right] + C.\end{aligned} \tag{6.4.3}$$

Without perturbations included the function $H(x, y)$ is simply given by the background components for the pressure and temperature. For both jets this is

$$H(x,y) = \frac{C_0}{\nu_E}\int_0^{\xi} rf\exp\left[-C_1\,(r-1.4)^2\right]dr - \frac{C_2}{\nu_E}\int_0^{\xi} rf\exp\left[-C_3\,(r-2.1)^2\right]dr + \mathcal{K}, \tag{6.4.4}$$

and for the single dominant eastward flow

$$H(x,y) = \frac{C_0}{\nu_E}\int_0^{\xi} rf\exp\left[-C_1\,(r-1.4)^2\right]dr + \mathcal{D}. \tag{6.4.5}$$

In the four definitions of $H(x, y)$ given by equations (6.4.2) – (6.4.5), $\mathcal{S}$, C, $\mathcal{K}$ and $\mathcal{D}$ are constants that make $H(x, y) = 0$ on the boundaries of the δ-plane. The velocity components are essentially geostrophic initially and therefore

$$u(x,y,0) = -\frac{\nu_E}{f\rho(x,y,0)}\frac{\partial p(x,y,0)}{\partial y}, \tag{6.4.6}$$

$$v(x,y,0) = \frac{\nu_E}{f\rho(x,y,0)}\frac{\partial p(x,y,0)}{\partial x}. \tag{6.4.7}$$

The equations (6.4.6) and (6.4.7) are further simplified by substituting the initial density condition (6.1.7) and the initial pressure function (6.4.1) resulting in

$$u(x,y,0) = -\frac{\nu_E}{f}\frac{\partial H(x,y)}{\partial y}, \tag{6.4.8}$$

$$v(x,y,0) = \frac{\nu_E}{f}\frac{\partial H(x,y)}{\partial x}. \tag{6.4.9}$$

The equations for the remaining initial Fourier coefficients $A_{mn}(0)$, $B_{mn}(0)$, $P_{mn}(0)$ and $T_{mn}(0)$ are determined through spectral decomposition, and their form changes depending on the type of boundary conditions used.

6.4.1 Initial Conditions for Dirichlet Boundary Problem

The initial Fourier coefficients $P_{mn}(0)$ and $T_{mn}(0)$ for the pressure and temperature are determined by considering the respective equations (6.3.6) and (6.3.8) at time $t = 0$ in conjunction with (6.4.1) so that

$$p(x,y,0) = 1 + \sum_{m=1}^{\infty}\sum_{n=1}^{\infty} P_{mn}(0)\,F_m(x)\,G_n(y) = 1 + H(x,y) = T(x,y,0), \tag{6.4.10}$$

in which, for the pressure variable,

$$H(x,y) = \sum_{m=1}^{\infty}\sum_{n=1}^{\infty} P_{mn}(0)\,F_m(x)\,G_n(y). \tag{6.4.11}$$

The basis functions $F_m(x)$, $G_n(y)$ given by equation (6.3.12) are purely sinusoidal in the Dirichlet problem and thus multiplying equation (6.4.11) by similar basis functions $F_k(x)$,$G_l(y)$ and integrating over the δ-plane region gives

$$P_{kl}(0) = \frac{1}{\lambda\omega}\int_{-\lambda}^{\lambda}\int_{-\omega}^{\omega} H(x,y)\,F_k(x)\,G_l(y)\,dydx. \tag{6.4.12}$$

As a consequence of the initial pressure and temperature having the same form (6.4.1), the initial Fourier coefficients for the temperature are

$$T_{kl}(0) = \frac{1}{\lambda\omega}\int_{-\lambda}^{\lambda}\int_{-\omega}^{\omega} H(x,y)\,F_k(x)\,G_l(y)\,dydx. \tag{6.4.13}$$

The initial Fourier coefficients for the velocity components $A_{mn}(0)$ and $B_{mn}(0)$ are similarly found by replacing the function $H(x,y)$ in the integrand of (6.4.12) with (6.4.8) and (6.4.9) respectively to give

$$A_{kl}(0) = \frac{1}{\lambda\omega}\int_{-\lambda}^{\lambda}\int_{-\omega}^{\omega} u(x,y,0)\,F_k(x)\,G_l(y)\,dydx, \tag{6.4.14}$$

$$B_{kl}(0) = \frac{1}{\lambda\omega}\int_{-\lambda}^{\lambda}\int_{-\omega}^{\omega} v(x,y,0)\,F_k(x)\,G_l(y)\,dydx. \tag{6.4.15}$$

6.4.2 Initial Conditions for Robin Boundary Problem

The basis functions used in the Robin boundary value problem are given by equations (5.2.28) and (5.2.29). In contrast to the Dirichlet problem these basis functions are not orthogonal and therefore the initial conditions for this specific boundary value problem are determined by solving a matrix equation of the general form

$$\sum_{m=1}^{M}\sum_{n=1}^{N} \mathbf{Q}_{klmn} S_{mn}(0) = \int_{-\lambda}^{\lambda}\int_{-\omega}^{\omega} S(x,y,0)\,F_k(x)\,G_l(y)\,dydx, \tag{6.4.16}$$

where $\mathbf{Q}_{klmn}$ is defined by (5.2.35), $S_{mn}(0)$ represents the initial Fourier coefficients to be determined and the function $S(x,y,0)$ is a function that defines the initial form of the variable to be solved. Table 6.2 shows what functions are needed to be substituted into the general form matrix equation (6.4.16) to determine the specific initial conditions for each of the time dependent variables pressure p, temperature T and velocity components u and v. There are four choices for the function $H(x,y)$ which are dependent upon the circumpolar jets and the number of perturbation anti-cyclones, as indicated in section 6.4.

Matrix equation inputs for initial Fourier coefficients		
Variable	Fourier coefficient $S_{mn}(0)$	Initial function $S(x,y,0)$
Pressure, p	$P_{mn}(0)$	$H(x,y)$
Temperature, T	$T_{mn}(0)$	$H(x,y)$
x-Velocity, u	$A_{mn}(0)$	$u(x,y,0)$ given by (6.4.8)
y-Velocity, v	$B_{mn}(0)$	$v(x,y,0)$ given by (6.4.9)

Table 6.2: Shows the corresponding input functions for determining the initial Fourier coefficients using the general matrix equation (6.4.16).

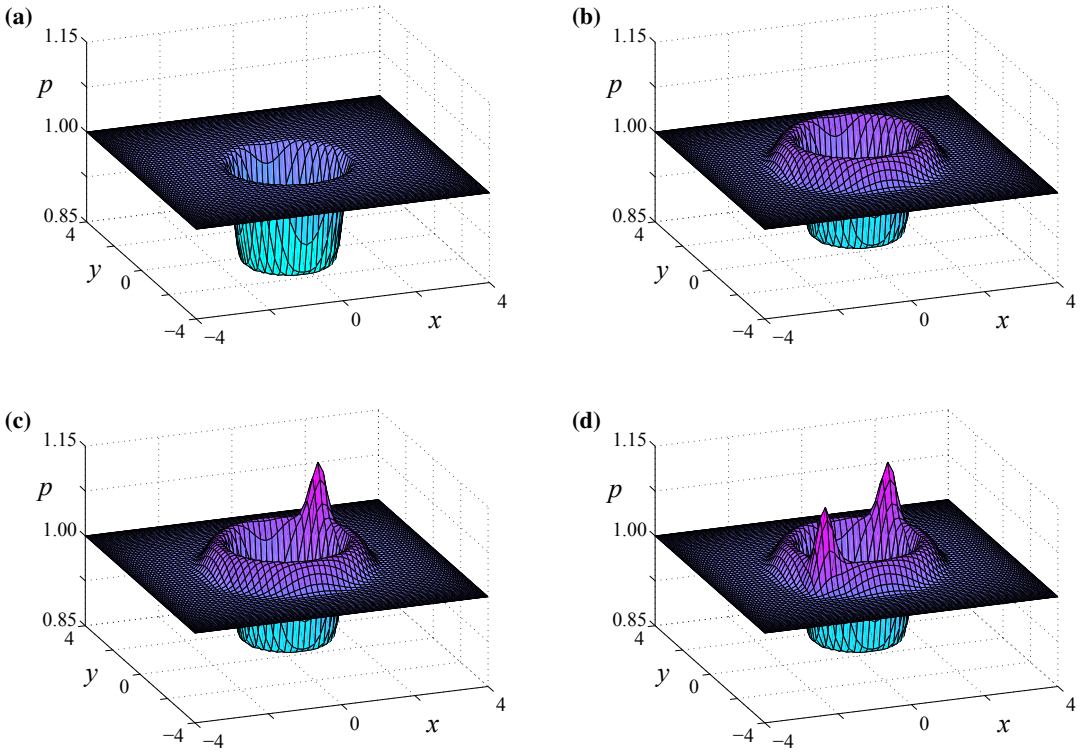

Figure 6.4.1: Sketch of four 3-dimensional initial pressure and temperature profiles for (a) eastward jet, (b) eastward and westward jets, (c) single perturbation and (d) binary perturbation

Figure 6.4.1 gives an indication of the initial pressure (and temperature) variation in the form of three-dimensional surface plots with increasing complexity in the pressure distribution. The pressure surfaces are computed using equation (6.4.1) together with the appropriately defined version of the function $H(x, y)$, either (6.4.2), (6.4.3), (6.4.4) or (6.4.5). The least complex pressure distribution arises when only the predominant eastward jet is part of the initial flow. The pressure surface in this instance is computed using equation (6.4.5) and is shown in Figure 6.4.1(a). The pressure ranges from $p \approx 0.84$ up to $p = 1.00$ on the boundaries. In contrast when the westward jet is also included using equation (6.4.4)), the westerly flow induces regions of high pressure illustrated in Figure 6.4.1(b). The actual pressure differential is exactly the same as in Figure 6.4.1(a); however, the minimum pressure is $p \approx 0.88$ and the maximum pressure is $p \approx 1.04$ with pressure $p = 1$ on the boundaries. Figures 6.4.1(c) and 6.4.1(d) are the respective surface plots when single and binary perturbing anti-cyclones are introduced to the background flow. In both cases the radii of the anti-cyclones are $\sigma_1 = \sigma_2 = \sigma = 0.3$ and the initial eye locations are $(x, y) = (1.4, 1.4)$ for the single perturbation and $(x, y) = \pm(1.4, 1.4)$ for the binary perturbation. The increase in

pressure is $\mu_1 = \mu_2 = \mu = 0.1$ and thus the pressure range in these two figures is up from $p \approx 0.88$ to $p \approx 1.14$. This change in pressure range can be directly attributed to the pressure in the anti-cyclones as the eyes of the perturbations are in close proximity of the centre of the westward flow.

6.5 Presentation of Results

An extension to the interaction behaviour between atmospheric vortices is considered in this section. In particular the formation of polygonal structures that arise due to the interaction of atmospheric polar vortices. Allison et al. [1] proposed that the Hexagonal feature centred at the North pole of Saturn is a Rossby wave which may have been caused by at least one perturbing anti-cyclone to the south. This section will outline whether or not it is possible for such a feature to be formed by an anti-cyclone impinging on the southern boundary of a larger cyclone. The majority of the results outlined in this section will be presented in the form of pressure contour charts. Solutions are given for both single and binary anti-cyclonic perturbations. The variation in the location, radius and pressure differential of the perturbing anti-cyclones will also be considered.

The pressure scale is $p_0 = \rho_0 R T_0 = 1$ bar $= 10^5$ Pa. At this pressure the Saturnian atmosphere has a temperature of approximately 134° K [75] and so the scale temperature $T_0 = 134°$ K and scale density of $\rho_0 = 0.186$ kg m^{-3} will be assumed. The dimensionless half-plane width and breadth are $\lambda = \omega = 6$, so that the δ-plane region is $-6 \leq x \leq 6$, $-6 \leq y \leq 6$. Again these values are chosen so that there is ample space between the actual flow of interest and the location of the artificial boundaries. In the results that follow the important flow features are more or less bounded by the region $-\frac{5}{2} < x < \frac{5}{2}$, $-\frac{5}{2} < y < \frac{5}{2}$ where there is much less than 1% difference between true Coriolis parameter value given by (3.2.1) and the associated δ-plane value (3.2.11) as the discussion about Figure 3.2.4 can attest.

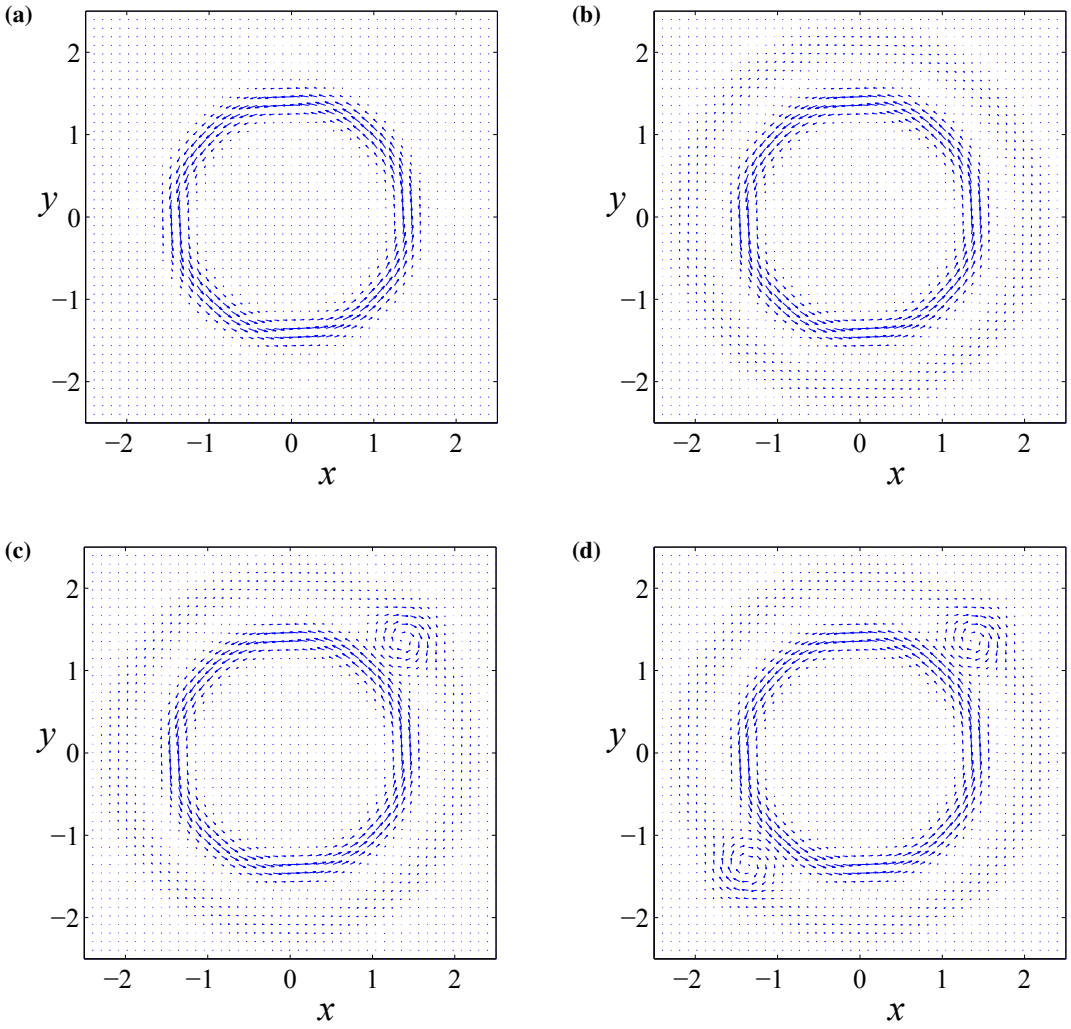

Figure 6.5.1: Quiver plots of the background velocity for the (a) eastward jet, (b) eastward and westward jets, (c) single perturbation and (d) binary perturbation.

The background flow will be perturbed with either a single anti-cyclone or a binary anti-cyclone system as given in the respective equations (6.2.1) and (6.2.2). The initial eye locations of the perturbing system(s) will be $(x, y) = (M, M)$ or $(x, y) = \pm(M, M)$, hereafter denoted M. This geometry is chosen so that the possible interference caused by reflections off the artificial boundaries when using spectral methods takes its maximum time to impact on the numerical solution and thus reliable, informative solutions can be obtained. The figures throughout this section will be magnified over a region smaller than the computational domain of $\lambda = \omega = 6$, so that the intricacies of the flow can be more readily shown. This section will attempt to answer the following questions: (1) Is it possible for perturbing anti-cyclones to produce a hexagonal structure over the

pole of Saturn? (2) What influence does the westward flow to the south have on the formation of the hexagon? and (3) What effect does the location, radius and pressure differential have on the formation of the hexagon?

The types of background flow coupled with the perturbation flow have varying degrees of influence on the evolving flow pattern. To get an overall feel for what is happening, quiver plots of the velocity fields induced by the three dimensional pressure surfaces given in Figure 6.4.1 are shown in Figure 6.5.1. The quiver plots are produced using the initial velocity components defined by equations (6.4.8) and (6.4.9) with the corresponding function $H(x, y)$ defined in section 6.4. Figure 6.5.1(a) is confirmation of the velocity components associated with the eastward jet as there is a thin band of anticlockwise directional quivers indicating an easterly current. The slower moving westward flow is illustrated in the quiver diagram of Figure 6.5.1(b) which shows the additional clockwise directional quivers. As expected there is an annulus of stagnation flow between eastward and westward polar jets. The perturbing quiver plots in Figures 6.5.1(c) and 6.5.1(d) clearly show the anti-cyclonic rotation of the high-pressure regions. The perturbing anti-cyclones also interrupt the stagnation ring observed in Figure 6.5.1(b), particularly in this case when the perturbations are in close proximity of the easterly circumpolar jet and thus impinge on the flow.

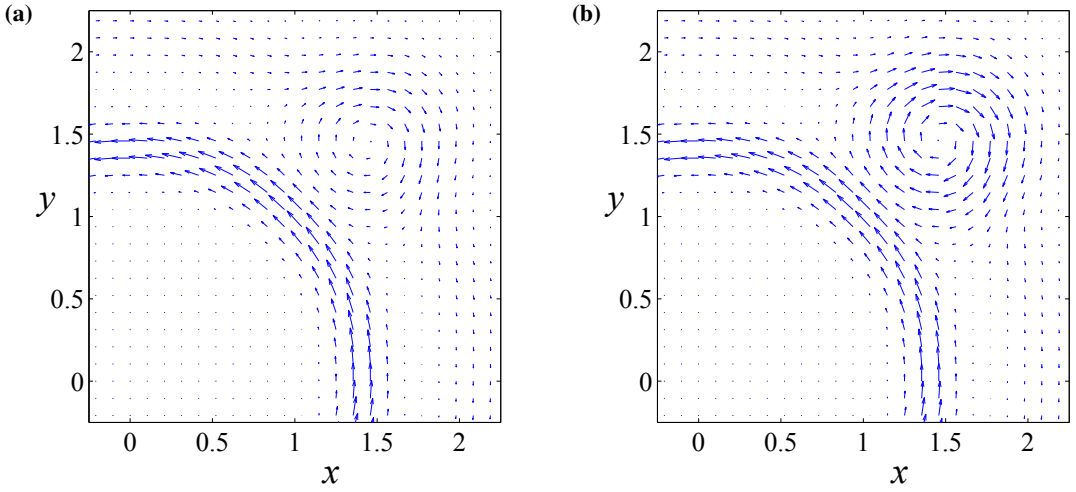

Figure 6.5.2: Quiver plots of the velocity induced by the background flow and a single perturbing anti-cyclone located at $(x, y) = (1.5, 1.5)$ with pressure differential (a) $\mu = 0.1$ and (b) $\mu = 0.2$.

The first published image of the North Polar Hexagon [31] showed that there was at least one

anti-cyclone to the south of the hexagonal structure. In particular it was proposed that the Hexagon may be the result of at least one perturbing anti-cyclone [1]. The key component to this proposal is the observed anti-cyclone impinging on the circumpolar flow and the resulting streamline maps produced by Godfrey [31] which indicate the presence of other anti-cyclonic flow regions, aligned along the edges of the Hexagon, that are not visibly observed. The pressure differential in such an anti-cyclone has a major impact on the flow strength around the eastward jet. Figures 6.5.2(a) and 6.5.2(b) show the quivers of the velocity field for the respective anti-cyclonic pressure differential of $\mu = 0.1$ and $\mu = 0.2$. In these figures the eyes of the anti-cyclones are located at $M = 1.5$ with radius $\sigma = 0.4$, and although generated over the entire computational domain, both figures are cropped so that the flow pattern and strength are emphasized. The larger the pressure differential value μ the more intense the perturbing system as indicated by the large-magnitude quivers in the top right corner of Figure 6.5.2(b). An additional result made clear in these two diagrams is the pin-wheel effect occurring in the interfacial region between the two opposing flow directions. This results in fluid being ejected tangentially towards the top left of the δ-plane.

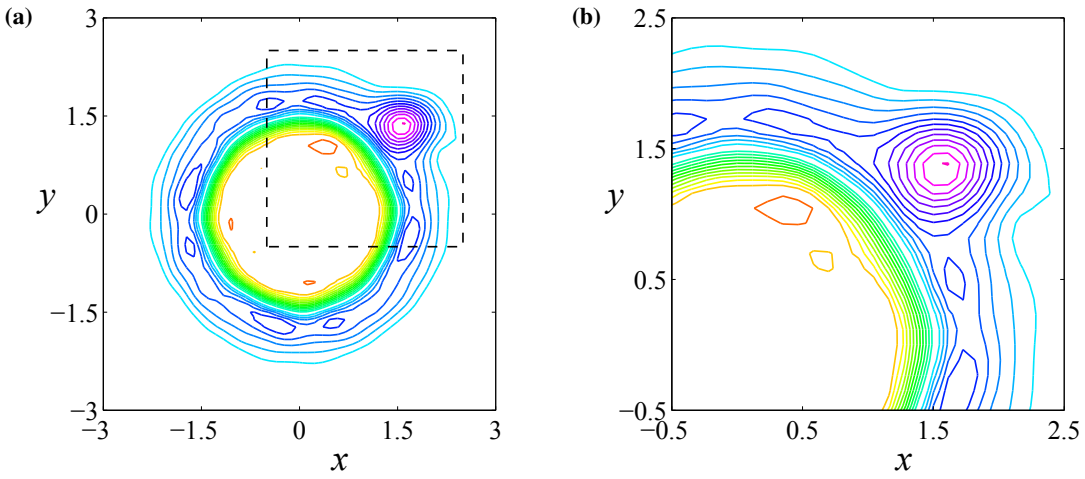

Figure 6.5.3: Pressure contour plots with single anti-cyclone located originally at $M = 1.5$ of radius $\sigma = 0.4$ at time $t = 1.6$ with pressure differential $\mu = 0.1$ plotted over the region (a) $-3 \leq x, y \leq 3$ and (b) $-0.5 \leq x, y \leq 2.5$.

The result of perturbing the underlying circumpolar jets with an anti-cyclone of radius $\sigma = 0.4$ located initially at $M = 1.5$ with $\mu = 0.1$ at time $t = 1.6$ is shown in Figure 6.5.3. This figure shows there is no significant change in the initial circular shape of the pressure system created by the eastward circumpolar current, which can be seen in Figure 6.5.3(a). There is an additional out-

line over the region bounded by $-0.5 \leq x, y \leq 2.5$ that encompasses the perturbing anti-cyclone. This highlighted region is shown in Figure 6.5.3(b) and indicates that an anti-cyclone of strength $\mu = 0.1$ at this location has little influence over the general flow of the circumpolar jet.

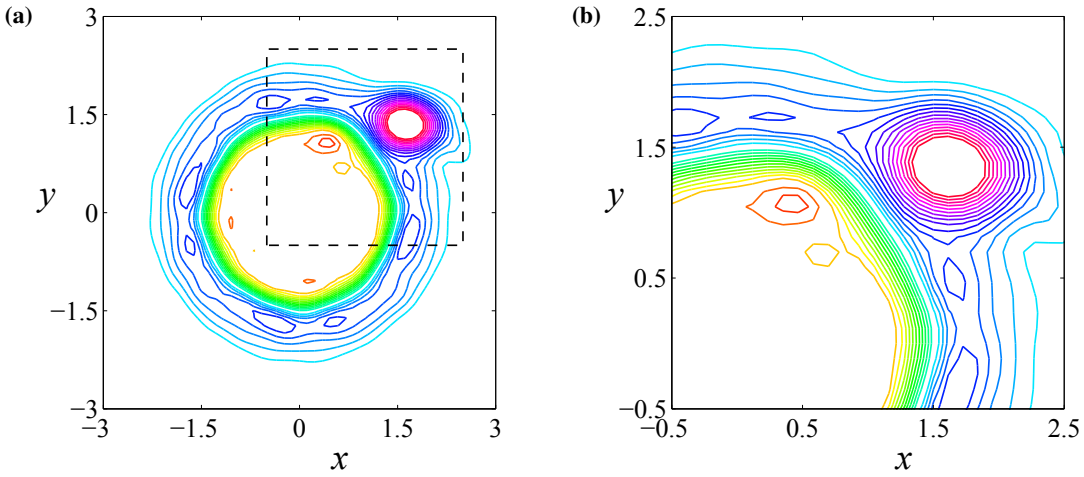

Figure 6.5.4: Pressure contour plots with single anti-cyclone located originally at $M = 1.5$ of radius $\sigma = 0.4$ at time $t = 1.6$ with pressure differential $\mu = 0.2$ plotted over the region (a) $-3 \leq x, y \leq 3$ and (b) $-0.5 \leq x, y \leq 2.5$.

Figure 6.5.4 shows the effect a single perturbing anti-cyclone with similar parameters used in Figure 6.5.3, except now the strength of the anti-cyclone has been increased to $\mu = 0.2$. This figure shows evidence of the anti-cyclone influencing the flow, in particular, the creation of a straight edge between the two opposing systems. Furthermore, there are two rounded vertices, one at each end of the edge, forming what could be interpreted as the beginning of a hexagonal portion of a trapezoid; this is best depicted in Figure 6.5.4(b) which shows a more detailed view of the highlighted box in Figure 6.5.4(a). The rounded vertices that are beginning to form may be the result of the pin-wheeling effect being overtaken by the effect of the circumpolar jets. The simulations using one anti-cyclone failed to produce a hexagonal feature, but instead, generated a circular-shaped region with one flattened side, as shown in Figure 6.5.4(a).

It must be reiterated here that Allison et al. [1] proposed that the Hexagon may be the result of at least one perturbing anti-cyclone. If one perturbing anti-cyclone could produce a trapezoid type structure as indicated in Figure 6.5.4, then two symmetrically placed anti-cyclones may just produce what is proposed.

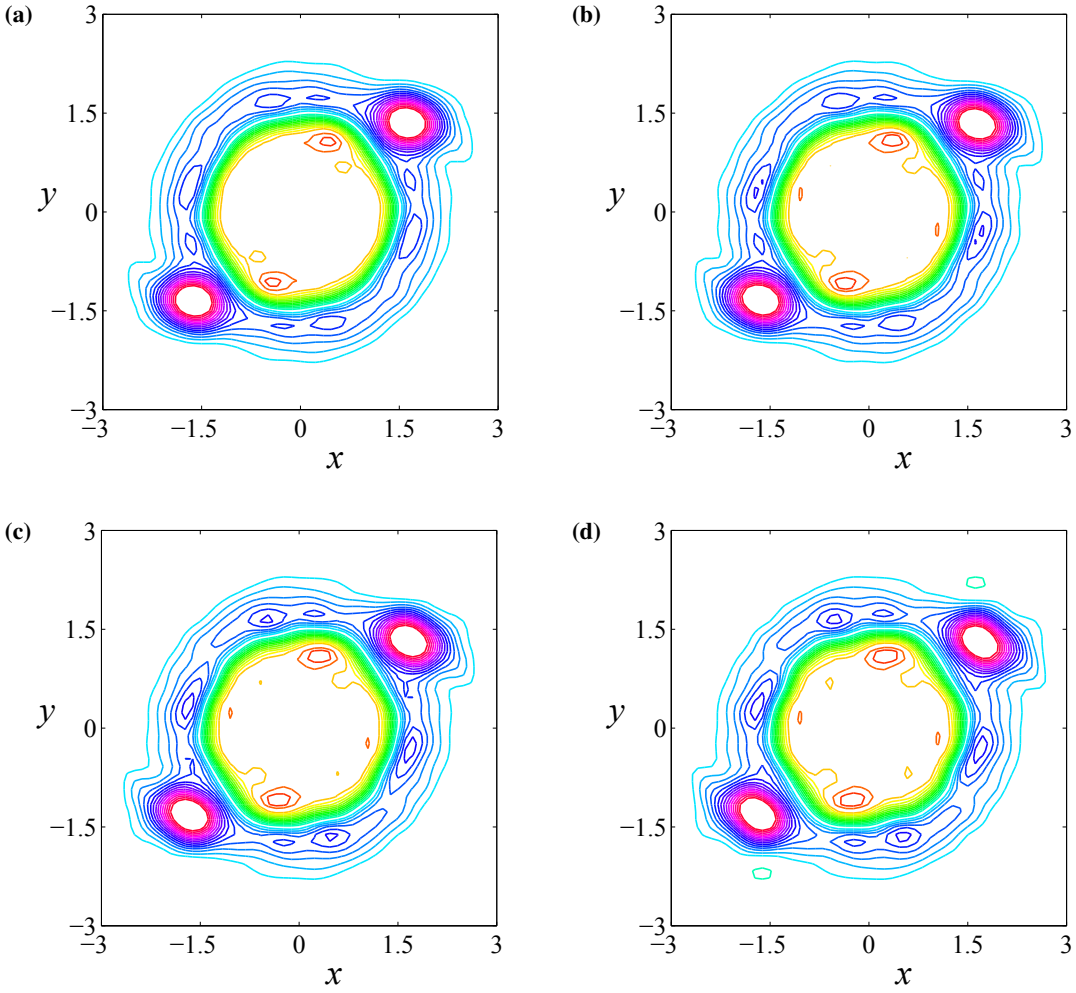

Figure 6.5.5: Pressure contour plots with two perturbing anti-cyclones located originally at $M = 1.5$ of radius $\sigma = 0.4$ with pressure differential $\mu = 0.2$ at times (a) $t = 1.6$, (b) $t = 1.8$, (c) $t = 2.0$ and (d) $t = 2.2$.

Figure 6.5.5 is a time lapse illustration of the influence two perturbing anti-cyclones have on the pressure structure over the polar region. The pair of anti-cyclones is modelled using equation (6.2.2). The initial placement of the anti-cyclones is $M = 1.5$ with $\sigma = 0.4$ and $\mu_1 = \mu_2 = 0.2$. Hereafter, if the pressure change is equal in both anti-cyclones ($\mu_1 = \mu_2$), then the pressure change will be expressed as μ alone. For the single perturbing anti-cyclone with the same characteristics as the pair in Figure 6.5.5, the trapezoidal formation was first observed at time $t = 1.6$. Thus, Figure 6.5.5(a) shows the contour map of the binary perturbation at the same time $t = 1.6$. At this time the hexagonal structure can already be seen. Figures 6.5.5(b) – 6.5.5(d) show the evolution of the pressure at the times $t = 1.8$, 2.0 and 2.2, respectively. As the time increases to $t = 2.0$ the

hexagon is at its most regular. Although the feature is still prominent at the later time $t = 2.2$, there are ripples forming along the edges non-adjacent to the anti-cyclones. At time $t = 3.0$, the hexagonal structure is still evident; however, there are clear indentations along the edges to the west of the anti-cyclones indicating the structure is beginning to collapse. This is shown in Figure 6.5.6. Due to the short lifespan of the hexagonal structures, it is hard to determine for how long the hexagon is approximately stationary. If it is stationary over the approximate dimensionless time $1.6 < t < 4.0$, this would correspond to a time interval of approximately 3 days. This is not the case for the perturbing anti-cyclones; the location of the anti-cyclones is within the westward jet and thus there is clear movement to their west.

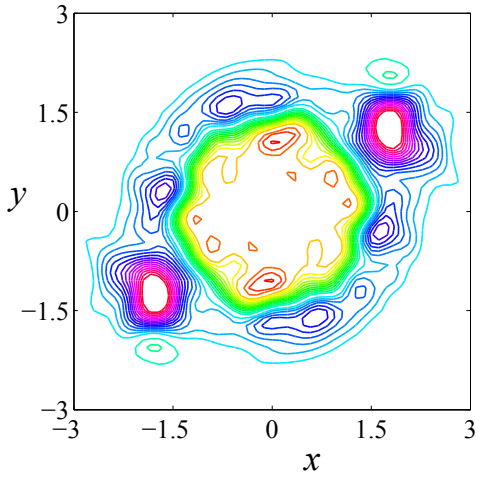

Figure 6.5.6: Pressure contour plot with two perturbing anti-cyclones located originally at $M = 1.5$ of radius $\sigma = 0.4$ with pressure differential $\mu = 0.2$ at time $t = 3.0$.

It is interesting to note the closed elliptical contours aligned centrally along the outer edges of the hexagonal structure. These are isolated regions of higher pressure in the form of smaller, less intense anti-cyclones, which is consistent with what Godfrey [31] observed through streamline maps.

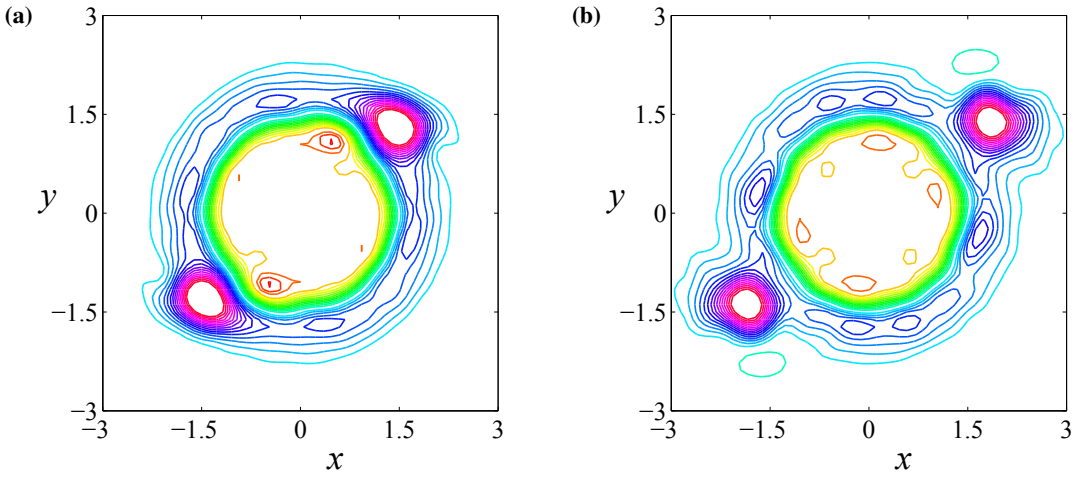

Figure 6.5.7: Pressure contour plots with two perturbing anti-cyclones of radius $\sigma = 0.4$ for (a) $M = 1.4$, $t = 1.2$ and (b) $M = 1.6$, $t = 2.4$.

It has now been shown that a hexagonal feature, although transient, can be formed through anti-cyclones impinging on the southern boundary of a circumpolar jet and thus the results shown in Figure 6.5.5 can be used as a baseline to determine the effects that the southern westward current, initial location M, radius σ and pressure differential μ have on the development of a hexagonal structure. The location of the initial anti-cyclones needs to be within a close enough proximity to influence the flow associated with the eastward jet. Moving the location of the anti-cyclones closer to the jet so that $M = 1.4$ and keeping all other baseline parameters identical, inhibits the formation of the furthest vertex from the anti-cyclones. This is depicted in Figure 6.5.7(a) and shows the most regular hexagonal type feature that occurred with $M = 1.4$. As would be expected, the hexagonal type structure formed at the earlier time of $t = 1.2$ compared to the baseline time of $t = 2.0$. Although there is a hexagonal structure, it is less defined than that of Figure 6.5.5. Conversely moving the initial eye out to $M = 1.6$ a hexagonal structure is never formed. However, there is a slight vertex being formed to the west of each anti-cyclone which may be the result of the pin-wheel effect; this is shown in Figure 6.5.7(b) at the later time $t = 2.4$.

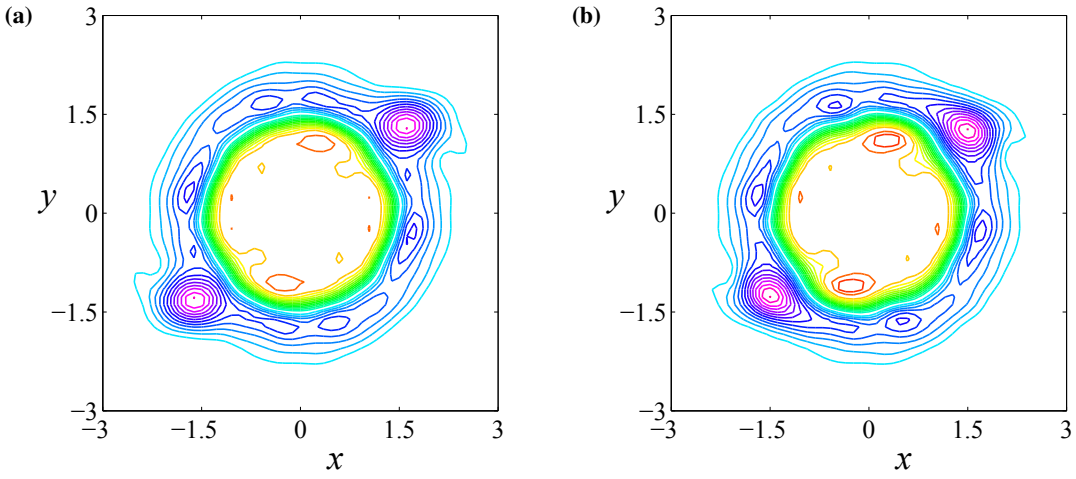

Figure 6.5.8: Pressure contour plots with two perturbing anti-cyclones of radius $\sigma = 0.4$, pressure differential $\mu = 0.1$ at time $t = 2.0$ for location (a) $M = 1.5$ and (b) $M = 1.4$.

Decreasing the magnitude of the pressure differential plays a significant role in the formation of a hexagonal structure. Figure 6.5.8(a) is the contour diagram at time $t = 2.0$ using the baseline parameters except that the pressure differential is now $\mu = 0.1$. At this time there is no identifiable hexagonal formation developing, whereas for the baseline simulation with $\mu = 0.2$ the hexagon was at its most regular. However, with this decrease in pressure differential a hexagon is produced at time $t = 2.0$ when the anti-cyclones are initially closer to the easterly jet. This is illustrated in Figure 6.5.8(b) which has $\mu = 0.1$ and $M = 1.4$. The closer location using $M = 1.4$ has enabled the less-intense anti-cyclone to influence the flow within the eastward jet.

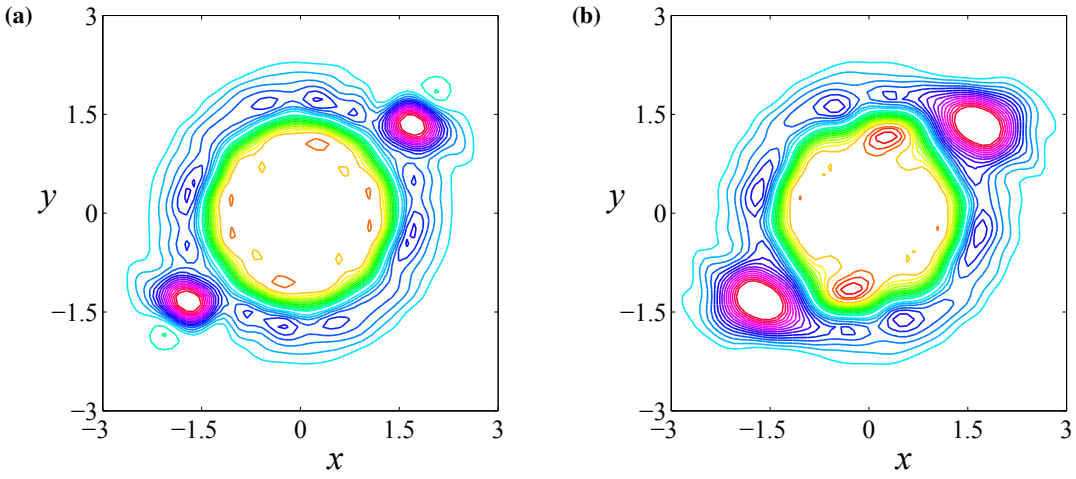

Figure 6.5.9: Pressure contour plots with two perturbing anti-cyclones located originally at $M = 1.5$ with pressure differential $\mu = 0.2$ at time $t = 2.0$, for radius (a) $\sigma = 0.3$ and (b) $\sigma = 0.5$.

It was shown previously in Chapter 5 that if the pressure differential μ is unchanged, the smaller the radius of the pressure system, the greater the internal flow velocity (refer to Figure 5.4.1). Figure 6.5.9 shows the effect of changing the radius of the anti-cyclones as compared to the baseline simulation. The respective pressure contour plots at time $t = 2.0$ with smaller radius $\sigma = 0.3$ and larger radius $\sigma = 0.5$ are shown in Figures 6.5.9(a) and 6.5.9(b). There is no indication of a hexagon being formed when $\sigma = 0.3$. This can be attributed to the fact that the anti-cyclones are sufficiently separated from the eastward jet, so that the greater internal velocity has no influence on the overall polar flow. The converse is true when the radius is $\sigma = 0.5$. The internal velocities are smaller in this case compared to when the radius is $\sigma = 0.3$, but due to the initial location being identical, the larger radius anti-cyclones have impact on the polar flow, and thus on the deformed hexagonal structure. For the larger radius $\sigma = 0.5$, the hexagonal feature was most regular at time $t = 1.5$.

Morales et al. [55] showed that stable polygons can be formed by 'vortex streets' with cyclonic and anti-cyclonic vortices aligning themselves on the pole and equator sides of the eastward circumpolar jet, respectively. However, they suggest that the vortex street model and the observed wind profile are incompatible. The governing equations used throughout these simulations are not formulated in terms of potential vorticity. However, as a bi-product of calculating the velocity components forward in time, the vorticity can be determined at any given time. Vorticity is a way to describe the local rotation of a fluid and is simply given by

$$\zeta = \frac{\partial v}{\partial x} - \frac{\partial u}{\partial y}. \tag{6.5.1}$$

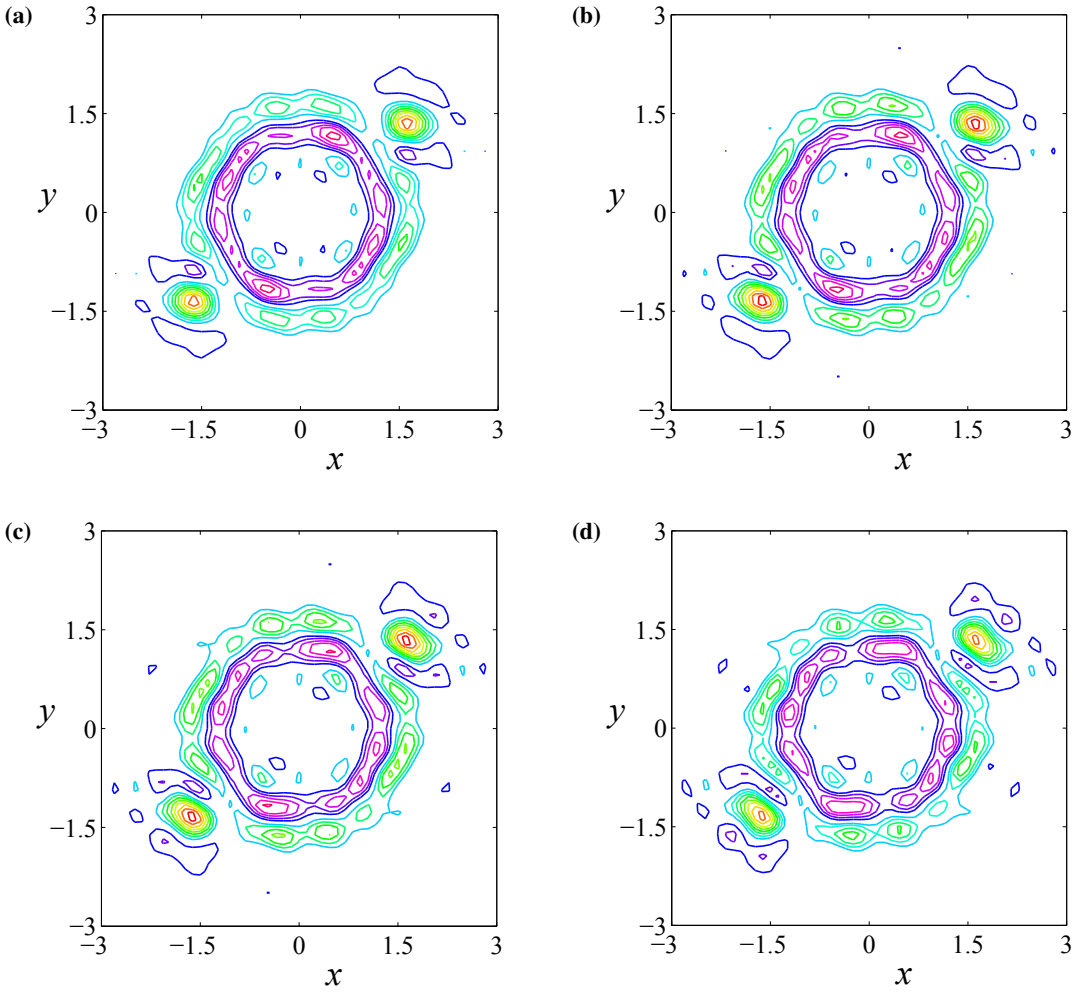

Figure 6.5.10: Vorticity contour plots with two perturbing anti-cyclones located originally at $M = 1.5$ of radius $\sigma = 0.4$ with pressure differential $\mu = 0.2$ at times (a) $t = 1.6$, (b) $t = 1.8$, (c) $t = 2.0$ and (d) $t = 2.2$.

The contour plots shown in Figure 6.5.10 are of the local vorticity of the baseline perturbing system in Figure 6.5.5. The vorticity (6.5.1) is computed by direct differentiation of the Fourier series (6.3.9), (6.3.10) at the desired time. As expected the perturbing anti-cyclones have negative vorticity, in the interval $-9 < \zeta < -1$, and the inner hexagonal region is the perturbed northern most section of the eastward jet and has positive vorticity ranging over $1 < \zeta < 5$. For the outer regions of the δ-plane, where the quiver plots indicate that there is negligible flow, the vorticity is similarly zero. There is remarkable agreement in the shape of the vorticity contours to those of the

pressure contours at the same times.

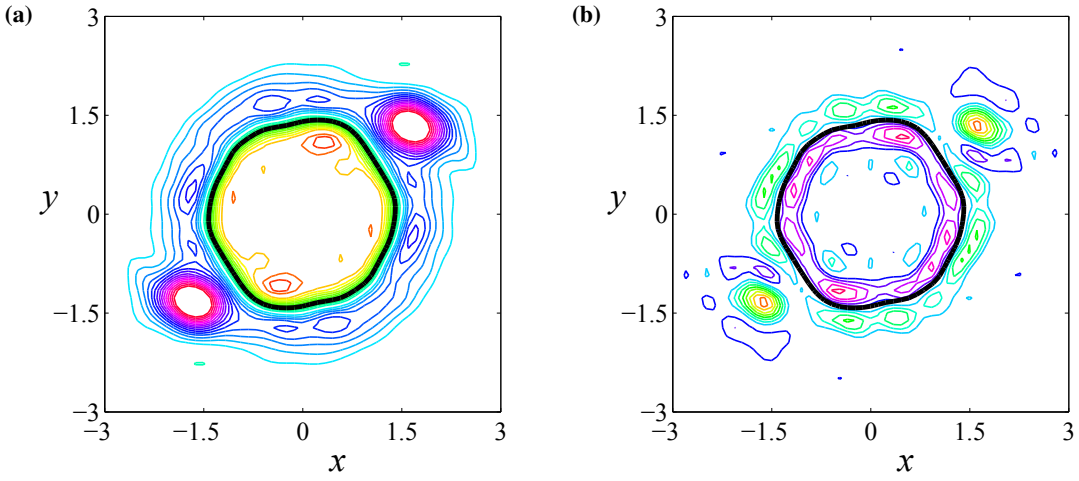

Figure 6.5.11: Contour plots with two perturbing anti-cyclones located originally at $M = 1.5$ of radius $\sigma = 0.4$ with pressure differential $\mu = 0.2$ at time $t = 1.9$ for (a) Pressure and (b) Vorticity. The thick black lines indicate the interfacial pressure contour $p = 0.96$.

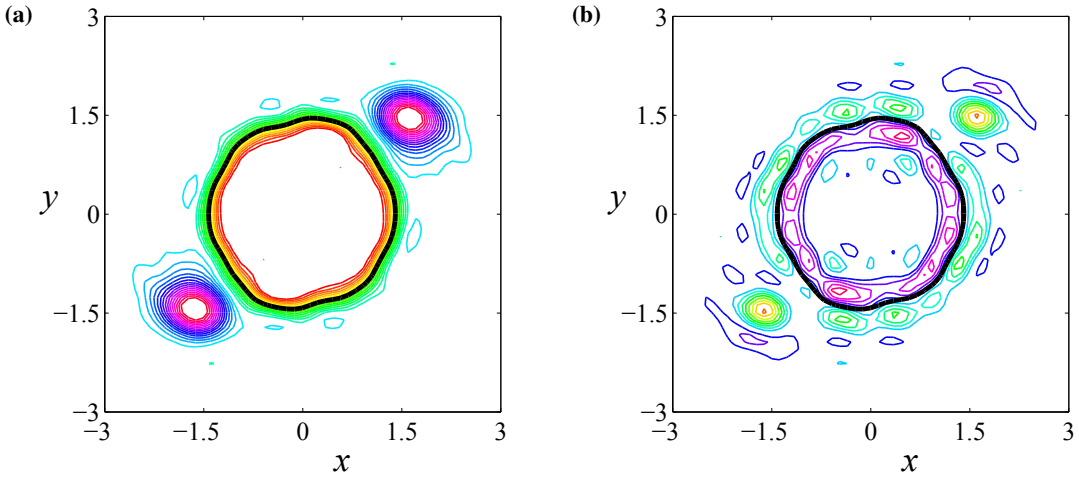

Figure 6.5.12: Eastward circumpolar current contour plots with two perturbing anti-cyclones located originally at $M = 1.5$ of radius $\sigma = 0.4$ with pressure differential $\mu = 0.2$ at time $t = 1.9$ for (a) Pressure and (b) Vorticity. The thick black lines indicate the interfacial pressure contour $p = 0.96$.

It was shown in Figure 6.4.1(b) that the unforced circumpolar jets have pressure ranging from $p = 0.88$ to $p = 1.04$. The intermediate pressure value $p = 0.96$ is a good indicator of the crossover from positive to negative vorticity regions, as well as the defining pressure contour of

the hexagonal structure. This fact is confirmed in Figure 6.5.11 and shows the pressure and vorticity contours in the respective subfigures (a) and (b) at time $t = 0.19$ for the baseline configuration $M = 1.5$, $\sigma = 0.4$ and $\mu = 0.2$, combined with the interfacial pressure contour $p = 0.96$ in black.

Figure 6.5.11 is an ideal comparative configuration to show the effect the westward current has not only on the polar flow but on the hexagonal formations. Figures 6.5.12(a) and 6.5.12(b) show the respective pressure and vorticity contours at time $t = 1.9$ for the baseline parameters with no westward background flow. Recall that Figure 6.4.1(a) showed the three-dimensional structure of the initial pressure induced solely by the eastward circumpolar jet with pressure in the range $0.84 < p < 1.00$. Similar to Figure 6.5.11, the thick black line shown in Figure 6.5.12 is the interfacial pressure contour; however, due to the circumpolar current only flowing in an easterly direction, the value of the interfacial pressure is now $p = 0.92$. This interfacial pressure contour is the defining boundary between positive and negative vorticity regions (Figure 6.4.1(b)) as well as the hexagonal feature (Figure 6.4.1(a)). A direct comparison of the interfacial contours shown in Figures 6.5.11 and 6.5.12 suggests that the westward flow has minimal effect over the formation of a hexagonal structure; nonetheless, it does seem to help develop a more defined edge to the east of the anti-cyclones and a more pointed vertex to the west of the perturbing anti-cyclones. The better defined vertex to the west can possibly be attributed to the fact that the westward circumpolar jet helps push the anti-cyclones further west than the purely easterly flow.

In trying to keep the simulations aligned with what was first observed by Godfrey [31], the parameter space for the single perturbing anti-cyclone was kept to eye locations $M \in [1.4, 1.5]$ and radii $\sigma = 0.3$ and $\sigma = 0.4$. It was evident from these simulations that a hexagonal structure was unlikely to be formed. However, the results obtained from the single anti-cyclone simulations indicated that it may be possible for a hexagonal feature to be formed by introducing a second symmetrically place anti-cyclone. Table 6.3 shows a list of all the space parameters investigated in this thesis for two perturbing anti-cyclones, the asterisk indicates that a single anti-cyclone perturbation was also simulated. The fourth column of Table 6.3 gives the lifespan of hexagonal structures that resulted. The lifespan of a hexagonal feature is the approximate time range from formation to dissipation.

Parameter models simulated			
Eye location (M)	Anti-cyclone radii (σ)	Pressure differential (μ)	Lifespan
1.3	0.3	0.1	$1.6 \leq t \leq 1.8$
1.3	0.3	0.2	
1.3	0.4	0.05	$2.0 \leq t \leq 2.3$
1.3	0.4	0.1	
1.3	0.4	0.2	
1.4*	0.3*	0.1*	
1.4*	0.3*	0.2*	$1.5 \leq t \leq 1.7$
1.4*	0.3*	0.3*	
1.4*	0.4*	0.1*	$1.4 \leq t \leq 2.2$
1.4*	0.4*	0.15*	$1.2 \leq t \leq 1.7$
1.4*	0.4*	0.2*	$1.0 \leq t \leq 1.4$
1.45*	0.4*	0.1*	$1.7 \leq t \leq 2.2$
1.45*	0.4*	0.2*	$1.1 \leq t \leq 1.8$
1.5*	0.3*	0.1*	
1.5*	0.3*	0.2*	
1.5*	0.4*	0.1*	
1.5*	0.4*	0.2*	$1.4 \leq t \leq 3.0$
1.5*	0.4*	0.3	
1.5	0.5	0.2	$1.2 \leq t \leq 1.8$
1.6	0.4	0.1	
1.6	0.4	0.2	
1.6	0.4	0.3	
1.6	0.5	0.1	
1.6	0.5	0.2	$1.4 \leq t \leq 2.3$
1.7	0.6	0.1	
1.7	0.6	0.2	$1.4 \leq t \leq 2.1$

Table 6.3: Shows all combinations of the simulation parameters considered in this thesis. The asterisks indicate that a single anti-cyclone perturbation was also simulated.

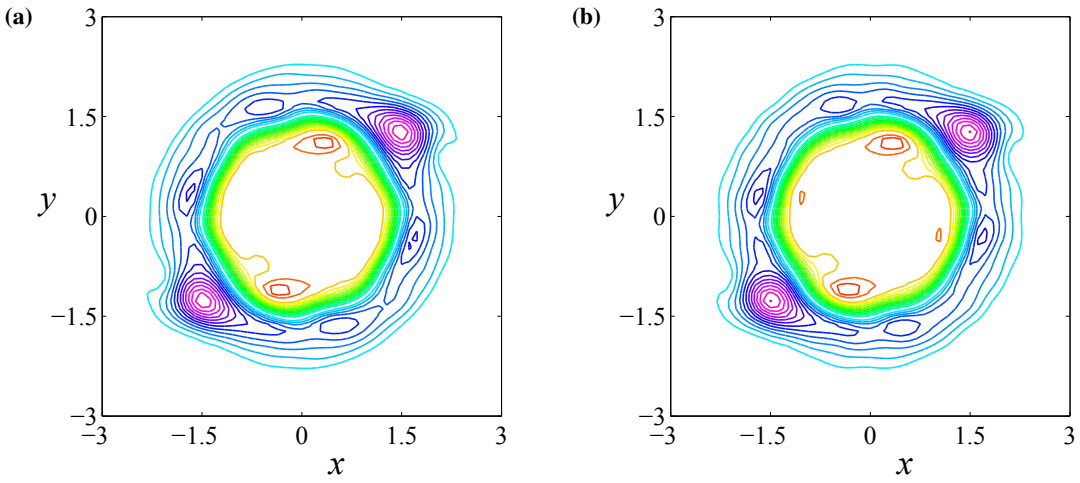

Figure 6.5.13: Pressure contour plots with two perturbing anti-cyclones located initially at $M = 1.4$ of radius $\sigma = 0.4$ and pressure differential $\mu = 0.1$ at time $t = 1.8$ using (a) Dirichlet BCs and (b) Robin BCs.

The results above arise from perturbing an eastward circumpolar jet with anti-cyclones to the south and thus the problem is essentially an interacting atmospheric vortex problem. It has been shown previously in Chapter 5 and in the subsequent article by Cosgrove and Forbes [17] that the results of simulating interacting atmospheric vortices using the f-plane approximation can be misleading due to false reflections off the artificial boundaries, especially when Dirichlet boundary conditions are involved. To overcome this phenomenon, Cosgrove and Forbes [17] used Robin boundary conditions to absorb and minimize the influence of such reflections. However, using the δ-plane approximation, the numerical solutions obtained using Dirichlet and Robin boundary conditions are virtually identical, indicating that the δ-plane approximation with its quadratic variation is capable of absorbing false reflections. An example of the similarity between the numerical solutions for the Dirichlet and Robin boundary value problems are shown in Figures 6.5.13(a) and 6.5.13(b), respectively.

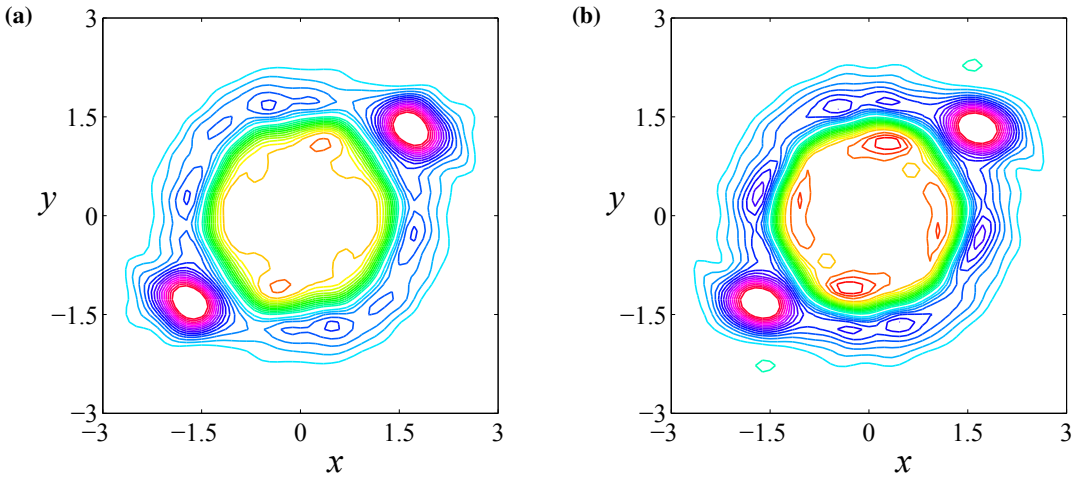

Figure 6.5.14: Pressure contour plots using baseline parameters with eastward jet having velocity (a) 75% at time $t = 2.2$ and (b) 125% at time $t = 1.8$.

It is clear from the smoothed zonal velocity profiles given by Godfrey [31], Baines *et al.* [4] and Antuñano *et al.* [2] that there is considerable change in the magnitude of the observed maximum velocity within the hexagonal structure. The one constant feature of all three aforementioned velocity profiles is that the maximum velocity is observed at approximately 76°N latitude within the hexagonal region and steadily declines towards the outer boundaries of 74°N and 78°N. Moreover, the most recent measurements reported by Antuñano *et al.* [2] have the velocity within the Hexagon being in the range 104 ± 15 ms^{-1}. To get an idea of the effect of the velocity variation, Figures 6.5.14(a) and 6.5.14(b) show the respective pressure contour diagrams using the baseline parameters with a maximum velocity that is 75% and 125% of that used in the simulations above. The smaller velocity magnitude forms a more regular hexagonal feature but takes longer to develop; conversely, the hexagonal feature formed using the increased velocity evolves more quickly but is less regular.

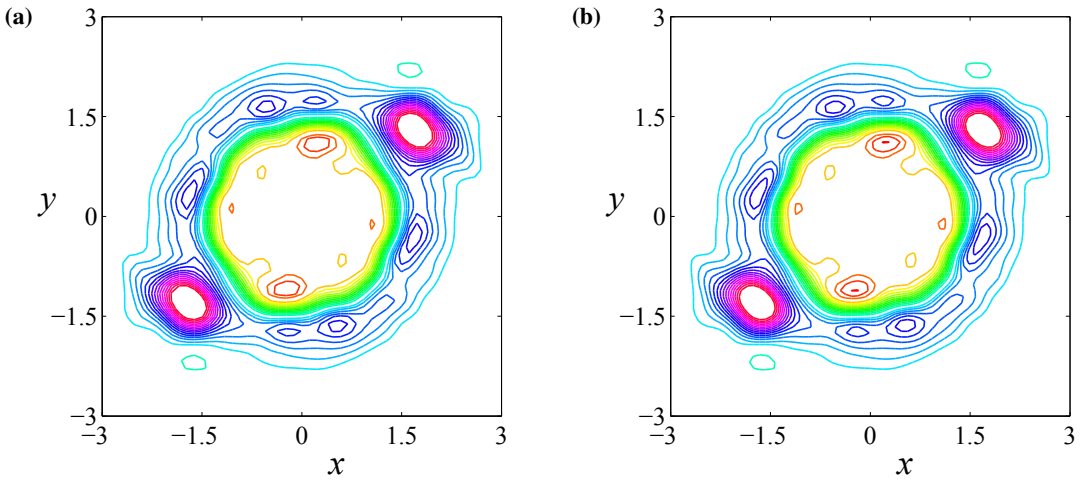

Figure 6.5.15: Pressure contour plots with two perturbing anti-cyclones located originally at $M = 1.5$ of radius $\sigma = 0.4$ with pressure differential $\mu = 0.2$ at time $t = 2.3$ with (a) 161 and (b) 201 grid points in each spatial variable.

The convergence of the numerical solution is essential and numerous checks have been done to ensure that this is in fact the case. The spectral representations of each variable have used $M = N = 41$ Fourier coefficients with 161 sample points in each spatial variable. The discussion that follows justifies the choice of the spectral truncation of 41 coefficients and the grid resolution of 161 sample points. The wavelength of each Fourier mode is given by

$$\lambda_M = \frac{2\lambda}{M}; \lambda_N = \frac{2\omega}{N}, \tag{6.5.2}$$

where λ_M and λ_N are the wavelengths of the M and N Fourier coefficient respectively and the constants λ and ω are the dimensionless half-width and half-breadth of the δ-plane defined in system (3.3.1). For the 41^{st} Fourier mode when $M = N = 41$ the dimensionless wavelength is approximately 0.29 using the computational δ-plane region of $-6 < \lambda < 6$, $-6 < \omega < 6$ in equation (6.5.2). Having such a large truncation in the spectral representation is meaningless unless the spatial resolution is able to interpret the wavelengths associated with the higher Fourier modes and thus the spatial sampling must also be investigated. With a spatial sampling of 161 data points in each spatial variable, every period of the highest Fourier mode is interpreted by approximately five data points, sufficient to sample the range in the highest Fourier mode. It was determined that beyond a mesh grid of 161 spatial points in each spatial variable the results are for all intents and purposes identical. This is confirmed and illustrated in Figures 6.5.15(a) and 6.5.15(b), which shows the contour diagrams at time $t = 2.3$ using the baseline parameters

with 161 and 201 grid points in each spatial variable, respectively.

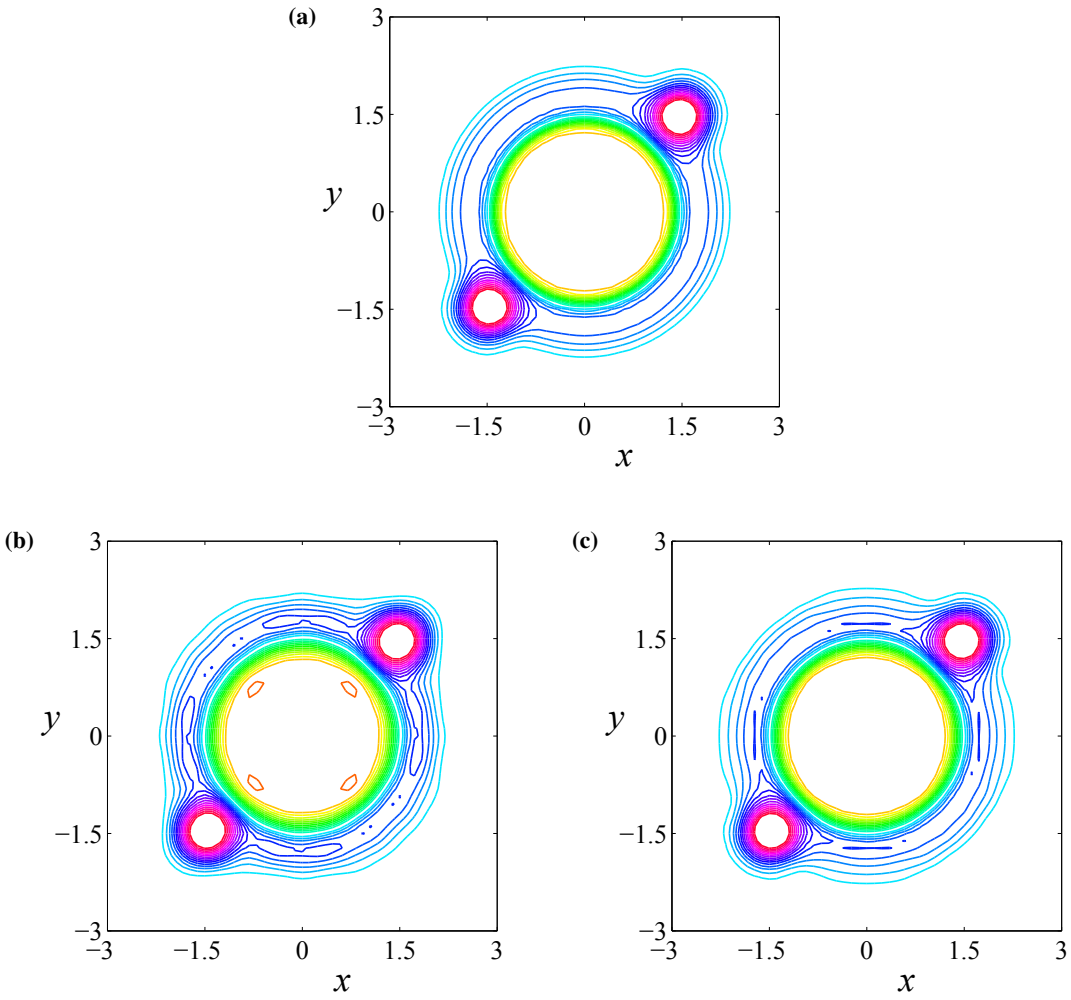

Figure 6.5.16: Initial pressure contour plots with two perturbing anti-cyclones located originally at $M = 1.5$ of radius $\sigma = 0.4$ with pressure differential $\mu = 0.2$ for (a) 'true' pressure and (b) spectral representation, $M = N = 31$ and (c) spectral representation, $M = N = 41$.

The simulations in this chapter rely on the initial spectral representations being sufficiently accurate to portray the initial 'true' closed form of the variables in question. For example, is the spectral representation for pressure at $t = 0$ using (6.3.6) equivalent to the sum of the closed form components (6.1.17) and (6.2.2)? Figure 6.5.16(a) illustrates the initial 'true' closed form of the pressure given by the sum of the components (6.1.17) and (6.2.2) and when compared to the spectral representation shown in Figure 6.5.16(b) using $M = N = 31$ Fourier coefficients there are considerable differences between the figures that indicate the spectral representation is not sufficiently mimicking the 'true' initial pressure structure. However, increasing the spectral truncation

to $M = N = 41$, there are only minor changes in the westward jet that produce contour slivers at 3, 6, 9 and 12 o'clock, and this is shown in Figure 6.5.16(c).

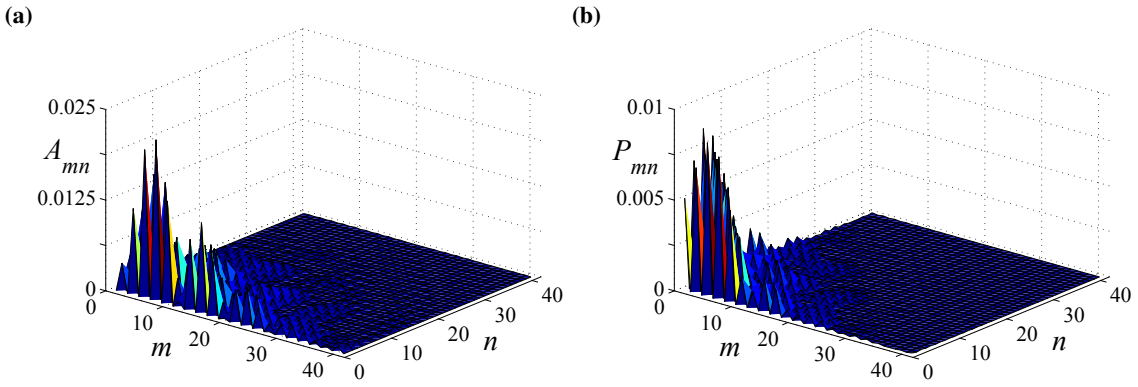

Figure 6.5.17: Absolute value of the initial Fourier coefficients for (a) $A_{mn}(t)$ and (b) $P_{mn}(t)$.

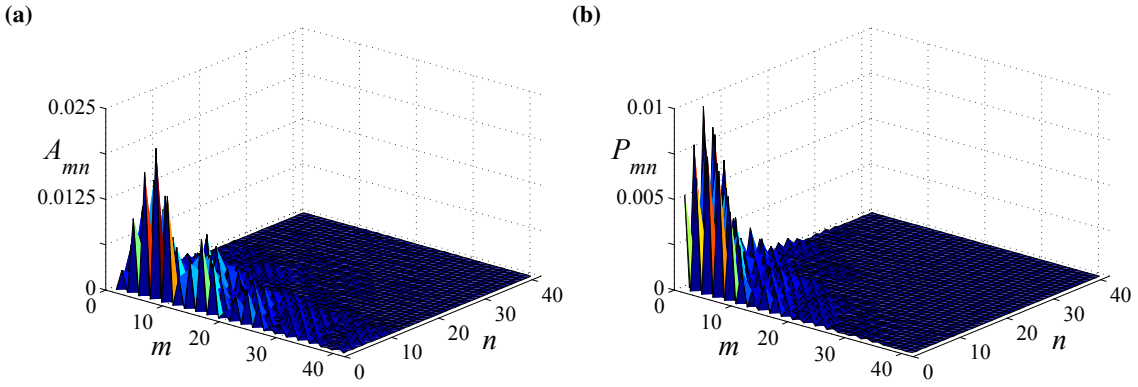

Figure 6.5.18: Absolute value of the Fourier coefficients at time $t = 2.0$ for (a) $A_{mn}(t)$ and (b) $P_{mn}(t)$.

The convergence of the initial Fourier coefficients is illustrated in Figure 6.5.17. The subfigures (a) and (b) show three-dimensional surface plots of the absolute value of the initial Fourier coefficients $A_{mn}(0)$ for the x-directed velocity and $P_{mn}(0)$ for the pressure, respectively, for the baseline simulation parameters. The magnitude of the Fourier coefficients decay steadily towards zero, indicating convergence. This behaviour is also replicated at the later time of $t = 2.0$ where the hexagonal structure is arguably at it most regular for the baseline simulation. The magnitudes of the Fourier coefficients at this time are shown in Figure 6.5.18.

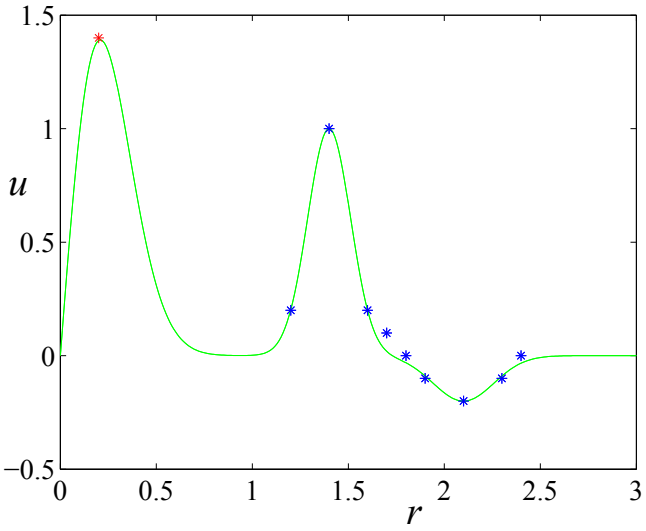

Figure 6.5.19: Curve fitted zonal velocity profile with polar cyclone components included. The blue asterisks are the data points given in Table 6.1.

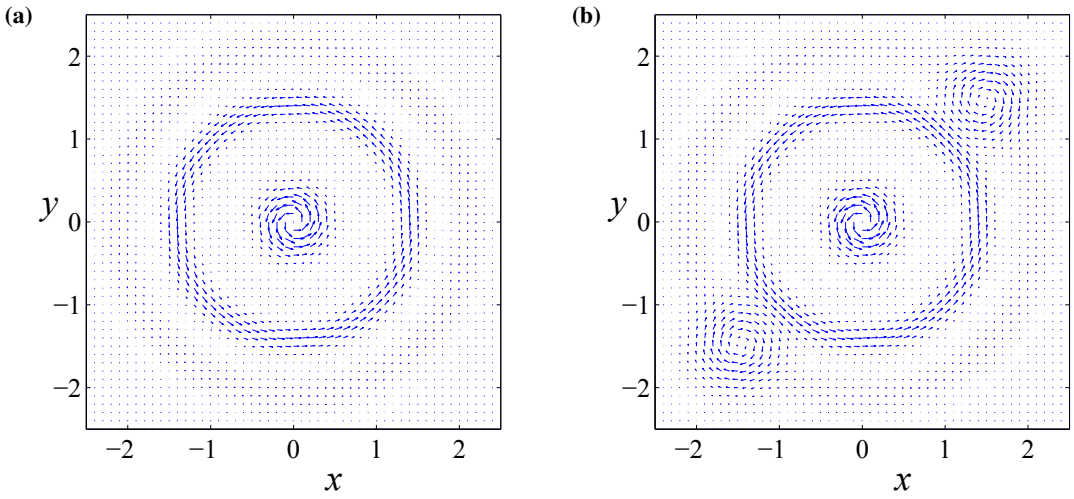

Figure 6.5.20: Quiver plots of the velocity induced by the background flow and polar cyclone components with (a) no perturbing anti-cyclones and (b) anti-cyclones at $M = 1.5$ of radius $\sigma = 0.4$ and strength $\mu = 0.2$.

The contour diagrams above have been generated by considering the impact of two symmetrically located anti-cyclones perturbing an eastward circumpolar jet. In reality, there is a polar cyclone centred at the pole [2, 4] and a visible anti-cyclone located within the interior of the North Polar Hexagon [2, 56]. The polar cyclone can have velocity in excess of 135 ms^{-1} [2, 4] and can be simulated by including an additional component to the background flow equations (6.1.5) and (6.1.6) of the form

$$u_{polar}(x,y) = -C_4\, y\, \exp\left[-C_5\left(x^2+y^2\right)\right], \tag{6.5.3}$$

$$v_{polar}(x,y) = C_4\, x\, \exp\left[-C_5\left(x^2+y^2\right)\right], \tag{6.5.4}$$

respectively, where $C_4 = 11.5$ and $C_5 = 11$. Figure 6.5.19 shows the zonal velocity profile as depicted in Figure 6.1.2 with the additional polar cyclone components (6.5.3) and (6.5.4) included. It shows that the peak dimensionless velocity is approximately 1.4 at a radius of $r = 0.2$, as indicated by the red asterisk and corresponds to the approximate dimensional velocity of 140 ms^{-1} at latitude $\phi = 88°\text{N}$ interpolated from Figure 7*A* of the article by Antuñano *et al.* [2]. The new velocity field induced by the inclusion of the polar cyclone components is shown in the quiver plots of Figure 6.5.20, which shows the polar cyclone alone encased by the eastward circumpolar jet in Figure 6.5.20(a) and with the additional baseline perturbation anti-cyclones in Figure 6.5.20(b). The latitude of the peak velocity, $\phi = 88°\text{N}$, confines the polar cyclone to a very narrow ring around the north pole of Saturn. This results in quite a large ring between the polar cyclone and the easterly jet that is relatively stagnant with respect to the velocities of the jet and polar cyclone. Thus it is to be expected that the polar cyclone flow has little effect on the easterly jet and subsequent formation of a hexagonal structure.

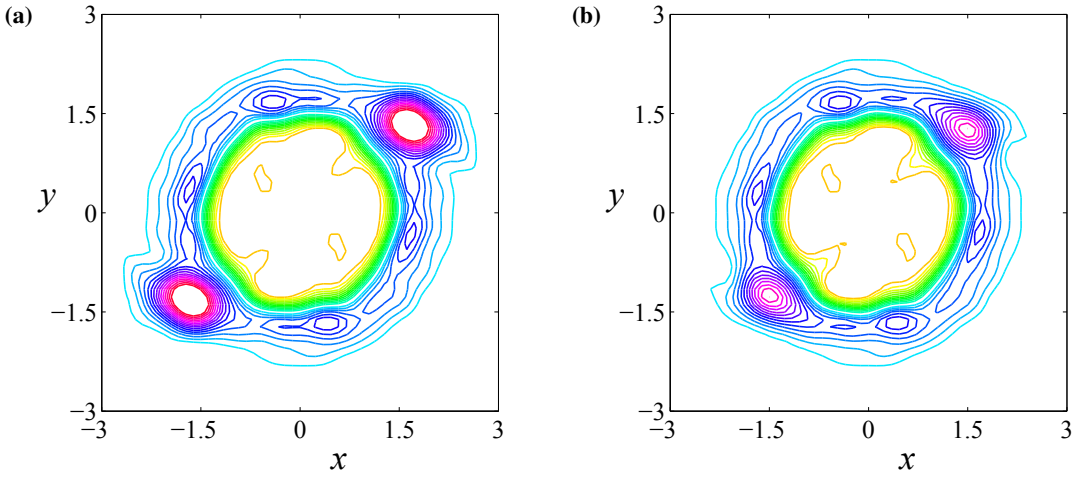

Figure 6.5.21: Pressure contour plots of systems with polar cyclone components included in the background flow at time $t = 2.0$ with (a) $M = 1.5$, $\sigma = 0.4$ and $\mu = 0.2$ and (b) $M = 1.4$, $\sigma = 0.4$ and $\mu = 0.1$.

Including the polar cyclone components into the background flow of simulation parameters

that are known to produce a hexagonal structure seems to have marginal influence over the formation of a hexagonal structure as indicated in Figure 6.5.21, which illustrates the pressure contour maps at time $t = 2.0$ of known hexagonal formation parameters with polar cyclone components added to the background flow. Figure 6.5.21(a) used the baseline parameters with polar cyclone components and Figure 6.5.21(b) used $M = 1.4$, $\sigma = 0.4$ and $\mu = 0.1$ along with the polar cyclone. There are small changes in the hexagonal structure when compared to their non-polar cyclonic flow equivalents, shown in Figures 6.5.5(c) and 6.5.8(b), respectively. An explanation for this similarity is that there is still a substantial ring within the hexagonal structure that is approximately stagnant and thus limits the effect of the polar cyclone's influence on the hexagon formation. However, there are still flow-on effects from the polar cyclone components and although slight, these differences may have been caused by increased internal shearing induced by the polar cyclone.

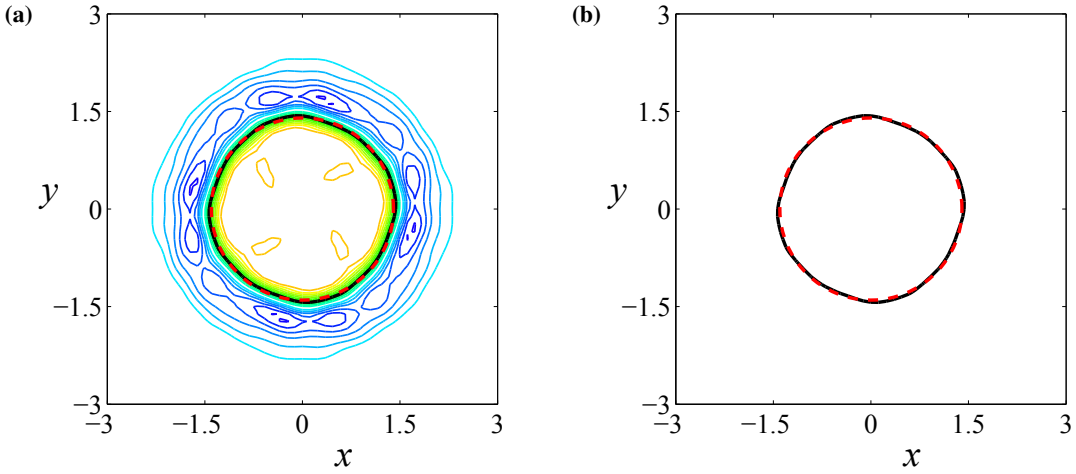

Figure 6.5.22: Unperturbed polar cyclone plot of the interfacial pressure contour (thick black line) at time $t = 2.0$ and the approximate $\phi = 76°$N parallel (thick dashed red line) (a) with entire pressure contour profile and (b) alone.

It has been shown in tank experiments that polygonal structures can be formed through forcing created by high rotation at the centre of a tank [6, 38]. In some respects this could be considered analogous to unperturbed polar cyclonic flow in the simulation parameters outlined above. However, considering the polar flow components alone does not produce any special feature and the associate pressure structure remains essentially circular and is illustrated in Figure 6.5.22(a). In this figure the thick black contour represents the interfacial pressure contour $p = 0.96$ and the thick dashed red line is a circle of dimensionless radius $r = 1.4$ that equates to the approximate

latitude $\phi = 76°$N. Figure 6.5.22(b) simply shows the interfacial contour with the circle of radius $r = 1.4$ to illustrate that the interfacial region is virtually circular in shape.

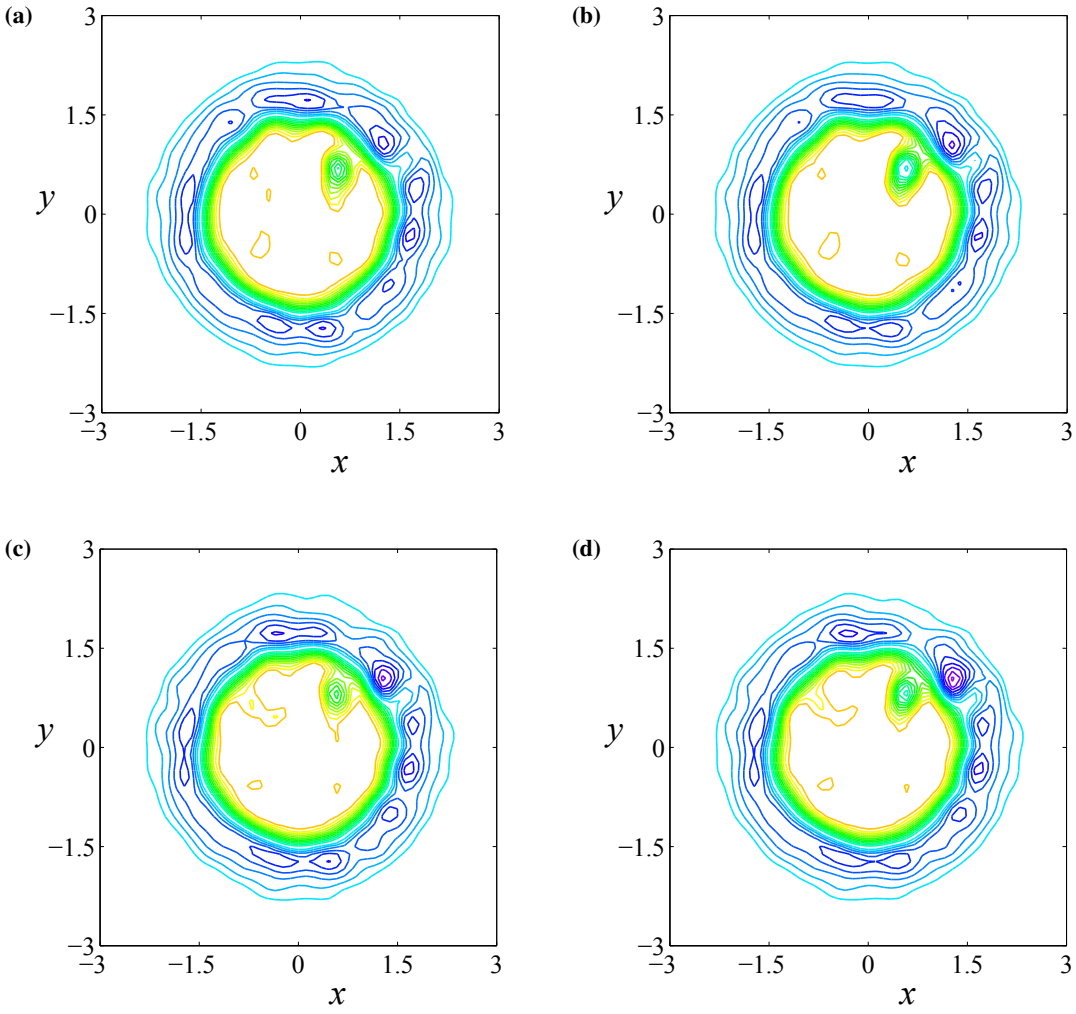

Figure 6.5.23: Pressure contour plots of circumpolar jets with internal spot of pressure differential $\mu = 0.2$ at time $t = 1.5$ with (a) $M = 0.6$, $\sigma = 0.15$, (b) $M = 0.6$, $\sigma = 0.2$, (c) $M = 0.7$, $\sigma = 0.15$ and (d) $M = 0.7$, $\sigma = 0.2$.

Incorporating an internal polar spot to the background flow, comprised of circumpolar jets and polar cyclone components, produces a distortion in the contour structure but never forms what could be interpreted as a hexagon. In fact, when the introduction of an internal spot influences the circumpolar jet, similar results are achieved to the single perturbing anti-cyclone simulations and produces a trapezoidal deformation in the pressure structure. For completeness this is shown in Figure 6.5.23 for four different parameter sets, with internal spot having pressure differential

$\mu = 0.2$ at time $t = 1.5$. The eye of the polar spot is located at the approximate latitude $\phi = 81°$N [2] and thus $M = 0.6$ and $M = 0.7$ are logical positions to simulate what is observed on Saturn. The four subfigures of Figure 6.5.23 represent all possible configurations with $M = 0.6$ or $M = 0.7$ and radius $\sigma = 0.15$ or $\sigma = 0.2$. Like the perturbing anti-cyclone simulations, when the pressure differential is reduced to $\mu = 0.1$ and all other parameters are kept identical, the overall affect on the pressure structure is less. To illustrate this point, Figures 6.5.24(a) and 6.5.24(b) show the equivalent plots to Figures 6.5.23(a) and 6.5.23(c), respectively, for $\mu = 0.1$. The reduced pressure differential has negligible impact and the pressure structure has maintained a circular appearance.

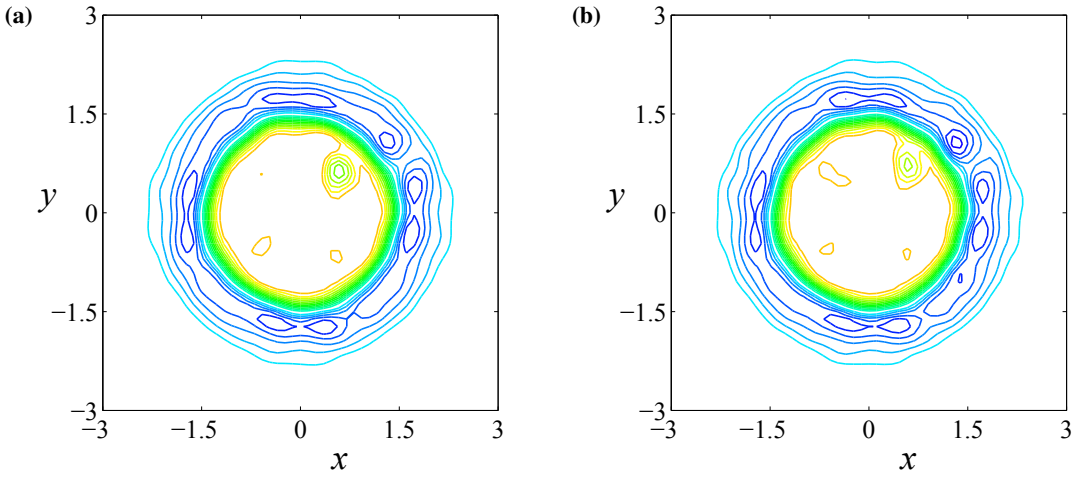

Figure 6.5.24: Pressure contour plots of circumpolar jets with internal spot of pressure differential $\mu = 0.1$ at time $t = 1.5$ with (a) $M = 0.6$, $\sigma = 0.15$ and (b) $M = 0.7$, $\sigma = 0.15$.

6.6 Discussion

This chapter has considered a possible trigger mechanism for the formation of the famed North Polar Hexagon on Saturn, in the form of perturbing anti-cyclones. The hexagonal feature is a long-lived atmospheric structure that continues to this day. It was theorised by Allison *et al.* [1] that the Hexagon structure was the result of a Rossby wave being perturbed by at least one anti-cyclone to the south. Although at this point in time there no evidence of a perturbing anti-cyclone, the claim by Allison *et al.* [1], in particular the perturbation aspect of the theory, has not been substantiated in the literature and thus is a focal point of this chapter. A high-latitude δ-plane approximation is used with tangent point located at the north pole, $\phi = 90°$N. In the δ-plane approximation, the

Coriolis acceleration varies quadratically with latitude.

The Hexagon is centrally located about 76°N latitude within an eastward circumpolar jet with an approximate maximum zonal velocity of 100 ms^{-1}. There is a smaller magnitude, 20 ms^{-1}, westward jet to the south at the approximate latitude of 69°N which seems to be ignored in some cases when modelling and simulating the formation of the Hexagon in the current literature. These circumpolar jets are simulated with a Gaussian profile function offset at the appropriate dimensionless distance from the pole. The perturbing anti-cyclones are modelled using an exponential function (6.2.1) with variable initial eye location M, radius σ and pressure differential μ. It was found that the most regular hexagonal structure formed at time $t = 2.0$ using the parameters $M = 1.5$, $\sigma = 0.4$ and $\mu = 0.2$. These were then used as the baseline values to determine the effect on hexagon formation of varying one of the parameters.

The pin-wheeling effect caused by the opposing rotations of the eastward jet and anti-cyclones being in close proximity is the major contributing factor in the formation of a hexagonal edge in the simulations. A result of moving the anti-cyclones closer to the jet is that the pin-wheeling may become non-tangential and a pronounced curve in the pressure contour structure can arise and block the formation of a hexagonal vertex, and although a hexagonal structure may eventuate, it will never be regular. Conversely, if the anti-cyclones are moved away such that there is no pin-wheel effect occurring, then an edge will never eventuate to form a hexagonal feature.

The pressure differential μ changes the internal velocity of the anti-cyclones and thus contributes to the pin-wheeling effect. Decreasing the pressure differential lessens the pin-wheeling effect between the polar jet and the anti-cyclones. To overcome this lack of influence, the location of the anti-cyclones must be moved closer to the circumpolar jet. Apart from the baseline parameters, it was also shown that a hexagonal structure is formed with decreased pressure differential $\mu = 0.1$, closer location of $M = 1.4$ and baseline radius of $\sigma = 0.4$ at time $t = 2.0$.

The radius of the anti-cyclone impacts on the internal velocity; if the pressure differential μ is identical, the smaller the radius of the anti-cyclone the more intense the internal velocity. However, the anti-cyclone must be within a close enough proximity to influence the flow of the polar jet.

The initial unperturbed pressure profile of the circumpolar jet had pressure in the range $p = 0.88$ to $p = 1.04$. The intermediate pressure contour $p = 0.96$ is used to define the hexagonal structure in the pressure contour maps. Surprisingly, the defining intermediate pressure value aligned itself extremely closely with the boundary between positive and negative local vorticity. Therefore it could be concluded that the hexagonal feature may be linked through pressure and local vorticity.

The simulations in this thesis indicate that the westward flow to the south of the predominant eastward circumpolar jet has little effect on the formation of hexagonal structures; however, it does seem to contribute to a slightly more defined edge to the east and a more defined vertex to the west of the perturbing anti-cyclones. These minimal differences could be associated with the increased movement to the west of the anti-cyclones due to them being located within the westerly jet.

It has been shown that a hexagonal feature can be formed through anti-cyclones impinging on the boundary of the eastward circumpolar jet, with varying parameters, even with considerable smaller magnitude velocities than observed in nature. This is not a solution to the famed North Polar Hexagon on Saturn, but a demonstration of a trigger mechanism in the form of perturbing anti-cyclones that could help form a hexagonal structure. The simulations produce hexagons that are transient, lasting approximately $t = 1.5$ (two days) in duration. The model used here was unable to replicate the stability that has been observed in reality and thus the longevity of the structure has to be attributed to other factors not considered in this paper. This merits further research.

Chapter 7

Conclusion

This thesis has considered numerical simulations of real world atmospheric phenomena, with a particular focus on the evolving nature of some of such events and the appropriate 'tangent plane' approximations to use so that reliable informed solutions are obtained. There were three 'tangent plane' approximations used throughout this thesis, the commonly used f-plane and β-plane approximations and the lesser known δ-plane (or γ-plane) approximation. Each of the 'tangent plane' approximations is valid over different regions of a celestial body.

The advantage of 'tangent plane' approximations is that they simplify the spherical nature of an atmosphere to a two-dimensional plane without losing the ability to model spherical effects. Two-dimensional compressible fluid equations are used on the 'tangent plane', to reflect the fact that the horizontal length scales are orders of magnitude greater than the vertical height. The "top" of the atmosphere is not modelled explicitly and thus is not a shallow-water approximation. Instead, the variables solved are in essence depth-averaged quantities, with weak tangential compressibility included to account for these effects. This is an extension of the approach of Meunier *et al.* [53] who similarly used planar equations, although under the assumption of an incompressible fluid. Allowing weak fluid-compressibility in the planar coordinates enables the same physical degree of freedom as classical shallow-water theories. This is analogous to the link between flow of a compressible fluid in a rigid pipe, and that of an incompressible fluid in an elastic-walled pipe [25, 43].

Three atmospheric phenomena were studied in depth using various 'tangent plane' approximations and celestial atmospheres. They are: (i) the formation of finger structures on the extremities of atmospheric vortices; (ii) the interaction or lack thereof between binary mid-latitude atmo-

spheric vortices; and (iii) anti-cyclones perturbing circumpolar flows to form a transient north polar hexagon.

It has been shown in Chapter 4 that at mid-latitudes the f-plane approximation, which assumes a constant Coriolis parameter, is in close agreement with the β-plane approximation, which enables the Coriolis parameter to vary linearly with latitude. Thus the f-plane is sufficiently accurate to enable the β-effect to be ignored at the mid-latitude 43.3°. This is particularly the case for the dimensionless 'tangent plane' region considered within Chapter 4 of this thesis. Conversely, at the mid-low latitude 27.2° considered in this thesis, the β-effect is significant and thus the β-term must be included in the Coriolis parameter.

Both the f-plane and β-plane approximations were used to simulate atmospheric finger structures on the periphery of an initial low-pressure system. The initial condition for pressure has a substantial impact on the subsequent development of the finger formations on the outer regions of the pressure system. A finger is defined to form at the latest time at which there is one closed interfacial pressure contour $p = 0.95$. Several perturbation modes, both sinusoidal and triangular, have been investigated throughout this thesis. The higher the perturbation mode and greater the amplitude, the more pronounced is the finger structure formed. The multi-modal triangular wave perturbations give similar results to those of the purely sinusoidal perturbation; however, the higher modes in the triangular waves smooth out the interfacial contours as time increases. In the cases where substantial finger structures arise, at later times the finger tips detach and secondary fingers begin to develop and grow from the troughs between the initial finger structures. These secondary fingers are smaller in amplitude and thus tertiary fingers never eventuate.

Although the interaction of tropical cyclones, hurricanes and typhoons has been of considerable interest, the interaction of large-scale binary systems in terms of extra-tropical cyclones and extra-tropical anti-cyclones that form in the mid-latitude regions of Earth has been less of a focus in the current literature. The elastic interaction, where vortices interact without any significant change in their intensity and structure, was of interest. The similarity in the numerical simulations using the f-plane and β-plane approximations at mid-latitudes, from Chapter 4, enabled the use of the simplified f-plane approximation in Chapter 5; however, due to the need of an expanded 'tangent plane' boundary, this approximation was used in conjunction with Robin boundary con-

ditions to absorb false reflections off the 'tangent plane' boundaries.

The binary systems were defined such that they could be in one of four possible configurations involving low-pressure (L) and high-pressure (H) placed initially in the south-west and north-east quadrants of the 'tangent plane', conveniently defined as an LL-binary system, HH-binary system, LH-binary system or an HL-binary system. By definition, interaction occurred if there was clear movement of one system caused by the other at time $t = 0.45$, approximately 12.5 hours. A scaling law was determined in terms of the ratio of the average radius σ and the initial eye location L and is given by equation (5.4.1) and interpolated from Figure 5.4.18. This law gives an indicator as to when interaction takes place at mid-latitudes. If the interaction ratio $I_r \geq 0.9$ then interaction occurred, otherwise negligibly weak or no interaction was observed.

The scaling law from Figure 5.4.18 was generalised to other latitudes $\phi \neq 43.3°$N where the time scale Rossby number is denoted $Ro_{T2} \neq 0.1$, to give an approximate rule as to when interaction may take place at other latitudes. This was achieved by calculating the effective radii at the standard latitude $\phi = 43.3°$N, for which the Rossby number is $Ro_T = 0.1$ and gave a conversion that is dependent on the two different Rossby numbers $Ro_T = 0.1$ and $Ro_{T2} \neq 0.1$.

The origin of Saturn's North Polar Hexagon has been a topic of debate since its discovery in the late 1980's. An often cited but previously untested theory suggested by Allison *et al.* [1], proposed that the Hexagon may be the result of a stationary planetary Rossby wave, centred at approximately 76° N, that is continually perturbed by at least one impinging anti-cyclonic vortex to the south. The actual Hexagon has its centre at the geographic north pole and thus the frequently used f-plane and β-plane theories are invalid when simulating such a phenomenon. A high-latitude δ-plane approximation with tangent point located at the north pole, $\phi = 90°$N, is used. The δ-plane approximation with polar tangent has solely quadratic variation in the Coriolis parameter, that decreases in magnitude away from the pole. This thesis has shown that a hexagonal structure can be formed by two symmetrically placed perturbing anti-cyclones to the south of an initially circular eastward circumpolar jet.

The eastward circumpolar jet and the perturbing anti-cyclones have opposing rotations, and when in close enough proximity, the pin-wheel effect caused by these counter rotations is the ma-

jor contributing factor in forming a hexagonal edge and subsequent hexagon. The pin-wheeling is highly dependent upon the initial location, radii and pressure differential of the perturbing anti-cyclones. A combination of the location and strength of the anti-cyclones, as determined by the pressure differential and radii of the anti-cyclones, has to be close enough to influence to flow of the circumpolar jet. Without substantial interference, a hexagonal structure will never eventuate. Although often neglected in numerical simulations of the North Polar Hexagon, the smaller magnitude westward circumpolar current to the south of the Hexagon has little impact on the development of known hexagonal structures.

This thesis has resulted in three peer-reviewed journal articles based on the simulations and results outlined in Chapters 4, 5 and 6, titled:

- 'The formation of large-amplitude fingers in atmospheric vortices' [16];
- 'Nonlinear behaviour of interacting mid-latitude atmospheric vortices' [17]; and
- 'A δ-plane simulation of anti-cyclones perturbing circumpolar flows to form a transient north polar hexagon' [18].

In relation to the research discussed in this thesis, there is considerable scope for future studies. In particular, it is likely that there are additional dynamics due to the β-effect that are not captured by the f-plane approximation when investigating the binary interaction of mid-latitude vortices. Also, the inability to replicate the longevity and stability that is observed in reality with respect to the North Polar Hexagon for the model used here requires further research.

Appendix A

Non-Dimensionalization

The following is an example of how the dimensionless equations are derived. In particular, it shows how the dimensional momentum equation (3.1.2) is converted to non-dimensional form (3.4.4) and the need for the dimensionless inverse Eckert number ν_E. The dimensional momentum equation (3.1.2) has the form

$$\frac{\partial u}{\partial t} + u\frac{\partial u}{\partial x} + v\frac{\partial u}{\partial y} - fv + \frac{1}{\rho}\frac{\partial p}{\partial x} = 0. \tag{A.0.1}$$

The non-dimensionalization of (A.0.1) uses the quantities given by (3.3.1), (3.3.2) and (3.4.1). Thus,

$$\begin{aligned} \frac{\partial u}{\partial t} \Rightarrow \frac{\partial}{\partial t}\left(\frac{A\tilde{u}}{\tau}\right) \\ &= \frac{A}{\tau}\frac{\partial \tilde{u}}{\partial t} \\ &= \frac{A}{\tau}\frac{\partial \tilde{u}}{\partial \tilde{t}}\frac{\partial \tilde{t}}{\partial t} \\ &= \frac{A}{\tau^2}\frac{\partial \tilde{u}}{\partial \tilde{t}} \end{aligned} \tag{A.0.2}$$

$$
\begin{aligned}
u\frac{\partial u}{\partial x} \Rightarrow & \frac{A\,\tilde{u}}{\tau}\frac{\partial}{\partial x}\left(\frac{A\,\tilde{u}}{\tau}\right) \\
&= \frac{A^2\,\tilde{u}}{\tau^2}\frac{\partial \tilde{u}}{\partial x} \\
&= \frac{A^2\,\tilde{u}}{\tau^2}\frac{\partial \tilde{u}}{\partial \tilde{x}}\frac{\partial \tilde{x}}{\partial x} \\
&= \frac{A}{\tau^2}\,\tilde{u}\frac{\partial \tilde{u}}{\partial \tilde{x}}
\end{aligned}
\tag{A.0.3}
$$

$$
\begin{aligned}
v\frac{\partial u}{\partial y} \Rightarrow & \frac{A\,\tilde{v}}{\tau}\frac{\partial}{\partial y}\left(\frac{A\,\tilde{u}}{\tau}\right) \\
&= \frac{A^2\,\tilde{v}}{\tau^2}\frac{\partial \tilde{u}}{\partial y} \\
&= \frac{A^2\,\tilde{v}}{\tau^2}\frac{\partial \tilde{u}}{\partial \tilde{y}}\frac{\partial \tilde{y}}{\partial y} \\
&= \frac{A}{\tau^2}\,\tilde{v}\frac{\partial \tilde{u}}{\partial \tilde{y}}
\end{aligned}
\tag{A.0.4}
$$

$$
f\,v \Rightarrow \frac{\tilde{f}}{\tau}\frac{A\,\tilde{v}}{\tau} = \frac{A}{\tau^2}\,\tilde{f}\,\tilde{v} \tag{A.0.5}
$$

$$
\begin{aligned}
\frac{1}{\rho}\frac{\partial p}{\partial x} \Rightarrow \frac{1}{\rho_0\tilde{\rho}}\frac{\partial}{\partial x}(\rho_0 R T_0 \tilde{p}) \\
&= \frac{R T_0}{\tilde{\rho}}\frac{\partial \tilde{p}}{\partial x} \\
&= \frac{R T_0}{\tilde{\rho}}\frac{\partial \tilde{p}}{\partial \tilde{x}}\frac{\partial \tilde{x}}{\partial x} \\
&= \frac{R T_0}{A}\frac{1}{\tilde{\rho}}\frac{\partial \tilde{p}}{\partial \tilde{x}} \\
&= \frac{R T_0}{A}\frac{A\tau^2}{A\tau^2}\frac{1}{\tilde{\rho}}\frac{\partial \tilde{p}}{\partial \tilde{x}} \\
&= \frac{A}{\tau^2}\frac{\tau^2 R T_0}{A^2}\frac{1}{\tilde{\rho}}\frac{\partial \tilde{p}}{\partial \tilde{x}} \\
&= \frac{A}{\tau^2}\frac{\nu_E}{\tilde{\rho}}\frac{\partial \tilde{p}}{\partial \tilde{x}}
\end{aligned}
\tag{A.0.6}
$$

Substituting the results from representations (A.0.2) – (A.0.6) into the dimensional form of the momentum equation given by (3.1.2) gives

$$
\frac{A}{\tau^2}\left[\frac{\partial \tilde{u}}{\partial \tilde{t}} + \tilde{u}\frac{\partial \tilde{u}}{\partial \tilde{x}} + \tilde{v}\frac{\partial \tilde{u}}{\partial \tilde{y}} - \tilde{f}\tilde{v} + \frac{\nu_E}{\tilde{\rho}}\frac{\partial \tilde{p}}{\partial \tilde{x}}\right] = 0,
$$

which simplifies further to give the non-dimensional representation

$$
\frac{\partial \tilde{u}}{\partial \tilde{t}} + \tilde{u}\frac{\partial \tilde{u}}{\partial \tilde{x}} + \tilde{v}\frac{\partial \tilde{u}}{\partial \tilde{y}} - \tilde{f}\tilde{v} + \frac{\nu_E}{\tilde{\rho}}\frac{\partial \tilde{p}}{\partial \tilde{x}} = 0,
$$

as given by equation (3.4.4).

Bibliography

[1] Allison, M., Godfrey, D. A. and Beebe, R. F., A wave dynamical interpretation of Saturn's polar hexagon, *Science*, **247**, 1990, 1061–1063.

[2] Antuñano A., del Rio-Gaztelurrutia T., Sanchez-Lavega A. and Hueso R., Dynamics of Saturn's polar regions, *Journal of Geophysical Research: Planets*, **120**, 2015, 155–176.

[3] Aris, R., *Vectors, tensors, and the basic equations of fluid mechanics*. Prentice-Hall, Inc, New Jersey, 1962.

[4] Baines, K. H., Momary, T. W., Fletcher, L. N., Showman, A. P., Roos-Serote, M., Brown, R. H., Buratti, B. J., Clark, R. N. and Nicholson, P. D., Saturn's north polar cyclone and hexagon at depth revealed by Cassini/VIMS, *Planetary and Space Science*, **57**, 2009, 1671–1681.

[5] Baker, G. R. and Pham, L. D., A comparison of blob methods for vortex sheet roll-up, *Journal of Fluid Mechanics*, **547**, 2006, 297–316.

[6] Barbosa-Aguiar, A. C., Read, P. L., Wordsworth, R. D., Salter, T. and Yamazaki, Y. H., A laboratory model of Saturn's North Polar Hexagon, *ICARUS*, **206**, 2010, 755–763.

[7] Batchelor, G. K., *An introduction to fluid dynamics*. Cambridge University Press, Cambridge, 1967.

[8] Brand, S., Interaction of binary tropical cyclones of the western North Pacific Ocean, *Journal of Applied Meteorology*, **9**, 1970, 433–441.

[9] Caflisch, R. E., Li, X. and Shelley, M. J., The collapse of an axi-symmetric, swirling vortex sheet, *Nonlinearity*, **6**, 1993, 843–867.

[10] Caldwell, J., Hua, X., Turgeon, B., Westphal, J. A. and Barnet, C. D., The drift of Saturn's north polar spot observed by the Hubble space telescope, *Science*, **260**, 1993, 326–329.

[11] Chan, J. C. L. and Law, A. C. K., The interaction of binary vortices in a barotropic model, *Meteorology and Atmospheric Physics*, **56**, 1995, 135–155.

[12] Chan, J. C. L. and Williams, R. T., Analytical and numerical studies of the beta-effect in tropical cyclone motion. Part I: Zero mean flow, *Journal of the Atmospheric Sciences*, **44**, 1987, 1257–1265.

[13] Chandrasekhar, S., *Hydrodynamic and hydromagnetic stability*. Dover, New York, 1981.

[14] Chang, S. W., A numerical study of the interactions between two tropical cyclones, *Monthly Weather Review*, **111**, 1983, 1806–1817.

[15] Chen, M. J. and Forbes, L. K., Accurate methods for computing inviscid and viscous Kelvin-Helmholtz instability, *Journal of Computational Physics*, **230**, 2011, 1499–1515.

[16] Cosgrove, J. M. and Forbes, L. K., The formation of large-amplitude fingers in atmospheric vortices, *ANZIAM Journal*, **56**, 2016, 395–416.

[17] Cosgrove, J. M. and Forbes, L. K., Nonlinear behaviour of interacting mid-latitude atmospheric vortices, *Journal of Engineering Mathematics*, **104**, 2017, 41–62.

[18] Cosgrove, J. M. and Forbes, L. K., A δ-plane simulation of anticyclones perturbing circumpolar flows to form a transient north polar hexagon, *Monthly Notices of the Royal Astronomical Society*, **469**, 2017, 4133–4147.

[19] Cowley, S. J., Baker, G. R. and Tanveer, S., On the formation of Moore curvature singularities in vortex sheets, *Journal of Fluid Mechanics*, **378**, 1999, 233–267.

[20] Crapper, G. D, Dombrowski, N. and Pyott, G. A. D., Kelvin-Helmholtz wave growth on cylindrical sheets, *Journal of Fluid Mechanics*, **68**, 1975, 497–502.

[21] Dong, K. and Neumann, C. J., On the relative motion of binary tropical cyclones, *Monthly Weather Review*, **111**, 1983, 945–953.

[22] Dormand, J. R. and Prince, P. J., A family of embedded Runge-Kutta formulae, *Journal of Computational and Applied Mathematics*, **6**, 1980, 19–26.

[23] Drazin, P. G. and Reid, W. H., *Hydrodynamic stability*. 2nd ed. Cambridge University Press, Cambridge, 2004.

[24] Dritschel, D. G. and Waugh, D. W., Quantification of the inelastic interaction of unequal vortices in two-dimensional vortex dynamics. *Physics of Fluids A* **4**, 1992, 1737–1744.

[25] Forbes, L. K., On the evolution of shock-waves in mathematical models of the aorta, *Journal of Australian Mathematical Society (Series B)*, **22**, 1981, 257–269.

[26] Forbes, L. K., The Rayleigh-Taylor instability for inviscid and viscous fluids, *Journal of Engineering Mathematics*, **65**, 2009, 273–290.

[27] Forbes, L. K., A cylindrical Rayleigh-Taylor instability: radial outflow from pipes or stars, *Journal of Engineering Mathematics*, **70**, 2011, 205–224.

[28] Forbes, L. K. and Cosgrove, J. M., A line vortex in a two-fluid system, *Journal of Engineering Mathematics*, **84**, 2014, 181–199.

[29] Fujiwhara, S., The mutual tendency towards symmetry of motion and its application as a principle in meteorology, *Quarterly Journal of the Royal Meteorological Society*, **47**, 1921, 287–293.

[30] Fujiwhara, S., On the growth and decay of vortical systems, *Quarterly Journal of the Royal Meteorological Society*, **49**, 1923, 75–104.

[31] Godfrey, D. A., A hexagonal feature around Saturn's north pole, *ICARUS*, **76**, 1988, 335–356.

[32] Godfrey, D. A., The rotation period of Saturn's polar hexagon, *Science*, **247**, 1990, 1206–1208.

[33] Harlander, U., A high-latitude quasi-geostrophic delta plane model derived from spherical geometry, *Tellus*, **57A**, 2005, 43–54.

[34] Harlander, U., Schonfeldt, H. -J. and Metz, W., Rossby waveguides in high-latitude shear flows with boundaries, *Journal of Geophysical Research*, **105**, 2000, 17063–17078.

[35] Holland, G. J. and Dietachmayer, G. S., On the interaction of tropical-cyclone-scale vortices. III: Continuous barotropic vortices, *Quarterly Journal of the Royal Meteorological Society*, **119**, 1993, 1381–1398.

[36] Holton, J. R., *An introduction to dynamic meteorology*. 3rd ed. Academic Press, Cambridge, 1992.

[37] Hopfinger, E. J. and van Heijst, G. J. F., Vortices in rotating fluids, *Annual Review of Fluid Mechanics* **25**, 1993, 241–289.

[38] Jansson, T. R. N., Haspang, M. P., Jensen, K. H., Hersen, P. and Bohr, T., Polygons on a rotating fluid surface, *Physical Review Letters*, **96**, 2006, 174502-1–174502-4.

[39] Kay, J. M. and Nedderman, R. M., *Fluid mechanics and transfer processes*. Cambridge University Press, Cambridge, 1985.

[40] Khain, A., Ginis, I., Falkovich, A. and Frumin, M., Interaction of binary tropical cyclones in a coupled tropical cyclone-ocean model, *Journal of Geophysical Research* **105**, 2000, 22337–22354.

[41] Krasny, R., Desingularization of periodic vortex sheet roll-up, *Journal of Computational Physics*, **65**, 1986, 292–313.

[42] Kuo, H. -C., Chen, G. T. -J. and Lin, C. -H., Merger of tropical cyclones Zeb and Alex. *Monthly Weather Review* **128**, 2000, 2967–2975.

[43] Lambert, J. W., On the nonlinearities of fluid flow in nonrigid tubes, *Journal of the Franklin Institute* **266**, 1958, 83–102.

[44] Lander, M. A., The merger of two tropical cyclones, *Monthly Weather Review*, **123**, 1995, 2260–2265.

[45] Lander, M. A. and Holland, G. J., On the interaction of tropical-cyclone-scale vortices. I: Observations, *Quarterly Journal of the Royal Meteorological Society*, **119**, 1993, 1347–1361.

[46] LeBlond, P. H., Planetary waves in a symmetrical polar basin, *Tellus*, **16**, 1964, 503–512.

[47] Liepmann, H. W. and Roshko, A., *Elements of gasdynamics*. John Wiley & Sons, Inc, New York, 1957.

[48] Lipps, F. B., A note on the beta-plane approximation, *Tellus*, **16**, 1964, 535–537.

[49] Marcus, P. S. and Lee, C., A model for eastward and westward jets in laboratory experiments and planetary atmospheres, *Physics of Fluids*, **10**, 1998, 1474–1489.

[50] Matsuoka, C. and Nishihara, K., Analytical and numerical study on a vortex sheet in incompressible Richtmyer-Meshkov instability in cylindrical geometry, *Physical Review E*, **74**, 2006, 066303 12 pages.

[51] McKiver, W. J. and Dritschel, D. G., The stability of a quasi-geostrophic ellipsoidal vortex in a background shear flow, *Journal of Fluid Mechanics*, **560**, 2006, 1–17.

[52] Melander, M. V., Zabusky, N. J. and McWilliams, J. C., Symmetric vortex merger in two dimensions: causes and conditions, *Journal of Fluid Mechanics*, **195**, 1988, 303–340.

[53] Meunier, P., Ehrenstein, U., Leweke, T. and Rossi, M., A merger criterion for two-dimensional co-rotating vortices, *Physics of Fluids*, **14**, 2002, 2757–2766.

[54] Moore, D. W., The spontaneous appearance of a singularity in the shape of an evolving vortex sheet, *Proceedings of the Royal Society of London A*, **365**, 1979, 105–119.

[55] Morales-Juberias, R., Sayanagi, K. M., Dowling, T. E. and Ingersoll, A. P., Emergence of polar-jet polygons from jet instabilities in a Saturn model, *ICARUS*, **211**, 2011, 1284–1293.

[56] Morales-Juberias, R., Sayanagi, K. M., Simon, A. A., Fletcher, L. N. and Cosentino, R. G., Meandering shallow atmospheric jet as a model of Saturn's North-Polar Hexagon, *The Astrophysical Journal Letters*, **806**, 2015, L18.

[57] Nof, D., Modons and monopoles on a γ-plane, *Geophysical and Astrophysical Fluid Dynamics*, **52**, 1990, 71–87.

[58] Phillips, N. A., Geostrophic motion, *Reviews of Geophysics*, **1**, 1963, 123–176.

[59] Prieto, R., McNoldy, B. D., Fulton, S. R. and Schubert, W. H., A classification of binary tropical cyclone-like vortex interactions, *Monthly Weather Review* **131**, 2003, 2656–2666.

[60] Ritchie, E. A. and Holland, G. J., On the interaction of tropical-cyclone-scale vortices. II: Discrete vortex patches, *Quarterly Journal of the Royal Meteorological Society*, **119**, 1993, 1363–1379.

[61] Rossby, C. G.,(and unnamed collaborators), Relation between variations in the intensity of the zonal circulation of the atmosphere and the displacement of the semi-permanent centers of action, *Journal of Marine Research*, **2**, 1939, 38–55.

[62] Sanchez-Lavega, A., Lecacheux, J., Colas, F. and Laques, P., Ground-based observations of Saturn's North polar spot and Hexagon, *Science*, **260**, 1993, 329–332.

[63] Sanchez-Lavega, A., del Rio-Gaztelurrutia, T., Hueso, R., Perez-Hoyos, S.,Garcia-Melendo, E., Antunano, A., Mendikoa, I., Rojas, J. F., Lillo, J., Barrado-Navascues, D., Gomez-Forrellad, J. M., Go, C., Peach, D., Barry, T., Milika, D. P., Nicholas, P. and Wesley, A., The long-term steady motion of Saturn's hexagon and the stability of its enclosed jet stream under seasonal changes, *Geophysical Research Letters*, **41**, 2014, 1425–1431.

[64] Sayanagi, K. M., Ewald, S. P. and Ingersoll, A. P., New Cassini ISS observations of Saturn's northern hemisphere ribbon and Hexagon. In:AAS/Division for Planetary Sciences Meeting Abstracts, volume 41 of ASS/Division for Planetary Sciences Meeting Abstracts, 2009, page 10.08, September.

[65] Shimokawa, S., Iizuka, S., Kayahara, T., Suzuki, S. and Murakami, T., Fujiwhara effect; the interaction between T0917 and T0918, *Natural Disaster Research Report of the National Institute for Earth Science and Disaster Prevention* **45**, 2001, 23–26.

[66] Smith, B. A., Briggs, G. A., Danielson, G. E., Cook, A. F., Davies, M. E., Hunt, G. E., Masursky, H., Soderblom, L. A., Owen, T. C., Sagan, C. and Suomi, V. E., Voyager imaging experiment, *Space Science Reviews*, **21**, 1977, 103–127.

[67] Smith, S. G. L., The motion of a non-isolated vortex on the beta-plane, *Journal of Fluid Mechanics*, **346**, 1997, 149–179.

[68] Sommeria, J., Meyers, S. D. and Swinney, H. L., Laboratory model of a planetary eastward jet, *Nature*, **337**, 1989, 58–61.

[69] Trefil, J. and Hazen, R. M., *Physics matters*. John Wiley & Sons, Inc, New York, 2004.

[70] Vallis, G. K., *Atmospheric and oceanic fluid dynamics*. Cambridge University Press, Cambridge, 2006.

[71] Vatistas, G. H., A note on liquid vortex sloshing and Kelvin's equilibria, *Journal of Fluid Mechanics*, **217**, 1990, 241–248.

[72] Vatistas, G. H., Wang, J. and Lin, S., Recent findings on Kelvin's equilibria, *Acta Mechanica*, **103**, 1994, 89–102.

[73] Walker, J., Resnick, R. and Halliday, D., *Halliday & Resnick fundamentals of physics*. 9th ed. John Wiley & Sons, Inc, New Jersey, 2011.

[74] Wang, Y. and Holland, G. J., On the interactions of tropical-cyclone-scale vortices. IV: baroclinic vortices, *Quarterly Journal of the Royal Meteorological Society*, **121**, 1995, 95–126.

[75] Williams, D. R., Saturn fact sheet, at:NASA website. `http://nssdc.gsfc.nasa.gov/planetary/factsheet/saturnfact.html`, 2015.

[76] Wu, C. -C., Huang, T. -S., Huang, W. -P. and Chou, K. -H., A new look at the binary interaction: potential vorticity diagnosis of the unusual southward movement of tropical storm Bopha (2000) and its interaction with supertyphoon Saomai (2000), *Monthly Weather Review*, **131**, 2003, 1289–1300.

[77] von Winckel, G., lgwt.m, at:MATLAB file exchange website. `http://www.mathworks.com/matlabcentral/fileexchange/loadFile.do?objectId=4540&objectType=file`, 2004.

[78] Yang, H., Evolution of a Rossby wave packet in barotropic flows with asymmetric basic current, topography and δ-effect, *Journal of the Atmospheric Sciences*, **44**, 1987, 2267–2276.

[79] Ziv, B. and Alpert, P., Rotation of binary cyclones - A data analysis study, *Journal of the Atmospheric Sciences*, **52**, 1995, 1357–1369.